VARIABILITY OF CIRCULATION AND SEA ICE OVER THE EASTERN CANADIAN SHELF AND IN THE ADJACENT NORTHERN NORTH ATLANTIC OCEAN

by

Yuan Wang

Submitted in partial fulfilment of the requirements
for the degree of Doctor of Philosophy

at

Dalhousie University
Halifax, Nova Scotia
July 2021

To my father, in loving memory.

Table of Contents

LIST OF TABLES

LIST OF FIGURES

ABSTRACT

A significant gap remains in our understanding regarding the temporal-spatial variability of hydrodynamics over the eastern Canadian shelf (ECS) and in the adjacent northern North Atlantic Ocean (nNA). This thesis is a combination of studies on the dynamics of the large-scale circulation in the nNA and the processes affecting the circulation and sea-ice over the ECS. Based on output from a high-resolution model configuration for the years 1960-2009, the main physical processes driving the barotropic transport in the nNA were examined using a decomposition method based on the vertically-averaged momentum equations. This decomposition method has the advantage of revealing the major oceanic processes driving transport in the Gulf Stream and around the Labrador Sea and for diagnosing quasi-steady meso-scale features. Our results show that the potential energy term dominates the variability in most of the nNA in the model, while the mean flow advection and eddy momentum flux terms are important in the western boundary currents. A coupled ice-ocean circulation model is applied to the ECS and the adjacent northwest Atlantic to examine the impact of tides on the baroclinic circulation and temporal-spatial variability of hydrography and sea-ice over the ECS. The results show that the circulation and hydrography are affected significantly by tides in the Gulf of Maine, Bay of Fundy, Georges Bank (GeB), and the St. Lawrence River Estuary. Significant hydrographic anomalies are generated by tidal mixing and frontal circulations at tidal fronts, and then spread by residual circulations into broader areas. Strong internal tides are generated at the shelf edge southeast of GeB. The analysis of simulated sea-ice volume in the Gulf of St. Lawrence demonstrates a dominant balance between the open water ice formation and the basal melt at the ice-ocean interface. The former is significantly affected by the winter air temperature, while the latter is controlled by the stratification and circulation.

LIST OF ABBREVIATIONS AND SYMBOLS USED

Abbreviation	Definition
3D	three-dimensional
AG	Anticosti Gyre
AGRIF	Adaptive Grid Refinement in FORTRAN
AI	Anticosti Island
AZMP	Atlantic Zone Monitoring Program
BoF	Bay of Fundy
BPT	Bottom Pressure Torque
CFSR	Climate Forecast System Reanalysis
CIL	Cold Intermediate Layer
CS	Cabot Strait
CTD	Conductivity-Temperature-Depth
DFO	Department of Fisheries and Oceans
EBn	Emerald Basin
ECh	Esquiman Channel
ECS	eastern Canadian shelf
EMCC	Eastern Maine Coastal Current
EMF	Eddy Momentum Flux
GB	Grand Banks
GeB	Georges Bank
GEBCO	General Bathymetric Chart of the Oceans
GEOMAR	Helmholtz Centre for Ocean Research Kiel
GSC	Great South Channel
GSL	Gulf of St. Lawrence
JEBAR	Joint Effect of Baroclinicity and Relief

Abbreviation	Definition
KE	Kinetic Energy
LC	Labrador Current
LIM2	Louvain-la-Neuve sea Ice Model version 2
LS	Labrador Shelf
ME	Mann Eddy
MEOPAR	Marine Environmental Observation Prediction and Response Network
NEMO	Nucleus for European Modelling of the Ocean
MFA	Mean Flow Advection
MI	Magdalen Islands
NAC	North Atlantic Current
NAO	North Atlantic Oscillation
NaS	Nantucket Shoals
NfS	Newfoundland Shelf
nNA	Northern North Atlantic
OSU	Oregon State University
OTIS	Oregon State University Tidal Inversion Software
PE	Potential Energy
RMSD	Root mean square difference
SBI	Strait of Belle Isle
SLRE	Strait of Belle Isle Estuary
ScS	Scotian Shelf
SST	Sea Surface Temperature
SSS	Sea Surface Salinity
SWM	Shallow Water Model
VIKING20	North Atlantic Nest at 1/20°
WMCC	Western Maine Coastal Currents

Symbol	Description	Units
a	radius of earth	Km
A_h	lateral eddy viscosity coefficient	$m^2\ s^{-1}$
A_v	vertical eddy diffusivity coefficient	$m^2\ s^{-1}$
C_{Ti}	sea ice concentration	
$\mathcal{F}$	external atmospheric forcing	
f	Coriolis parameter	s^{-1}
(F_x, F_y)	Laplacian lateral mixing term	$m^2\ s^{-1}$
g	acceleration due to gravity	$m\ s^{-2}$
H	water depth	M
p_a	atmospheric pressure	Pa
r	linear bottom friction coefficient	$m\ s^{-1}$
T_i	tidal impact index	
(u, v, w)	velocity vector	$m\ s^{-1}$
$\mathbf{U}^T$	horizontal current vectors from WithTide	$m\ s^{-1}$
$\mathbf{U}^{NT}$	horizontal current vectors from NoTide	$m\ s^{-1}$
ϵ_A	tidal magnitude average error	M
$\epsilon_\emptyset$	tidal phase average error	^{o}
θ	Latitude	^{o}
ρ_o	reference water density	$kg\ m^{-3}$
ρ_m	horizontally averaged mean density	$kg\ m^{-3}$
λ	Longitude	^{o}

ACKNOWLEDGEMENTS

I would like to thank my co-supervisors for their help and support in my PhD study. Jinyu Sheng, for his dedicated supervision, meticulous revisions and encouragements, and generous financial support to make this thesis a reality. Richard Greatbatch, for his constructive guidance for the two fruitful research visits in Kiel, his inspiration and optimism, as well as the sense of humour. It is my great honour to have them. I would also like to thank the members of my advisory committee, Katja Fennel, Youyu Lu, Eric Oliver, and Hal Ritchie, for their contribution and insightful comments to improve this thesis. I am particularly grateful to Youyu Lu for his great help in setting up the model and constructive comments on the tidal work.

Many thanks to Martin Claus, my collaborator in Helmholtz Centre for Ocean Research Kiel (GEOMAR), for making my research visits in Kiel successful and pleasant. Special thanks also go to Swantje Bastin, Annika Drews, and Gereon Gollan for their insightful discussions during my stay in Kiel.

I want to thank the members of the Ocean Modeling Group, Colin Hughes, Shangfei Lin, Kyoko Ohashi, Albert Pei, Qingtao Song, Shiliang Shan, Yi Sui, Jorge Urrego-Blanco, Pengcheng Wang, Qi Wang, Shengmu Yang, and Heng Zhang, for sharing knowledge and cheering together. Many thanks go to my TOSST and HOSST colleagues for sharing the great experience over those years. Special thanks go to Jackie Hurst, Lori Lawton, and Daniel Morrison for their professional support.

Finally, I would like to thank my wife and parents, for their endless love and support throughout the delight, depression, and grief over the years. My beloved father would be in great happiness if he could survive cancer this winter.

This PhD work was supported by the TOSST program, Marine Environmental Observation Prediction and Response Network (MEOPAR), the Natural Sciences and Engineering Research Council of Canada (NSERC), Helmholtz Centre for Ocean Research Kiel (GEOMAR), and the Ocean Frontier Institute (OFI).

CHAPTER 1

INTRODUCTION

The ocean is an essential component in the global climate system (e.g. Rhein et al. 2013). In particular, the ocean circulation plays an important role for understanding the distribution and transport of heat, salt, carbon and many other biogeochemical species that are important for global climate and climate change. The great progress in remote sensing and Argo technology in recent decades enables us to reconstruct ocean conditions in space and time with significantly improved coverage compared to earlier times (Robinson 2004; Roemmich et al. 2019). In comparison with other ocean basins, the North Atlantic is the most intensively observed basin but only a few circulation components, and often at a few limited locations, have been well measured. Meanwhile, ocean circulation models have been used in companion with observations to provide a complete spatial coverage, while a satisfactory representation in the model of many oceanic features is still missing (see reviews in Schmitz and McCartney 1993; Reid 1994; and Fox-Kemper et al. 2019). Better understanding of the main physical processing affecting the ocean circulation and the associated variability would be beneficial to the development of ocean models as well as the planning of observational programs. Further studies are required to examine the role of physical processes driving the ocean circulation in the North Atlantic.

1.1 The Large-scale Circulation in the northern North Atlantic Ocean

The northern North Atlantic Ocean (nNA) to be considered in this thesis is the Atlantic Ocean north of 30°N, excluding waters to the east and north of Iceland. The large-scale circulation over this region consists of two major gyre circulations (Figure 1.1).

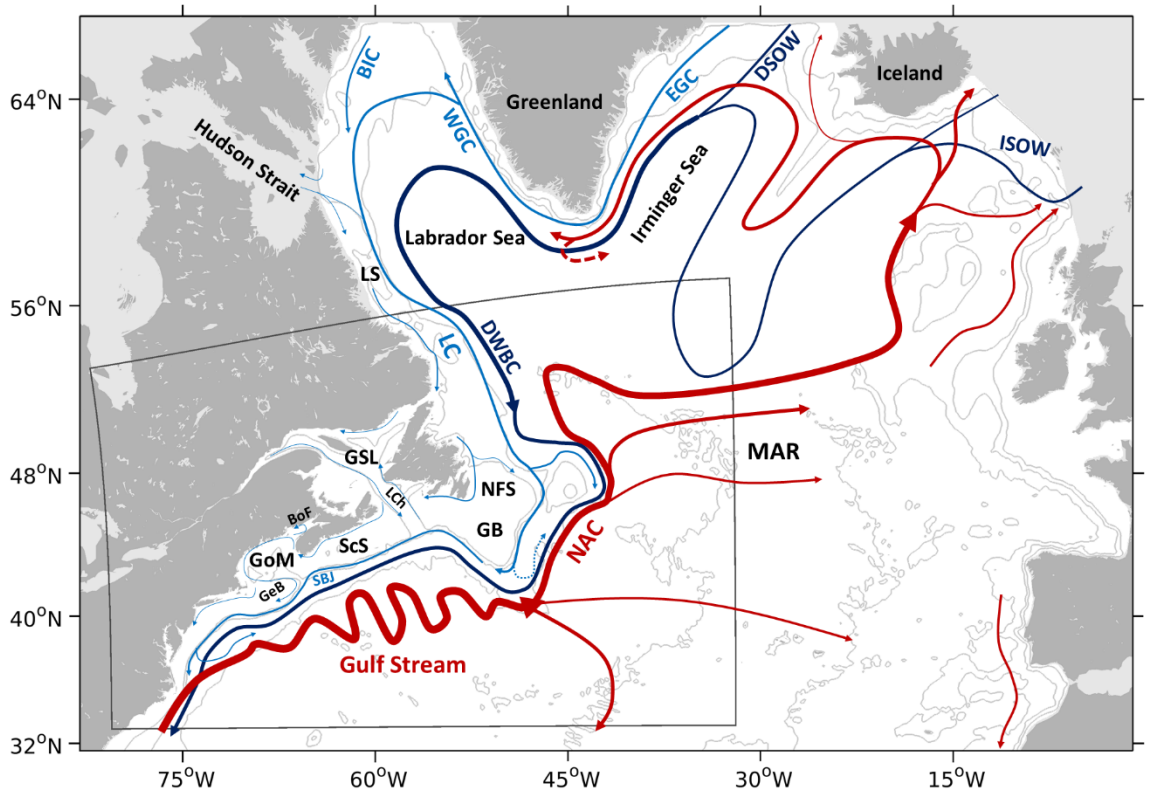

Figure 1.1. Schematic of general circulation features over the northern North Atlantic. Contours are the smoothed isobaths for 200, 1000, and 4000m depth. The domain of the regional model is shown in the black box. Abbreviations are given for the Labrador Shelf (LS), Newfoundland Shelf (NFS), Grand Banks (GB), Gulf of St. Lawrence (GSL), Laurentian Channel (LCh), Scotian Shelf (ScS), Gulf of Maine (GoM), Bay of Fundy (BoF), Georges Bank (GeB), Mid Atlantic Ridge (MAR), East Greenland Current (EGC), West Greenland Current (WGC), Baffin Island Current (BIC), Labrador Current (LC), Shelf Break Jet (SBJ), Deep Western Boundary Current (DWBC), North Atlantic Current (NAC), Iceland-Scotland Overflow Water (ISOW), and Denmark Strait Overflow Water (DSOW).

The subtropical gyre, over the southern part of this region, is dominated by the Gulf Stream, which is the continuation of the poleward Florida Current. The Gulf Stream turns eastward at Cape Hatteras and reaches a maximum transport of about 150 Sv near 60°W (Hogg 1992). Over the Southeastern Newfoundland Rise, the Gulf Stream separates into three branches (Rossby 1996): a broad return flow feeding a recirculation back toward

Cape Hatteras (Hogg 1992); a branch drifting eastward as part of the Azores Current (Käse and Siedler 1982); and a branch turning northward, known as the North Atlantic Current (NAC) (Krauss 1986). To the east of the GB, the NAC flows northeastward on the offshore side of the LC and turns sharply eastward at about 52°N, in an area known as the Northwest Corner (Lazier 1994). The eastward flowing NAC crosses the Mid Atlantic Ridge in three main branches associated with the topographic fracture zones (Bower and von Appen 2008; Roessler et al. 2015). The NAC waters either continue northeastward into the Norwegian Sea, or merge into the subpolar gyre circulation, to the east of Greenland, as the Irminger Current (Rossby 1996; Reid 1994; Read 2000). Over the south tip of Greenland, a significant portion of the Irminger Current is retroflected to recirculate in the Irminger Sea, while the rest flows on the upper slope along with the West Greenland Current (Cuny et al. 2002; Holliday et al. 2007; Fratantoni and Pickart 2007; Myers et al. 2009; Våge et al. 2011). The variability of the NAC plays a significant role in climate shifts at higher latitudes (Krauss 1986; Czaja and Frankignoul 2002) and in changes in deep convection (e.g. Renssen et al. 2002).

The subpolar gyre features a sharp thermohaline front at the shelf break, extending from the Greenland coast, around the Labrador Sea, along the Newfoundland Shelf, Scotian Shelf, and Georges Bank, and to the Mid Atlantic Bight. The currents associated with these thermohaline fronts, sustained by Arctic-origin waters and coastal runoffs, have various regional names, including the East Greenland Current, West Greenland Current, Labrador Current, and the Shelf Break Jet. Despite the distance of more than 5000 km, this is a single large-scale current based on its isotopic and hydrographic characteristics (Chapman and Beardsley 1989; Fratantoni and Pickart 2007). Apart from this current at the shelf break in the upper ocean, the deep circulation residing at 500 m to over 4000 m depth includes the lower limb of the Atlantic Meridional Overturning Circulation. The Atlantic Deep Western Boundary Current (DWBC) forms on the eastern continental slope of Greenland, by combining Denmark Strait Overflow Water and the Iceland-Scotland Overflow Water traveling across the Mid Atlantic Ridge, as well as waters produced by deep convection in the Labrador and Irminger Seas (McCartney 1992; Spall and Pickart 2001; Pickart et al. 2003). The DWBC flows equatorward around the Labrador Sea, along the continental slope of the ECS, and under the Gulf Stream near Cape Hatteras (Pickart and Smethie 1993).

The dynamics of the barotropic (vertically-averaged) circulation of the North Atlantic have been examined in the past in terms of the vorticity equation (e.g. Myers et al., 1996). The dynamics of the western boundary currents (e.g., the Gulf Stream/NAC), however, remain a significant challenge to be reproduced by numerical ocean circulation models (e.g. Chassignet and Marshall 2008; Drews et al. 2015; Brennan et al. 2016). The importance of the wind stress curl in the dynamics of wind-driven gyres was revealed in the early studies of Stommel (1948) and Munk (1950) based on models with a flat-bottomed ocean and uniform density, extending the work of Sverdrup (1947). Later, the important role of the Joint Effect of Baroclinicity And Relief (JEBAR) was recognised by Sarkisyan and Ivanov (1971). By including JEBAR in a model with variable bottom topography, the simulated maximum transport of the Gulf Stream increased from 14 Sv to 81 Sv, which is a significant improvement in reconstructing the observed transport of the Gulf Stream using a ocean circulation model (Holland and Hirschman 1972). Meanwhile, Holland (1973) demonstrated that the bottom pressure torque (BPT), arising by including bottom topography and baroclinic effects in a wind and thermohaline-driven ocean model, can significantly enhance the transport of the western boundary current, enabling it to exceed the transport that is predicted by the flat-bottom Sverdrup relation. Both the JEBAR and BPT are derived from the pressure gradient term in the momentum equations, depending on whether the momentum equations are vertically-averaged (the former) or vertically-integrated (the latter). Greatbatch et al. (1991) compared the JEBAR and BPT, using the diagnostic model of Mellor et al. (1982) combined with an estimate for the observed density field. These authors also suggested a streamfunction decomposition based on the linear momentum/vorticity balance. Later, Greatbatch et al. (2010) demonstrated the significant contribution of the eddy momentum flux, arising from the non-linear advection term in the momentum equation, for determining the Gulf Stream transport. However, that contribution was computed using a diagnostic barotropic model driven by satellite-derived eddy momentum forcing with a presumed vertical profile, and could not easily be compared to the contribution by the other terms in the momentum equation in the same context. Several previous studies were conducted for exploring the impact of the topography, wind, and baroclinic effects on the large-scale circulation (e.g., Mertz and Wright 1992; Hallberg and Rhines 1996; Myers et al. 1996; Bell 1999; Yeager 2015),

especially the western boundary currents. Relatively little work, however, has been done for determining the role of the non-linear advection of momentum and vorticity, in comparison to the wind and baroclinic effects, a research topic explored in Chapters 2 and 3 of this thesis.

1.2 From the Deep Ocean to the Shelf Waters

The shelf break, where the bottom slope, connecting the coastal and shelf waters to the deep ocean, suddenly increases, applies a strong dynamical (geostrophic) constraint on the low-frequency circulation (e.g. Smith and Sandstrom 1988; Allen et al. 2009; Brink 2016). The hydrodynamics over the shelf break and adjacent waters are also associated with high frequency non-linear processes. The ability of models to simulate correctly the shelf-ocean exchange across the shelf break is critical for many studies, such as the influence of climate change and large-scale climate variability on the shelf from the neighbouring North Atlantic (e.g. Condron and Winsor 2011; Saba et al. 2015). In particular, the ECS and its adjacent northwest Atlantic Ocean lie in the confluence zone of the North Atlantic subpolar gyre and the North Atlantic subtropical gyre. The interaction between the two gyres introduces substantial variability of circulation and hydrography over the ECS and the adjacent North Atlantic waters (Petrie and Drinkwater 1993; Lazier 1994).

The ECS considered in this thesis consists of five sub-regions: the Labrador Shelf (LS), Newfoundland Shelf (NFS), Gulf of St. Lawrence (GSL), Scotian Shelf (ScS), and Gulf of Maine (GoM) (Figure 1.1). The general circulation on the ECS is affected significantly by the equatorward LC. The LC has an inshore branch near the coast and a major offshore branch on the shelf break over the Labrador and Newfoundland Shelves, and also on the continental slope further offshore (Lazier and Wright 1993). Over the inner shelves and gulfs of the ECS, the cold and fresh subarctic origin waters, associated with the inshore branch of the LC, are gradually transformed by interactions under the action of the local dynamics, including wind, buoyancy fluxes, tides, sea-ice, and the highly irregular topography (Loder et al. 1998). A small portion of the inshore branch of the LC enters the GSL via the Strait of Belle Isle (SBI) (Petrie et al. 1988), and the remainder flows around the east and south coasts of Newfoundland to the Laurentian Channel (LCh) (Petrie and

Anderson 1983; Urrego-Blanco and Sheng 2014a). These two branches of the inshore LC merge with the Gulf-wide cyclonic circulation in the GSL. The GSL circulation features a two-way flow in the LCh, with landward (seaward) flow along the east (west) side of the Channel (Koutitonsky and Bugden 1991). This seaward flow bifurcates over the eastern edge of the ScS. One branch is confined over the inner shelf of the ScS to flow southwestward as the Nova Scotian Current, which then enters the GoM. The other branch flows southeastward over the western side of the LCh and then merges with the offshore branch of the equatorward LC, where it is called the Shelf Break Jet. The Shelf Break Jet enters the GoM via the Northeast Channel. The circulation in the GoM follows the topography in a cyclonic pattern around the inner Basin but with anticyclonic flow around Georges Bank (Lynch et al. 1996). A cyclonic circulation is found in the Bay of Fundy (Aretxabaleta et al. 2008).

On the ECS, the relative cold and fresh LC flows equatorward along the shelf break of the Labrador Shelf without significant offshore transport (Loder et al. 1998; Myers 2005) until significant interaction takes place with the NAC to the east of the Grand Banks. The remaining LC, downstream of the Grand Banks, plays a big role in the interannual variability of the adjacent shelf waters, including the GSL, the ScS, and the GoM (Petrie and Drinkwater 1993; Pershing et al. 2002; Urrego-Blanco and Sheng 2012; Brickman et al. 2018). Various processes are known to be involved in the shelf-ocean exchange on the ECS, such as flow associated with the deep channels, frontal eddies, and rings shed from the Gulf Stream (Smith and Sandstrom 1988; Joyce et al. 1992; Allen et al. 2009). Hence, to model shelf-ocean exchange, good models are required of which the model presented in Chapter 4 as a start.

1.3 Important Processes on the Hydrodynamics over the ECS

The circulation and hydrography on the ECS are affected significantly by the topography, winds, tides, buoyancy forcing, and occasionally tropical and winter storms (Smith and Schwing 1991; Loder et al. 1998). A wide range of temporal and spatial scales of physical processes result in large variability in the water mass structure and circulation, making the

ECS one of the most variable areas of the North Atlantic and Pacific Oceans (Thompson et al. 1988; Loder et al. 1998). Three important processes are examined in this thesis.

1.3.1 Tides

Two thirds of the tidal energy is dissipated on continental shelves globally (~2 TW), with about 60 GW over the GSL, ScS, and GoM-BoF (Egbert and Ray 2000, 2003). The highest tides on the ECS reach a range of about 16 m in the upper BoF due to the resonant effect (Garrett, 1972) and are regarded as the highest tides in the world. The barotropic tidal circulation has been widely studied over the ECS (e.g. Greenberg 1983; Petrie et al. 1987; Pingree and Griffiths 1980; Dupont et al. 2002). Considerable interactions between tides and topography and baroclinic effects are suggested to take place over the GSL, the shallow banks of the ScS, GoM-BoF, and Georges Bank (Loder 1980; Loder and Wright 1985; Tee et al. 1993; Han et al. 1999; Lu et al. 2001a; Hannah et al. 2001), which are important for transforming tidal energy (primarily at semi-diurnal and diurnal frequency) to much longer time scales. Recent studies with high-resolution models show significant seasonal variability in the interaction between the tidal circulation and baroclinic circulation on the southwestern ScS and northern flanks of the Georges Bank (Ohashi et al. 2009; Katavouta et al. 2016; Chegini et al. 2018). The temporal-spatial tidal impact on the circulation and hydrography over the ECS remains to be fully studied.

Regarding the large-scale circulation in the ocean, tidal dissipation is responsible for half of the energy required to maintain the thermohaline circulation on the millennium time scale (Munk and Wunsch 1998; Egbert and Ray 2000). By including tides in a global climate model, Müller et al. (2010) found the modelled pathway of the North Atlantic Current is improved in a 50 years simulation. On the other hand, the long-term impact (longer than the residence time of the shelf waters of O(1) years) of tides on the circulation and hydrography of the ECS still need to be examined and quantified. Chapter 4 contributes to this goal.

1.3.2 Deep Channel Flows

Deep channels and canyons are common over the ECS, and have significant implications for the shelf-ocean exchange important for the GSL, ScS, and GoM (Ramp et al. 1985;

Bugden 1988; Petrie and Drinkwater 1993). Among those channels and canyons, the LCh is the most distinguished one. The LCh extends NW–SE over 900 km from the St. Lawrence River Estuary (SLRE), across the GSL to the edge of the continental shelf south of Newfoundland. The LCh, up to 450 m deep at the mouth on the shelf break, is the only pathway for the deep water to enter the GSL. The landward flow entering the GSL through Cabot Strait accounts for the major part (~80% (Urrego-Blanco and Sheng 2014a)) of the transport exchange between the GSL and the Atlantic Ocean (Koutitonsky and Bugden 1991). The landward flowing waters are dominated by the subpolar water near the surface and become relatively warm and salty in the deep layer (150-350 m). The water mass in the deep layer of this landward flow is a mixture of the subpolar water and the subtropical water in variable proportions (Bugden 1991; Gilbert et al. 2005), which is, in turn, affected by the LC passing the tail of the GB (Loder et al. 1998; Fratantoni and McCartney 2010; Urrego-Blanco and Sheng 2012). Gilbert et al. (2005) suggested that up to two thirds of the long-term decline in oxygen levels in the deep water of the SLRE can be attributed to the increased proportion of the subtropical water in the landward flow.

The LCh shoals from over 200 m to 50 m depth at its head in the SLRE, where the relatively warm and nutrient-rich deep water is found partly upwelled and vertically mixed due to tides (Ingram 1983; Saucier and Chassé 2000; Cyr et al. 2015). Such upwelling and mixing leads to a wintertime sensible heat polynya (Saucier 2003), and also dramatically affects the food web dynamics in the GSL (Ouellet et al. 2013; Cyr et al. 2015). However, the variability of the flow in the LCh and its impact on the circulation and hydrography in the GSL are still not well understood (Drinkwater and Bugden 1994; Koutitonsky and Bugden 1991). The along channel propagation of the anomalies generated in deep waters (Urrego-Blanco and Sheng 2012; Brickman et al. 2018), cross channel mixing, and the role of different processes in the low frequency variability (e.g., interannual) of the flow in the LCh are still open for further studies. The model described in Chapter 4 offers a tool for this purpose.

1.3.3 Sea-ice

Sea-ice cover advances and retreats seasonally over the LS, GSL, and occasionally the eastern ScS (Canadian Ice Service 2009). The GSL, with ice cover from late December to

May, is at the southern margin of the winter ice cover in the Northern Hemisphere. Sea-ice is suggested to be an important component in air-sea interaction processes over the GSL, which affects regional climate, ocean circulation, and water mass formation (Saucier 2003; Pellerin et al. 2004; Smith et al. 2006a; Urrego-Blanco and Sheng 2014b). The sea-ice formation associated brine rejection enhances winter convection and mixing in the GSL. Nutrients are brought to the surface by the winter convection and mixing, supporting the biologically productive GSL which accounts for nearly 25% of the total Canadian commercial fish catch by weight (Koutitonsky and Bugden 1991).

Sea-ice observational data for the GSL used in many previous studies, are primarily the sea-ice concentrations inferred from satellite images (Canadian Ice Service 2006). Studies have been made to understand the climatology and anomaly of the sea-ice area (integrated from sea-ice concentrations) (e.g. Drinkwater et al. 1999). The long-term trend of the sea-ice area is decreasing in recent decades over the Northern Hemisphere, but the trend in the GSL is not as significant as that for many other regions in the Northern Hemisphere (Parkinson and Cavalieri 2008; Cavalieri and Parkinson 2012). The role of environmental forcings on the interannual/seasonal variability of the sea-ice area in the GSL is still not well understood (Li 2000). The limited direct measurement of ice thickness in the GSL and large uncertainty in converting the stage of development to ice thickness discourage budget analysis of the sea-ice in the GSL, which is important for a comprehensive understanding of the sea-ice variability.

Various types of ocean models were used for simulating circulation and sea ice in the GSL. The first coupled circulation-ice model for the GSL was developed by Saucier et al. (2003), and their model results suggested significant sensitivity of the sea-ice volumetric growth to the ocean stratification in late fall. With a 17-year simulation, Urrego-Blanco and Sheng (2014b) identified the primary ice formation areas to be over the northern GSL coast. They also found the thermodynamic contribution to the sea-ice volume variability to be comparable to that of the advection, but with a decreasing importance for thermodynamics seaward from Cabot Strait. Although ocean models can provide sea-ice fields with good temporal and spatial coverage for in-depth analysis, challenges in reproducing the observed sea-ice distributions in the GSL were also noted (Saucier 2003;

Urrego-Blanco and Sheng 2014b; Brickman and Drozdowski 2012). It follows that the validity of conclusions drawn from studies is still limited by model performance issues.

Further studies are necessary to identify the main processes determining the overall magnitude of the sea-ice fields and their spatial variability in the GSL, and to achieve a budget of the sea-ice in the GSL, including distinguishing local and non-local sources and sinks. A model with improved performance can be used to examine the role of sea-ice in this coupled air-ice-ocean system.

1.4 Objectives and Thesis Outline

The main objective of this thesis is to improve our understanding of the temporal-spatial variability of circulation and sea ice over the ECS and of the dynamics of the large-scale circulation in the nNA, especially the western boundary currents that impose significant impact on the ECS. The following scientific questions are considered in this thesis:

(1) What is the contribution to the barotropic transport in the nNA from the four major dynamical terms arising from the vertically-averaged momentum equations, assessed by applying the corresponding forcings to a linear shallow water model (SWM), following the approach of Greatbatch et al. (2010)? The four major dynamic terms in the vertically-averaged momentum equation represent respectively the wind forcing (for a uniform density ocean), the potential energy (baroclinic effects), mean flow advection, and the eddy momentum flux. These four teams can be computed from the model output of VIKING20. VIKING20 is a high-resolution (1/20°) ocean model configuration for the northern North Atlantic Ocean (Behrens 2013). By diagnosing the contribution of the four terms in the same framework, one can examine what the relative importance of the four terms in driving the barotropic transport of the nNA are in the model.

(2) How good is this linear combination of contributions, regarding the four terms, at representing and explaining the interannual variability of the barotropic transport in the VIKING20 model configuration? What is the contribution from the four terms mentioned above to the temporal variability in response to forcing from the atmosphere, in particular the North Atlantic Oscillation (NAO)?

(3) Given that tides are not included in VIKING20, a regional model including tidal dynamics is explored. What are the impacts of tides on the circulation and associated hydrographic variability on the ECS and in adjacent deep waters?

(4) What are main physical processes affecting the seasonal sea-ice growth, maintenance, and decay in the GSL? Is the sea-ice in the GSL driven only by local dynamics?

The structure of this thesis is as follows. Chapter 2 presents the contribution of the four terms in driving the mean barotropic circulation over the nNA in VIKING20. Chapter 3 examines the variability of the barotropic circulation in VIKING20, particularly in response to the NAO. Chapter 4 presents the tidal impacts on the baroclinic circulation on the ECS, and Chapter 5 examines the main physical processes affecting the sea-ice in the GSL. A summary of the main results and an outlook of future work are presented in Chapter 6.

Chapters 2-5 are based on four separate papers. Therefore, some similar background material occurs in these Chapters, in particular regarding the methodology of the streamfunction decomposition, and the model setup of a Northwest Atlantic regional model. Chapter 2 was published in Geophysical Research Letters under the title of "Decomposition of the mean barotropic transport in a high-resolution model of the North Atlantic Ocean" (Wang et al. 2017). Chapter 3 was published in Journal of Geophysical Research-Oceans under the title of "Decomposing barotropic transport variability in a high‐resolution model of the North Atlantic Ocean" (Wang et al. 2020a). Chapter 4 was published in Progress in Oceanography under the title of "Examining tidal impacts on seasonal circulation and hydrography variability over the eastern Canadian shelf using a coupled circulation-ice regional model" (Wang et al. 2020b). Chapter 5 will be submitted after revision to Continental Shelf Research under the title of "The main physical processes affecting the sea-ice in the Gulf of St. Lawrence".

CHAPTER 2

DECOMPOSITION OF THE MEAN BAROTROPIC TRANSPORT IN A HIGH-RESOLUTION MODEL OF THE NORTHERN NORTH ATLANTIC OCEAN[1]

2.1 Introduction

The Gulf Stream and its extensions play an important role in the Northern Hemisphere climate (Minobe et al. 2008; Scaife et al. 2014; O'Reilly et al. 2016), because of its massive volume transport and associated redistribution of heat and salinity (Böning et al. 2016; Trenberth and Caron 2001). After the Gulf Stream detaches from the shelf break at Cape Hatteras, its volume transport increases dramatically up to about 150 Sv (Fuglister 1963). This increase in transport has been attributed to the presence of the Northern Recirculation Gyre on its north side and the Worthington Gyre on its south side (Hogg et al. 1986; Hogg 1992; Worthington 1976). The Gulf Stream re-attaches to the bottom slope at the southern tip of the Grand Banks of Newfoundland and the Newfoundland Ridge. Its main branch follows the slope of the Newfoundland Shelf northward as the North Atlantic Current (NAC), before it turns sharply eastward at the northwest corner, heading towards Europe.

The dynamics of the northwest corner (centered at about 50°N and 45°W) (Lazier 1994) and the recirculation gyres associated with the Gulf Stream and its extensions are not fully understood, and general circulation models have trouble reproducing these features of the circulation. Typically, for example, the northwest corner is missing due to the misplaced

[1] Wang, Y., M. Claus, R. J. Greatbatch, and J. Sheng, 2017: Decomposition of the Mean Barotropic Transport in a High-Resolution Model of the North Atlantic Ocean. *Geophys. Res. Lett.*, **44**, 11,537-11,546.

NAC (see Delworth et al. 2012; Flato et al. 2013; Drews et al. 2015; Griffies et al. 2015), leading to the so-called "cold bias" that, in turn, can be detrimental to the representation of low frequency variability in models (Drews and Greatbatch 2016, 2017) and also to the overlying atmosphere in coupled models (Scaife et al. 2011; Keeley et al. 2012). Furthermore, the region of the Mann Eddy (centered at about 42°N and 46°W) is suggested to be a pivotal point in modulating variability of the Atlantic Meridional Overturning Circulation (Tulloch and Marshall 2012).

The main dynamics driving the recirculation gyres have long been studied. It was suggested that the deep circulation plays an important role in their dynamics through the bottom pressure torque and associated bottom vortex stretching (Holland 1973; Greatbatch et al. 1991; Zhang and Vallis 2007). Recirculation gyres were also modelled using extensions to a stratified ocean of the Fofonoff (1954) model (Marshall and Nurser 1986; Greatbatch 1987). In these models, the eddy fluxes provide a weak forcing while it is the advection by the mean flow, in particular the advection of mean vorticity in the time-averaged vorticity equation, that shields the recirculation gyres from the influence of the eastern boundary and allows the transport to exceed the Sverdrup transport. Hogg and Stommel (1985) noted earlier that closed potential vorticity contours can occur beneath the Gulf Stream due to the tilt of the isopycnals and the underlying topography (see also Greatbatch and Zhai 2006) and that transient eddies can drive large transports within these contours. More recently, Greatbatch et al. (2010) estimated that the transport driven by the eddy momentum fluxes alone is comparable to the observed total transport in the Gulf Stream and North Atlantic Current region. In that paper, the surface eddy momentum fluxes were derived from satellite altimetry observations. However, a vertical profile for the eddy momentum fluxes had to be assumed to calculate the vertical integral of the fluxes that is difficult to verify given the limited observations. One of the aims of the present study is to assess the importance of the eddy momentum fluxes, compared to other drivers for vertically-integrated transport, in a high resolution ocean model.

Traditionally, the vertically-integrated (barotropic) gyre transport in the ocean has been examined in terms of the vorticity equation derived from either the vertically-integrated or the vertically-averaged momentum equations (see, for example, Bell (1999) and Yeager

(2015)). The former approach (see Eq. (A.24) in Appendix A), based on vortex stretching of the water column, takes the flat-bottom Sverdrup transport (Eq. (A.25)) implied by the surface wind stress as its reference point, and the effect of variable bottom topography enters by means of the bottom pressure torque (see Holland (1973) for an early example). On the other hand, when considering the vorticity equation derived from the vertically-averaged momentum equations (Eq. (A.21)), the reference is the topographic Sverdrup transport for a uniform density ocean (Eq. (A.22)). The effect of density stratification is included by means of the JEBAR term (see Mertz and Wright (1992) for a detailed discussion of JEBAR), an approach dating back to Sarkisyan and Ivanov (1971). Greatbatch et al. (1991) exploited these two different approaches in order to suggest a decomposition of the gyre transport into its different components and illustrated their decomposition for the North Atlantic using the diagnostic model of Mellor et al. (1982). Bell (1999) and Yeager (2015) discussed both approaches applied as model diagnostics, the former focusing on the North Atlantic and the representation of the Gulf Stream in models, and latter showing how the same approach can be used to provide a decomposition for the meridional overturning circulation in models. Neither Bell (1999) nor Yeager (2015) used circulation models that included eddies and were, therefore, unable to make a statement about the transport that is driven by the eddy momentum fluxes.

In order to infer the transport driven by the eddy momentum fluxes, Greatbatch et al. (2010) used a barotropic, linear shallow water model driven by forcing terms that were specified in the horizontal momentum equations. The barotropic model solves for the vertically-averaged (barotropic) velocity and the forcing terms were derived by vertically-averaging the momentum flux convergence implied by the satellite-derived surface eddy momentum fluxes based on the assumed vertical profile. Their approach is therefore based on the vertically-averaged, rather than the vertically-integrated, momentum equations. In the present study, we extend this approach to include, additionally, forcing terms associated with mean flow advection, the potential energy (which leads to the JEBAR term in the vorticity equation) and direct wind forcing (as for a uniform density ocean) – see Eq. (A.11). A detailed derivation of the forcing terms is given in Appendix A. The forcing terms are, in turn, derived from a high-resolution ocean model that includes mesoscale eddies. We show that the local vorticity budget in the model is quite noisy and is dominated by small

spatial scales from which it is difficult to infer the relative importance of the different forcing terms. Dynamically computing the implied transport using the shallow water model acts as an effective filter enabling the transport streamfunction from the high-resolution model to be decomposed into its separate parts.

Model outputs from a high-resolution ocean model VIKING20 (Behrens 2013) are used here. VIKING20 has the advantage that it captures the Gulf Stream, NAC and their associated recirculation gyres without data assimilation (see Mertens et al. (2014) and Breckenfelder et al. (2017) for a detailed assessment of the performance of VIKING20). Section 2.2 presents the four forcing terms and discusses the setup of the linear shallow water model used to compute the transport driven by each forcing term. Results for the mean transport averaged over 50 years (1960-2009) are shown and discussed in Section 2.3. A summary and discussion are given in Section 2.4.

2.2 Method

VIKING20 uses a two-way nested ocean model configuration, which consists of a high-resolution (1/20°) component (referred to as the nest in the following) for the northern North Atlantic (nNA, about 30°N-85°N) and a global component of roughly 1/4° horizontal resolution (referred to as the base). Both components are composed of the Nucleus for European Modelling of the Ocean (NEMO) (Madec 2008), using the Océan PArallélisé (OPA) system for ocean circulation, and the Louvain-la-Neuve Ice Model (LIM2) for sea ice. The two-way nesting is accomplished with the help of the AGRIF system (see Behrens (2013) and Böning et al. (2016) for the details). After a 30-year spin-up of the base component alone, VIKING20 was integrated from 1948 to 2009 using the CORE2 atmospheric forcing (Large and Yeager 2009). Output produced by the nest component of VIKING20 during the period 1960-2009 is used in this study to calculate the forcing terms for the vertically- and time-averaged horizontal momentum equations. It should be noted that the separation between the mean and the perturbation velocity is carried out each year separately, following Rieck et al. (2015). As such, the mean flow advection forcing also includes a rectified contribution from the interannual variability.

To compute the barotropic transport driven by each of the forcing terms, we use a linear, barotropic shallow water model (SWM) that is run to steady state. In steady state, the equations governing the SWM are:

$$-fv = Z - \frac{1}{\rho_0 a cos\theta}\frac{\partial p_b}{\partial \lambda} - \frac{ru}{H} + F_x \tag{2.1}$$

$$fu = M - \frac{1}{\rho_0 a}\frac{\partial p_b}{\partial \theta} - \frac{rv}{H} + F_y \tag{2.2}$$

$$0 = \frac{1}{acos\theta}\left[\frac{\partial Hu}{\partial \lambda} + \frac{\partial cos\theta Hv}{\partial \theta}\right] \tag{2.3}$$

where each of the four forcing terms in turn is denoted as (Z, M), where Z is the zonal component and M the meridional component. It should be noted that the free surface variable in the SWM should be interpreted as the bottom pressure, p_b, a is the radius of the Earth, (λ, θ) are longitude and latitude, u and v are vertically-averaged velocities in the eastward and northward directions, respectively, H is the ocean bottom depth, r is a linear bottom friction coefficient and (F_x, F_y) denotes a horizontal Laplacian viscosity term with lateral eddy viscosity coefficient given by A_h (see Appendix A for the detailed expression).

The forcing terms, (Z, M), are computed from the output of the nest component of VIKING20 for each year separately and then averaged over all years to provide the forcing for the SWM. The formulation of (Z, M) in the four cases is given below (the detailed derivation is given in Appendix A), where an overbar denotes a time average over a single year (following Rieck et al. (2015)) and $< >$ a vertical integral from $z = -H$ (corresponding to the ocean bottom) to $z = 0$ (the ocean surface):

1. The potential energy term:

$$Z = -\frac{1}{Hacos\theta}\left[\frac{\partial}{\partial \lambda}\left\langle g\frac{\overline{(\rho - \rho_m)}}{\rho_0} z\right\rangle\right] \tag{2.4}$$

$$M = -\frac{1}{Ha}\left[\frac{\partial}{\partial\theta}\left\langle g\,\overline{\frac{(\rho-\rho_m)}{\rho_0}}\,z\right\rangle\right] \tag{2.5}$$

where ρ represents the in-situ density and ρ_m represents the horizontally-averaged mean density.

2. Mean flow advection:

$$Z = -\frac{1}{Hacos\theta}\left[\frac{\partial\langle\overline{u}\,\overline{u}\rangle}{\partial\lambda} + \frac{\partial cos\theta\langle\overline{u}\,\overline{v}\rangle}{\partial\theta}\right] \tag{2.6}$$

$$M = -\frac{1}{Hacos\theta}\left[\frac{\partial\langle\overline{v}\,\overline{u}\rangle}{\partial\lambda} + \frac{\partial cos\theta\langle\overline{v}\,\overline{v}\rangle}{\partial\theta}\right] \tag{2.7}$$

3. Eddy momentum flux:

$$Z = -\frac{1}{Hacos\theta}\left[\frac{\partial\langle\overline{u'u'}\rangle}{\partial\lambda} + \frac{\partial cos\theta\langle\overline{u'v'}\rangle}{\partial\theta}\right] \tag{2.8}$$

$$M = -\frac{1}{Hacos\theta}\left[\frac{\partial\langle\overline{u'v'}\rangle}{\partial\lambda} + \frac{\partial cos\theta\langle\overline{v'v'}\rangle}{\partial\theta}\right] \tag{2.9}$$

4. The wind stress term:

$$Z = \frac{\overline{\tau_s^x}}{\rho_0 H} \tag{2.10}$$

$$M = \frac{\overline{\tau_s^y}}{\rho_0 H} \tag{2.11}$$

The SWM in this study is very similar to the model described by Greatbatch et al. (2010), and is set up for the model domain covered by the high-resolution nest component of VIKING20. The model uses a staggered latitude/longitude C-grid with a horizontal resolution of 1/20° covering the North Atlantic between 85°W to 5°E and from 31°N to 67°N. The bottom topography is interpolated from that of the VIKING20 nest component to the SWM grid. To keep the model stable and restrict noise, a linear bottom friction

coefficient with $r = 5 \times 10^{-4}$ m s^{-1} and Laplacian horizontal viscosity coefficient $A_h = 150$ m^2 s^{-1} are applied. While there is some sensitivity to the choice of these values, the streamfunction computed from the SWM, when all four forcings are used together, is close to that from VIKING20, as we show in Figure 2.1 (more discussion later), suggesting that these values effectively mimic the dissipation in VIKING20. No attempt was made to extract the dissipation terms from VIKING20 itself (which, in any case, are not part of the available model output). In addition, to inhibit topographic instability associated with the steep and rough topography (Killworth 1987) on the high-resolution SWM grid, a 3-by-3 running average filter is applied to smooth regions with water depth less than 1000 m. Note that we want to preserve the topography in the deep ocean as close as possible to that of the nest component of VIKING20 since this study focuses on the large-scale barotropic transport in the open ocean rather than on the shelf. In addition, Hudson Strait, Davis Strait, Denmark Strait, the Faroe Bank Channels, the English Channel and the Strait of Gibraltar are all closed in the model.

Unlike the VIKING20 nest, the lateral boundaries of the SWM are closed, since we do not attempt to decompose the open boundary forcing for the VIKING20 nest component according to each forcing term. Since there are f/H contours that enter the model domain at the southern boundary, transport driven by each forcing term outside the SWM domain (which is the same as that of the VIKING20 nest) is not taken care of by our model solution and this indeed has an impact on the computed barotropic transport, as we discuss later. While this is a disadvantage of our method as applied to VIKING20, the problem would not arise if the southern boundary of the nest extended south of the equator since then the southern boundary of the SWM domain would not cross f/H contours.

2.3 Results

Figure 2.1a presents the total barotropic transport computed directly from VIKING20 within the region of the VIKING20 nest and Figure 2.1b presents the sum of the barotropic transport from the SWM driven by each of the four forcing terms separately (note that since the SWM is linear, this is the same as the transport driven by all four terms together). The barotropic transport from the VIKING20 nest (Figure 2.1a) depicts a well-developed

northern recirculation gyre south of Atlantic Canada, and recirculation gyres associated with the North Atlantic Current, including the anticyclonic Mann Eddy centered at 42°N 46°W and the northwest corner near 50°N 45°W. The recirculation gyres in the SWM are at the same locations and of similar strengths to those in the VIKING20 nest, which indicates that our linear decomposition method is able reproduce their dynamics from VIKING20. Nevertheless, the combined barotropic transport from the SWM is weaker in the subtropical gyre and a bit stronger in the subpolar gyre. The difference, as shown in Figure 1c, is mostly associated with the closed southern boundary in the SWM; indeed, the difference in the barotropic transport is generally anticyclonic, following the f/H contours. It is also possible that some of the difference is related to the different friction parameterizations used in the SWM and VIKING20. Nevertheless, the unexplained barotropic transport does not exhibit the recirculation gyres or quasi-stationary eddies along the Gulf Stream and the North Atlantic Current, which implies that the dynamics of these recirculation gyres are primarily explained by the four forcing terms specified within the SWM domain.

Figure 2.2 shows the fifty-year mean barotropic transport driven by the potential energy (PE), mean flow advection, eddy momentum flux and the wind stress terms (here the wind-driven transport for an ocean of uniform density), and the ratio of their contributions to the total explained barotropic transport from the SWM. The PE term plays a dominant role over most parts of the model domain, especially in the subpolar gyre, the Northern Recirculation Gyre and the Gulf Stream separation region, including the Worthington Gyre, consistent with previous studies (e.g. Greatbatch et al. 1991; Myers et al. 1996). The PE term also plays the primary role along the path of the Gulf Stream, where it is complemented by the mean flow advection and eddy momentum flux terms.

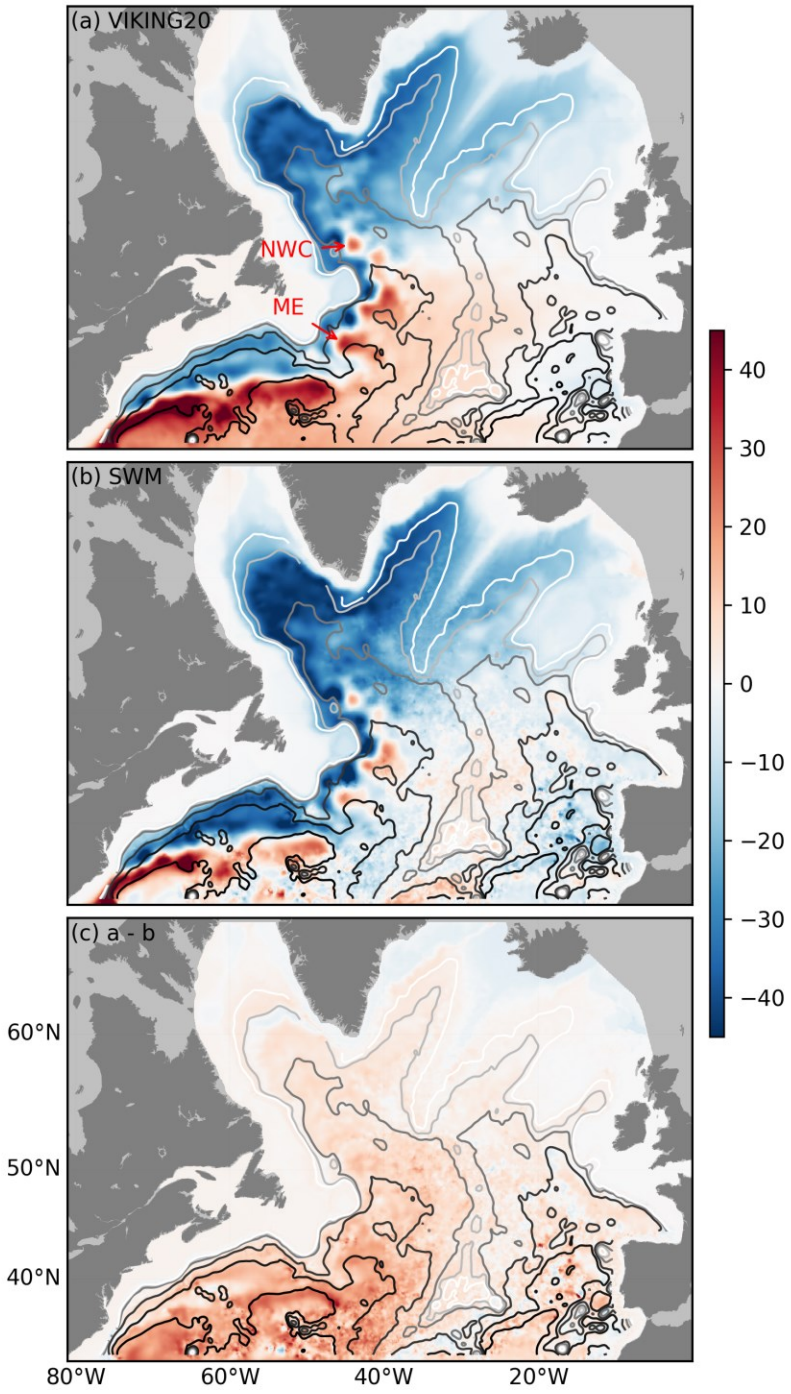

Figure 2.1. Model-computed 50-year mean barotropic transport (color shading in units of Sverdrups) for (a) the VIKING20 nest, (b) the sum of the four cases computed by the SWM, and (c) a - b. Lines are f/H contours of 17, 20, 25, 35,45, and 55 in units of 10^{-9} s^{-1} m^{-1}, which are smoothed using a Gaussian filter with a standard deviation of 0.5° in latitude and longitude. The locations of the northwest corner (NWC) and Mann Eddy (ME) are shown (a).

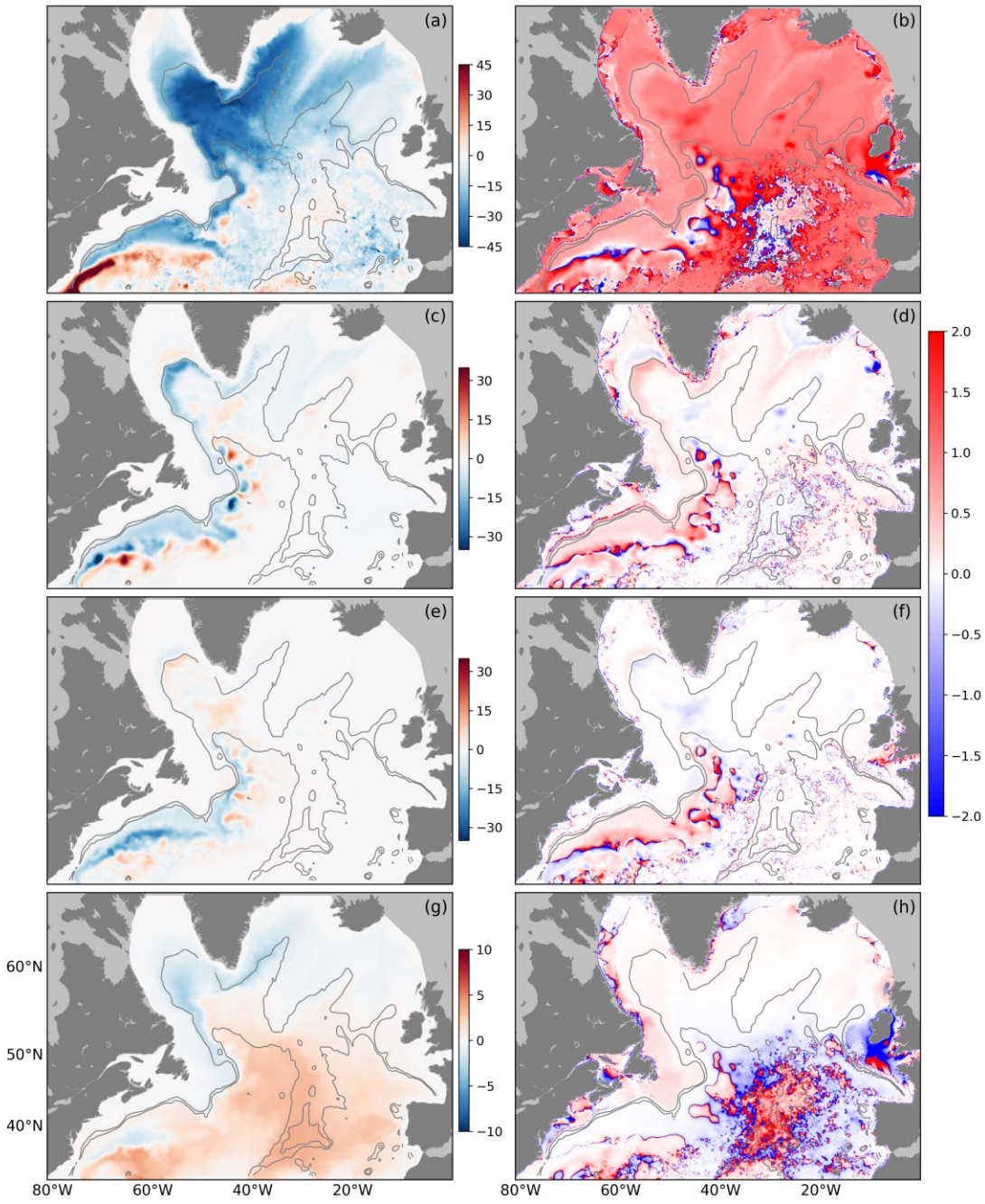

Figure 2.2. Model-computed 50-year mean barotropic transport (color shading in units of Sverdrups) driven by (a) the PE (JEBAR), (c) mean flow advection, (e) eddy momentum flux, and (g) wind stress terms. Note that the color coding is not the same in all panels. Panels (b), (d), (f) and (h) show the ratio of the corresponding barotropic transport to the total barotropic transport (as shown in Figure 1b). The contours are f/H contours of 30 and 45 in units of 10^{-9} s^{-1} m^{-1}, which are smoothed using a Gaussian filter with a standard deviation of 0.5° in latitude and longitude.

The mean flow advection term also drives considerable barotropic transport around the western subpolar gyre associated with the recirculating boundary current around the Labrador Sea and Irminger Sea (Lavender et al. 2000; Fischer et al. 2015). The mean flow advection and, to some extent, the eddy momentum flux terms, drive a series of recirculations along the path of the Gulf Stream and the North Atlantic Current, including in the northwest corner, not unlike the eddy-driven transport inferred for this region by Zhai et al. (2004). In the northwest corner, the mean flow advection term predominantly drives the anti-cyclonic mesoscale recirculation centered at 50°N and 45°W, but with some role for the PE and eddy momentum flux terms. For the Mann Eddy the mean flow advection/eddy momentum flux and PE terms are dominant over the eastern and western halves, respectively. This implies that all three dynamical processes are working together to shape this semi-permanent anti-cyclonic eddy. The location of the Mann Eddy and the adjacent North Atlantic Current is observed to migrate over 200 km (Meinen 2001) suggesting variability in the relative importance of these terms over time.

Figure A.1 shows the local vorticity budget diagnosed from VIKING20 and based on equation (A.21). It should be noted that the plotted fields have been smoothed to reduce noise. The plotted fields nevertheless exhibit mostly small-scale features, and it is difficult to infer the relative importance of the different forcing terms. Similar plots in Bell (1999) and Yeager (2015) are more informative but it should be noted that the models they used have much coarser resolution with much less detailed bottom topography (a major source of noise) than is carried by VIKING20. An advantage of our method is that the SWM effectively integrates the forcing terms to provide transport fields (without smoothing) that not only closely resemble that in VIKING20 (Figure 2.1) but also provide an effective decomposition of the transport in VIKING20 into its constituent parts (Figure 2.2). Furthermore, as we noted earlier, the southern boundary of the VIKING20 nest would be much less troublesome if it was located either at or south of the equator. A good example, illustrating the power of our method, is provided by the eddy momentum flux forcing. From Figure A.1, this appears weak and much less important than implied by Figure 2.2. Nevertheless, some useful information can be gained from Figure A.1. The general tendency (although not universal) for the JEBAR term to balance the advection of planetary vorticity is consistent with the dominance of the PE term for explaining the transport in

VIKING20 (Figure 2.2). Furthermore, it is seen that the mean flow advection term is most important in the region of the East Greenland Current and it appears that this region plays a role in driving the recirculation gyre around the rim of the Labrador Sea that can be seen in Figure 2.2b.

Compared to the barotropic transport driven by the eddy momentum fluxes in Greatbatch et al. (2010) using satellite altimetry derived forcing, the SWM, using the forcing derived from the output of the VIKING20 nest, generates a very similar pattern but less magnitude. As noted earlier, Greatbatch et al. (2010) had to assume a vertical profile for the eddy momentum fluxes and, as noted by these authors, the more surface trapped the profile the less the transport that is driven by these terms. Since the eddy momentum fluxes derived from the VIKING20 nest have a similar magnitude at the surface to those seen in the altimeter data (not shown), the explanation for the reduced transport computed here is almost certainly that the vertical profile of the fluxes in the model is surface intensified (see Figure A.2), rather than linear, as assumed by Greatbatch et al. (2010). Furthermore, the vertical integral of the vertical profile shown in Figure A.2 has about 25% the magnitude of the corresponding linear profile assumed by Greatbatch et al. (2010), similar to the reduction in the magnitude of the transport that is driven by these terms (Figure 2.2c) compared to that reported by Greatbatch et al. (2010).

The barotropic transport that is directly driven by the surface wind stress within the SWM domain (Figure 2.2g) is weak but, nevertheless, has a role to play over the Mid-Atlantic Ridge south of the Charlie-Gibbs Fracture zone (Figure 2.2h). Note that the wind-driven transport presented here is the wind-forced response of a uniform density ocean which, as noted by Greatbatch et al. (1991), is very different in the nNA from that of the flat-bottom Sverdrup transport (see Figures 2.2g and 2.3c for this comparison directly). This is because the presence of the Mid-Atlantic Ridge causes the f/H contours to exhibit large latitudinal excursions. Furthermore, our diagnosis of the response to this term is affected by the closed southern boundary and is missing transport that would otherwise propagate into the SWM domain from the south along the western side of the mid-Atlantic ridge and also near the eastern boundary. For example, a comparison with Figure 2.2a in

Greatbatch et al. (1991) shows much more transport in the subtropical gyre region, west of the Mid-Atlantic Ridge, than can be seen in Figure 2.2g.

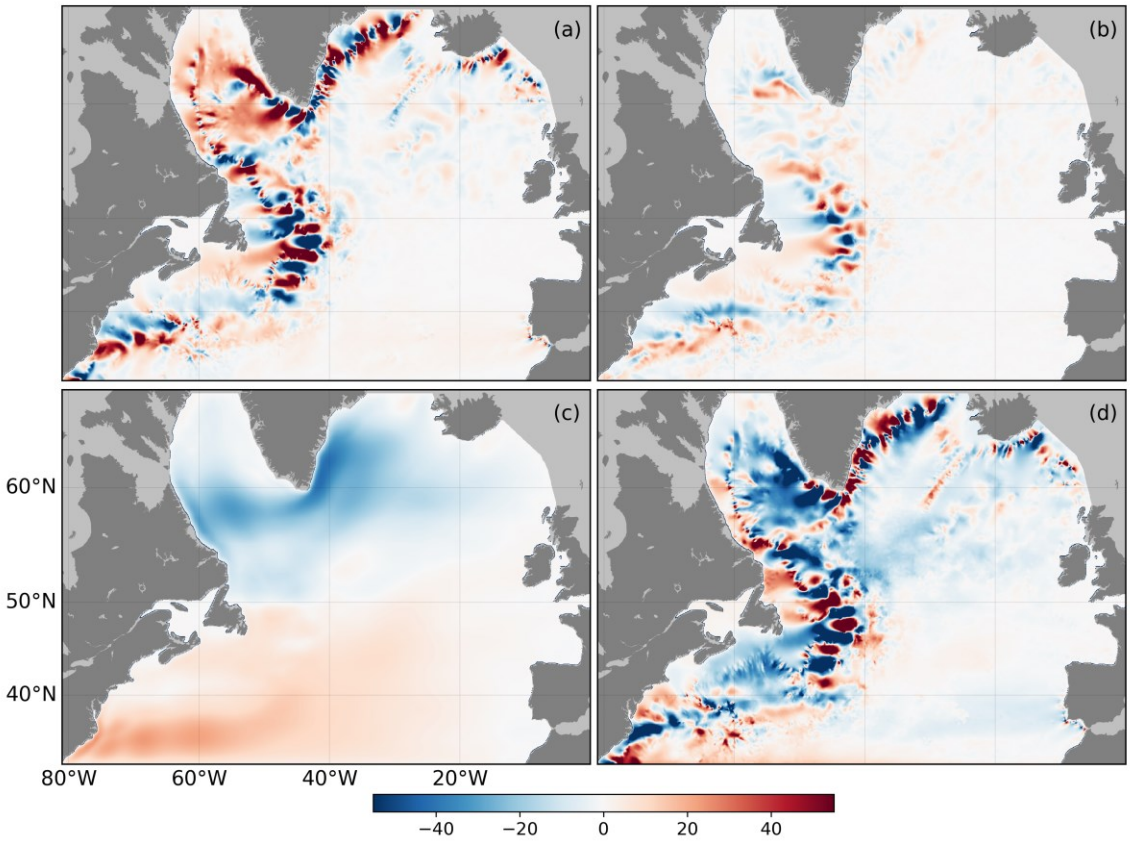

Figure 2.3. Model-computed 50-year mean barotropic transport (color shading in units of Sverdrups) for the flat bottom case driven by (a) mean flow advection, (b) eddy momentum flux, (c) wind stress, and (d) the part that is estimated to be driven by bottom pressure torque.

We can also decompose the barotropic transport following Eq. (A.24) in Appendix A. Since Eq. (A.24) is the vorticity balance for the vertically-integrated, as distinct from the vertically-averaged, momentum equations, the forcing terms are the eddy momentum flux, mean flow advection and wind stress terms given in the Methods section but now multiplied by the local depth H, and the SWM is run using a uniform depth, here taken to be 4000 m with the lateral eddy viscosity is reduced to 2 $m^2 s^{-1}$. (Note that using the value

of 150 $m^2 s^{-1}$ reduces the amplitude shown but does not affect the spatial pattern, and also that integrating the forcing terms directly along lines of latitude, following Eq. (A.24), leads to a very noisy solution from which it is hard to extract the signal). To estimate the barotropic transport driven by the bottom pressure torque (Figure 2.3d), we take the transport streamfunction from VIKING20 shown in Figure 2.1a and subtract the parts that are associated with the eddy momentum fluxes (Figure 2.3a), mean flow advection (Figure 2.3b) and surface wind stress (Figure 2.3c), the latter corresponding to the flat-bottom Sverdrup transport given by Eq. (A.25) (modified by the lateral mixing as in the model of Munk (1950)). From Figure 3, we see that the implied transport driven by the bottom pressure torque is strongly influenced by the mean flow advection and eddy momentum flux contributions, especially the former. Indeed, it is clear that there is a lot of cancellation between Figures 2.3a and 2.3d suggesting that the mean flow advection has a big influence on how the circulation interacts with the sloping bottom topography in the model, appearing, in fact, to be more important than the spreading of newly formed dense water masses.

2.4 Summary and Discussions

In this study, the mean barotropic transport in the northern North Atlantic (nNA) was diagnosed using a Shallow Water Model (SWM) driven by forcing terms derived from the high-resolution component of a nested ocean circulation model configuration, VIKING20. By this method, the mean barotropic transport over the period 1960 – 2009 simulated by VIKING20 (without data assimilation) can be attributed to four forcing terms in the vertically-averaged momentum equation; the eddy momentum flux, mean flow advection, potential energy (PE), and wind stress forcing for an ocean of uniform density (Figure 2.2). We have seen that the local vorticity budget is noisy and characterized by small spatial scales (Figure A.1) from which it is difficult to infer the relative importance of the different forcing terms. For example, the eddy momentum flux terms appear to be unimportant in Figure A.1, yet are a significant contributor to the transport of the Gulf Stream and its recirculations. Indeed, the SWM approach adopted here offers a powerful tool for diagnosing the transport output from high resolution ocean models and is an effective

alternative when analyzing models that include eddies to the approaches adopted to Bell (1999) and Yeager (2015).

Regarding the four forcing terms, the PE term is the primary forcing, including in the northwest corner region east of Newfoundland where models have great difficulty simulating the circulation (see Delworth et al. 2012; Flato et al. 2013; Drews et al. 2015; Griffies et al. 2015) and the recirculation gyres associated with the Gulf Stream Extension, consistent with previous work (e.g. Greatbatch et al. 1991; Zhang and Vallis 2007). Both the eddy momentum flux and the mean flow advection terms play a significant role in the Gulf Stream region and its extensions, including the North Atlantic Current and the mean flow advection is found to be an important driver for transport around the rim of the Labrador Sea (this is the recirculation gyre noted by Lavender et al. (2000) based on drifter data). The transport driven by the eddy momentum fluxes shows a very similar pattern to the transport streamfunction derived in a previous study using eddy momentum fluxes derived from satellite data (Greatbatch et al. 2010) apart from the lower amplitude, which we attribute to the vertical profile of eddy momentum fluxes assumed in that study; in the VIKING20 nest the eddy momentum fluxes are more surface intensified (Figure A.2). Interestingly, in addition to PE forcing (i.e. JEBAR), both the eddy momentum fluxes and mean flow advection play a role in driving the Gulf Stream recirculation gyres either side of the Gulf Stream Extension (Hogg, 1992). The fact the eddy momentum fluxes are important shows that, unlike in the theories of Marshall and Nurser (1986) and Greatbatch (1987), the eddy forcing of these gyres is not "weak". The theory in those papers depends on the mean flow advection term playing a major role and it is interesting that some role for this term is, indeed, found. In general, the wind stress forcing (which leads to the response for a uniform density ocean) has a relatively minor contribution that arises from the blocking of the f/H contours by the Mid-Atlantic Ridge (Figure 2.1c) (Greatbatch et al., 1991) and the closed southern boundary for our SWM.

This study explicitly illustrates the dynamics governing the recirculation gyres associated with the Gulf Stream and North Atlantic Current, including the northwest corner, which are not well understood. It is demonstrated that the northwest corner is primarily driven by the combination of the PE and mean flow advection terms with some role for the

eddy momentum fluxes. The role of the PE forcing is anticipated given the impact of the flow-field correction in alleviating the "cold bias" in Drews et al. (2015), since the correction assumes that a diagnostic calculation, in which the density field is specified, is capable of reproducing the northwest corner in a model. Another example is the Mann Eddy, which is a semi-permanent anti-cyclonic eddy that is observed to migrate sometimes over a distance of 200 km (Meinen 2001). Figure 2.2 suggests that the east/west side of the Mann Eddy is primarily driven by the mean flow advection and eddy momentum flux/PE terms. This explains the eastward shift in the position of the Mann Eddy in the study using only the eddy momentum flux forcing by Greatbatch et al. (2010), and may also explain the challenge for a 1/4° horizontal resolution model to reproduce the eastern branch of the Mann Eddy (See Figure 2.5a in Urrego-Blanco and Sheng 2012).

It is still a great challenge for numerical models to reproduce many observed recirculation gyres, especially for climate models that trade-off resolution and dynamics for efficiency, which can be significantly detrimental to the model veracity (e.g. the "cold bias"). Numerical corrections, such as described by Drews et al. (2015), turn out to be one possible way to improve the model performance, while the lack of knowledge on dynamics driving those recirculation gyres imposes difficulties. The importance of the PE term in the dynamics of the northwest corner is consistent with previous studies (e.g. Zhang et al. 2011). Nevertheless, a new and surprising result is the influence that the mean flow advection has on the interaction between the circulation and the sloping bottom topography, i.e. the bottom pressure torque (see Figure 2.3). This suggests a feedback between the circulation in the continental slope region and the mean flow advection that might well contribute to the difficulties models have with, for example, Gulf Stream separation and the northwest corner. We suggest that the method presented here, using a linear shallow water model, is an effective tool with which to diagnose the drivers for transport in high resolution ocean models, including models that do not exhibit a northwest corner or a correct Gulf Stream separation. Such diagnoses are needed in order to disentangle the different feedbacks operating in these models.

CHAPTER 3

BAROTROPIC TRANSPORT VARIABILITY IN A HIGH-RESOLUTION OCEAN MODEL OF THE NORTHERN NORTH ATLANTIC OCEAN[1]

3.1 Introduction

There is evidence of significant interannual to decadal variability in the circulation of the North Atlantic Ocean (e.g. Greatbatch et al. 1991; Joyce et al. 2000; Eden and Willebrand 2001; Eden and Jung 2001; DiNezio et al. 2009; Rossby et al. 2010; McCarthy et al. 2018; Smeed et al. 2018). Meanwhile, the oceanic variability of the North Atlantic Ocean is suggested to be closely associated with the North Atlantic Oscillation (NAO), which is the dominant mode of low frequency variability in the atmospheric circulation over the North Atlantic (Greatbatch 2000; Marshall et al. 2001; Hurrell et al. 2003). The Gulf Stream is suggested to vary in transport by up to 8 Sv in response to the NAO and move north (south) in the positive (negative) NAO phase with a shift in order of 10 km (e.g. Taylor and Stephens, 1998; De Coëtlogon et al., 2006; Joyce and Zhang, 2010; Watelet et al., 2017). In the subpolar gyre, the lateral transport is thought to play a role in climate variability (e.g. Delworth et al., 1993), and the thermohaline forcing exhibits a close relationship to the NAO index (Dickson et al., 1996; Curry and McCartney, 2001; Yashayaev, 2007). In addition, the convectively formed water masses are estimated to have a residence time of approximately 4-5 years in the Labrador basin (Straneo et al. 2003),

[1] Wang, Y., R. J. Greatbatch, M. Claus, and J. Sheng, 2020: Decomposing barotropic transport variability in a high-resolution model of the North Atlantic Ocean. *J. Geophys. Res. Ocean.*, 1–13.

and to arrive in the Irminger and Iceland basins with typical delays up to 5 years (Yashayaev 2007).

In the present study, we focus on the vertically-integrated (barotropic) gyre transport variability in a high resolution model of the northern North Atlantic (nNA). Such variability can be understood in terms of the vorticity equation derived from either the vertically-integrated or the vertically-averaged momentum equations (e.g. Bell 1999; Yeager 2015). Using the diagnostic model of Mellor et al. (1982), Greatbatch et al. (1991) exploited both approaches and suggested a decomposition based on the linear momentum/vorticity balance. Much less work has been done on the role played by the nonlinear advection terms in the momentum equations. Using an approach based on integrating a linear shallow water model to a steady state, with the eddy momentum flux specified based on satellite data, Greatbatch et al. (2010) suggested an important role for the eddy momentum flux terms in driving mean transport in the Gulf Stream extension region. The same methodology was later extended by Wang et al. (2017) to study the dynamics of the time-mean barotropic transport streamfunction, where the primary forcing terms for a linear shallow water model, based on the vertically-averaged momentum equations, are diagnosed from a high resolution ocean model of the nNA. These primary forcing terms include (1) the potential energy (PE) term (which leads to the JEBAR term in the vorticity equation) associated with the density field, (2) the mean flow advection (MFA) and (3) eddy momentum flux (EMF) terms that arise from the non-linear advection terms in the momentum equations carried by VIKING20, and (4) the wind stress (WS) term, in this case the effect of the surface wind stress applied to a uniform density ocean.

Here, the methodology of Wang et al. (2017) (section 2.2 of this thesis) is used to decompose the temporal variability in the same high resolution ocean model of the nNA into the four transport components. The decomposition is then illustrated by using it to interpret the response of the transport to the winter NAO index. The data and methods are described in Section 3.2, the results are presented in Section 3.3, and a summary is provided in Section 3.4.

3.2 Data and Methods

To compute the annual-mean barotropic transport driven by each of the four forcing terms, the linear and barotropic shallow water model (SWM) described in Section 2.2 is run to steady state for each year and each forcing term separately. The forcing terms in Eqs. (2.1) and (2.2) (Z, M), are computed from VIKING20 (Behrens 2013). Output from VIKING20 covering the 50-year period 1960-2009 is used here. The forcing terms (Z, M) are calculated using the output for each year separately (see Section 2.2 for details).

It should be noted that, the PE term appears as the JEBAR term in the vorticity equation that can be derived from Eqs. (2.1)-(2.3) (Greatbatch et al. 1991; Mertz and Wright 1992). Both the MFA and EMF terms arise from the nonlinear advection terms in the momentum equations carried by VIKING20. Since the overbar corresponds to an annual mean, the MFA term includes the interannual variability, whereas the EMF term takes account of variability on intra-seasonal to seasonal time scales. In the following discussion, when referring to the SWM reconstruction, we refer to the sum, for each year, of the transport streamfunctions computed using each forcing term separately.

Since the f/H contours enter the model domain at the southern boundary, there is transport that is driven by each of the forcing terms outside the SWM domain that is not accounted for by our model solution. We shall see that for the variability, the role of this "residual part" is not as important as was found for the mean circulation in Section 2.3.

The winter NAO index used in this study is the December-March (DJFM) North Atlantic Oscillation Index (PC-Based) (Hurrell 1995), and was downloaded from https://climatedataguide.ucar.edu. It should be noted that for the analysis in the following sections, the time series have all been detrended.

3.3 Results

Figure 3.1a shows the standard deviation of the annual mean barotropic transport streamfunction in VIKING20 for the 50-year analysis period 1960-2009. Over most of the model domain, the standard deviation is less than 10 Sv, while somewhat larger variability

(>20 Sv) is seen along the pathway of the Gulf Stream and the North Atlantic Current extending into the northwest corner region (Lazier 1994). As noted by Wang et al. (2017) (see also Drews et al. 2015), realistic simulation of circulation and hydrography over the northwest corner is a great challenge for most circulation models. In VIKING20, the northwest corner is present but also extends too far northward into the Labrador Sea (see Breckenfelder et al. 2017).

To compare the SWM results with VIKING20, we compute the percentage of variance of the streamfunction variability in VIKING20 that can be accounted for by the SWM reconstruction as well as the time series of annual mean streamfunction associated with the different forcing terms. Here, explained variance P at each grid point is calculated as

$$P = \left(1 - \frac{var(\psi_{vk} - \psi)}{var(\psi_{vk})}\right) \times 100 \qquad (3.1)$$

where ψ_{vk} is the time series of the annual mean streamfunction from VIKING20, $var(\psi_{vk})$ is the variance of ψ_{vk}, and ψ is a time series of an annual mean streamfunction computed using the SWM. It should be noted that, in all cases, the results are almost the same if the explained variance is computed as the square of the correlation coefficient between the times series of the two annual mean streamfunctions.

Figure 3.1b presents the distribution of P computed using the SWM reconstruction, i.e. the sum of the streamfunctions computed separately using the four forcing terms. The SWM reconstruction accounts for the most part of the variance seen in VIKING20. Exceptions are near the southern open boundary and in the continental shelf regions. The latter is because the bottom topography used for the SWM differs from that in VIKING20 on the shelf. As explained Section 2.2, this was done for numerical reasons. The discrepancy near the southern open boundary is because the SWM does not account for streamfunction variations that are generated south of the model domain and propagate into the domain along f/H contours.

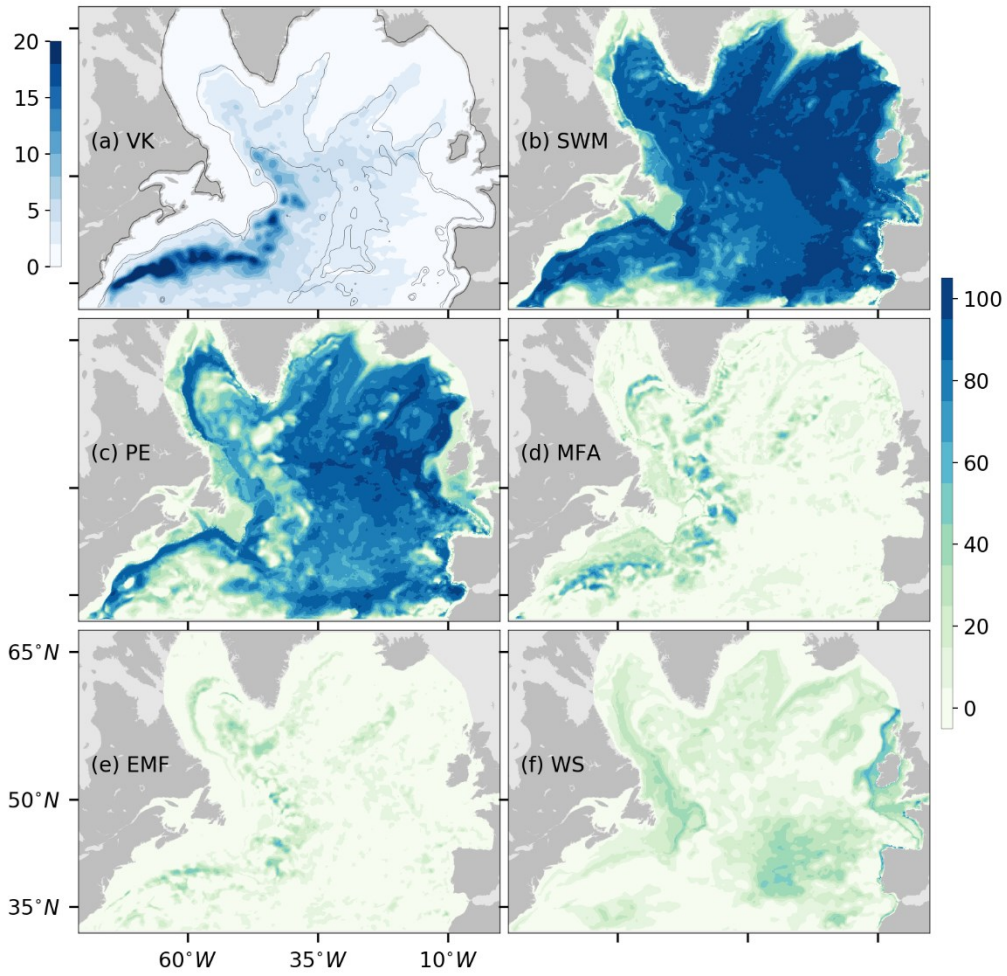

Figure 3.1. Standard deviation of the annual mean barotropic transport streamfunction (color image in units of Sverdrups) from VIKING20 (VK), and the percentage of variance in VIKING20 accounted for by (b) the SWM reconstruction, (c) the potential energy (PE), (d) the mean flow advection (MFA), (e) the eddy momentum flux (EMF), and (f) the wind stress (WS) contributions Here, explained variance is computed using Eq. (3.1).

The other panels in Figure 3.1 show the percent variance of the temporal variability in VIKING20 that is explained by streamfunction variability driven by each of the forcing terms used to drive the SWM using Eq. (3.1). Most of the variance seen in VIKING20 is explained by the SWM in the PE case, although there are regions, particularly on the western side of the basin, where in other cases, especially in MFA and to some extent in the EMF, play a more important role. This is especially true in the region of the Gulf Stream and associated recirculation gyres south of Atlantic Canada and also in the Labrador Sea.

The surface wind stress (Figure 3.1f) generally plays only a minor role in the barotropic transport variability over the Northern North Atlantic. This is because the WS case corresponds to the transport streamfunction variability for the wind-driven response of the ocean as if it had uniform density. Even in the mean, the transport for a uniform density ocean is quite small in the nNA, especially in the region of the subpolar gyre (see Figure 3.2a in Greatbatch et al. 1991).

Direct wind forcing does, however, influence the PE term, e.g. through Ekman pumping, and also indirectly the MFA and EMF terms to some extent. To illustrate this, Figure 3.2 shows the dependence, as obtained from the linear regression, of the transport streamfunction on the winter NAO index. Here, the transport streamfunction is a time series of annual means and the winter NAO index is for the months of December-March (DJFM), where January, February and March (JFM) overlap with the year used to compute the annual mean streamfunction. The WS case is very similar to the response to wind forcing at lag zero noted by Eden and Willibrand (2001) and corresponds to the topographic Sverdrup response to wind forcing. The PE case shows the impact of Ekman pumping, with the tendency to have enhanced gyre transport for both the subpolar and subtropical gyres when the NAO is positive, the latter extending northeastwards towards the British Isles. There is also good agreement between VIKING20 and the SWM reconstruction. The feature extending towards the British Isles is enhanced in VIKING20 and the SWM reconstruction compared to the PE case alone through the combination of the contributions from the PE and WS cases. The contributions from the MFA and EMF cases are very localized and do not appear to be important. The WS case will not be discussed further in this Chapter.

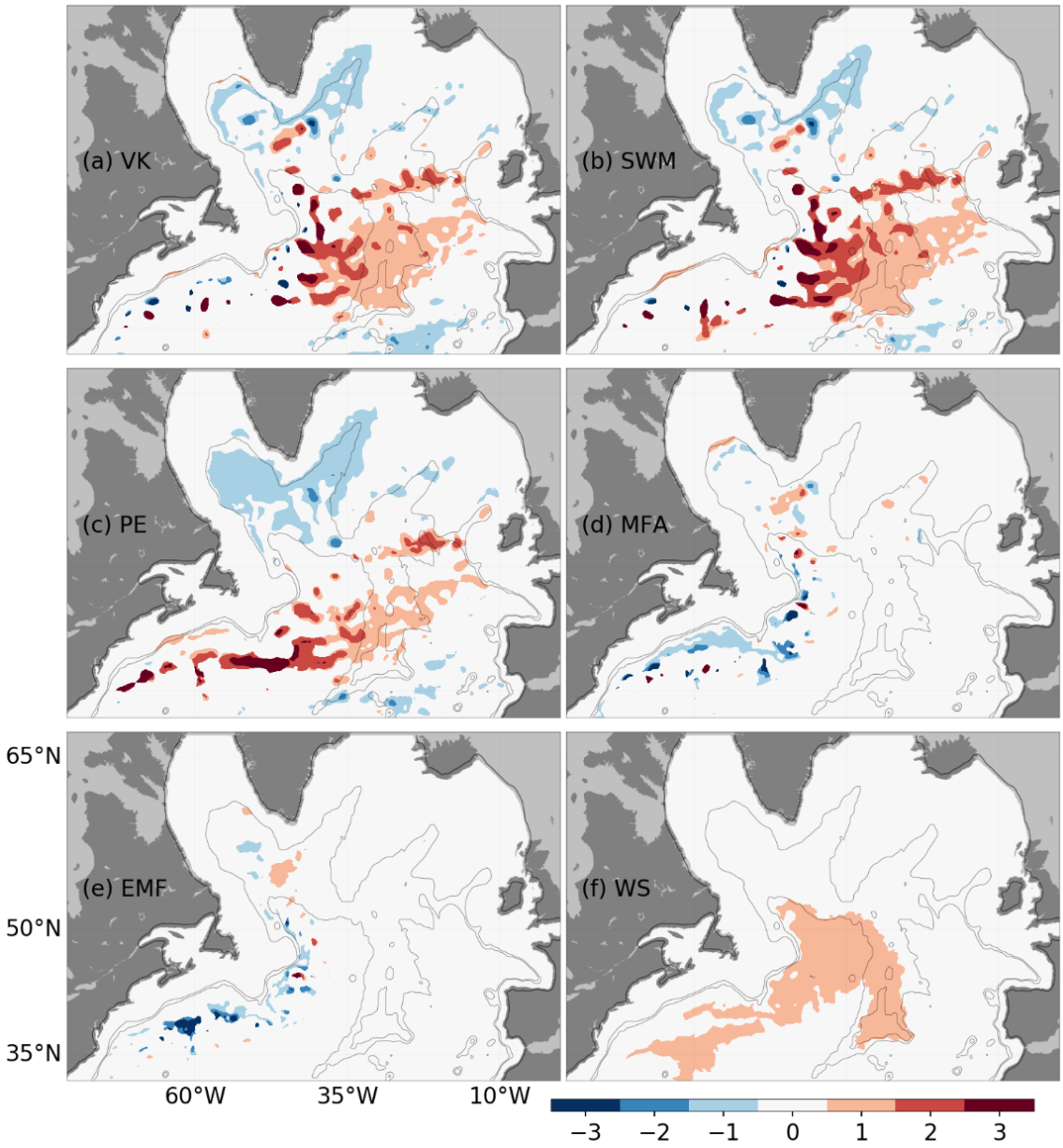

Figure 3.2. The dependence of the transport streamfunction on the winter NAO index as obtained using the linear regression for (a) VIKING20 (VK), (b) the SWM, (c) potential energy (PE) (d) mean flow advection (MFA), (e) eddy momentum flux (EMF) and (f) wind stress (WS) contributions. The units are Sv per unit for the NAO index and only those regions are plotted where the associated correlation exceeds the 95% significance level according to a Students t-test.

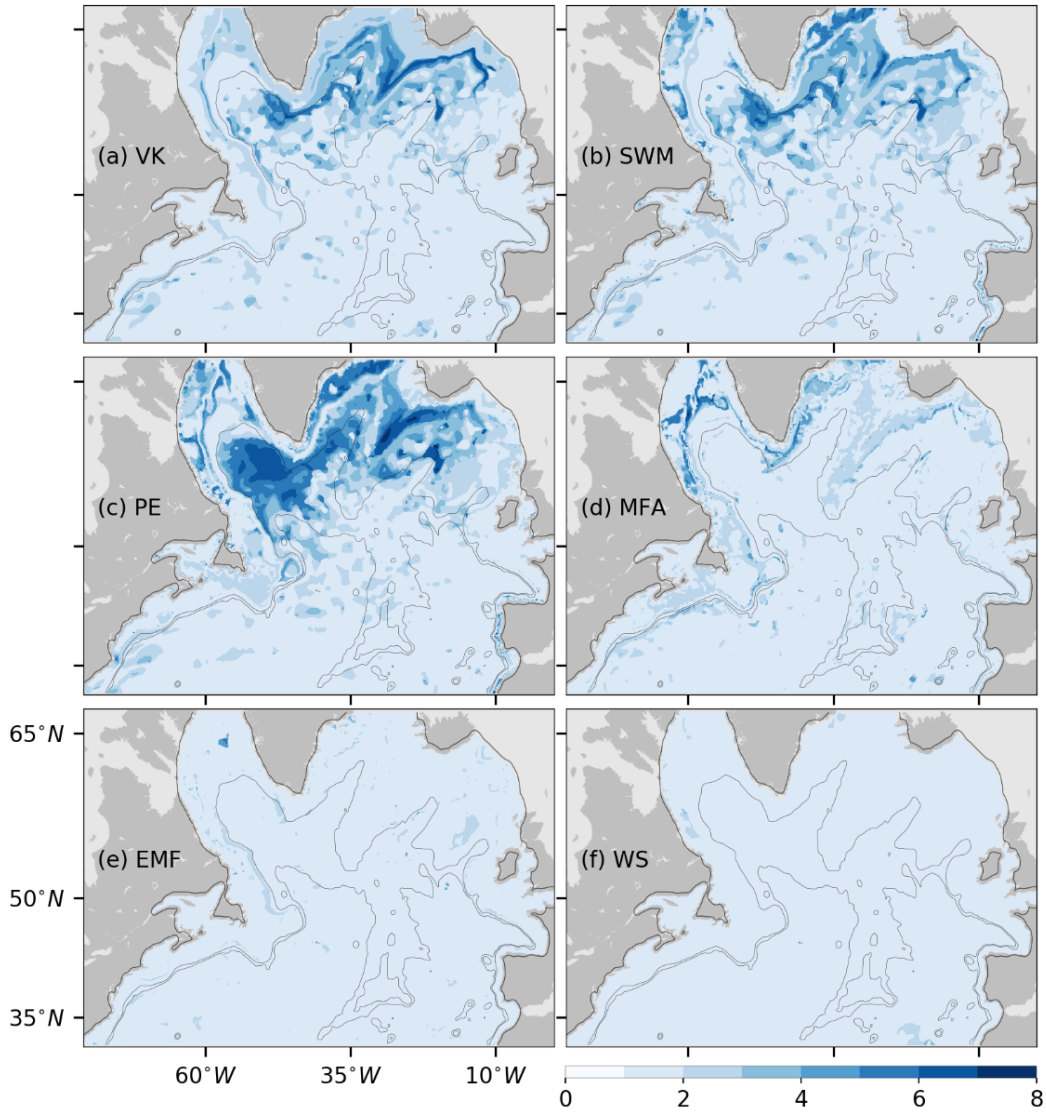

Figure 3.3. The time in years for the autocorrelation of the transport streamfunction to drop to a value of 1/e or less in (a) VIKING20 (VK), (b) the SWM reconstruction, and for the streamfunction driven by each of (c) the potential energy (PE), (d) mean flow advection (MFA), (e) eddy momentum flux (EMF), (f) and wind stress (WS) terms.

We can also examine how much the year-to-year memory is contained in the computed streamfunctions. Figure 3.3 shows the time (in years) for the autocorrelation of the streamfunction to drop to a value of 1/e or less for each case. In order to remove the grid point noise, a centered star-shaped 5-point average with equal weighting for each point is applied in both the zonal and meridional directions to the transport streamfunction before computing the autocorrelation with a weighting of 1/8 at the outer grid points and 1/2 at

the center grid point. In both VIKING20 (Figure 3.3a) and the SWM reconstruction (Figure 3.3b), the memory is up to at least 5 years around the northern part of the subpolar gyre. This memory derives almost entirely from the PE contribution (Figure 3.3c), i.e. the density field. Interestingly, the PE contribution also shows memory extending out to 5 years in the Labrador Sea that is not so evident in either VIKING20 or the SWM reconstruction, indicating how signals in the density field can be obscured by the MFA and EMF contributions. The memory in the PE contribution is consistent with the estimated residence time scale for convectively-formed water masses in the Labrador basin (Straneo et al. 2003). The MFA contribution also exhibits some long-term memory in the northern recirculation gyre region south of Atlantic Canada and also around the northern rim of the Labrador Sea, in the region of the so-called Lavender gyre (Lavender et al. 2000), although neither of these features appear in VIKING20 or the SWM reconstruction.

We next demonstrate how the decomposition technique can be used to understand transport variability associated with the NAO in more detail. In the introduction, we noted that the Gulf Stream tends to be further north/south in years following positive/negative NAO winters and although we find some evidence of this in VIKING20 (not shown), the horizontal resolution of the model (1/20 degree, but still only about 5 km in the Gulf Stream region) and the number of years available (50) is such that it is hard to detect movements in the Gulf Stream position with any certainty. Instead we illustrate the transport variability showing, first, the dependence of the transport variability between the two positions marked by stars shown in Figure 3.4f. These two positions sit on the northern and southern sides of the Gulf Stream in the model, with one position in the northern recirculation gyre and the other on the southern flank of the Gulf Stream (Figure 3.4f). As before, the streamfunction has been filtered to remove the grid point noise before applying the analysis and all the analysis uses detrended time series. The light blue dots in Figure 3.4 represent the annual mean transport between the two stars as a function of the winter NAO index along the x-axis. Here, as before, the winter NAO index is for DJFM and the annual mean is for the year containing JFM (lead year 0). The red straight line is the best fit obtained using the linear regression and the significance of the slope is obtained by randomly shuffling the annual mean transport amongst the years 10,000 times and repeating the regression analysis. The histogram of the distribution of the regression slope is presented

in the lower left sub-panel. The grey bars indicate the 95% significance level for the slope (that is 2.5% of the total slopes are beyond the grey bar at each end of the histogram) and the slope of the red line is indicated by the red bar. The histogram consists of 100 equally-spanned bins from the minimum to the maximum. The percentage of regression slopes from the shuffled samples less than that of the red line is shown: the closer the red line is to the extremes at the two sides of the distribution, the more significant is the dependence shown by the red line. The grey shading shows the 95% confidence interval of the regressed red line as estimated by randomly resampling the two variables, i.e., winter NAO index (x) and transport (y), in pairs, allowing repeated pairs. A distribution of predicted y is obtained by 10,000 regressions on resampled x and y pairs, in this way accounting for noise in both the winter NAO index and the transport.

From Figure 3.4, we see that in VIKING20, there is a weak tendency at lead year 0 for the transport to increase with increasing NAO index, although this is not statistically significant. This behavior is reproduced by the SWM reconstruction and is a feature of the different contributions to the SWM calculated transport, with the most significant contribution coming from the MFA contribution. In VIKING20, the dependence on the NAO is stronger and more significant one year later (lead year 1, Figure 3.5) and this is also reproduced by the SWM reconstruction. This time, in addition to the MFA contribution, the EMF contribution plays an important role. One year later again (lead year 2, Figure 3.6), the dependence on the NAO is even stronger in VIKING20 and exceeds the 95% significance threshold, behavior that is again reproduced by the SWM reconstruction. This time, however, it is the EMF contribution that dominates with no significant role for the MFA contribution, but with the PE contribution becoming more important. The results for lead year 3 (not shown) are very similar to those for lead year 2 (Figure 3.6) and it is only in lead year 4 (not shown) that the significance levels start to drop, with no significant relationship between the NAO and the transport variations in lead year 5 (not shown).

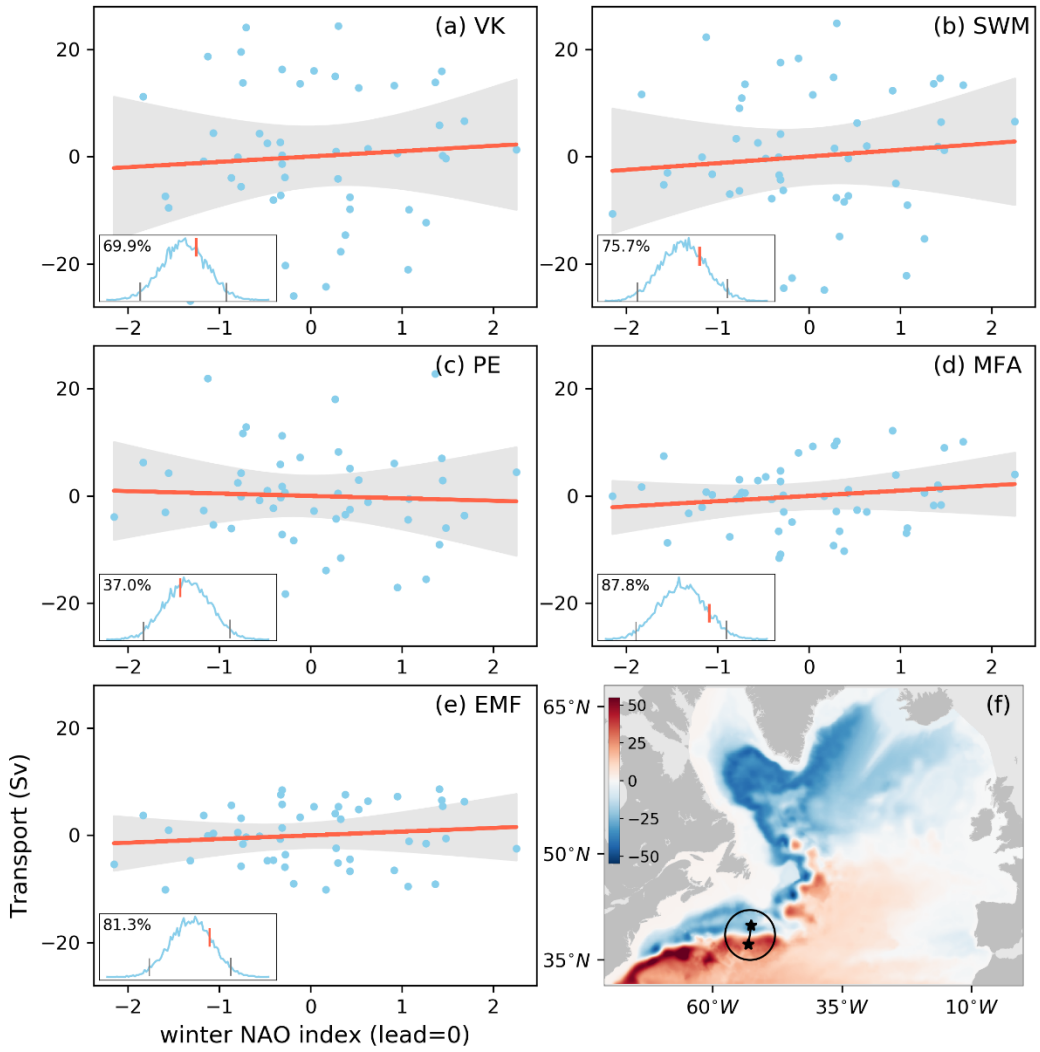

Figure 3.4. Scatterplot showing, for each year, the winter NAO index and barotropic transport between the two positions marked by stars shown in (f) for (a) VIKING20 (VK), (b) the SWM reconstruction and the contributions from (c) the potential energy (PE), (d) mean flow advection (MFA), and (e) eddy momentum flux (EMF) terms. Here the year and winter used for the NAO index overlap in January, February and March. The time-mean streamfunction from VIKING20 (color shading) is shown in (f). The red lines are the best fits obtained by the linear regression with the 95% confidence interval shaded in grey (see text for details). The lower left sub-panel shows the histogram of the linear regression slopes, with the 95% significance level, as obtained by randomly reshuffling the years, indicated by the grey lines (see text for details). The percentages shown on the histogram plots indicate the percentage of linear regression slopes from the Monte Carlo method that are less than the slope of the red line.

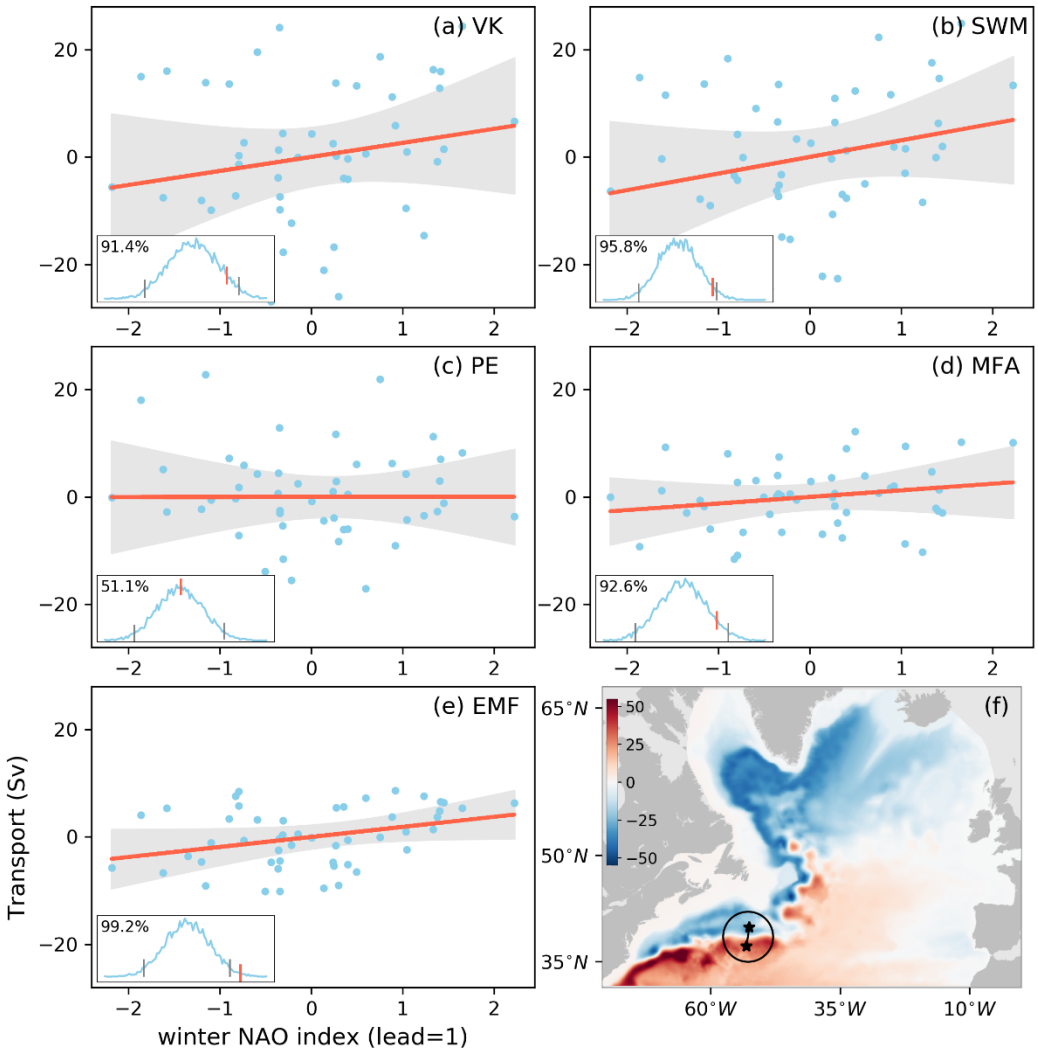

Figure 3.5. As the Figure 3.4, but for the barotropic transport one year later (lead year 1).

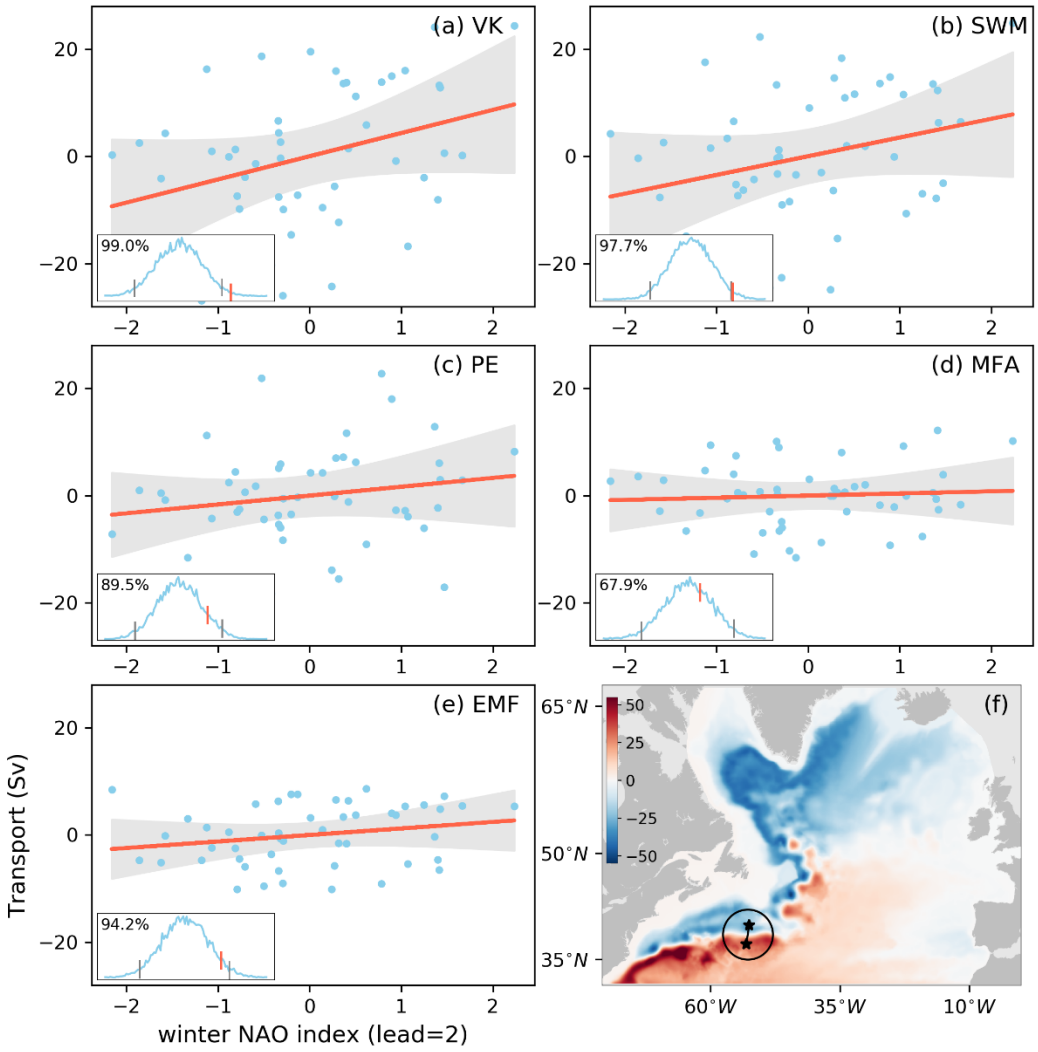

Figure 3.6. As the Figure 3,4, but for the barotropic transport two years later (lead year 2).

The general features of results shown in Figures 3.4-3.6 are not sensitive to the choice of location either side of the Gulf Stream to compute the transport and show that the variability of the Gulf Stream transport in the recirculation region in the model in response to the winter NAO index is not significant in lead year 0 but is dominated by the MFA and EMF contributions in lead years 1 and 2 (the terms arising from the nonlinear terms in the momentum equations). Only in lead year 2, does the baroclinic response (the PE contribution) start to be important and it is the EMF and PE contributions that dominate in lead years 3 and 4. The delayed baroclinic response agrees with the finding of Eden and Willebrand (2001). The reason for the relatively rapid response through the MFA and EMF

terms is less clear, and constitutes a new result, but suggests that the eddy field may, itself, have some dependence in the NAO. It has been suggested that interannual variability of the eddy kinetic energy in the North Atlantic has a dependence on the NAO (e.g. Stammer and Wunsch 1999) with a lag of 4 to 12 months (Penduff et al. 2004). Nevertheless, there is no obvious dependence of the eddy kinetic energy on the NAO in VIKING20.

As another example, Figure 3.7 shows the dependence of the streamfunction itself at a location marked by the star in Figure 3.7f within the Lavender gyre (Lavender et al. 2000) in the northern Labrador Sea. In VIKING20, the streamfunction shows a significant decreasing dependence on the NAO at lag 0, corresponding to an increase in gyre transport as the NAO index becomes more positive. This behavior is reproduced by the SWM reconstruction and is accounted for by the PE and MFA contributions. It is worth noting that the MFA term is the primary term driving the Lavender gyre in the mean, as noted by Wang et al. (2017). At lead year 1 (Figure 3.8), the relationship between the NAO and streamfunction in VIKING20 and the SWM reconstruction becomes less significant, despite a strong contribution from the PE case. The reason for this is that the MFA and EMF contributions, both of which pass the 95% significance threshold, oppose the contribution from the PE case. This is another example of how signals, e.g. from the PE term that are intrinsic to the density field, can be masked by and sometimes even countered by the MFA and EMF contributions.

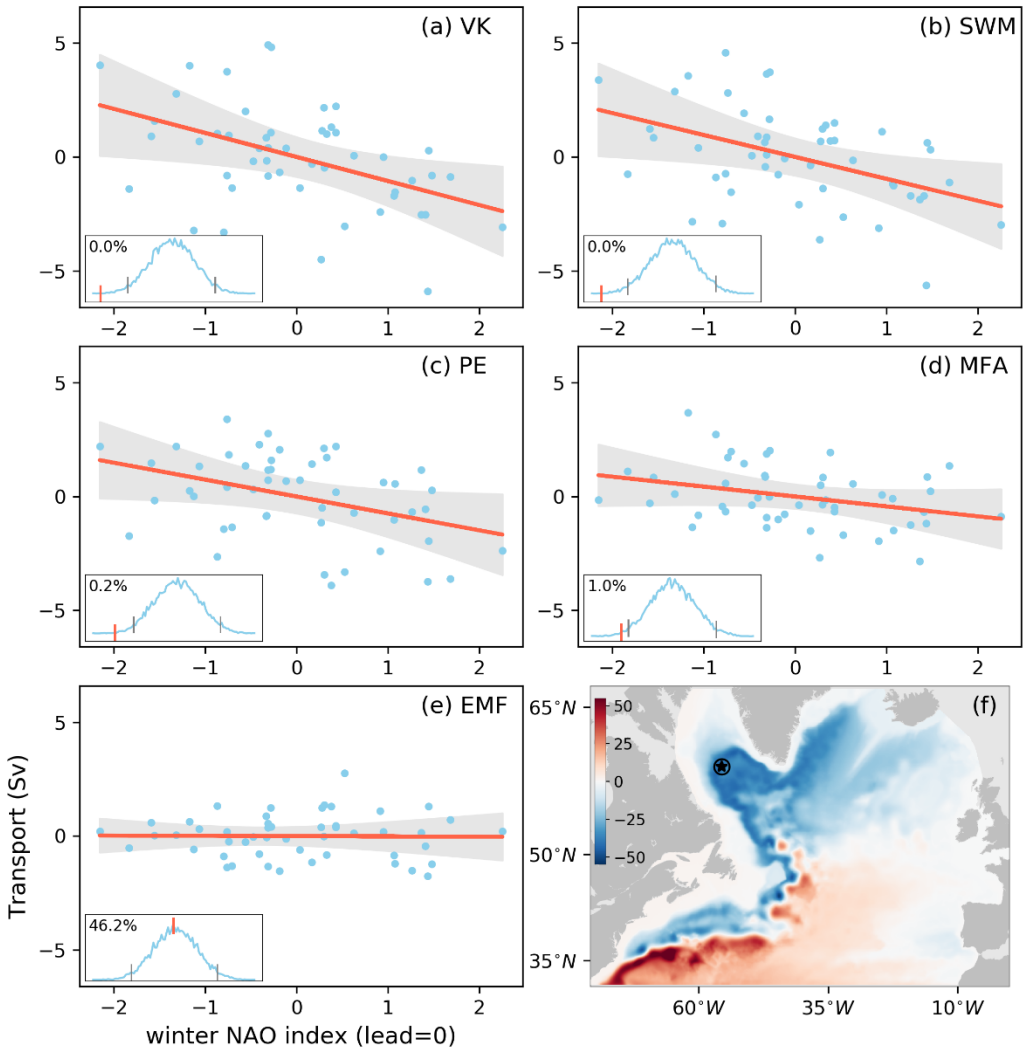

Figure 3.7. As the Figure 3.4, but for the streamfunction at the location in the Lavender gyre shown by the star in panel (f).

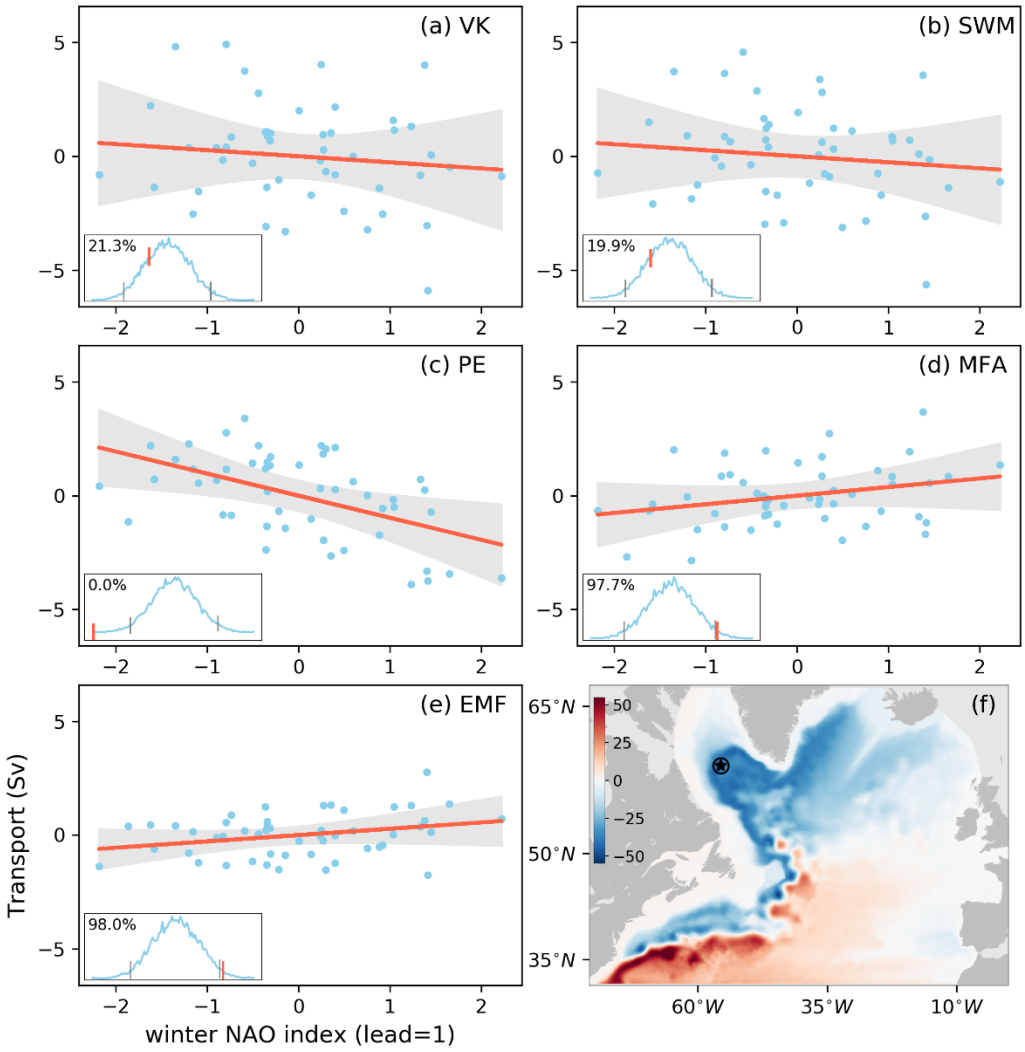

Figure 3.8. As the Figure 3.7, but for the streamfunction one year later.

3.4 Summary and Discussion

We have shown how the decomposition method introduced in Chapter 2 is useful for examining the variability of the barotropic streamfunction and associated transport in a high-resolution model configuration for the northern North Atlantic Ocean, VIKING20 (Behrens 2013; Böning et al. 2016). The decomposition is based on the vertically-averaged momentum equations and is carried out by running a linear shallow water model (SWM) to steady state with the forcing terms diagnosed from VIKING20 output. The dominant contribution is from the potential energy (PE) forcing term (which appears as the JEBAR

term in the vorticity equation), but with important contributions from the mean flow advection (MFA) and eddy momentum flux (EMF) cases in the Gulf Stream recirculation, North Atlantic Current regions, and the Lavender gyre. It should be noted that the MFA and EMF arise from the nonlinear advection terms in the momentum equations carried by VIKING20.

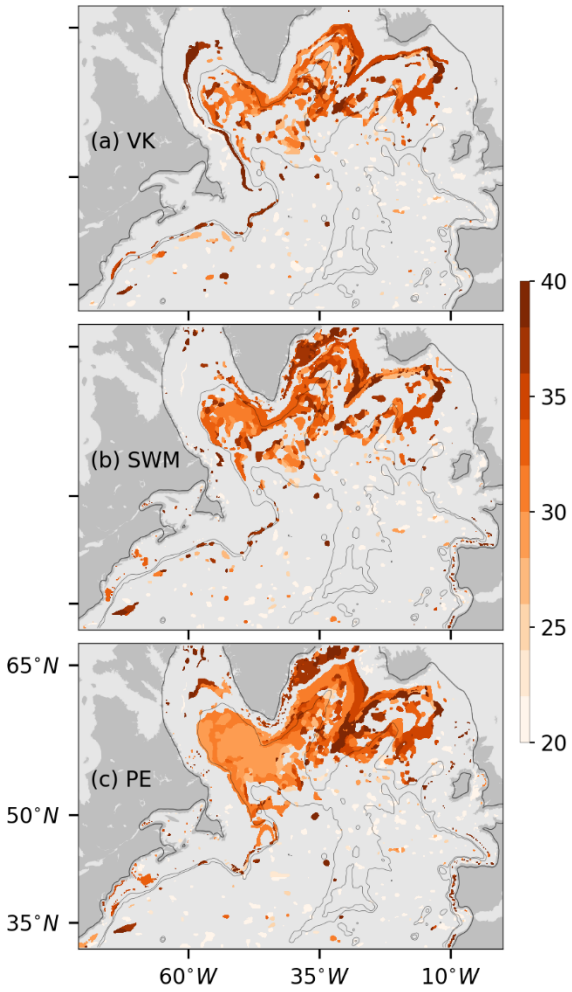

Figure 3.9. The estimate period (in years) for the internal oscillation implied by the autocorrelation of the transport streamfunction in (a) VIKING20 (VK), (b) the SWM reconstruction, and (c) the potential energy (PE) contribution. The period is estimated by doubling the time at which the autocorrelation reaches a minimum that is negative. To be acceptable, the minimum must satisfy two requirements: (1) the minimum autocorrelation must be less than -1/e with a 95% significance level, and (2) the autocorrelations must be increase afterwards to be positive with a 95% significance level.

The autocorrelation analyses of the transport streamfunctions demonstrated that the PE contribution, which is intrinsic to the density field, leads to significant memory of the transport streamfunction in the Labrador Sea and Irminger Sea regions where newly formed waters by deep convection reside. The autocorrelation associated with the PE term remains higher than 1/e for over 5 years in these regions (Figure 3.3). There is also the suggestion of periodic behavior with a period approaching 30 years (Figure 3.9). Since this oscillatory behavior is not found in the NAO index, it seems likely that the oscillatory behavior indicates an internal oceanic mode of variability in the model. Such internal modes of variability in the subpolar gyre region have been suggested by a number of authors, e.g. Eden and Greatbatch (2003), Mecking et al. (2015). The tendency to have the oscillatory behavior is also seen in VIKING20 and the SWM but only around the northern rim of the Irminger and Labrador Seas, and not in the interior. This is an example of how the transport variability associated with the PE term can be hidden by variability in the MFA and EMF terms arising from the nonlinearity of the momentum equations in VIKING20.

The advantage of the decomposition was also illustrated by examining how the annual mean barotropic transport in VIKING20 responds to the winter NAO. In particular, we analyzed the transport variability in the Gulf Stream recirculation region in VIKING20. Despite there being no significant transport variability associated with the NAO in lead year 0, a tendency for the transport to increase as the winter NAO index increases gradually emerges in lead years 1 and 2 (NAO leading), mostly associated with the MFA and EMF contributions. At lead years 2 and 3, the PE contribution starts to play a role consistent with earlier studies (e.g. Eden and Willebrand 2001; Marshall et al. 2001; Rossby et al. 2010) indicating a slow emergence of the baroclinic response to the NAO. It is only in lead year 4 that the response in both VIKING20 and the SWM reconstruction starts to lose significance. The mechanism responsible for the strong rapid response associated with the non-linear (MFA and EMF) terms requires further investigation. Nevertheless, the importance of the MFA and EMF terms in lead years 1 and 2 is a new result here.

In the Lavender gyre (Lavender et al. 2000) in the northern Labrador Sea, both the PE contribution associated with the density field and the MFA advection contribution play an important role in the strong dependence of the transport streamfunction on the NAO in lead year 0: the more positive the NAO, the stronger the circulation. In the following year (lead year 1), despite a strong contribution from the PE term, the dependence of the streamfunction on the NAO in both VIKING20 and the SWM reconstruction is much weaker, with the MFA and EMF contributions opposing the dependence from the PE contribution. This again indicates how the nonlinear terms in the momentum equations can obscure transport variability intrinsic to the density field (i.e. the PE contribution) in VIKING20.

CHAPTER 4

EXAMINING TIDAL IMPACTS ON SEASONAL CIRCULATION AND HYDROGRAPHY VARIABILITY OVER THE EASTERN CANADIAN SHELF USING A COUPLED CIRCULATION-ICE REGIONAL MODEL[1]

4.1 Introduction

The eastern Canadian shelf (ECS) considered in this study comprises the southern Labrador Shelf (LS), Newfoundland Shelf (NfS), Gulf of St. Lawrence (GSL), Scotian Shelf (ScS), Bay of Fundy (BoF), Gulf of Maine (GoM) and their adjacent slope waters (Figure 4.1). The general circulation over this region is affected by the Gulf Stream, Labrador Current, local winds, river runoff and tides (e.g., Loder et al. 1998). The ECS has significant seasonal variability in hydrographic distribution and circulation. The water temperature over the ScS, for example, has a seasonal range of over 16 °C (Loder et al. 1998). The dynamic complexities in this region also lead to large spatial variability. Significant efforts have been made in the past to describe and quantify the regional seasonality in hydrography and circulation (Han et al. 1999, 2008; Hannah et al. 2001a; Loder et al. 1997; Xue et al. 2000).

The ECS features large tidal elevations and intense tidal currents in the BoF and the northwestern GSL (Garrett 1972; Greenberg 1979; Saucier and Chassé 2000). The tidal range in the upper BoF reaches about 16 m, among the largest in the world, due to the

[1] Wang, Y., J. Sheng, and Y. Lu, 2020: Examining tidal impacts on seasonal circulation and hydrography variability over the eastern Canadian shelf using a coupled circulation-ice regional model. *Prog. Oceanogr.*, **189**, 102448.

resonant frequency of the BoF being close to the frequencies of the semi-diurnal tides (Garrett 1972). Strong tidal currents affect sub-tidal circulation and hydrography through the nonlinear tidal rectification and tidal mixing (Garrett et al. 1978; Pingree and Griffiths 1980; Loder 1980; Loder and Wright 1985; Loder and Greenberg 1986; Tee et al. 1993; Xue et al. 2000; Lu et al. 2001b; Hannah et al. 2001; Chegini et al. 2018). Tidal currents can increase the stress and strain of sea ice and cause the periodic opening of the ice leads, thus affecting the air-sea fluxes (Kowalik and Proshutinsky 2013). Tidal circulation and mixing can also increase the heat exchange between the deep and surface layers, reducing the ice coverage and thickness and possibly creating polynyas (Maqueda et al. 2004; Hannah et al. 2009; Postlethwaite et al. 2011).

With the increase of computer power, high resolution numerical ocean circulation models have increasingly been used in simulating the three-dimensional (3D) tidal and sub-tidal ocean circulations, hydrography and sea ice in the ECS (Han et al. 2008; Hannah et al. 2001; Saucier 2003; Xue et al. 2000). Several modelling studies in the past examined interactions between tides and seasonal stratification over the ECS. Ohashi et al. (2009) found that the seasonal variation of the stratification affects the M_2 tidal currents over the shelf break and deep waters off the ScS. Katavouta et al. (2016) found that internal tides lead to striations in surface currents to be aligned with the northern edge of GeB in the GoM in summer. Off southwest Nova Scotia, Chegini et al. (2018) studied the influence of the seasonal varying coastal current (the Nova Scotia Current) on coastal upwelling, through the onshore bottom currents induced by tides.

Previous studies also demonstrated the importance of tidal impacts over various sub-regions of the ECS. In this study we further examine the impacts of tides on seasonal variations of circulation, hydrography and sea ice over the ECS based on quantitative analyses of a hindcast simulation and a series of sensitivity experiments with a newly developed regional coupled circulation and sea ice model. While the analysis is focused on seasonal variations, the analysis methods and results are valuable for further studies on the inter-annual and long-term variabilities in the region, or in other regions with similar dynamic conditions with the presence of significant tides, river runoff and sea ice. Furthermore, the development, evaluation and improvement of high-resolution ocean

circulation and sea ice models are important for quantitative and dynamic analyses of marine environmental conditions and associated variabilities.

Sections 4.2, 4.3 and 4.4 describe model setup and design of simulations, observational data and model evaluation, respectively. The tidal impacts on sub-tidal dynamics are analyzed in Section 4.5. A summary of conclusions is provided in Section 4.6.

4.2 Coupled Circulation-Ice Model

The coupled circulation and sea ice model used in this study is based on version 3.6 of the Nucleus for European Modelling of the Ocean (NEMO; Madec 2008). The model domain covers the ECS (Figure 4.1), with a nominal horizontal resolution of 1/12° in latitude/longitude, or about 7 km in grid spacing. There are 50 z-levels in the vertical with the level thickness being 1 m near the sea surface and increasing with depths. That is, the cell thickness is about 8, 15, 28 and 52 m at depths of 50, 100, 200 and 400 m, respectively. The "bottom partial cells" are used for an accurate representation of the varying bathymetry. The sea ice component is the version 2 of the Louvain-la-Neuve model (LIM2, Bouillon et al., 2009). The model bathymetry was created from the 30 arc-second global dataset of the General Bathymetric Chart of the Oceans (Weatherall et al. 2015).

The coupled model is driven by a suite of external forcing. The atmospheric forcing at the sea surface was taken from the Climate Forecast System Reanalysis (CFSR; Saha et al. 2010) with a horizontal resolution of 1/3°. The atmospheric variables include the hourly wind velocities at 10 m and 6-hourly air temperature and humidity at 2 m above the mean sea level, shortwave and longwave radiations, and precipitation. The surface latent and sensible heat fluxes and wind stress are computed in the model with the bulk formulae developed for the Coordinated Ocean-Ice Reference Experiment (Large and Yeager 2004) and the drag-coefficient parameterization suggested by Large and Yeager (2009). The rate of surface evaporation is calculated using the latent heat flux. Freshwater inputs from 15 major rivers are based on a monthly climatology (Global Runoff Data Center 2001).

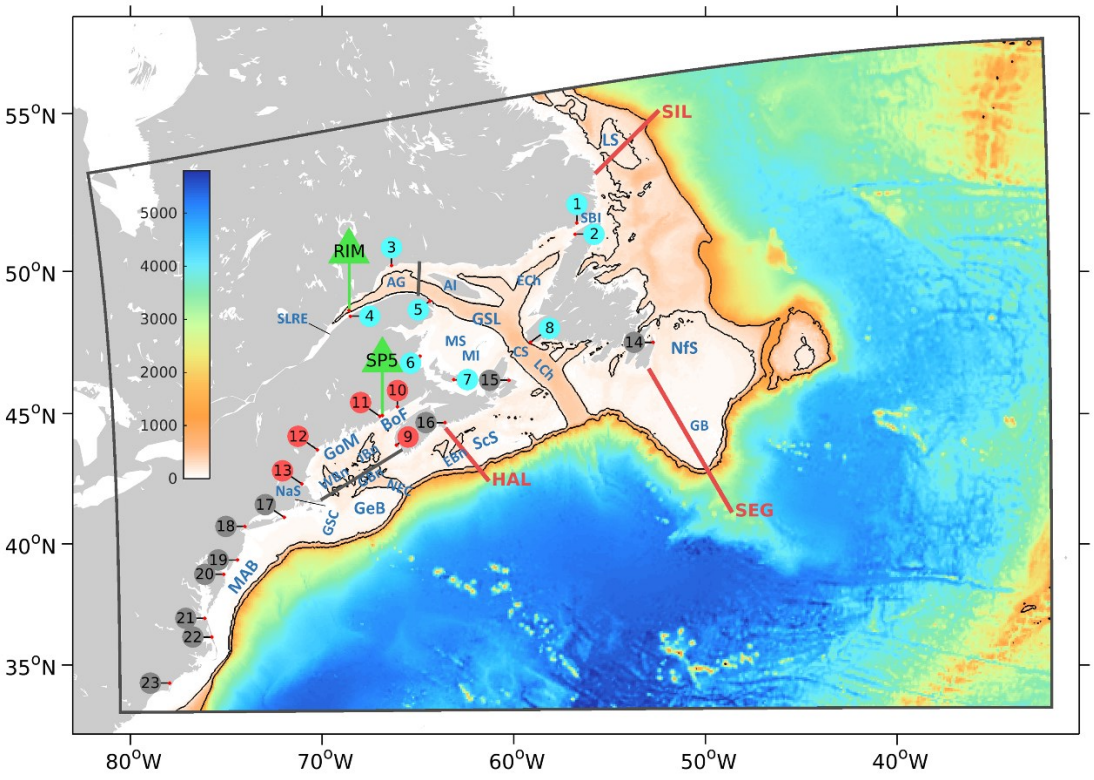

Figure 4.1. The model domain of the eastern Canadian shelf and adjacent northwest Atlantic Ocean. Color shading shows the bathymetry and the contours are isobaths of 200 and 1000 m, respectively. Abbreviations are used for the Labrador Shelf (LS), Newfoundland Shelf (NfS), Grand Bank (GB), Gulf of St. Lawrence (GSL), St. Lawrence River Estuary (SLRE), Anticosti Gyre (AG), Anticosti Island (AI), Magdalen Islands (MI), Magdalen Shallows (MS), Cabot Strait (CS), Laurentian Channel (LCh), Esquiman Channel (ECh), Strait of Belle Isle (SBI), Scotian Shelf (ScS), Emerald Basin (EBn), Gulf of Maine (GoM), Bay of Fundy (BoF), Georges Bank (GeB), Northeast Channel (NEC), Georges Basin (GBn), Jordan Basin (JBn), Wilkinson Basin (WBn), Great South Channel (GSC), Nantucket Shoals (NaS), and Mid-Atlantic Bight (MAB). The circles with numbers inside denote positions of 23 tidal stations: 1-8 (cyan) in the GSL, 9-13 (red) in the GoM, and 14-23 (grey) in other shelf areas. Selective observation sites of the Atlantic Zone Monitoring Program include two hydrographic stations, RIM and SP5 (green triangle), and three transects, SIL, SEG, and HAL (red lines).

The tidal forcing includes two parts. The first part is the tide-generating potential as the body forcing in the momentum equations. The second part is introduced through the lateral open boundaries of the model, using the tidal surface elevations and depth-averaged

currents of five major constituents (M_2, N_2, S_2, K_1 and O_1) taken from an Atlantic Ocean database with 1/12° resolution, created with the Oregon State University Tidal Inversion Software (OTIS; Egbert and Erofeeva 2002; volkov.oce.orst.edu/tides/AO.html). The non-tidal components of the open boundary forcing are taken from the monthly mean sea surface heights (SSH), currents, temperature (T) and salinity (S) produced by the Hybrid Coordinate Ocean Model (HYCOM experiment 19.1, www.hycom.org/data/glbu0pt08/expt-19pt1; Bleck 2002). The barotropic flow normal to the open boundary is specified using the radiation scheme of Flather (1994), using the sum of the tidal and non-tidal components of the depth-averaged flow and the sea surface height (SSH) provided by the input data. For the three-dimensional baroclinic flows (residuals of depth-averaged flows), T and S, a flow relaxation scheme (Engedahl 1995) is applied within a relaxation zone of 10-grid wide inside the open boundaries.

The vertical eddy viscosity and diffusivity coefficients are calculated based on the turbulent kinetic energy scheme embedded in NEMO (Blanke and Delecluse 1993). The lateral mixing is parameterized using a Laplacian scheme with the horizontal diffusion and viscosity coefficients of 50 and 100 $m^2 s^{-1}$, respectively. The lateral mixing operates along isopycnal surfaces for T and S, and along geopotential surfaces for momentum. The bottom drag is parametrized in the quadratic form using the near-bottom velocity and a constant drag coefficient of 2.5×10^{-3}. The air-ice and ice-water drag are also parameterized in the quadratic form, with drag coefficients of 1.4×10^{-3} and 5.0×10^{-3}, respectively. The characteristic thickness for ice growth in the open water area (parameter *hiccrit* in LIM2) is set to 0.3 m.

Four model experiments were carried out (Table 4.1). In experiment WithTide (or the control run), the model is driven by the full suite of external forcing mentioned above. In experiment NoTide, the model setup is the same as WithTide except for the exclusion of tidal forcing. The simulations of WithTide and NoTide are carried out for 15 years from 1996 to 2010, and the model results of the last 13 years are analyzed. In experiment BaroTide, the initial T and S are set to 25 ºC and 35 psu respectively, and the model is driven by the tidal forcing only and integrated for 60 days. Finally, the fourth simulation, WithTideRe, uses the same settings as WithTide except for being initialized from the

NoTide state at 00:00 UTC on July 1, 2004, and the results during July-August 2004 of this experiment are analyzed to examine the establishment and spreading of tidal impacts.

Table 4.1. Model setup of four numerical experiments.

Experiment	Initial condition	Tidal forcing	Non-tidal open boundary forcing	Atmospheric forcing
WithTide	Climatology	On	On	On
NoTide	Climatology	Off	On	On
BaroTide	Uniform temperature (25 °C) and salinity (35 psu)	On	Off	Off
WithTideRe	NoTide at 00:00 UTC on July 1, 2004	On	On	On

4.4.3 Observational and Reanalysis Data

Several types of observational data are used to assess the model performance. The first type of data includes the sea surface temperature (SST) and SSH based on satellite remote sensing observations. Both data are in the gridded format with a spatial resolution of 1/4° in longitude/latitude, and at daily frequency (www.esrl.noaa.gov/psd/data/gridded/data.noaa.oisst.v2.highres.html). The SST data are the Level 4 product derived from the Advanced Very High-Resolution Radiometers (AVHRR) measurements, which were calibrated by and blended with in-situ observations (Reynolds et al. 2007). The SSH data are the Level 4 product created by merging the multi-mission altimetry observations including the TOPEX/Poseidon, Jason 1, ERS1/2 and ENVISAT (www.aviso.altimetry.fr/en/data/products/sea-surface-height-products/global.html).

The second type of data is time series of hourly sea levels observed at 23 tidal stations over the study region (Figure 4.1), including 5 (8) stations in the semi-closed GoM-BoF (GSL) and 10 stations in the other areas. These sea level data were provided by the Marine Environmental Data Service of Fisheries and Oceans Canada (DFO; www.meds-sdmm.dfo-mpo.gc.ca) and the University of Hawaii Sea Level Center (Caldwell et al. 2015; uhslc.soest.hawaii.edu).

The third type of data is the observed vertical profiles of T and S along three transects and at two hydrographic stations (Figure 4.1): SIL (in LS), SEG (in NfS), HAL (in ScS), SP5 (in BoF), and RIM (in the northwestern GSL). The observations were made by the Atlantic Zone Monitoring Program (AZMP) of DFO (www.meds-sdmm.dfo-mpo.gc.ca/isdm-gdsi/azmp-pmza/hydro/index-eng.html). The observed in-situ temperatures are converted to the potential temperatures.

The fourth type of data is the digital sea ice charts created through manual analyses of in situ, satellite, and aerial reconnaissance data (Canadian Ice Service 2009; nsidc.org/data/G02171/versions/1). The weekly sea ice concentration over the GSL and adjacent areas during 2006-2010 is used in this study.

4.4 Model Evaluation

4.4.1 Tidal Elevation

The model performance in simulating tidal elevations is assessed by comparing the amplitudes and phases of five tidal constituents (M_2, N_2, S_2, K_1 and O_1) from model results in WithTide with observations at 23 tidal stations (locations shown in Figure 4.1). The amplitudes and phases are obtained by applying a harmonic analysis to the hourly mean data in 1998, when the coverage of the observational data exceeds 70% at all the stations. The analyses are summarized in Table 4.2. By separating the 23 stations into three groups according to their geological regions, the average errors for the tidal magnitude (ϵ_A) and phase ($\epsilon_\emptyset$) for each group are calculated using (Hasegawa et al. ,2011):

$$\epsilon_A = \frac{\sum_{i=1}^{N} \left| \mathrm{A}_i^O - \mathrm{A}_i^M \right|}{\sum_{i=1}^{N} \mathrm{A}_i^O} \tag{4.1}$$

$$\epsilon_\emptyset = \frac{1}{N} \sum_{i=1}^{N} \left| \emptyset_i^O - \emptyset_i^M \right| \tag{4.2}$$

where A_i^O ($\emptyset_i^O$) and A_i^M ($\emptyset_i^O$) denote the observed and simulated amplitude (phase) for each tidal constituent at station i, and N is the total number of stations in each group.

Table 4.3 lists the model error statistics for stations in two semi-closed gulfs, i.e., the GSL (stations 1-8) and the GoM-BoF (stations 9-13), and over the other shelf areas (stations 14-23). In the GSL, the $\epsilon_{\emptyset}$ values are less than 8° and ϵ_A values are generally less than 10%, except for the K_1 constituent due to the overestimation of the K_1 amplitudes by about 4 cm at West St. Modeste (station 1) and Charlottetown (station 7) (Table 4.2). In the GoM-BoF (stations 9-13), the $\epsilon_{\emptyset}$ values are less than 5° and ϵ_A values are more than 10% for M_2, N_2, S_2 and O_1, and in particularly the N_2 amplitude is overestimated by 10 cm at Saint John (station 10). Over the other shelf areas, relatively larger error value ($\epsilon_{\emptyset}$> 10° and ϵ_A>10%) are obtained, and errors are in particularly large at New York City (station 18), Chesepeake Bay (station 21), and Wilmington (station 23). It should be noted that these three stations are located inshore of small bays or river channels, which are not adequately resolved by the model. In general, the model has a good skill in simulating tidal elevations over the ECS. The simulated tides are strong in the western GSL and GoM-BoF, and weaker elsewhere. Previous studies have shown that tides have minor impacts on circulation and hydrography over the LS and NfS (e.g., Han et al. 2008).

In the Appendix B, maps of amplitudes and phases of tidal elevations and ellipses of tidal currents for selected constituents from the WithTide simulation are presented. The model results agree well with OTIS, historical observational data and previous modelling studies in the region (e.g., Saucier and Chassé 2000; Lu et al. 2001; Saucier et al. 2003). The Appendix also presents the differences in the ellipses of tidal currents between simulations of WithTide and BaroTide, and the evidence of internal tides simulated by WithTide.

Table 4.2 Amplitudes (m) and phases (in brackets, in degree relative to the midnight GMT) of the tidal surface elevation at 23 stations shown in Figure 4.1. Numbers obtained from WithTide are shown in black, and numbers derived from tidal observations are shown in dark grey.

	Station	M_2	N_2	S_2	K_1	O_1
1	West St. Modeste	0.25 (21)	0.06 (353)	0.11 (24)	0.09 (217)	0.06 (194)
		0.19 (24)	0.05 (360)	0.08 (38)	0.05 (216)	0.04 (187)
2	Anchor Point	0.42 (74)	0.08 (48)	0.11 (86)	0.11 (274)	0.10 (257)
		0.42 (81)	0.08 (57)	0.13 (102)	0.10 (279)	0.11 (257)
3	Sept-Îles	0.88 (190)	0.20 (163)	0.27 (228)	0.24 (281)	0.20 (253)
		0.91 (185)	0.19 (159)	0.27 (227)	0.21 (277)	0.19 (250)
4	Rimouski	1.23 (211)	0.27 (180)	0.38 (246)	0.26 (286)	0.22 (257)
		1.26 (200)	0.27 (174)	0.41(243)	0.23 (280)	0.21 (251)
5	Rivière-au-Renard	0.48 (189)	0.11 (166)	0.14 (229)	0.21 (286)	0.18 (258)
		0.50 (189)	0.11 (165)	0.14 (231)	0.19 (284)	0.18 (254)
6	Lower Escuminac	0.29 (229)	0.08 (217)	0.08 (277)	0.23 (298)	0.20 (270)
		0.24 (245)	0.07 (227)	0.06 (288)	0.20 (299)	0.18 (269)
7	Charlottetown	0.63 (56)	0.17 (30)	0.17 (122)	0.29 (328)	0.23 (294)
		0.73 (63)	0.16 (29)	0.17 (133)	0.25 (327)	0.22 (294)
8	Port-aux-Basques	0.44 (16)	0.10 (354)	0.12 (50)	0.08 (251)	0.08 (231)
		0.44 (13)	0.09 (352)	0.13 (52)	0.08 (253)	0.09 (230)
9	Yarmouth	1.90 (66)	0.42 (38)	0.30 (102)	0.14 (189)	0.12 (169)
		1.63 (63)	0.35 (33)	0.25 (98)	0.14 (183)	0.11 (163)
10	Saint John	3.35 (100)	0.70 (69)	0.52 (138)	0.16 (199)	0.13 (178)
		2.97 (99)	0.60 (67)	0.46 (140)	0.15 (195)	0.12 (174)
11	Eastport	2.86 (98)	0.61 (68)	0.44 (136)	0.16 (199)	0.13 (179)
		2.61 (99)	0.54 (68)	0.41 (139)	0.15 (197)	0.12 (175)
12	Portland	1.43 (97)	0.33 (67)	0.22 (133)	0.14 (204)	0.12 (185)
		1.35 (103)	0.30 (71)	0.20 (139)	0.14 (203)	0.11 (182)
13	Boston	1.46 (104)	0.34 (73)	0.23 (140)	0.14 (208)	0.12 (189)
		1.35 (109)	0.30 (78)	0.20 (146)	0.14 (205)	0.11 (186)
14	St. John's	0.40 (305)	0.08 (289)	0.16 (351)	0.09 (153)	0.07 (126)
		0.36 (314)	0.07 (302)	0.15 (1)	0.08 (161)	0.07 (126)
15	North Sydney	0.35 (354)	0.08 (331)	0.10 (37)	0.08 (330)	0.08 (290)
		0.36 (353)	0.08 (329)	0.11 (41)	0.08 (123)	0.08 (284)
16	Halifax	0.62 (349)	0.14 (328)	0.13 (20)	0.13 (125)	0.06 (96)
		0.62 (353)	0.13 (330)	0.13 (24)	0.10 (123)	0.04 (97)
17	Montauk	0.26 (34)	0.07 (11)	0.06 (41)	0.08 (163)	0.04 (194)
		0.29 (47)	0.08 (22)	0.06 (57)	0.07 (176)	0.05 (209)
18	New York City	0.76 (351)	0.18 (334)	0.14 (12)	0.13 (167)	0.07 (154)
		0.66 (19)	0.15 (360)	0.12 (44)	0.10 (177)	0.05 (176)
19	Atlantic City	0.58 (355)	0.13 (336)	0.10 (15)	0.12 (182)	0.09 (163)
		0.58 (356)	0.13 (335)	0.11 (18)	0.11 (181)	0.07 (165)
20	Lewes	0.51 (22)	0.12 (358)	0.09 (37)	0.10 (201)	0.10 (188)
		0.59 (31)	0.13 (8)	0.10 (57)	0.10 (201)	0.08 (188)
21	Chesapeake Bay	0.51 (8)	0.12 (353)	0.09 (31)	0.07 (179)	0.05 (208)
		0.38 (21)	0.09 (360)	0.06 (46)	0.05 (184)	0.04 (213)
22	Hatteras	0.49 (358)	0.11 (339)	0.08 (17)	0.10 (172)	0.06 (183)
		0.48 (358)	0.11 (337)	0.08 (22)	0.08 (170)	0.06 (196)
23	Wilmington	0.60 (348)	0.15 (330)	0.10 (3)	0.10 (185)	0.08 (189)
		0.60 (64)	0.11 (50)	0.07 (101)	0.08 (230)	0.06 (237)

Table 4.3. The averaged relative amplitude errors (ϵ_A) and averaged-phase errors ($\epsilon_\emptyset$) of WithTide in predicting tidal surface elevations for the three groups of stations. The ϵ_A is shown in a unit of percentage, while $\epsilon_\emptyset$ is shown in a unit of degree in brackets.

M_2	N_2	S_2	K_1	O_1
Gulf of St. Lawrence (8 stations)				
6.1% (6.4°)	3.4% (4.9°)	7.4% (7.4°)	14.0% (2.8°)	9.3% (2.8°)
Gulf of Maine and Bay of Fundy (5 stations)				
10.8% (3.4°)	14.9% (2.9°)	12.5% (4.1°)	2.4% (3.3°)	13.0% (4.2°)
The rest (10 stations)				
8.7% (15.3°)	11.8% (15.2°)	11.5% (20.8°)	14.5% (9.3°)	17.2% (11.3°)

4.4.2 Temperature and Salinity

Figure 4.2 presents the monthly mean SST in February and August averaged over 13 years (1998-2010) from satellite observations and the simulation in WithTide. In February, both the observed and modelled SSTs feature consistent large-scale distributions characterized by the sharp gradients between the subpolar and subtropical gyres. The SST is lower than 2 °C over the LS, NfS, GSL, ScS and upper BoF, and higher than 15 °C south of the main pathways of the Gulf Stream and the North Atlantic Current. The surface water is relatively warm with SST of 5-10 °C over the "Northwest Corner" area centered approximately at 45°W and 50°N (Lazier 1994), and the recirculation areas over the southwestern Grand Banks and the central ScS (Hannah et al. 2001). In August, the surface water is significantly warmer than in February over the whole sub-regions from the deep ocean to coastal waters, e.g., reaching up to 20 °C over the southwestern GSL. The SST is about 18°C over large areas of the southern GSL, ScS and GoM, and lower than 15°C along coasts of the GoM and over the southwestern ScS and northern GSL, and over the northern GeB, SLRE and LS. The sharp thermal gradients between the subpolar and subtropical gyres are still present in August. Figures 4.2c and 4.2f present the SST differences defined

as the model results minus observations. In February, the SST differences are within ±1.0 °C over most parts of the model domain with the presence of both positive and negative small differences. In August, the SST differences are mostly positive and less than 1.0 °C over most of the ECS, but are up to ~3.0 °C over the central GoM, and up to ~2.0 °C over the southern LS and eastern NfS.

Next, the simulated T and S are compared with in-situ hydrographic observations along three AZMP transects extending from the coast to shelf break (locations shown in Figure 4.1). The observed data collected during 1999-2010 are interpolated onto model grids and then time averaged, while the daily mean values from the WithTide simulation are selected when observations are available. Figures 4.3 and 4.4 present the spatial distributions of observed and simulated T and S.

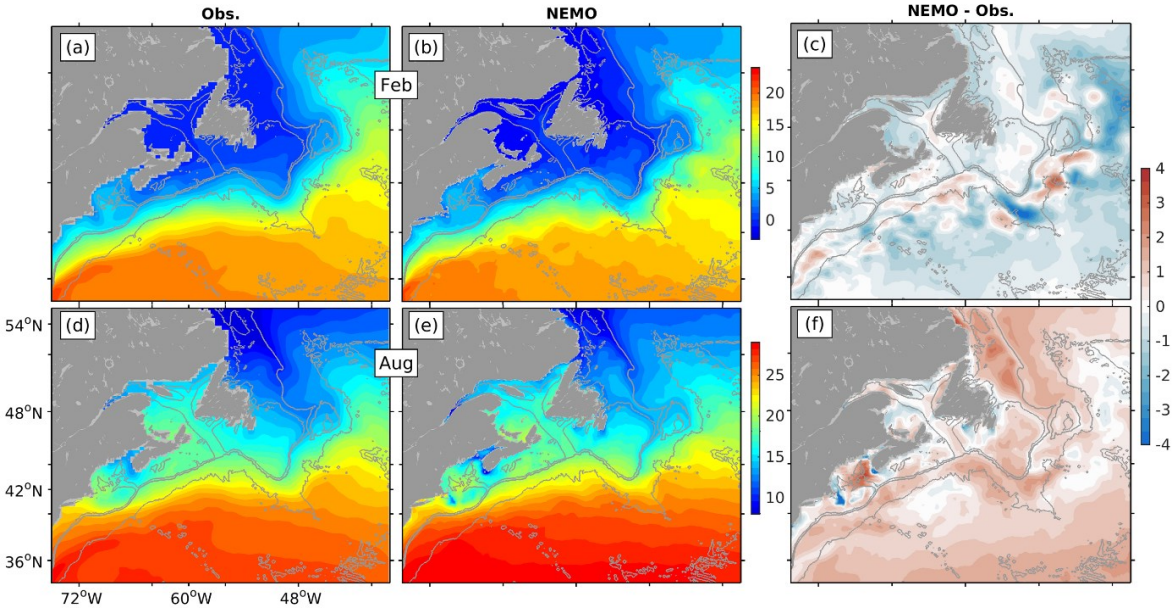

Figure 4.2. Distributions of monthly mean SST (in °C) in February (upper) and August (lower) averaged over 1998-2010, from (left) satellite remote sensing observations, (middle) model results in WithTide, and (right) model results minus observations. Dark grey contours are isobaths of 200 m, 1000 m, and 4000 m, respectively.

The hydrographic observations along the SIL transect of the southern LS (Figures 4.3a and 4.4a) feature the presence of cold and fresh waters originated from the Nordic Seas, Baffin Bay and Hudson Strait (Lazier and Wright 1993). Over the shelf and upper slope,

the cold (about -1 °C) sub-surface water is formed in winter, and the warm surface layer mainly represents the summer condition. The surface water is fresher than the sub-surface water on the shelf along the SIL transect. The cold and fresh water on shelf changes to relatively warmer (~4 °C) and saltier water below surface off the shelf break. The modelled T and S distributions (Figures 4.3b and 4.4b) are very similar to observations. The model overestimates the shelf water temperatures by about 0.9 °C, and underestimates the warmer upper slope water by ~0.3 °C. The model also underestimates the salinity on the shelf of the transect, particularly towards the bottom. For all the available data values, i.e., without applying averaging according to locations, the observed and simulated hydrographic values have a correlation coefficient of 0.89 for T and 0.90 for S. Their differences, measured by the Root Mean Squared Difference (RMSD), are 1.65 °C for T and 0.55 psu for S (Table 4.4).

The hydrographic observations over the SEG transect over the NfS (Figures 4.3c and 4.4c) feature cold (<2 °C) and fresh (<33.0 psu) waters over the shelf. Close to the sea bottom near the coast and over the shelf break, the temperature is the lowest (about 1 °C) but salinity is higher than in the upper layer. Off the shelf break of the transect, the Gulf Stream water is clearly identified by the warm (>7 °C) water located in the upper 300 m layer, but less obvious by salinity. The model overestimates the temperature of the coldest near bottom water over the shelf break and obtains a more diffusive distribution of T associated with the Gulf Stream (Figure 4.3d).

For salinity, according to observations, the low salinity shelf waters (represented by the isohaline of 33.5 psu in Figure 4.4c) reaches ~200 m depth over the shelf break, but according to model simulation (Figure 4.4d) this isohaline reaches a shallower depth of ~170 m. For all the available observational data over the SEG transect, the observed and simulated values have a correlation coefficient of 0.77 for T and 0.89 for S. The RMSD is 2.52 °C for T and 0.44 psu for S (Table 4.4).

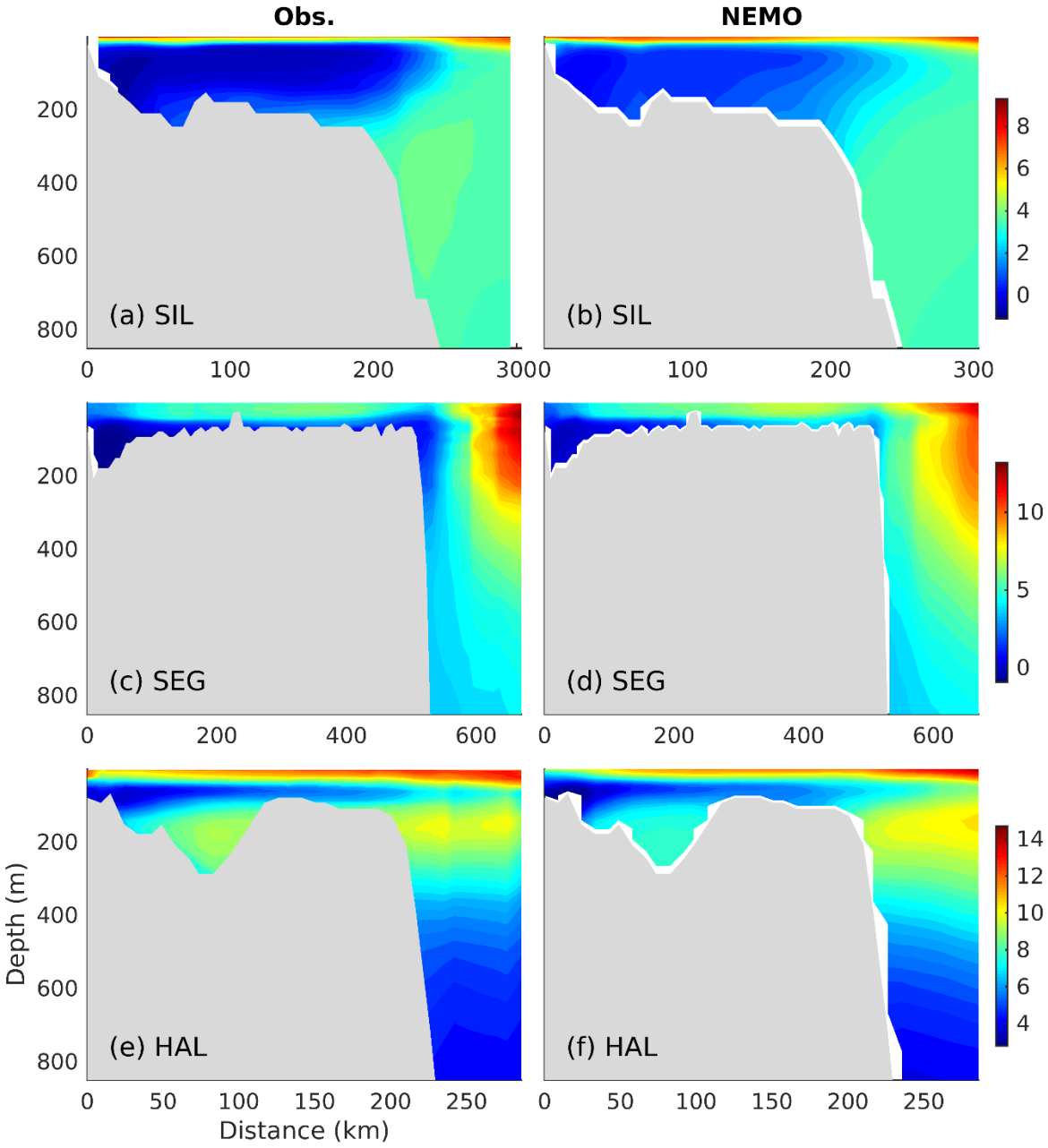

Figure 4.3. Time-averaged potential temperatures (in °C) from AZMP observations (left) and model results in WithTide (right) at transects of SIL (upper row), SEG (center row) and HAL (lower row). The AZMP data collected during 1999-2010 are interpolated onto mode grids, and the daily mean model results are selected when observations are available. Averaging is applied to data values at the same location.

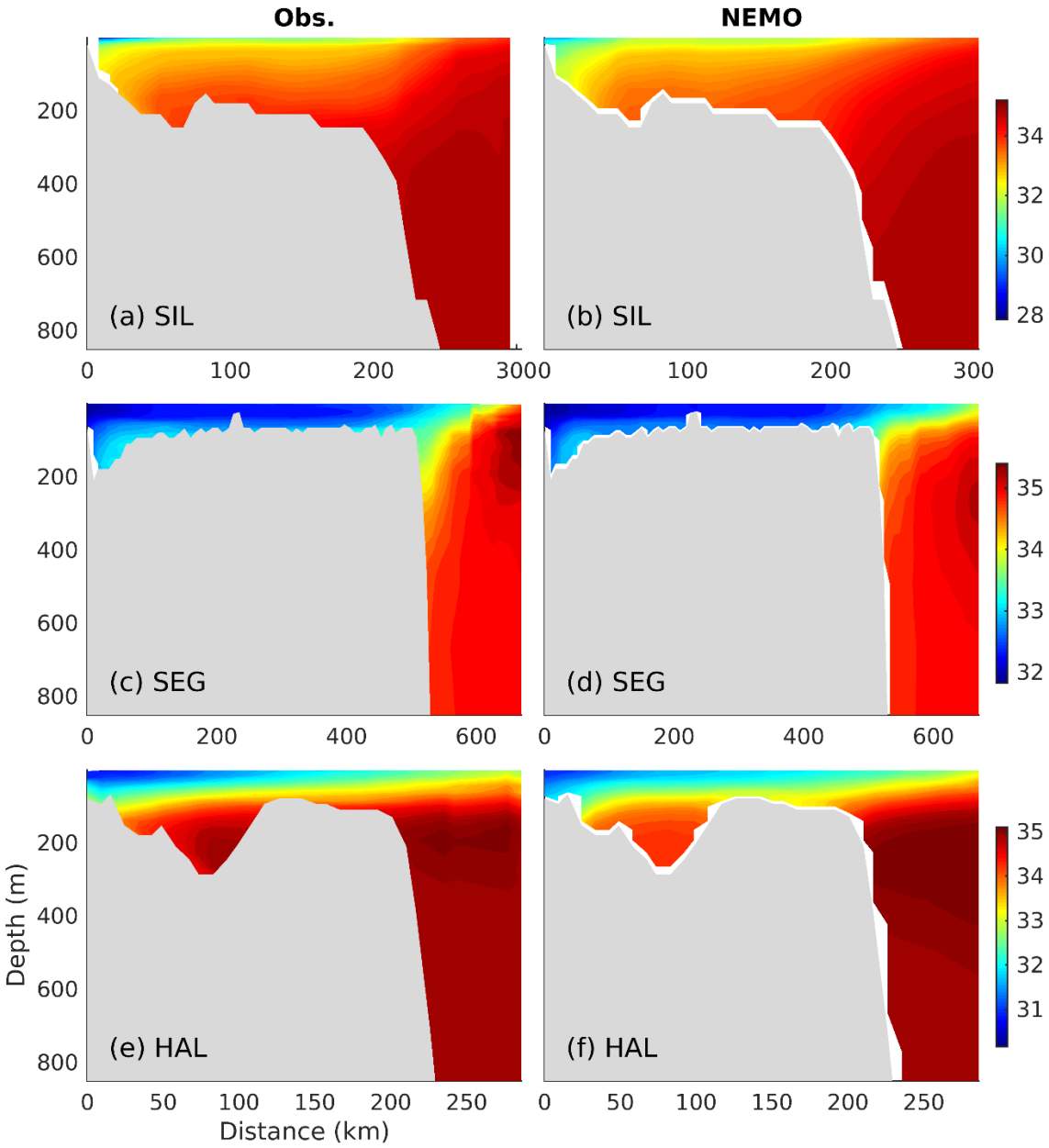

Figure 4.4. Same as Figure 4.3 but for salinity (psu).

The hydrographic observations over the HAL transect over the ScS (Figures 4.3e and 4.4e) feature three layers in the vertical on the shelf: a warm and salty surface layer, a cold and fresh intermediate layer reaching about 100 m depth contributed by winter cooling and waters from the GSL (Loder et al. 2003), and a warm and salty bottom layer primarily contributed by the Slope Water (Dever et al. 2016). The warm (~8-10 °C) slope water occupies 100-300 m depth extending from the shelf break to the deep water, while along

the SIL and SEG transects the similar layer is occupied by the cold water (<2 °C) associated with the Labrador Current (Fratantoni and Pickart 2007; Loder et al. 1998). The model generates lower T and S (Figures 4.3f and 4.4f) than observed at the intermediate and bottom layers on the shelf, likely due to underestimation of the intrusion of the warm slope water into the Emerald Basin (EBn). The model obtains higher temperature than observed for the warm layer at 100-300 m depth over and away from the shelf break. For all the available observations along the HAL transect, the observed and simulated hydrographic values have a correlation coefficient of 0.85 for T and 0.89 for S. The RMSD is 2.41 °C for T and 0.62 psu for S (Table 4.4).

Table 4.4. The RMSDs and correlation coefficients (in brackets) for temperature and salinity produced by the model in WithTide and NoTide in comparsion with observed in the AZMP three transects and two stations, respectively.

	WithTide		NoTide	
Name	Temperature (°C)	Salinity (psu)	Temperature (°C)	Salinity (psu)
SIL	1.65 (0.89)	0.55 (0.90)	1.68 (0.89)	0.55 (0.90)
SEG	2.52 (0.77)	0.44 (0.89)	2.40 (0.78)	0.45 (0.89)
HAL	2.41 (0.85)	0.62 (0.89)	2.73 (0.82)	0.70 (0.89)
RIM	1.29 (0.88)	1.04 (0.96)	2.87 (0.49)	2.46 (0.67)
SP5	0.56 (0.99)	0.29 (0.85)	3.57 (0.63)	1.19 (0.47)

4.4.3 The Gulf Stream and Meso-Scale Eddies

One of the major challenges in modelling the 3D circulation in the North Atlantic is to correctly simulate the separation of the Gulf Stream near the Cape Hatteras. In many numerical circulation models, the Gulf Stream “overshoots” northward before turning eastward (see a review by Chassignet and Marshall 2008), leading to a significant

northward bias in the pathway of the Gulf Stream between Cape Hatteras and the southern tip of the Grand Banks of Newfoundland. Such a large model bias shall affect the model performance in simulating 3D circulation over many regions including the Scotian Slope region and on the ScS and GoM.

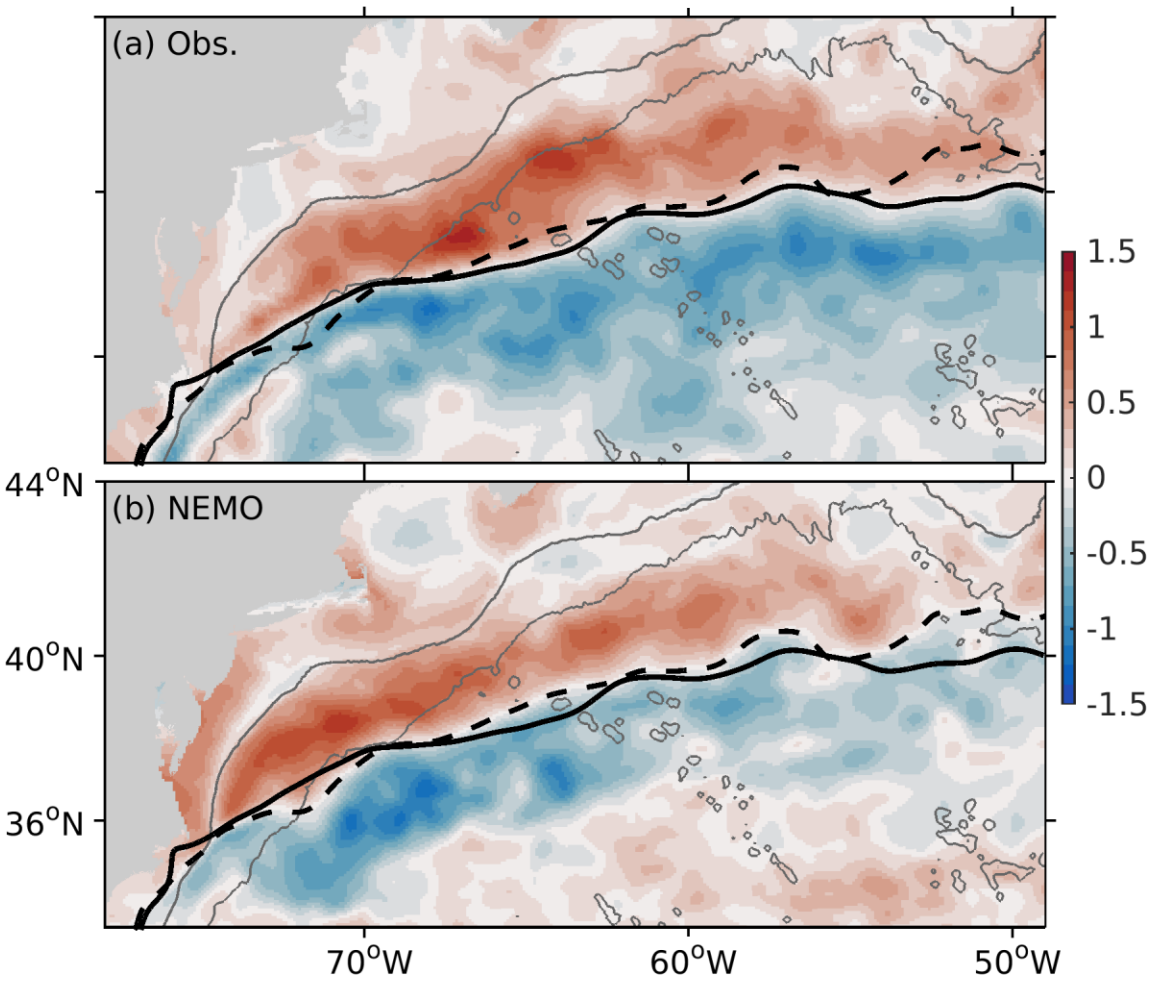

Figure 4.5. Distributions of the skewness of sea surface height anomalies during 1998–2010 based on (a) the gridded satellite altimeter data and (b) model results in WithTide. The solid and dashed thick black lines denote the mean path of the Gulf Stream defined by the zero contour of the skewness smoothed by a 50 x 50 km box moving average, for the observed and model results, respectively. The thin grey contours are isobaths of 200 m, 1000 m, and 4000 m, respectively.

There are various ways to evaluate the model simulated Gulf Stream pathway. Here we follow Thompson and Demirov (2006) and compare the skewness of SSH anomalies during 1998-2010, based on the gridded altimetry data and the simulation in WithTide (Figure 4.5). The areas with positive (negative) skewness are related to variations of the anti-cyclonic (cyclonic), or warm (cold) core eddies, and the zero-skewness in between corresponds to the mean path of the Gulf Stream. Compared with observations, the model reproduces similar spatial distributions of the skewness, and the positions of the zero-skewness line with a slight northward shift to the east of 67°W. This suggests that the circulation model with the model setup and forcing has good skills in simulating the Gulf Stream pathway and the spatial distributions of meso-scale eddies.

4.4.4 Sea Ice

In our study region, sea ice presents in winter in the GSL, along the coast of Newfoundland and Labrador, and occasionally along the coast of Nova Scotia (Canadian Ice Service 2009). Here we evaluate the modelled sea ice in the GSL and the adjacent ScS, where the impacts of tides on sea ice are expected to be significant.

Figure 4.6 presents the ice concentrations from January to April, based on ice observations (the ice charts from the Canadian Ice Service) and model results in WithTide and NoTide. According to observations, ice starts to form in limited coastal areas in December. In January, ice spreads over the GSL with higher concentrations in the SLRE and along the southwestern and northern coasts. In February, ice reaches its maximum concentrations, and covers nearly the whole GSL except for the southeastern areas along the Newfoundland coast. In March, ice starts to melt with lower concentrations than in February. In April, ice nearly completely disappears, except for some coastal waters such as the MS and the northeastern GSL. Overall, the seasonal ice evolution from WithTide agrees well with the observations, except for an overestimation of the ice concentrations by 20-40% during January - March in the northwestern GSL. The difference between WithTide and NoTide in sea ice will further be discussed in Section 4.5.4.

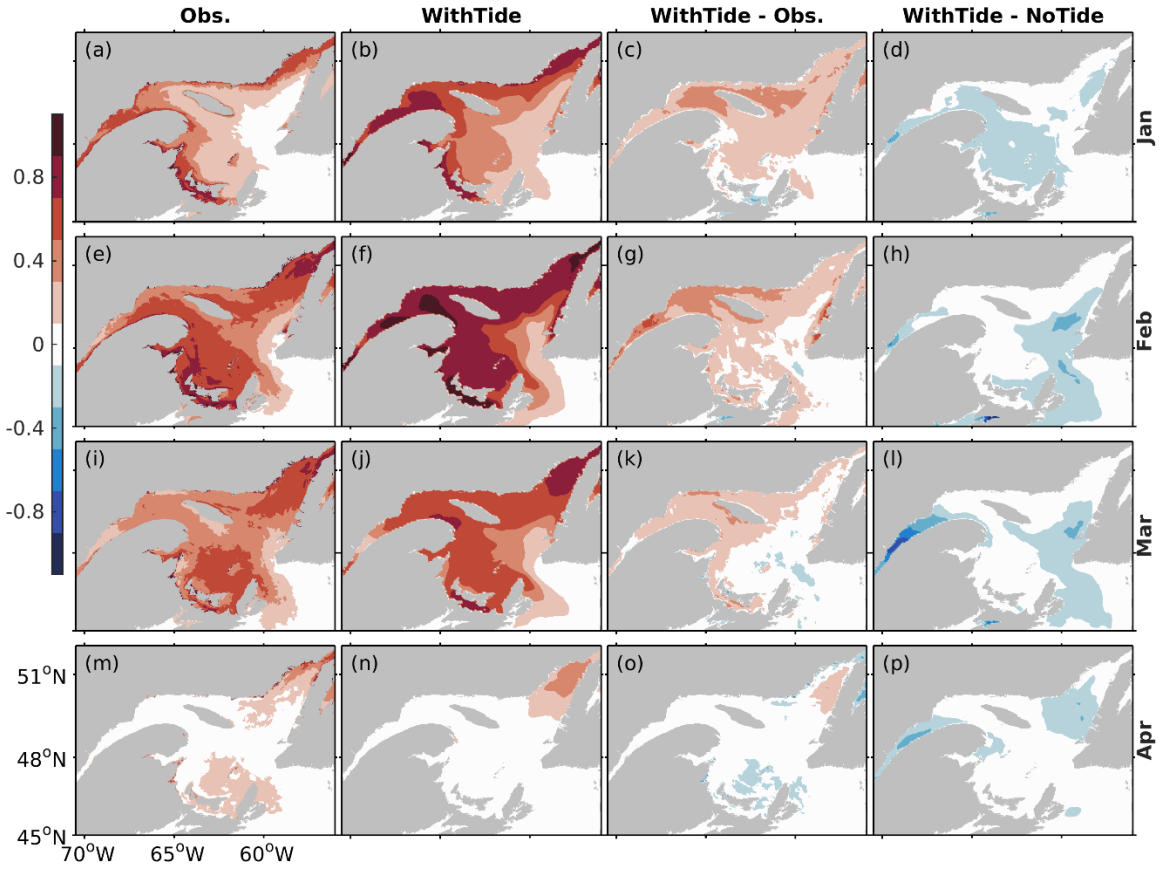

Figure 4.6. Sea ice concentrations in the GSL in (from top to bottom) January, February, March, and April averaged over four years (2007-2010) based on (from left to right) observations (based on the Canadian Ice Service charts), model results in WithTide, WithTide minus observations, and WithTide minus NoTide.

4.5 Impacts of Tides on Sub-Tidal Dynamics

The analyses in this Section are focused on two sub-regions: the GSL and GoM-BoF (including ScS for some aspects), because the tidal impacts are expected to be significant over these two sub-regions due to the presence of strong tidal elevations and flows. The tidal impact on the seasonal circulation is quantified using a tidal impact index (T_i) defined as:

$$T_i = \frac{|\mathbf{U}^T - \mathbf{U}^{NT}|}{|\mathbf{U}^T| + |\mathbf{U}^{NT}|} \tag{4.3}$$

where $\mathbf{U}^T$ and $\mathbf{U}^{NT}$ represent respectively the monthly mean horizontal current vectors from WithTide and NoTide, and the operator $|\cdot|$ represents the amplitude of the current vector. In this analysis T_i was computed only if $|\mathbf{U}^T - \mathbf{U}^{NT}|$>0.01 m s^{-1} in areas shallower than 2000 m, because eddies and meanders are often dominant in the circulation variability in the deep waters beyond the shelf edge of the ScS (Urrego-Blanco and Sheng 2012).

4.5.1 Tidal Impacts on Seasonal Circulation in the GSL

a. Upper layer (surface to 50 m average)

Figures 4.7a and 4.7c present the multi-year (1998-2010) averaged upper layer circulation in February and August from WithTide in the GSL. The general features are consistent with previous studies over this region (Han et al. 1999; Saucier et al. 2003; Urrego-Blanco and Sheng 2014b). In February, the time mean circulation is strong, with an intense southwestward jet (up to 0.3 m s^{-1}) located roughly over the 100 m isobath in the northeastern GSL. This jet bifurcates to the east of Anticosti Island (AI) with two branches. One branch flows northwestward and then westward to join the cyclonic circulation over the northwestern GSL between the AI and SLRE. The other branch flows around the coast of the southern AI to be part of the intense currents along the western flank of the LCh over the southern GSL. The southeastward (seaward) current (up to 0.3 m s^{-1}) exits the GSL through the western part of the Cabot Strait (CS). Through the eastern part of CS, the northwestward (landward) flow enters the GSL. This inward flow turns northeastward to form a weak cyclonic gyre over the Esquiman Channel (ECh). Along the Gaspe Peninsula, the meandering jet is known as the Gaspe Current (Sheng, 2001). Over the southwestern GSL, the relatively broad southward currents turn eastward to the north of the Prince Edward Island and then northeastward off the northwestern Cape Breton Island, and finally join the outward flow over the western portion of CS.

In August, the upper layer estuarine circulation in the SLRE and the southward currents over the southwestern GSL are stronger than in February (Figures 4.7a and 4.7c), due mainly to the larger freshwater discharge from the St. Lawrence River (Ohashi and Sheng 2013). The Gaspe Current intrudes onto the Shallows to the west of the Magdalen Islands (MI), resulting in strong density fronts (Koutitonsky and Bugden 1991). Over other parts

of the GSL the currents in August are weaker than in February, due mainly to weaker wind forcing in summer (Murty and Taylor 1970). Over the eastern GSL, the southwestward jet is narrower and closer to the Quebec Lower North Shore in August than in February. This southwestward jet bifurcates, with the main branch flowing westward through the passage between the Lower North Shore and AI, and a smaller branch flowing southwestward and then anti-cyclonically along the coast of the southeastern AI.

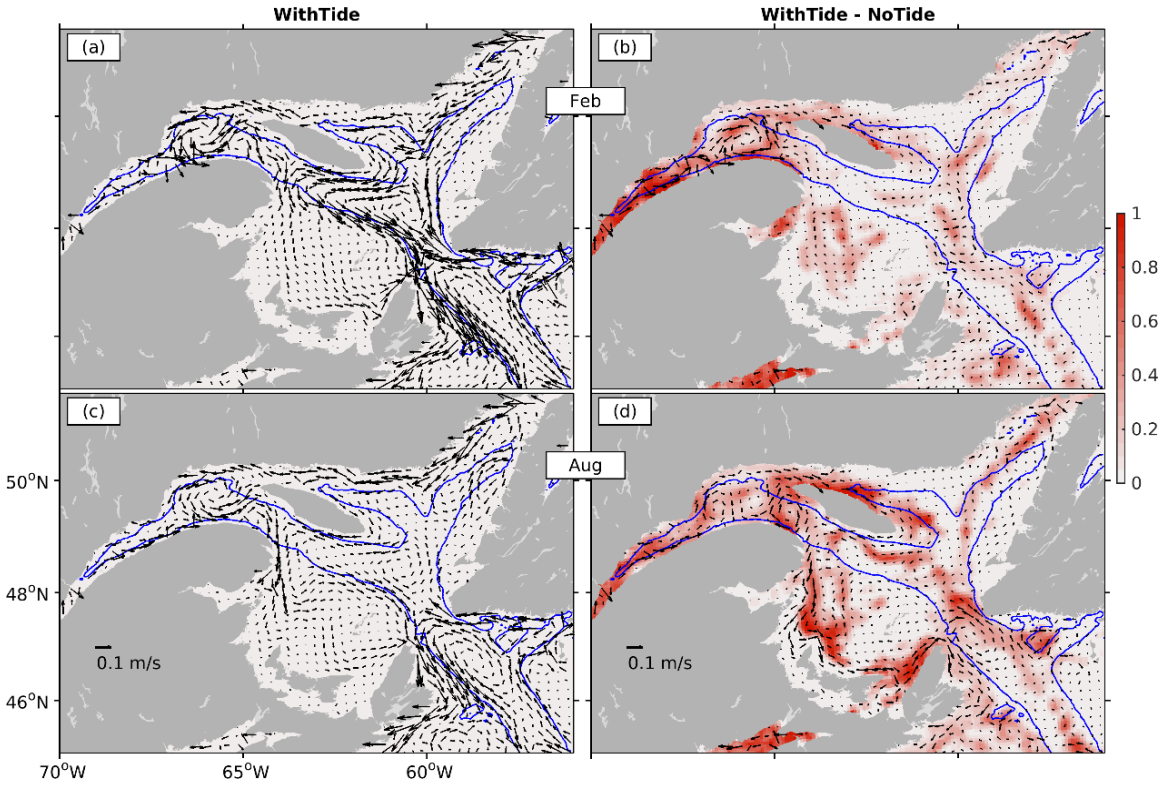

Figure 4.7. Distributions of multi-year (1998-2010) averaged currents in the upper layer from surface to 50 m (left) from model results in WithTide, and (right) current vector differences of WithTide minus NoTide, in (a,b) February and (c,d) August, in the GSL and adjacent waters. Vectors are shown in every 3rd model grid point along both latitudinal and longitudinal directions. The color shading in the right panels represents the tidal impact index (T_i) after applying a running mean horizontal filter (3 points by 3 points with uniform weights) to eliminate grid-point noise. Black contours are isobaths of 200 m and 1000 m, respectively.

Figures 4.7b and 4.7d present the tidal effects on the mean circulation in the GSL. In February (Figure 4.7b), the tidally induced mean currents are up to 0.1 m s^{-1} over the SLRE

and the northwestern GSL, with a cyclonic recirculation over the northwestern GSL between the SLRE and AI. There are several small-size recirculation cells over the southwestern GSL, and a relatively weak tidally induced anti-cyclonic recirculation over CS. In August (Figure 4.7d), the tidally induced mean currents are seaward along the south shore of the SLRE, off the Gaspe Peninsula and in the shallow waters over the southwestern GSL. The recirculation cells between the SLRE and AI and over CS are in August similar as in February. The anti-cyclonic circulation around AI becomes more evident in August than in February.

Values of the tidal impact index (T_i) are relatively large in the SLRE and coastal waters of the Gaspe Peninsula, and are greater in February than in August (Figure 4.7). In the SLRE, the tidal impacts on the estuarine circulation can be attributed to the modification of density by the strong tidal mixing (Forrester, 1974; Ingram, 1983; Saucier and Chassé, 2000). On the other hand, the reduced sea ice concentrations (and thickness) due to tides (to be discussed in Section 4.5.4) can enhance the wind-driven circulation. This may explain the greater T_i values in February than in August. Over serval other areas in the GSL, the T_i values are usually greater in August than in February, evidently in the western GSL, around AI, and along the eastern flank of CS and the lower LCh. Over these areas the impacts of tides on sea ice are less evident, hence the tidal impacts on the wind-driven circulation (stronger in winter than in summer) are not significant. Thus, the greater T_i values in August can be explained by the stronger tidal impacts on the estuarine circulation that is stronger in summer than in winter.

b. Lower layer (50 – 200 m average)

Figures 4.8a and 4.8c present the multi-year (1998-2010) averaged currents in the lower layer of the GSL in February and August from model results in WithTide. In February, the lower layer time-mean circulation (Figure 4.8a) shows similar features as in the upper layer (Figure 4.7a), due mainly to the weak vertical stratification in winter (Koutitonsky and Bugden 1991). The lower layer circulation has three well-defined and strong cyclonic gyres (with the maximum speed up to 0.06 m s^{-1}) in the central LCh, the northwest GSL and the central ECh. To the south of the GSL, there is an intense cyclonic gyre over CS and the lower LCh, with the maximum speed of about 0.05 m s^{-1}. In August, the lower-layer time-

mean circulation in the GSL and adjacent waters (Figure 4.8c) is much weaker than in February (Figure 4.8a). Nevertheless, the three cyclonic gyres in the GSL are still noticeable in August, and the cyclonic gyre in CS and the lower LCh is still strong with the maximum speed up to 0.04 m s^{-1}.

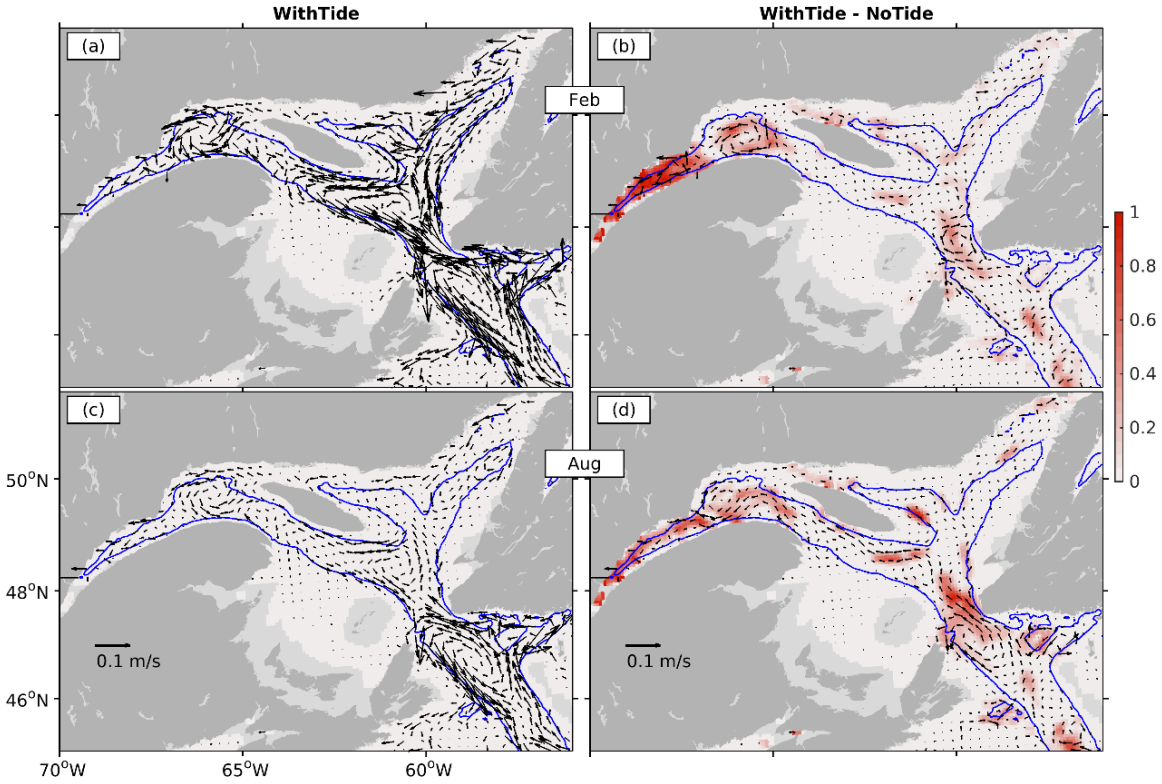

Figure 4.8. Same as Figure 4.7 except for in the lower layer between 50 and 200 m.

In both February and August, the values of T_i (Figures 4.8b and 4.8d) are relatively large in the SLRE, the northwest GSL, LCh, and CS. The tidally induced mean currents In the SLRE are up to 0.06 m s^{-1} in February and stronger than in August. This may again be attributed to the reduced sea ice in winter that enhanced the upper layer wind-driven circulation. Near the entrance of the SLRE, the tidally induced mean currents feature a small-scale cyclonic gyre in February, but an anti-cyclonic gyre in August. Outside of the SLRE, the tidally induced lower-layer mean currents in August are landward

(northwestward) along the LCh from CS at least to the entrance of the SLRE, favoring enhancement of the estuarine circulation.

4.5.2 Tidal Impacts on Seasonal Circulation in the GoM and Western ScS

a. Upper layer (surface to 50 m average)

Figure 4.9a presents the multi-year (1998-2020) mean upper layer circulation in February in the GoM and over the western ScS from WithTide. The Nova Scotia Current flows southwestward as an intense coastal jet over the western ScS. The Current bifurcates after passing EBn. The main branch flows offshore to join the southwestward jet at the shelf break of the southwestern ScS. The smaller branch continues along the coast of southwest Nova Scotia and then turns northwest to enter the GoM. The shelf break jet flows southwestward onto the southern flank of GeB, with a small portion entering the GoM through the eastern part of the Northeast Channel. This small portion flows firstly northwestward and then northward to join the coastal branch of the Nova Scotia Current, to form a gulf-wide cyclonic circulation in the inner GoM (Figure 4.9a). This gulf-wide cyclonic circulation includes the Eastern Maine Coastal Current (EMCC) and the Western Maine Coastal Currents (WMCC) over the western GoM (Xue et al. 2000). The EMCC extends along the eastern coast of Maine to Penobscot Bay, and the WMCC extends westward from Penobscot Bay to Massachusetts Bay. The WMCC flows southeastward over the southern flank of Wilkinson Basin and then splits into two branches, with the main branch flowing eastward to be part of an intense anti-cyclonic gyre over GeB, and a small branch flowing southward through the Great South Channel (GSC). Over the western GoM, there are broad and southwestward currents (up to 0.13 m s^{-1}). All of these major features of the upper-layer time-mean circulation in the GoM and the western ScS (Figure 4.9) are consistent with previous studies (Greenberg 1983; Ramp et al. 1985; Xue et al. 2000; Hannah et al. 2001; Wu et al. 2012; Katavouta and Thompson 2016; Urrego-Blanco and Sheng 2014). The horizontal resolution of the present model does not resolve the gyre-type mean circulations around Minas Passage in the BoF, as reported previously by Hasegawa et al. (2011).

In August, the simulated time-mean upper layer circulation over the GoM and western ScS (Figure 4.9c) has the large-scale features highly similar to those in February. Noticeable differences include the weaker Nova Scotia Current and shelf break jet in the western ScS (Han et al. 1997; Urrego-Blanco and Sheng 2014), and the relatively stronger and narrower EMCC in August than in February. As suggested by Xue et al. (2000), the differential surface heating, coastal run-offs and the tides intensify the coastal currents to form a gulf-wide cyclonic gyre in the GoM, which is stronger in summer than in winter (Figure 4.9). The anti-cyclonic circulation over GeB is also intensified in summer due to seasonal changes in sea level gradients and reduced vertical eddy viscosity (Katavouta et al. 2016).

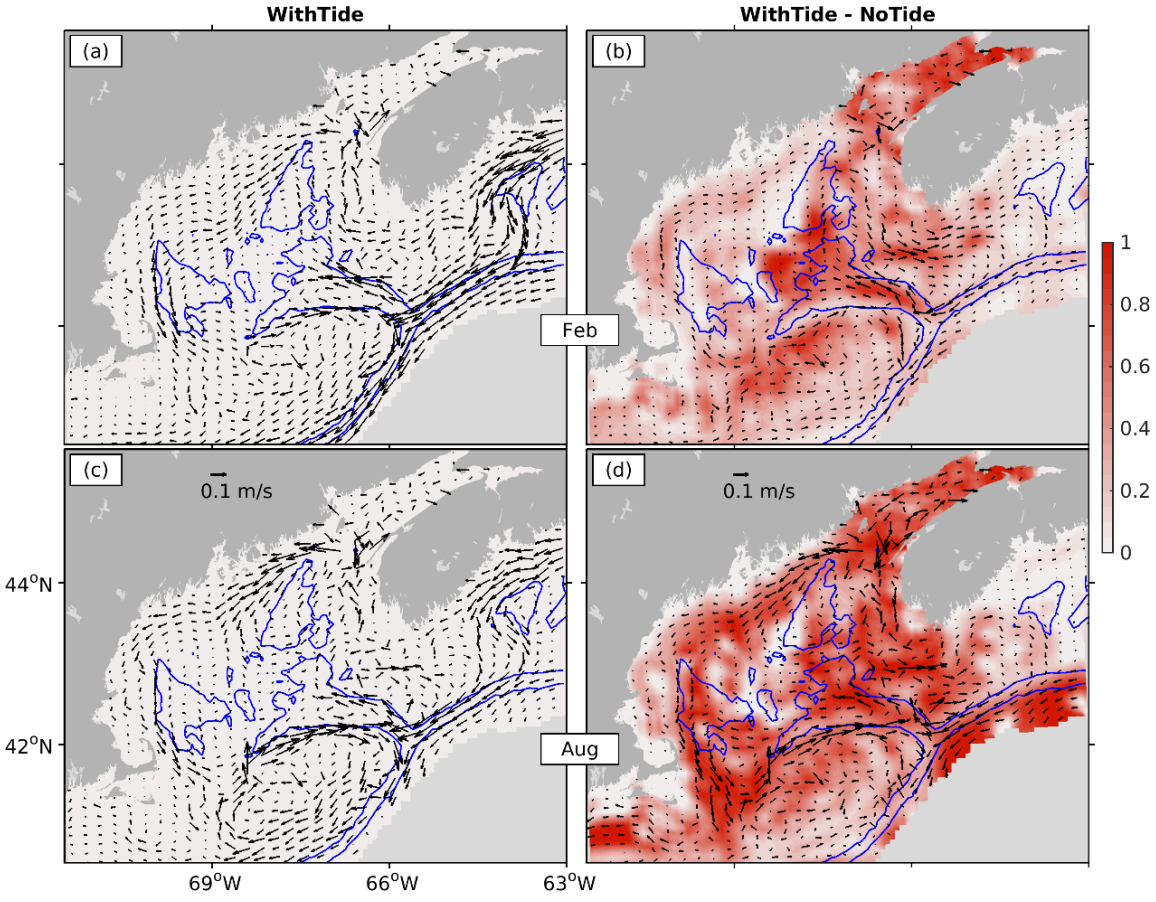

Figure 4.9. Same as Figure 4.7 except for in the upper layer from surface to 50 m in the GoM, BoF and western ScS.

In February, the tidal impact index (T_i) on the mean circulation (Figure 4.9b) has the largest values (greater than 0.7) in the BoF, the Northeast Channel, the northern part of GeB and coastal waters of the southwestern ScS. The tidally induced mean currents have speeds larger than 0.15 m s^{-1} over several areas. Regarding the current directions, the tidally induced currents direct southwestward over the western ScS, roughly in the opposite direction of the coastal branch of the Nova Scotia Current. The tidally induced currents are anti-cyclonic in the inner GoM, also in the opposite direction of the total mean cyclonic circulation. The currents direct southwestward over the shelf break of the southwestern ScS and the GoM, in the same direction as the total mean currents. Over the Northeast Channel, the tidally induced currents are strong and bifurcate into two branches. One branch turns northward and separates into two parts to enter the BoF and to flow southwestward into the GoM, respectively. The other branch turns eastward to join the anti-cyclonic cell over Browns Bank to the east of the Northeast Channel.

In August, the values of the tidal impact index (T_i) (Figure 4.9d) are overall larger than in February, with the largest values greater than 0.8 in the BoF, Northeast Channel, northern part of the GeB and coastal waters of the southwestern ScS. The tidally induced mean currents show a strong southwestward jet over the shelf break of the southwestern ScS, intense eastward flow (up to 0.2 m s^{-1}) over the northern flank of GeB, and strong and northwestward flow over the outer BoF (Aretxabaleta et al. 2008). The tidally induced mean currents are also strong along the northern and western coasts of the GoM in the same direction of the EMCC and WMCC, and feature an intensified anti-cyclonic recirculation around Browns Bank.

b. Lower layer (50 – 200 m average)

In February (Figure 4.10a), the lower layer time mean (1998-2020) circulation over the GoM and western ScS shows highly similar spatial patterns to those in the upper layer, Indicating the barotropic characteristics of the circulation due to weak stratification in winter (Xue et al. 2000). In August, the simulated mean circulation in the lower layer (Figure 4.10c) also has spatial patterns similar to those in the upper layer, except for much reduced amplitudes due to the enhanced stratification in the central GoM and western ScS.

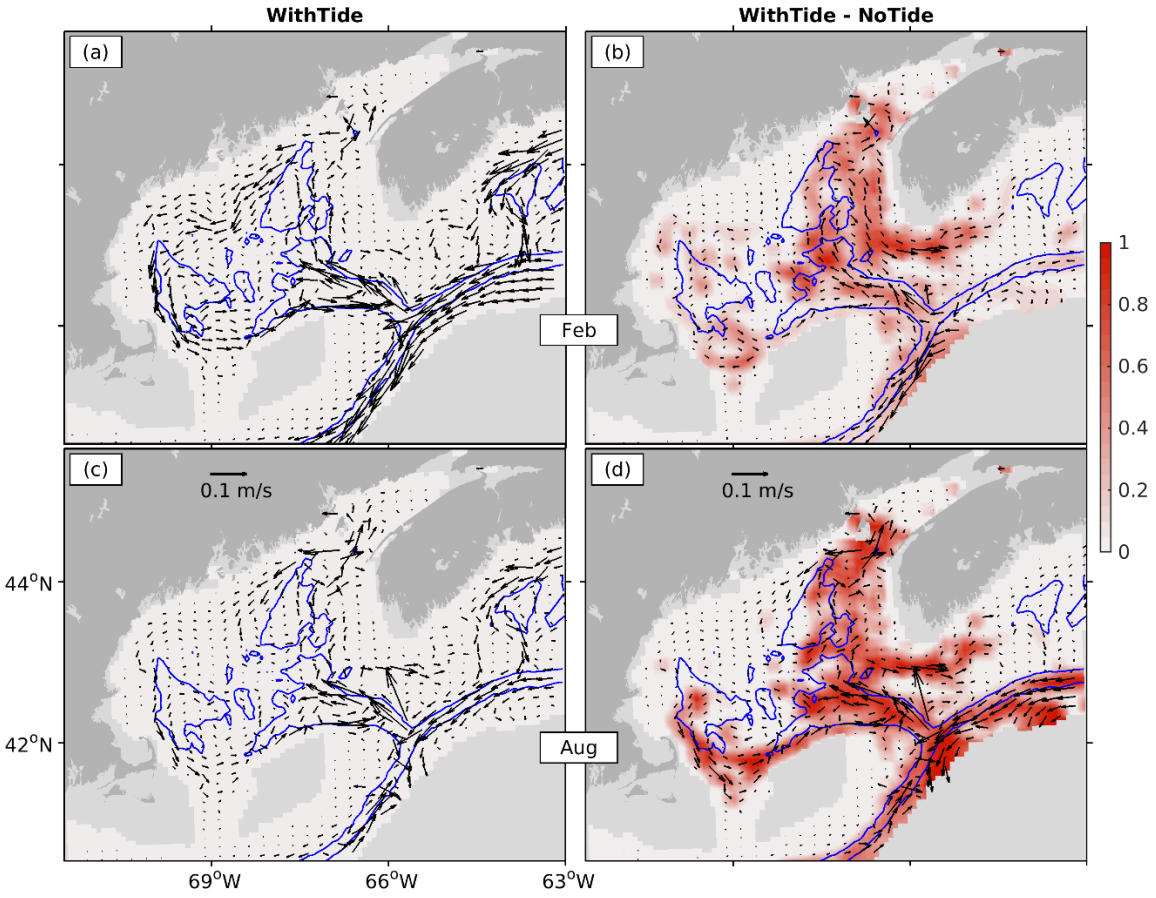

Figure 4.10. Same as Figure 4.9 except for in the lower layer between 50 and 200 m.

In February, the tidally induced mean currents (Figure 4.10b) are relatively strong over the eastern GoM and along the shelf break of the GoM, with an intense northwestward jet over the Northeast Channel. This jet gradually turns northward and northeastward to enter the central GoM and then veers anti-cyclonically to flow southward and then southeastward along the west coast of Nova Scotia. The latter is in the opposite direction of the mean total currents. Along the shelf break off the GoM, the tidally induced mean currents are southwestward, in the same direction as the mean total currents. In August, the tidally induced mean currents (Figure 4.10d) are stronger over the eastern GoM and northern flank of the GoM than in February, indicating stronger tidal effects on the mean currents in summer than in winter. In both February and August, the tidal impact index (T_i) (Figures 4.10b and 4.10d) has relatively large values in the Northeast Channel, the eastern GoM,

and the lower BoF. In August, the tidal impact index (T_i) is larger than in February over the Northeast Channel, the shelf breaks, and the northern flank of GeB.

4.5.3 Tidal Impacts on Hydrography

The differences between WithTide and NoTide in the multi-year (1998-2010) averaged SST and SSS in February and August are presented in Figure 4.11. As discussed earlier, the simulated monthly mean SST from WithTide agrees well with observations (Figure 4.2). Therefore, the differences in SST shown in Figure 4.11a suggest that NoTide has larger model biases. In February, large differences in SST occur over the GoM, Nantucket Shoals (NaS), GeB, and western ScS, where the SST from WithTide is higher than NoTide by up to 4 °C. Such large differences suggest the tidally induced onshore transport of relatively warm (and salty) waters on slope (Figures 4.9 and 4.10). In comparison with NoTide, the SSS from WithTide (Figure 4.11b) is higher by up to 1.6 psu in the BoF, about 1 psu over the southwestern GSL, and by more than 2 psu in the SLRE with the largest differences reaching 20 psu in the upper SLRE. In August, WithTide obtains significantly lower SST than NoTide over the GSL, GeB, and the GoM-BoF (Figure 4.11c). WithTide obtains significantly higher SSS than NoTide, by up to 2 psu near the Churchill River mouth in the LS, up to 20 psu in the SLRE, and more than 0.6 psu over the GoM-BoF and GeB (Figure 4.11d).

In the western GSL, particularly in the SLRE, tidal forcing leads to much reduced SST in summer, and increased SSS in both winter and summer. We now examine the tidal impacts on vertical stratification at station RIM in the SLRE. Figure 4.12 (upper row) presents the observed T and S profiles. It should be noted that few vertical profiles of observed hydrography are available in winter due to the ice cover. During the ice-free period, the observed T shows a three-layer structure (Figure 4.12a), consisting of a surface mixed layer reaching roughly 50 m depth, a cold intermediate layer at 50-150 m, and a relatively warm bottom layer. The seasonal freshening in the upper layer (Figure 4.12b) is associated with freshwater input from rivers, with the dominant discharge from the St. Lawrence River (Ohashi and Sheng 2013). Model results in WithTide have a similar three-

layer vertical structure for T as observed and suggests the local formation of the cold intermediate layer associated with winter cooling (Figure 4.12c), and similar seasonal evolution of S (Figure 12d). Model results in NoTide have an unrealistically thin and highly stratified upper layer and a much thinker cold intermediate layer (Figures 4.12e and 4.12f). This is because lacking of tidal mixing, NoTide has a weaker estuarine circulation (Figures 4.7 and 4.8) for the replenishment of the cold intermediate layer waters (Smith et al. 2006b). Relative to observations, WithTide has a significantly higher correlation and lower RMSDs than NoTide (Table 4.4).

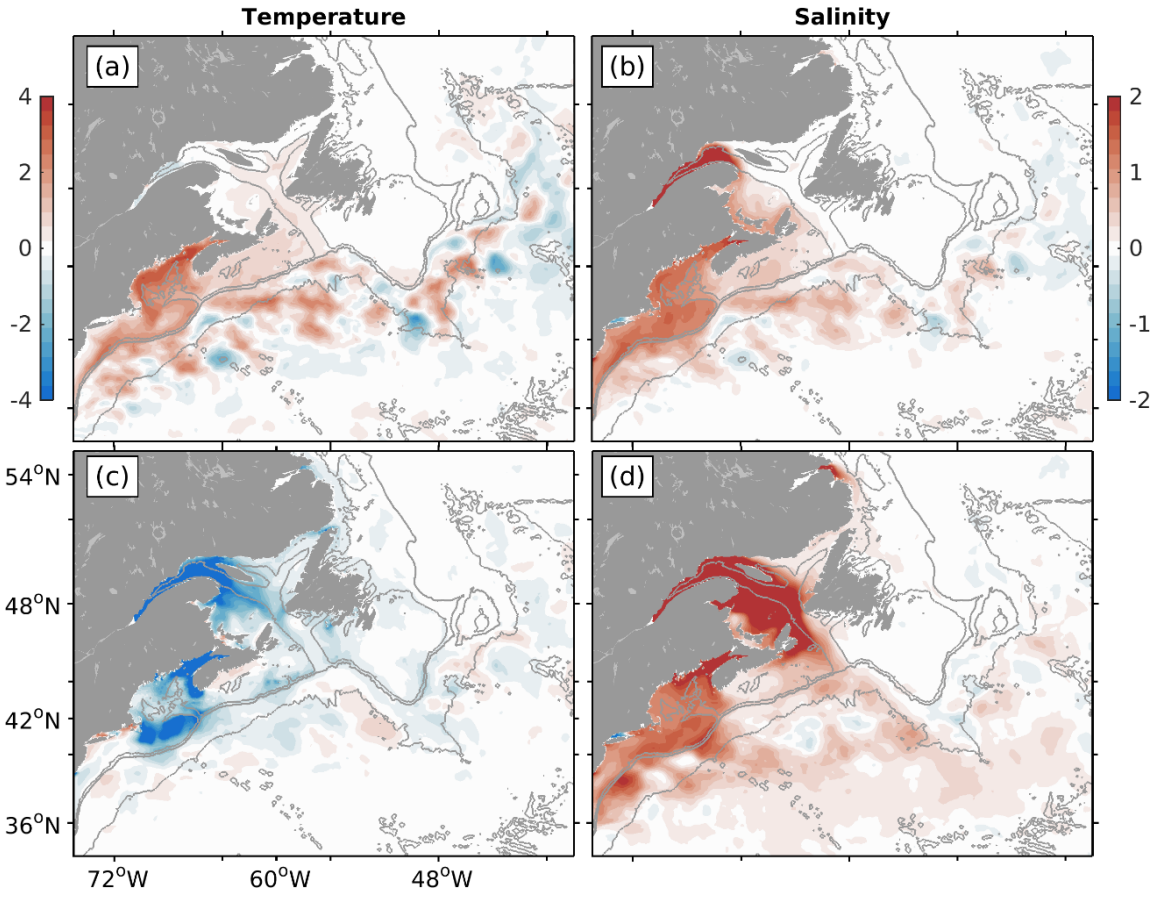

Figure 4.11. Differences in simulated multi-year (1998-2010) averaged SST (left) and SSS (right) between WithTide and NoTide in February (upper row) and August (lower row). Contours are isobaths of 200 m, 1000 m, and 4000 m, respectively.

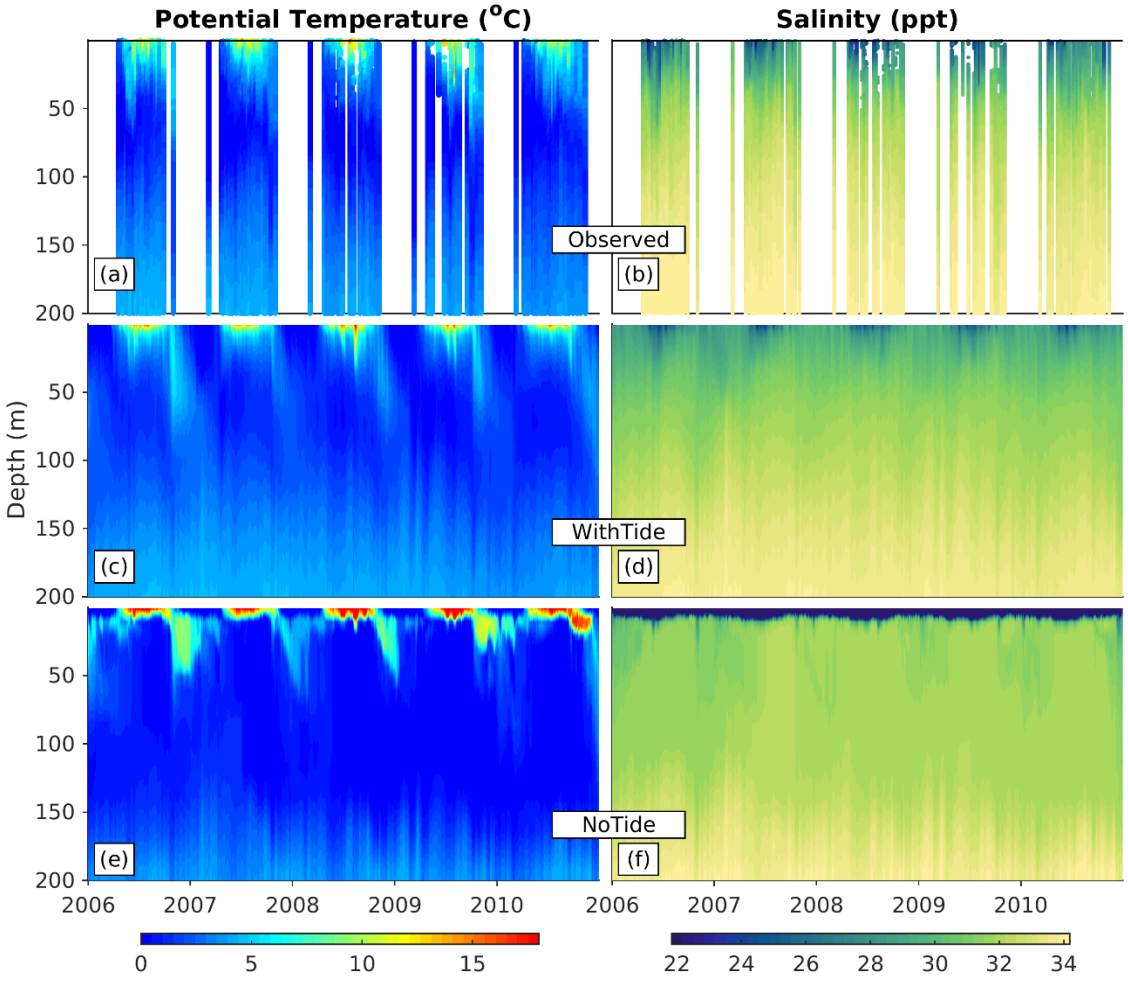

Figure 4.12. Time-depth distributions of potential temperatures (left) and salinities (right) at station RIM in the St. Lawrence Estuary during 2006-2010, calculated from in-situ observations (upper row), and model results in WithTide (center row) and NoTide (lower row). White spaces in the top panels indicate data unavailability.

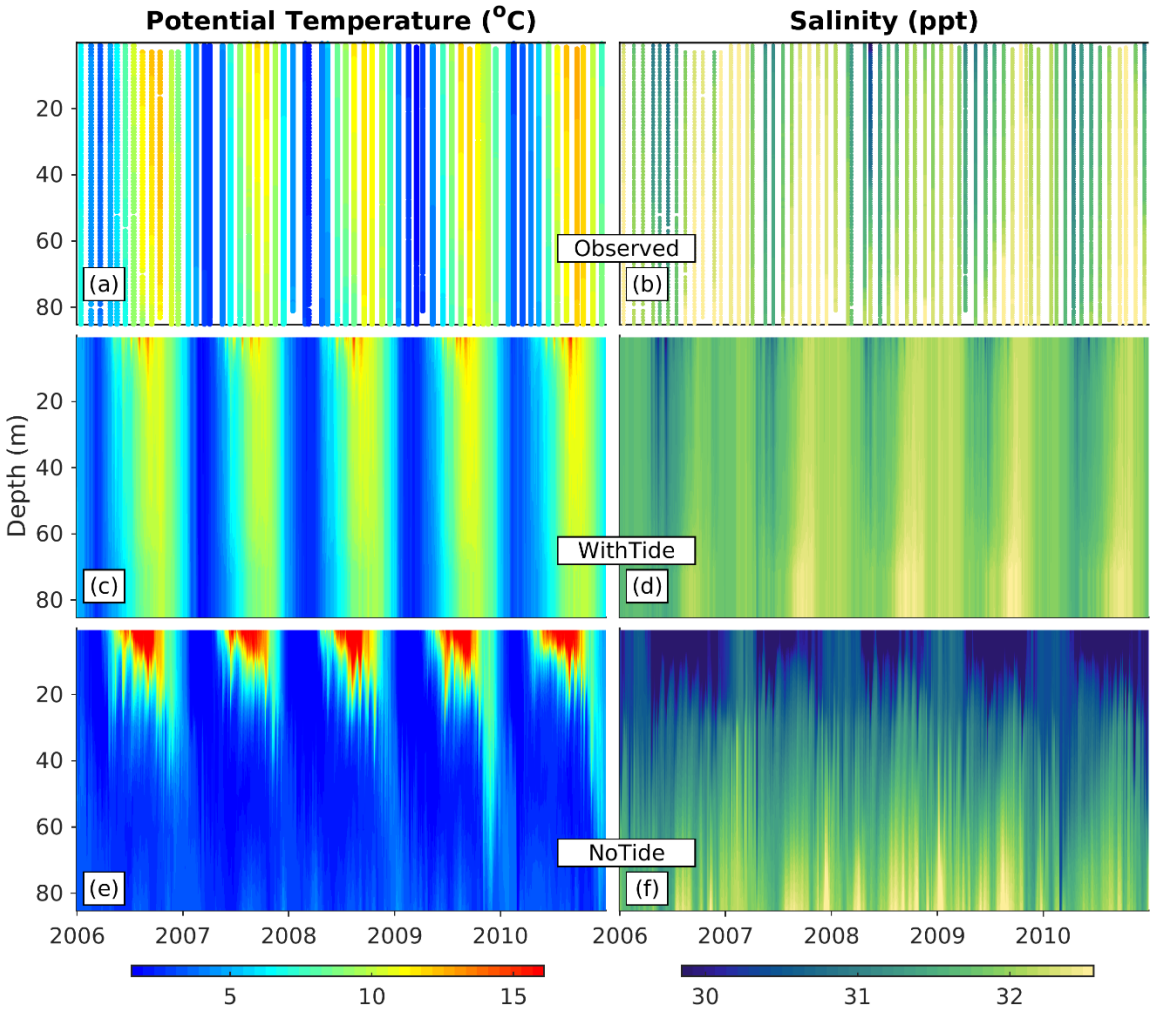

Figure 4.13. As the Figure 12, but for the station SP5 in the Bay of Fundy.

WithTide also has significant cooling over the BoF, GeB, the western ScS and adjacent waters, due to strong tidal mixing and upwelling (e.g., Garret et al. 1978; Chegini et al. 2018). Over these areas, WithTide generates surface cooling which agrees with the satellite remote sensing data (Figure 4.2) and observed hydrographic profiles (Figures 4.12 and 4.13). The tidal impacts on vertical stratification at station SP5 in the BoF are presented in Figure 4.13. The observed profiles of T and S are nearly uniform in the vertical (Figures 4.13a and 13b), due to strong tidal mixing. The model results in WithTide are in very good agreement with the observations (Figures 4.13c and 4.13d). By comparison, NoTide obtains a seasonally varying upper layer that is well mixed in winter but highly stratified

during summer (Figures 4.13e and 4.13f) that can be explained by the lack of tidal mixing. Relative to observations, WithTide obtains a significantly higher correlation coefficient and lower RMSD than NoTide (Table 4.4).

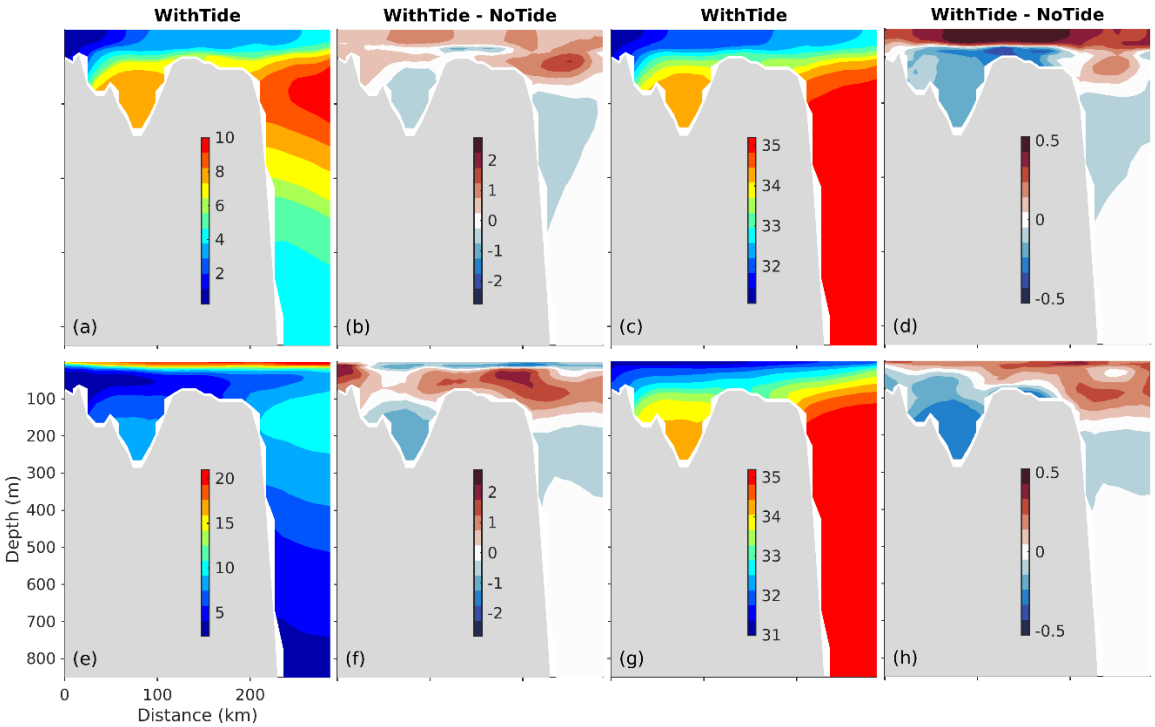

Figure 4.14. Distributions of simulated (from left to right) temperatures in WithTide and WithTide minus NoTide, salinities in WithTide and WithTide minus NoTide of monthly means averaged over 1999-2010 at transect HAL (Figure 1) in February (upper row) and August (lower row), respectively.

Table 4.4 lists the performances of WithTide and NoTide at three AZMP sections. In comparison with observations, the two simulations obtain similar values of the RMSDs and correlation coefficients for T and S at all three sections across the LS, NfS and the eastern ScS, due to the weaker tidal impacts in these areas in comparison with in the GSL and BoF. However, systematic differences between the two solutions occur along the HAL transect over the ScS. Figure 4.14 presents the multi-year averaged T and S simulated by WithTide, and the differences between WithTide and Notide, along this transect. In

February, WithTide obtains a warmer (by about 1°C) upper layer from surface to about 150 m depth, both on the shelf and off the shelf break; and a saltier (by more than 0.5 psu) upper layer from surface to less than 100 m on the ScS, and to about 150 m off the shelf break. In the deep layer in EBn, WithTide obtains slightly lower T and S (by less than 0.5 °C and 0.2 psu, respectively), and the lower salinity layer extends to the banks toward the shelf break. The differences between the two simulations can be explained by the vertical tidal mixing, because tidal currents are not negligible on the ScS (Figure B.2), and may also be related to the tidal residual circulation (Figures 4.9 and 4.10). In August, the differences between WithTide and NoTide are similar as in February, expect that WithTide obtains a colder and saltier (by about 1 °C and less than 0.5 psu, respectively) in the surface layer of about 10 m thick. These differences within this shallow surface layer can be explained similarly for the differences in SST and SSS shown in Figure 4.11 and are further discussed in Section 4.5.6.

In the next section we will discuss the tidal impacts on sea ice in the GSL. It should be noted that the differences in sea ice between WithTide and NoTide may have impacts on differences in SST and SSS over the ice covered areas, but these impacts should be less than those due to tidal mixing and tidally modified estuarine circulation. One evidence is that the larger difference in SST in the SLRE occurs in summer than winter, and differences in SSS occur throughout the year (Figure 4.11).

4.5.4 Tidal Impacts on Sea Ice in the GSL

As sea ice ridging and rafting are not parameterized in this model, the simulated sea ice variability is affected by the ice advection and local thermodynamic contribution (ice formation and melting). The latter includes open water ice formation, congelation ice growth and basal melt at the ice-ocean interface, and snow/ice formation/melting at the ice-air interface. Figures 4.15a and 4.15b show the annual net thermodynamic contributions in WithTide and NoTide, calculated by averaging the daily model diagnosis over four years during 2007-2010. The positive (negative) values can be interpreted as the annual net ice export (import) due to advection, because the annual-mean thermodynamics contributions for seasonal ice should be zero at each model grid in absence of the ice advection. Thus, according to WithTide, ice is mainly exported out from the head of the upper SLRE, along

the northern coast from the SLRE to the Strait of Belle Isle, along the southwestern coast of the GSL, and adjacent to the MI. Ice is imported into the middle of the GSL, over the Gaspe Current and its extensions, over the western side of CS, and off the west coast of Newfoundland in the northeastern GSL. This distribution of the annual thermodynamic contribution agrees with the previous model study by Urrego-Blanco and Sheng (2014).

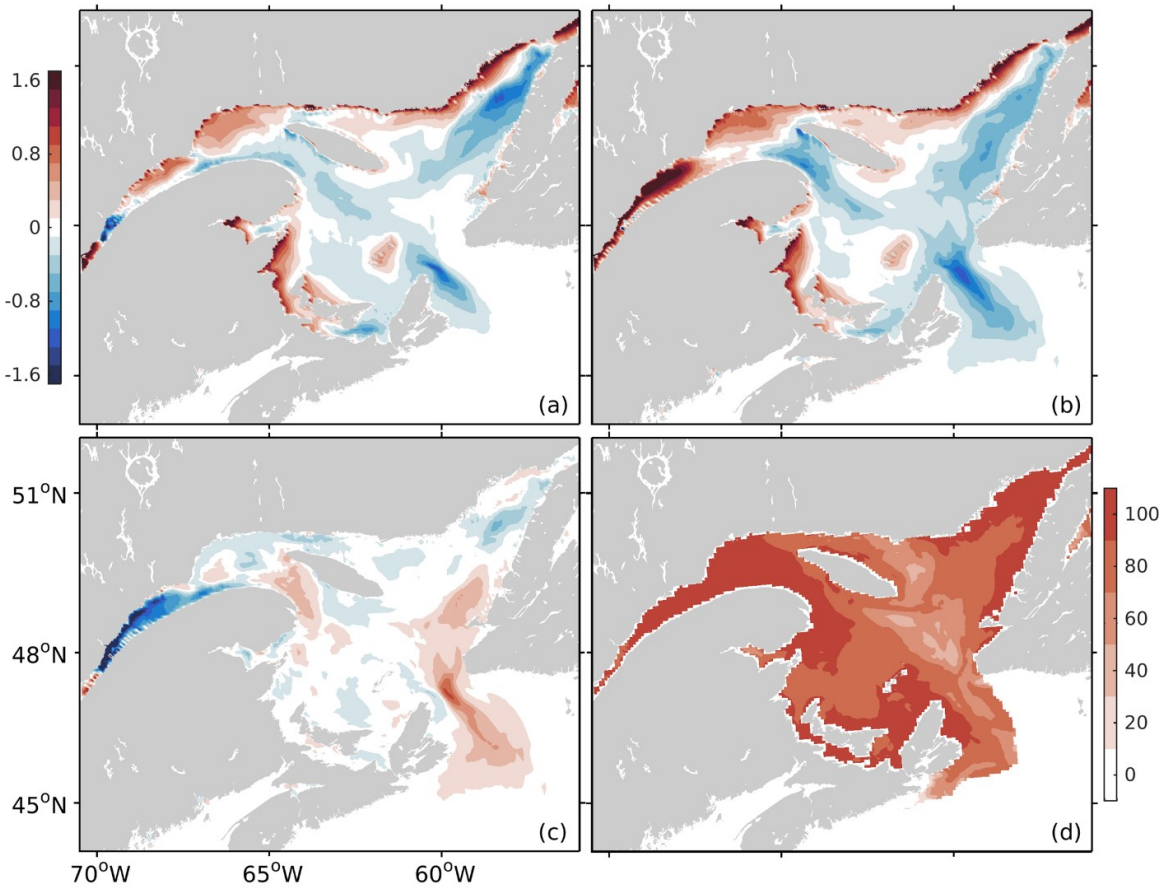

Figure 4.15. Distributions of the annual net sea ice production averaged over 2007-2010 due to thermodynamic processes (m) from (a) WithTide, (b) NoTide, and (c) WithTide minus NoTide. (d) The squared correlation coefficients (in percentage) between ΔV_{tot} and ΔV_{adv}, denoting the differences between WithTide and NoTide in the daily total change and advection of ice volume, during December to April in 2007-2010.

The annual thermodynamic contribution in NoTide (Figure 4.15b) has high similarities to that in WithTide (Figure 4.15a). Significant differences between the two solutions (Figure 4.15c) occur over the following four areas. In the SLRE and the northeastern GSL, WithTide obtains less thermodynamic contributions, consistent with the less ice formation (Figure 4.6), hence less ice is exported out of the two areas. Southwest of the AI downstream of the Gaspe Current and over the southeastern GSL toward the CS, the increased thermodynamic contributions in WithTide are related to less ice imported from the upstream.

In terms of the temporal variability in the ice volume in the GSL, Urrego-Blanco and Sheng (2014) found that both the ice advection and the net thermodynamic contribution are important. To quantify the relative importance of these two factors, we calculate the differences for both the daily total change (ΔV_{tot}) and advection (ΔV_{adv}) of the ice volume between WithTide and NoTide, during the ice season (December to April) in 2007-2010. Figure 4.15d shows the squared correlation coefficient between ΔV_{adv} and ΔV_{tot}. These values are high and above 80% over the northeastern and southern GSL. This suggests that the major differences between WithTide and NoTide in the temporal variability in the ice volume can be mostly explained by the advection.

The tidal impacts on ice concentrations are quantified by ΔC_{Ti}, which are differences in ice concentrations between WithTide and NoTide (Figure 4.6, right column). Averaged over 2007-2010 in the winter season, WithTide obtains less ice concentrations than NoTide (negative ΔC_{Ti}), and the differences are the most significant in the northwestern GSL in March when ice starts to melt. Noticeable differences also occur in the southwestern GSL in January, and in the southeastern GSL in February and March. Because WithTide overestimates the ice concentrations, the negative ΔC_{Ti} values mean that the model bias is reduced in WithTide. In Minas Basin of the upper Bay of Fundy, ice is not present in WithTide, but appears in NoTide, due to the overestimation in stratification in NoTide (Figure 4.13f).

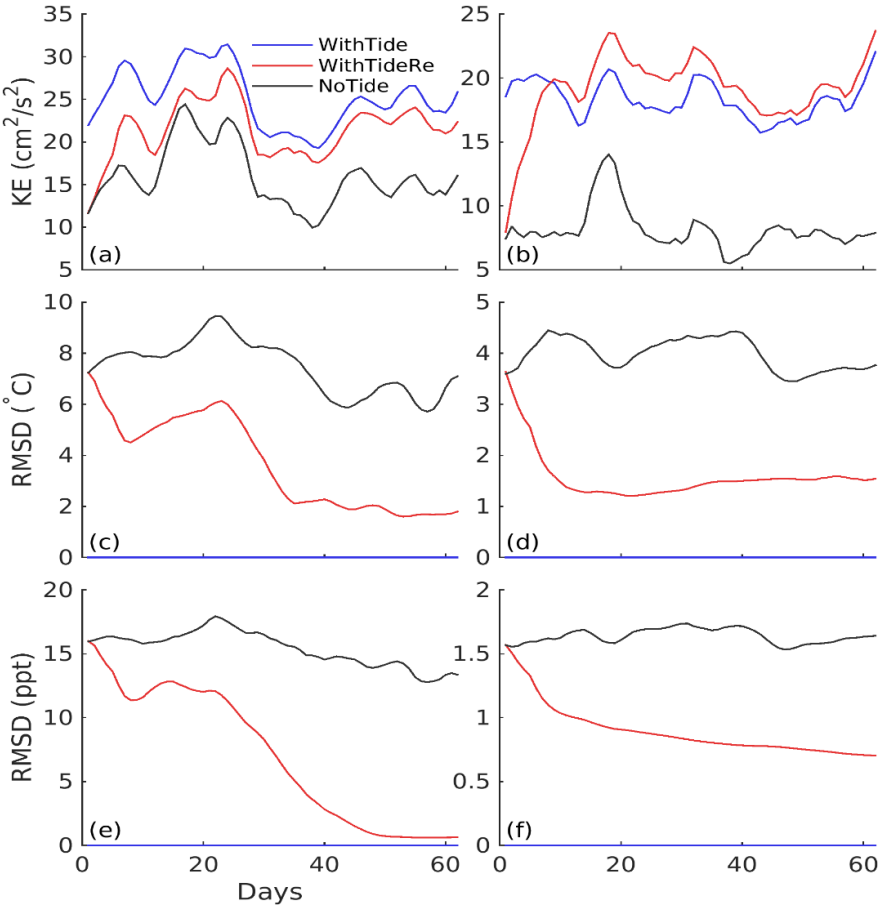

Figure 4.16. Daily time series over 60 days (starting from July 1, 2004) of (upper row) kinetic energy, and RMSDs of (center row) SST and (lower row) SSS, averaged over (left) the northwestern GSL and (right) GoM-BoF. The RMSDs are computed from model results in WithTideRe and NoTide relative to WithTide. The results of WithTideRe are in red, NoTide in black, and WithTide in blue.

Several important factors contribute to the large differences in ice concentrations over the SLRE between WithTide and NoTide (Figures 4.6 and 4.15). Firstly, in NoTide, the water column is strongly stratified (Figure 4.12f), hence the surface layer cools down much faster than in WithTide during fall and the early winter (Figure 4.12e), especially in the SLRE. This favors earlier ice formations and larger ice growth rates in NoTide than in WithTide. A second factor that favors more ice formation in NoTide is the higher freezing temperature of the sea water (by up to ~1 °C), resulting from the significantly lower SSS (by up to 20 psu) in the upper SLRE in NoTide than in WithTide (Figures 4.11 and 4.12). In WithTide, the less ice formation in January and February leads to lower ice

concentrations (and thickness) in March and April when ice melts (Figure 4.6), and the reduced ice concentration makes more solar radiation to be absorbed in the upper layer to accelerate the ice melting. Thirdly, the tidal mixing and tidal motions lead to the formation of a wintertime sensible heat polynya in the SLRE (Saucier et al., 2003) which is associated with relatively higher SST at the head of the LCh (Figure 4.11a). This polynya results in significant ice melt (Figure 4.15a) and reduction of ice concentrations (Figure 4.6).

4.5.5 Time Evolution of Tidal Impacts

To examine the evolution of tidal impacts on circulation and hydrography, Figure 4.16 presents time series of regional statistics in the northwestern GSL and GoM-BoF (bounded by coastlines and black transects in Figure 4.1) based on the daily mean model outputs in WithTide, NoTide, and WithTideRe (Table 4.1). The kinetic energy in Figures 4.16a and 4.16b is defined as $\langle \frac{1}{2}(u^2 + v^2) \rangle$, where u and v are daily mean horizontal currents, and $\langle \cdot \rangle$ indicates the regional mean weighted by the grid volume. In the northwestern GSL, the kinetic energy in WithTide is much higher than in NoTide, and the kinetic energy in WithTideRe increases quickly with the arriving of tides (Figure 4.16a). Next, we examine the RMSD of SST and SSS calculated from model results in WithTideRe and NoTide relative to WithTide. NoTide has large values of RMSD. By including tides, WithTideRe has significantly smaller RMSD of SST and SSS (Figures 4.16c and 4.16e). Overall, the reduction of RMSD in WithTideRe corresponds to increase of kinetic energy. The RMSD in WithTideRe reaches the lowest values after about 35 days for SST and 47 days for SSS.

In the GoM-BoF (Figure 4.16b), the kinetic energy in WithTideRe increases quickly and becomes larger than that in WithTide after 8 days. The RMSD of SST and SSS drops below 1.4 °C and 1.0 psu after 8 days (Figures 4.16d and 4.16f). Over both the northwestern GSL and GoM-BoF, the tidally induced (residual) circulation is significant in the daily mean kinetic energy because tidal variations are mostly filtered out. The tidally induced residual circulation builds up quickly in about a week due to the fast barotropic response, and slowly varies in accordance to the interaction between the circulation and stratification.

4.5.6 The Role of Tidal Mixing and Advection

In this section, we examine the time-mean (during the first two months in WithTideRe) values of various dynamic terms in the following salinity equation:

$$\frac{\partial S}{\partial t} = -\nabla \cdot (\boldsymbol{u}S) + \nabla_h \cdot (A_h \nabla_h S) + \frac{\partial}{\partial z} A_v \frac{\partial S}{\partial z} + \mathcal{F} \tag{4.4}$$

where S is salinity, $\boldsymbol{u}$ is the three-dimensional velocity vector, A_h and A_v are respectively the horizontal and vertical eddy diffusivity coefficients, and $\mathcal{F}$ is the external forcing (such as the net freshwater flux at the sea surface). The term on the left-hand side of Eq. (4.4) is the local rate of change for salinity. The four terms on the right-hand side of Eq. (4.4) are the advection, horizontal diffusion, vertical diffusion, and external forcing terms, respectively. Here we quantify the impacts of tides using differences in each term between WithTideRe and NoTide.Figures 4.17a, 4.17d, 4.17g, and 4.17j present the spatial distributions of tidally induced differences (WithTideRe minus NoTide) of main terms of the salinity equation, averaged vertically over the upper 50 m and over July-August 2004. Note that for the upper layer salinity, the forcing term $\mathcal{F}$ in the two simulations is similar because it is dominated by the same input of precipitation. The tidal impacts on salinity show several “hot-spots”, near the presence of tidal fronts (Garrett et al. 1978; Pingree and Griffiths 1980; Lu et al. 2001), including the upper SLRE, northwest to AI, Strait of Belle Isle, southwestern NS, BoF, NaS, and GeB. over these sub-regions, the tidal impacts on salinity are primarily due to advection (Figure 4.17d). The horizontal diffusion due to tides is significant in the SLRE, where strong salinity gradients present (Figure 4.17g). The large values of vertical diffusion are associated with strong tides off southwestern Nova Scotia, in the BoF and along edges of GeB. The tidally induced vertical diffusion pumps salt from the lower layer to the upper layer (large positive values in Figure 4.17j), and the advection then exports salt into adjacent areas (large negative values in Figure 4.17d). The mean horizontal circulation (Figures 4.7 and 4.9) plays an important role for spreading the differences in salinity between WithTideRe and NoTide near fronts to broader areas. The RMSD for SSS differences between in WithTideRe and WithTide is significantly reduced in comparison with the value between NoTide and WithTide (Figure 4.16). Because the upper SLRE is relative shallow (less than 50 m) (light grey shading areas in middle and

right panels of Figure 4.17), the vertical mixing between the upper and lower layers only becomes important over small areas with water depths larger than 50 m.

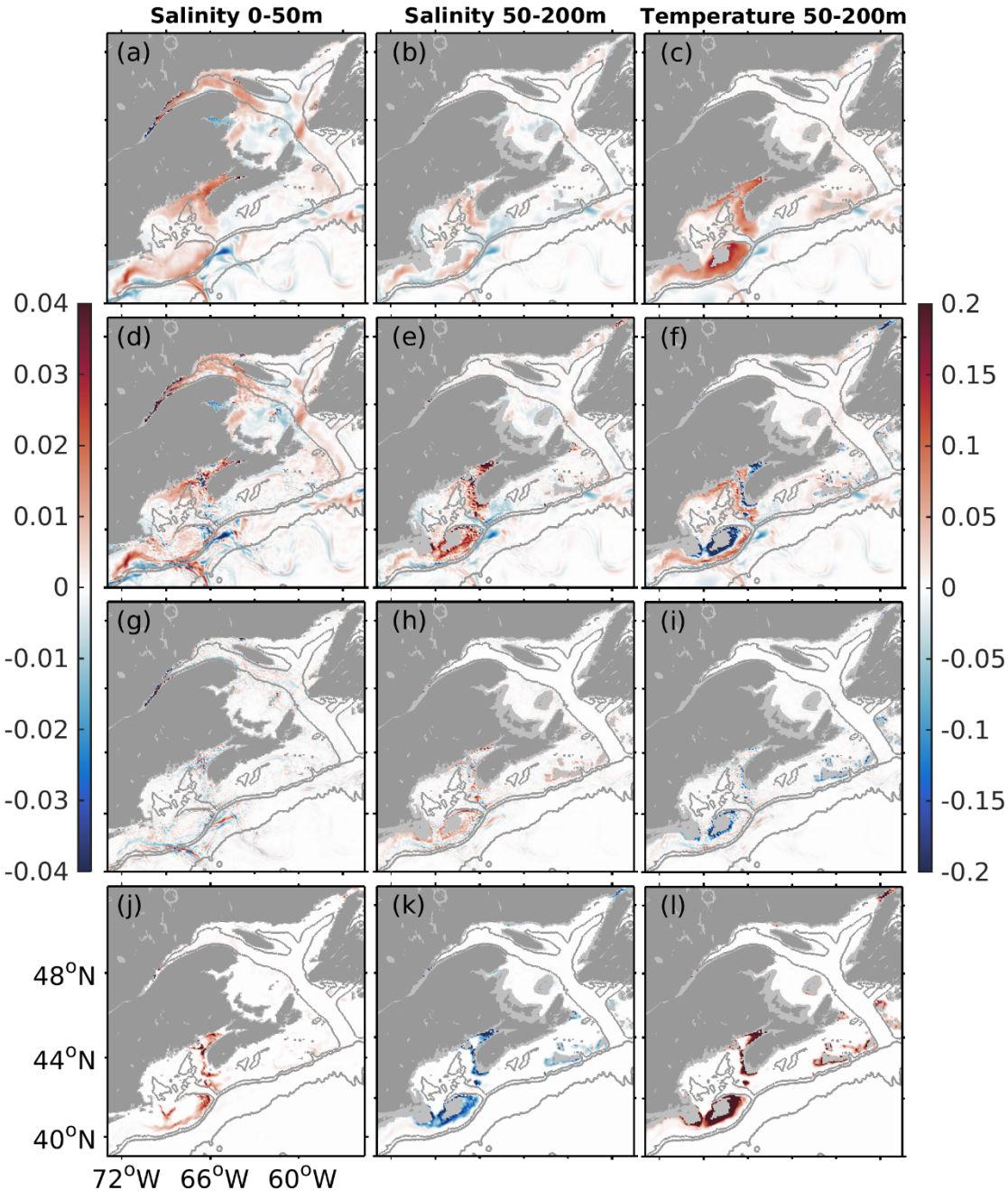

Figure 4.17. Distributions of differences in state variable trends between WithTideRe and NoTide, averaged over two months of July-August, 2004, of (from top to bottom) the time derivative, advection, horizontal diffusion, and vertical diffusion terms, for (left column) salinity in the upper 50 m, (middle column) salinity and (right column) temperature in the layer between 50 and 200 m. Color scale is in unit of ppt/day (°C/day) for salinity (temperature) trends. Contours are isobaths of 200 m, 1000 m, and 4000 m, respectively.

In the lower layer between 50 and 200 m, the salt export by vertical diffusion occurs in areas near tidal fronts (large negative values in Figure 4.17k), and the salt export is mostly balanced by the import due to advection (large positive values in Figure 4.17e). This suggests the important role played by frontal currents associated with tidal mixing. Overall, the tidal impacts cause increases in salinity in the lower layer of the southwestern NS, GoM-BoF, and southern GeB (Figure 4.17b). The tidal impacts on salinity in the lower layer are significantly smaller than in the upper layer (comparing Figures 4.17b and 4.17a) due to the much less spatial gradient in salinity in the former than in the latter.

Similar to salinity, we evaluate the tidal influence on temperature. The equation for temperature takes the same form as Eq. (4.4). Figures 4.17c, 4.17f, 4.17i, and 4.17l present the tidally induced differences (WithTideRe minus NoTide) of the main terms averaged over the lower layer. The vertical diffusion imports heat from the upper layer into the lower layer (large positive values in Figure 4.17l), and the advection of frontal circulation acts to remove the localized heat input (large negative values in Figure 4.17f). Overall, the tidal impacts increase the lower layer temperatures beyond the frontal areas (Figure 17c) due to advection (Figure 4.17f). In comparison with salinity, the role of advection is more significant for temperature due to the larger horizontal gradient in the lower layer temperature in summer. The tidal impacts on temperature can also be partially attributed to the differences in the forcing term $\mathcal{F}$ representing the surface sensible and latent heat fluxes (which depend on SST). This differences in $\mathcal{F}$ lead to differences in temperature in the upper layer and also in the lower layer through vertical mixing.

4.6 Conclusion

A coupled circulation-ice model based on NEMO was used to examine the role of tides over the eastern Canadian shelf (ECS). The model domain covers the region from the Mid-Atlantic Bight to the Labrador Shelf and from the east coast of the United States to the Mid-Atlantic Ridge. The control simulation (WithTide) was driven by a suite of external forcing including the atmospheric forcing at surface, river runoff, and tides and large-scale atmosphere-ocean influences introduced at the lateral open boundaries. The model in WithTide was integrated for 15 years from 1996 to 2010. The model performance in

WithTide was assessed using available observations from tidal gauges, CTD, and satellite remote sensing. The model was found to well reproduce the observed tidal elevations, seasonal variability of sea surface temperature, vertical profiles of temperature and salinity, the distributions of meso-scale eddies, the mean path of the Gulf Stream, and the seasonal variability of sea ice in the Gulf of St. Lawrence (Section 4.4).

The differences in model results between WithTide and NoTide were used to quantify the tidal impacts on the seasonal variability of circulation, hydrography and sea-ice over the ECS. The tidal impacts have significant spatial variability, relatively small over the Labrador Shelf (LS) and Newfoundland Shelf (NfS), moderate over the Scotian Shelf (ScS), and significant over the St. Lawrence River Estuary (SLRE), the northwestern Gulf of St. Lawrence (GSL), the southwestern ScS, the Gulf of Maine (GoM), and Bay of Fundy (BoF). The tidal impacts are particularly large over the central eastern GoM, the upper BoF, and the northern flank of Georges Bank (GeB).

The tidal impacts on the monthly-mean circulations were quantified using a tidal impact index (T_i) based on model results in WithTide and NoTide. In the GSL, T_i has large values in the SLRE for both the upper and lower layers, and the tidal impacts are stronger in winter than in summer. The tidal impacts are also significant off the Gaspe Peninsula, in both the upper and lower layers. Around Anticosti Island and over the southwestern GSL, tidal impacts are significant on the circulation in the upper layer, and stronger in summer than in winter. For the GoM and ScS, the tidal impacts on the mean circulation are large for both the upper and lower layers, and are stronger in summer than in winter, over the BoF, the central and eastern GoM, the northern flank of the GeB, the southwestern ScS, and associated shelf breaks.

In winter (February), the tidal impacts (differences in model temperatures between WithTide and NoTide) result in higher SST by up to 4°C over the GoM and ScS, Nantucket Shoals (NaS), GeB, and western ScS. In summer (August), tidal impacts lead to reduction of SST by more than 4°C in the above areas, and also in the SLRE and the northwestern GSL. Tidal impacts cause increase in SSS both in winter and summer, reaching 20 psu in the SLRE. In February, the increases in SSS are about 0.5 psu over the southwestern GSL,

and up to 1.6 psu in the BoF. In August, the increases in SSS are larger than in February, over 2 psu in the southwestern GSL and in the BoF. In comparison with the observed vertical profiles of temperature and salinity, it is found that, in the SLRE, the tidal impacts modify the upper layer stratification and the cold intermediate layer. In the BoF, tides play an important role in generating the seasonal varying and vertically well mixed water masses.

Tidal impacts also lead to reduction in sea ice concentrations in the GSL from January to April, with the most significant reduction found in the SLRE in March when ice starts to melt. The differences are attributed to less ice formation due to changes in hydrography, and hence less ice export from the SLRE in WithTide. In terms of time variations of sea ice volume changes, the differences between WithTide and NoTide can be mostly explained by the role of sea ice advection.

The differences between WithTideRe and NoTide for summer conditions were examined. The differences in kinetic energy of daily mean flow suggests that the tidally induced residual circulation is significant over both the northwestern GSL and GoM-BoF. Tidal impacts on temperature and salinity are the most significant near tidal fronts, where tidal mixing results in substantial vertical fluxes of salt and heat between the upper and lower layers. Frontal circulation usually compensates the impacts of tidal mixing, while the horizontal residual circulation can spread the tidal impacts generated in frontal areas into broader areas.

The model in WithTide also simulates internal tides generated on the shelf break to the southeast of GeB year-round. These internal tides are predominated by the M_2 constituent and exhibit streaks of peaks and troughs aligned with the shelf-edge with a wavelength of about 130 km. The isopycnal displacements associated with the internal tides at 500 m depth over this area are up to 80 m and damp out from the shelf-edge to the deep water. Due to the limitation of the spatial resolution, however, the model can only resolve low-mode internal tides. Further studies are required to evaluate the simulated internal tides with observations, examine the interaction between the internal tides and ocean currents (e.g., the Gulf Stream) (Kelly et al. 2016), and characterize the impacts of internal tides on coastal dynamics.

CHAPTER 5

THE MAIN PHYSICAL PROCESSES AFFECTING THE SEA-ICE IN THE GULF OF ST. LAWRENCE

5.1 Introduction

The Gulf of St. Lawrence (GSL) is a semi-closed sea with a surface area of about 2.26 $\times 10^5$ km^2 and a volume of about 3.45 $\times 10^4$ km^3. Two openings allow water exchange between the GSL and the Atlantic Ocean: The Strait of Belle Isle (SBI) to the northeast and Cabot Strait to the south. The SBI has a width of about 15 km and a maximum water depth of 60 m, which allows intrusion of ice from the Labrador Shelf and relatively salty and cold Arctic origin waters. Cabot Strait is ~100 km wide with a maximum water depth of 480 m. One of the important topographic features in the GSL is the Laurentian Channel, which is a deep trench, with the maximum water depth of about 500 m, extending from the St. Lawrence River Estuary to the continental shelf through Cabot Strait (Figure 5.1).

The GSL is a part of the subarctic system in the northern North Atlantic Ocean with the sea-ice cover advancing and retreating annually. The seasonal ice formation in the GSL plays an important role in winter convection and vertical mixing which bring nutrients to the surface. The GSL is biologically productive and yields nearly 25% of the total Canadian commercial fish catch by weight (Koutitonsky and Bugden 1991). Sea-ice also plays a significant role in the regional climate of the GSL by affecting the surface albedo and air-sea fluxes of heat and momentum (Pellerin et al., 2004; Saucier et al., 2003; Smith et al., 2006; Urrego-Blanco & Sheng, 2014).

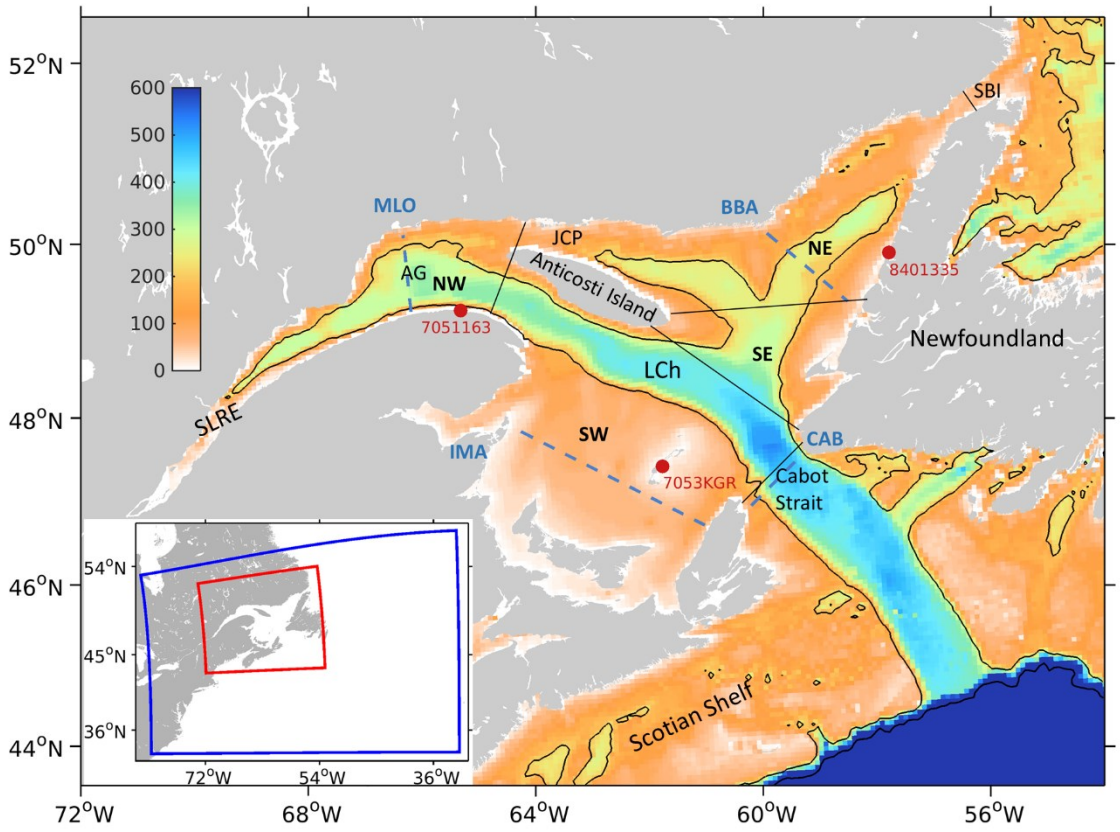

Figure 5.1. The model domain (blue box) and study region (red box) of the Gulf of St. Lawrence and adjacent coastal waters. Color shading shows the bathymetry, and the contours are the isobaths of 200 and 1000 m depth, respectively. Abbreviations are used for the Strait of Belle Isle (SBI), Jacques Cartier Passage (JCP), Anticosti Gyre (AG), St. Lawrence River Estuary (SLRE), Laurentian Channel (LCh). Three meteorological stations, 8401335, 7051163, and 7053KGR are shown as red circles. Four observational transects from the Atlantic Zone Monitoring Program, BBA, MLO, IMA, and CAB are shown as blue dashed lines. The four sub regions, the northwest (NW), northeast (NE), southwest (SW), and the southeast (SE) are shown and defined by their boundaries (black solid lines).

Many observational studies, including early measurements in 1940s, were made to examine the mean state and variability of the sea-ice distribution in the GSL (e.g. Forward 1952). The typical seasonal cycle of the sea-ice cover in the GSL was characterized (e.g. Black 1961; Drinkwater et al., 1999; Brickman and Drozdowski 2012). In the GSL, sea-ice generally starts to form in late December over the northern Gulf and the western shore of the Magdalen Shallows. By the end of January, the ice cover gradually expands to almost the whole GSL, except for the southeastern Gulf along the Newfoundland coast. The ice

cover thickens and spreads onto the northeastern Scotian Shelf via Cabot Strait in February and March. The ice in the GSL melts down quickly in April. The ice can sometimes last into May over the southwestern shore and the SBI. The ice observational data used in the most previous studies for the GSL are mainly the sea-ice concentrations inferred from the satellite and aerial remote sensing data (Canadian Ice Service 2006). Based on the observed ice concentrations in the GSL, it was found that the long-term trend of the sea-ice extent in the GSL is decreasing, but not as significant as that for many other regions in the Northern Hemisphere (Parkinson and Cavalieri 2008; Cavalieri and Parkinson 2012). Li (2000) studied the correlation between the seasonal/interannual variability of the sea-ice area and environmental factors in the GSL for the years 1963-1996. The spatial distributions of sea-ice concentrations were interpolated by Li (2000) on one degree resolution grids. The study made by Li suggested that the surface air temperature, wind, sea surface salinity and temperature, river runoff, and stratification all affect the sea-ice area variability. Among all environmental factors considered by Li (2000), the surface air temperature was found to account for the largest variance of the sea-ice area (40%), followed by the sea surface temperature in late fall (27%). Due to the complexity in sea-ice dynamics in the GSL (Koutitonsky and Bugden 1991) and difficulties in obtaining in-situ sea-ice measurements in winter months, available observations are not able to provide a comprehensive understanding of sea-ice dynamics and its interaction with the oceanic process in the GSL.

Stefan's law is the classical analytical model for predicting the growth of sea ice (Stefan 1891), using a simple thermodynamic balance between the heat loss at the ice-air interface and the latent heat of fusion for the ice growth at the ice-ocean interface. Such a thermodynamic balance is successful in simulating the sea-ice growth in the central Arctic (e.g. Maykut and Untersteiner 1971), but it can greatly overestimate sea-ice growth in the Southern Ocean, where much greater turbulent heat fluxes across the thermocline to the ocean surface are permitted than in the Arctic (Weller 1968; Allison 1981; Shaw et al. 2009). The oceanic heat flux at the ice-ocean interface can restrict the ice growth at the ice bottom, and can significantly affect the sea-ice cover such as in the Southern Ocean (e.g. Gordon and Huber 1990). Similarly, DeTracey (1995) found that prescribed oceanic heat fluxes are required to balance the excessive growth of ice in the GSL with a standalone ice

model. Hence, coupled ice-ocean circulation models are needed to understand the main physical processes affecting sea-ice conditions in the GSL.

Saucier et al. (2003) developed the first coupled ice-ocean circulation numerical model for the GSL and used this coupled model to simulate the seasonal cycle for 1996-1997. Their model results suggested that the overall sea-ice growth in the GSL is sensitive to the stratification in late fall, and identified a wintertime sensible heat polynya at the head of the Laurentian Channel. This polynya has a signature of relatively warmer sea surface temperature (0.5–1 °C) than nearby waters due to tidal upwelling and mixing. Urrego-Blanco and Sheng (2014) examined the relative importance of the advection and thermodynamic for the sea-ice distribution in the GSL, using a coupled ice-ocean circulation model employing both spectral nudging (Thompson et al. 2006) and semi-prognostic methods (Sheng et al. 2001; Greatbatch et al. 2004). Both the methods were used to constrain systematic model drift. Urrego-Blanco and Sheng (2014) demonstrated that the sea-ice in the GSL in the coupled model is primarily produced over the northern and southwestern coastal waters of the GSL and then advected away from coastal waters by ocean currents and surface winds. The advection was found to make comparable contributions to thermodynamics for determining the local ice volume in the GSL. Urrego-Blanco and Sheng (2014) also suggested that the existence of ice cover can significantly reduce the circulation strength in the GSL. The role of the oceanic heat flux versus the solar radiation in the sea-ice budget in the GSL is still not fully understood. In addition, little is known about the role of non-local processes on the sea-ice in the GSL, including the role of ice import through the SBI.

The main objective of this chapter is to identify the main physical processes affecting the temporal and spatial variability of sea-ice conditions in the GSL based on model results produced by a coupled ice-ocean circulation model in purely prognostic mode (without the use of correction techniques). The structure of this chapter is as follows. The model setup and observational data are described in Section 5.2, The simulated sea-ice variability and the relationship to oceanic processes are discussed in Section 5.3. A summary is provided in Section 5.4.

5.2 Model Setup and Observational Data

5.2.1 Coupled Ice-Ocean Circulation Model

The coupled ice-circulation model setup and external forcing used in this study are the same as in Chapter 4. A brief description of the sea-ice model is provided here. The sea-ice component of the coupled model is version 2 of the Louvain-la-Neuve model (LIM2, Fichefet and Maqueda 1997; Goosse and Fichefet 1999). The LIM2 uses the revisited C-grid elastic–viscous–plastic rheology of Bouillon et al. (2013) and a second-order moment-conserving advection scheme (Prather 1986). The LIM2 distinguishes open water and a single sea-ice category by the sea-ice concentration. The three-layer thermodynamics component has a virtual reservoir of shortwave radiation (Semtner 1976), with parameterization of brine inclusions. The open water ice formation has a characteristic thickness (parameter hiccrit in LIM2) of 0.3 m, when the net heat flux is from the ocean to air and the sea surface temperature (SST) is at or below the freezing point (Wang et al. 2010). The drag coefficients of the air-ice and ice-water drag are 1.4×10^{-3} and 5.0×10^{-3}, respectively. The open boundaries are closed for the sea-ice in this simulation, which means all the modeled sea-ice is generated within the model domain. However, as a test, results from two exemplary years, 2004 and 2005, are shown in Appendix D in which ice is specified at the northern boundary of the model domain based on observations. These additional runs are used to assess the influence of sea-ice from the Labrador Shelf, outside the model domain to the north.

5.2.2 Observational Data for Sea-Ice in the Gulf of St. Lawrence

The sea-ice observations used in this study were derived from weekly Eastern Coast regional sea-ice charts from the Canadian Ice Service (CIS) digital archive. The ice charts were created through comprehensive analysis of data from a variety of sources, such as satellite, and ship and aircraft-based visual observations (Galley et al. 2016). A review of the main sources of uncertainties can be found in Tivy et al. (2011).

Table 5.1. Chart for the conversion from the stage of development to ice thickness.

Code	Stage of Development	Thickness (cm)
81	New ice	5
82	Nilas, ice rind	5
83	Young ice	15
84	Grey ice	15
85	Grey-white ice	23
86	First year ice	50
87	Thin first year ice	50
91	Medium first year ice	95
93	Thick first year ice	120

The CIS data provide the partial ice concentrations and stages of ice development for up to three predominant groups of ice which are described as the “thickest ice”, “second thickest ice”, and “third thickest ice” (Canadian Ice Service 2009). The sea-ice concentration categories (in tenths from 1/10 to 10/10) are digitized with a mean value of each ice concentration category. However, there is no direct measure of sea-ice thickness. Instead, the charts record the development stage of ice, and thickness is estimated, following Saucier et al. (2003), from the stages of development as given by Table 5.1. Since the three predominant ice groups assume a descending order in thickness, the ice groups of data are eliminated if they are incompliant with the descending order. Finally, the total ice concentration and volume are the sum of that for all available groups.

The data in sea-ice charts are originally recorded in geographical polygons. In this study, the sea-ice concentration and thickness are gridded into a regular grid, covering the same area as the charts, with a nominal horizontal resolution of 1/40° using a MATLAB® mapping toolbox. The value associated with each gridded polygon is assigned to the corresponding grids. Each grid with overlapping polygons has the mean value of all corresponding sources. To compare the CIS data with model results, the gridded CIS data

are then interpolated to the model grid. The daily-mean model results are averaged over each consecutive 7-day ending in the recording date of the CIS weekly chart.

To examine the spatial variability of sea ice conditions in the GSL, the Gulf is divided in to four subregions. The southeast (SE) subregion has the least sea-ice cover due to the warm inflow at the eastern side of Cabot Strait. The northeast (NE) subregion is one of the important ice production subregions and receives significant ice transport through the Strait of Belle Isle from the Labrador Shelf. The northwest (NW) subregion has the most active sea-ice production and transport in the GSL. The southwest (SW) subregion accumulates nearly half of the total sea-ice volume in the GSL, with substantial import from the NW subregion and export to the eastern Scotian Shelf.

The performance assessment of the coupled ice-circulation model was given in Section 4.4. An additional assessment of the model performance in simulating hydrography and sea ice conditions in the GSL is presented in Appendix C. The coupled ice-ocean circulation model in the purely prognostic mode (no nudging and data assimilation) is integrated for the years 1996-2010, and the model results for the years 1998-2010 are used for this Chapter.

5.3 Results

5.3.1 Sea-Ice Distribution in the Gulf of St. Lawrence

Figures 5.2 and 5.3 present observed and simulated monthly mean sea-ice concentrations and thicknesses (cell mean) in the GSL and adjacent coastal waters of the eastern Scotian Shelf and western Grand Banks from January to March averaged over the period 1998–2010. The monthly-mean observations shown in these figures demonstrate that the sea-ice normally starts to form in limited coastal areas in the GSL in December (not shown). In January, ice occurs over the northern and southwestern coastal waters in the GSL, with the observed ice concentrations up to ~40% over the St. Lawrence Estuary and the northeastern Gulf. The maximum observed ice concentrations in January are ~70% over the Northumberland Strait. In February, ice covers almost the whole GSL with ice concentrations higher than in January. Sea-ice also covers inshore waters of the eastern

Scotian Shelf near Cabot Strait with ice concentrations up to ~50%. In March, ice concentrations in the GSL start to decrease, but high concentrations still occur over the Northumberland Strait and the northeastern Gulf. In April, ice melts down significantly in the whole GSL, except for areas near the SBI (not shown). The area with relatively low ice concentrations at the head of the Laurentian Channel is a sensible heat polynya (Saucier et al. 2003), which is induced by tidal mixing and upwelling at the head of the Laurentian Channel (Wang et al. 2020b).

The monthly-mean sea-ice concentrations produced by the coupled model have a similar seasonal cycle as the observations, with some differences in magnitude. In January, modelled ice concentrations, in comparison with observations, are relatively lower in the southeast GSL, but higher over the southwestern and northern coasts and the northwestern GSL. Nevertheless, a considerable portion of modelled sea-ice is very thin (<1 cm) and does not have noticeable contributions to the ice volume in those areas. It should also be noted that sea-ice concentrations from observations can be underestimated over areas covered by small ice floes with 3 tenths or less concentrations, since the data sources used for charts heavily rely on satellite data in the GSL since 1996 (Canadian Ice Service Archive Documentation 2007). In February and March, the modelled ice concentrations are higher than observations by up to 40% in the northern GSL and along the southwestern GSL coast, but lower than observations by up to 30% over the southern GSL, except for waters along the southwestern coast.

The observed monthly-mean sea-ice thicknesses have a similar cycle to the ice concentrations. In January, the ice thicknesses are relatively thin in general (<10 cm), and the maximum thicknesses of ~20 cm occur over the Northumberland Strait. In February, the ice thicknesses reach over 20 cm along the Gaspe Current and over the northeastern and southwestern GSL. The maximum thicknesses (~40 cm) in February occur in the Northumberland Strait and the northeastern GSL. In March, the sea-ice concentrations start to decrease in the whole GSL, but the ice thicknesses continue to grow over the northeastern and southwestern GSL. It should be noted that the ice volume in April over the northwestern GSL reduces significantly, due partially to southwestward advection of sea-ice from this subregion with the Gaspe Current (Saucier et al. 2003). A significant

portion of sea-ice is also advected on to the eastern Scotian Shelf along with the equatorward outflow through Cabot Strait.

In February and March, the modelled ice thicknesses are higher than observations over a few limited areas, including areas close to the SBI and over the Gaspe Current. The modeled ice thicknesses are thinner than observed in February and March by up ~5 cm over the eastern GSL and up to ~20 cm over the southwestern GSL (Figure 5.3f and 5.3i). The large differences in the sea-ice thickness between the model results and observations can be attributed to the significant uncertainties in derived observational thicknesses (Saucier et al. 2003) and model deficiencies. The significantly underestimated sea-ice thicknesses in the model over the southern GSL are discussed in Section 5.3 and 5.4.

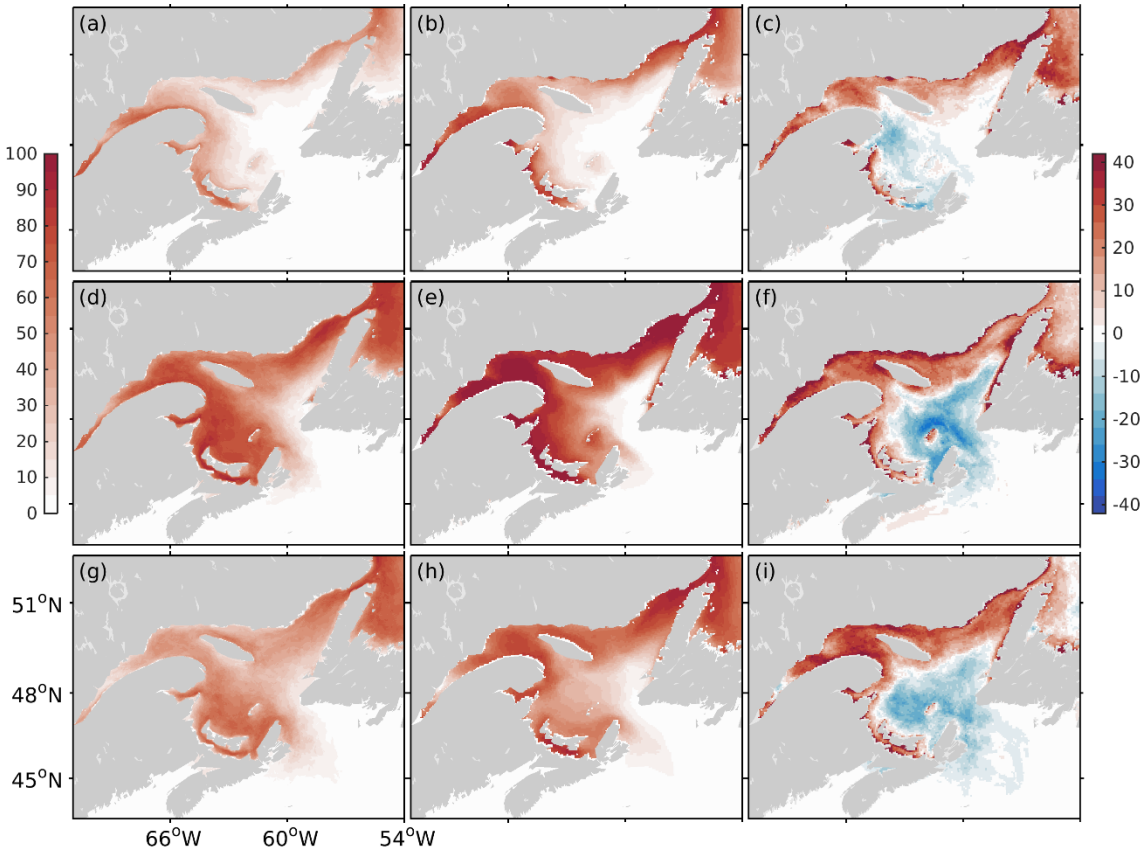

Figure 5.2. Monthly mean sea-ice concentrations in the GSL in (from top to bottom) January, February, and March averaged over thirteen years (1998-2010) based on (from left to right) observations (based on the Canadian Ice Service charts), the model, and the model minus observations.

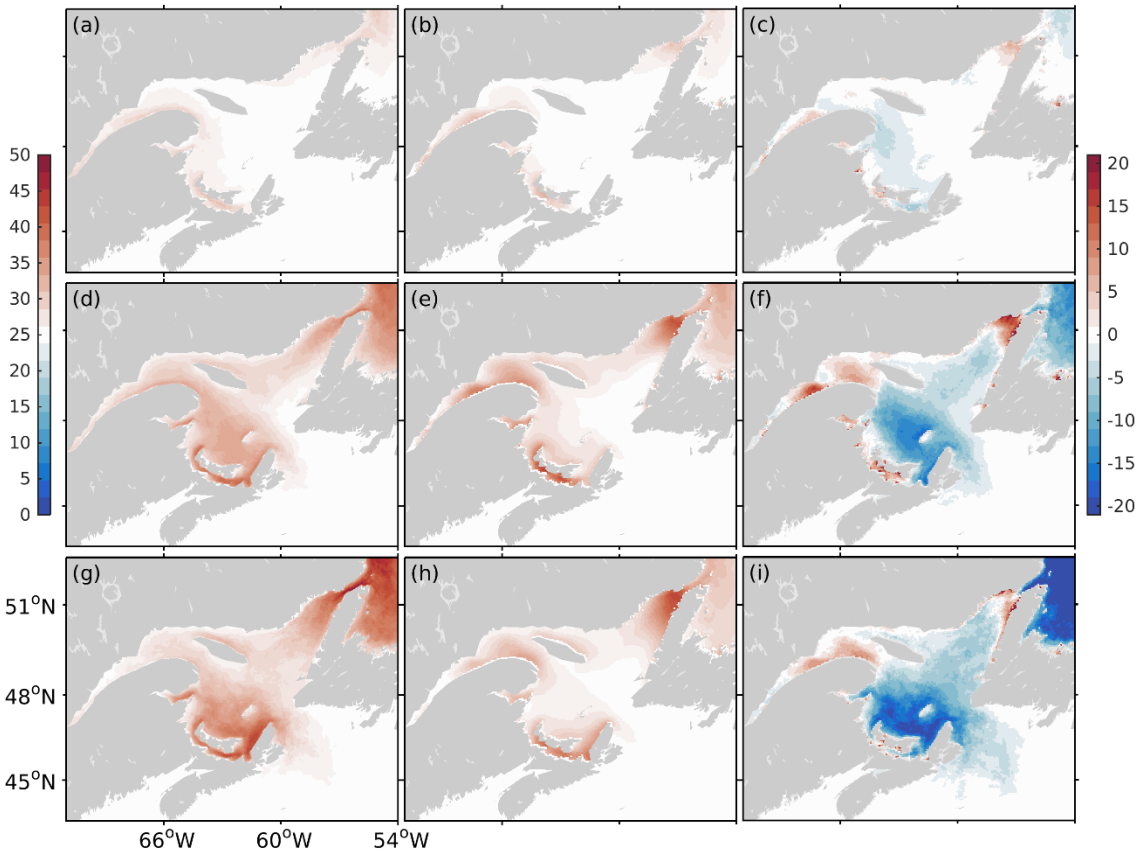

Figure 5.3. Same as Figure 5.2 but for ice thicknesses (cm).

To examine the temporal variability of sea-ice in the GSL, time series of the observed and simulated weekly-mean sea-ice area and volume for the years 1998–2010 and for the four subregions and the whole GSL are shown in Figures 5.4 and 5.5, respectively. The simulated values in these figures are calculated using model results at the same times as that of the observations to match the available CIS charts. The root mean square differences (RMSDs) and correlation coefficients are calculated when valid observational values (non-zero) are available. For the sea-ice area integrated over the whole GSL (Figure 5.4e), the CIS data exhibit significant synoptic, seasonal, and interannual variability over the study period, with the seasonal maxima ranging from ~10^5 km^2 to 2x10^5 km^2. Both the NW and NE subregions have large synoptic variability, and regional-integrated sea-ice areas can drop by more than 50% in a few weeks, associated with widely distributed leads and active sea-ice advection (Saucier et al. 2003). The ice in the SE subregion is primarily imported from other subregions, which depends largely on the variability of both the advection and

sea-ice formation in the source regions, and thus exhibits large temporal variability. The seasonal variability of simulated sea-ice areas over the four subregions and in the whole GSL are in a good agreement with observed seasonal variabilities. The correlation coefficients between the sea-ice area calculated from the model results and the CIS are 0.95, 0.78, 0.87, 0.94, and 0.82 for the whole GSL, and the NW, NE, SW, and SE subregions, respectively. The large synoptic variability in the observations over the NW and NE subregions, however, is not well reproduced by the coupled ice-ocean circulation model. Challenges in reproducing the observed synoptic variability of sea-ice in the GSL were also noticed by earlier model studies (e.g., Saucier et al. 2003).

For the ice volume, the coupled ice-ocean circulation model reproduces basic features observed in the CIS in the temporal variability, with correlation coefficients of 0.91, 0.79, 0.80, 0.86, and 0.85 for the whole GSL and the NW, NE, SW, and SE subregions, respectively. The RMSDs are 9.74, 1.23, 2.71, 7.87, and 3.08 km^3 for the whole GSL and the NW, NE, SW, and SE subregions, respectively. The RMSD value for the whole GSL is primarily attributed to underestimated ice volume by the coupled model in the SW subregion. The coupled model reproduces reasonably well the observed ice volumes in both NW and NE subregions in general. These two subregions are the primary sea-ice production areas in the GSL (Urrego-Blanco and Sheng 2014). By comparison, the coupled model often underestimates the ice volume in the NE subregion in April and May, which may be attributed to the reduced ice import through the SBI due to the closed sea-ice transport at the model northern boundary at ~54.5°N.

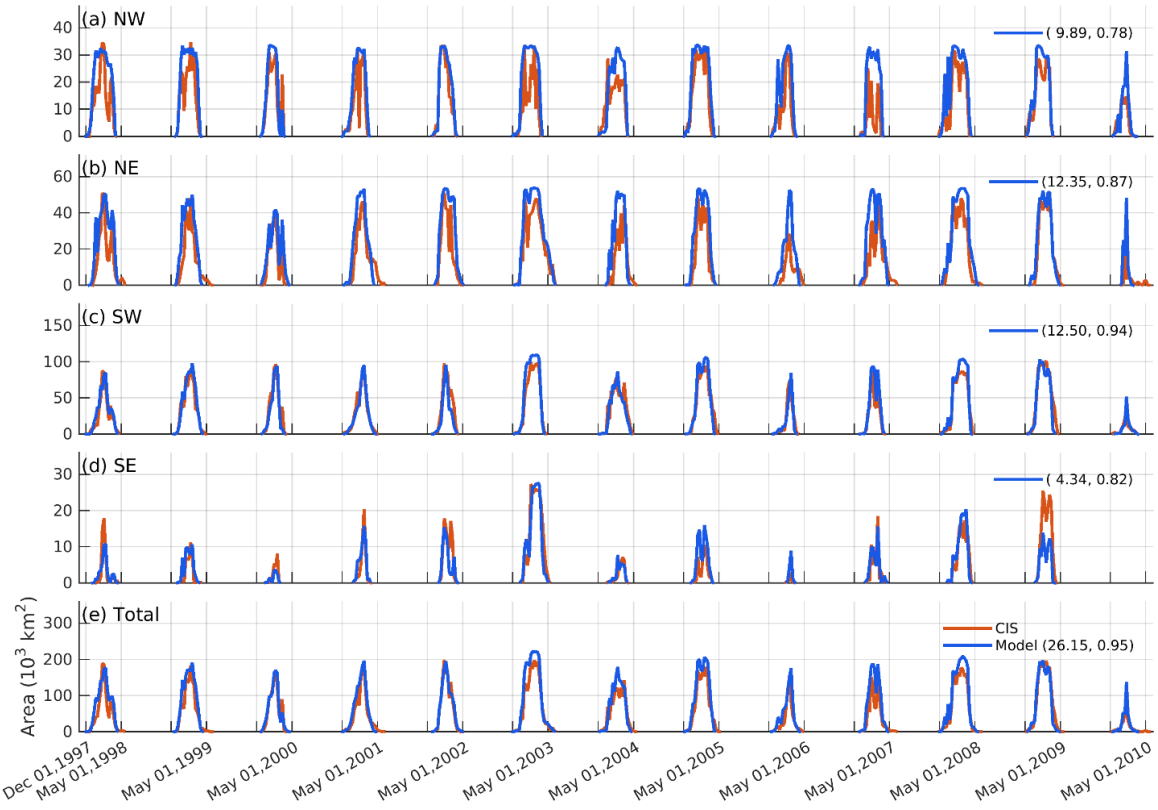

Figure 5.4. Time series of weekly-mean regional-integrated sea-ice area (10^3 km^2) for the years 1998-2010 based on the CIS (red) and the model (blue) in the (a) NW, (b) NE, (c) SW, (d) SE subregions, and (e) the whole GSL. Numbers in the bracket are the RMSD and the correlation coefficient.

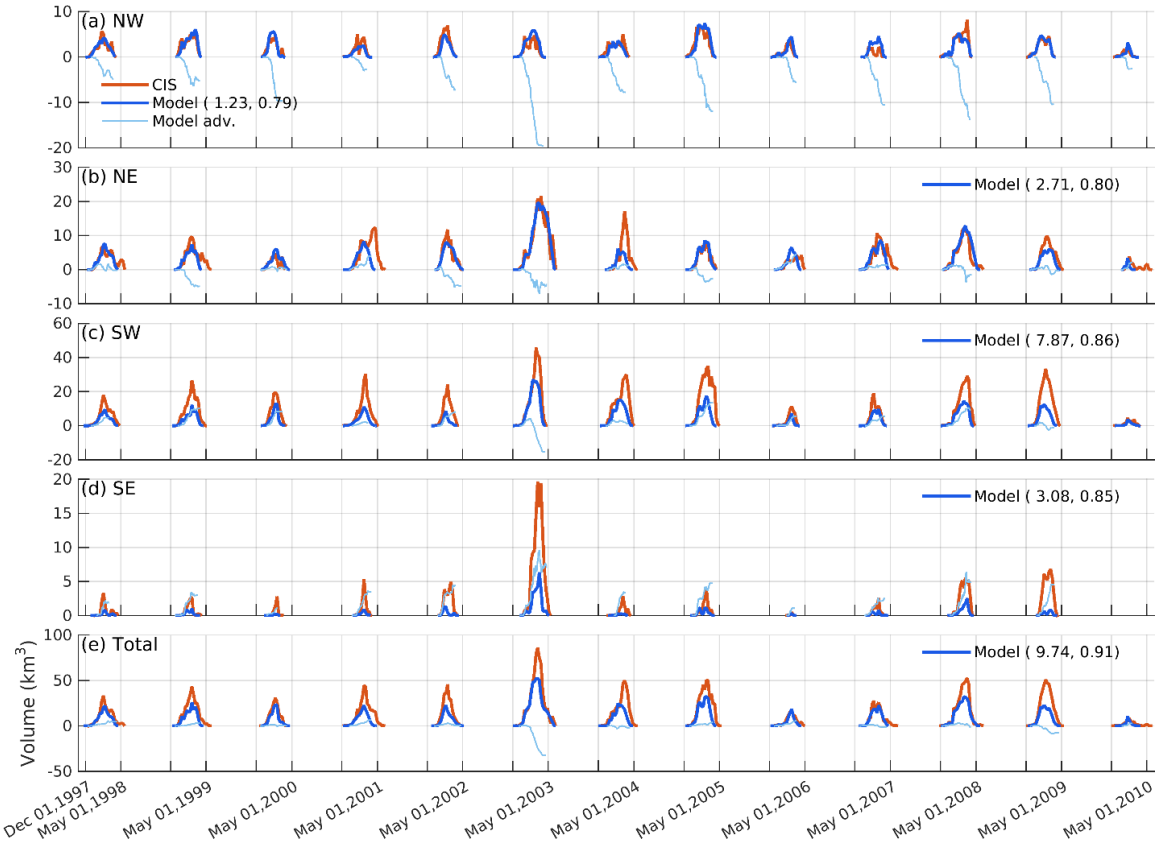

Figure 5.5. Same as Figure 5.4 but for sea-ice volume (km^3). The accumulated regional-integrated sea-ice advection is shown by the cyan line, with negative (positive) values indicating export from (import into) the region.

5.3.2 Sea-Ice Transport

Sea-ice advection was suggested to be of comparable importance for determining sea-ice volume as thermodynamic processes in the GSL (Urrego-Blanco and Sheng 2014). However, the regional budget of sea-ice advection has not been examined in the past. In this study, the net advection of sea-ice, i.e. import and export, for each subregion is calculated from the daily-mean of the sectional-integrated ice transport across subregional boundaries (see Figure 5.1). The seasonal-accumulated net ice transports (typically from early December to May in the next year) are presented in Figure 5.5 by cyan lines. The seasonal-integrated transports at the boundaries for the four subregions in the GSL

averaged over 1998-2010 produced by the model are presented in Figure 5.6 showing the mean and one standard deviation (in the unit of km^3).

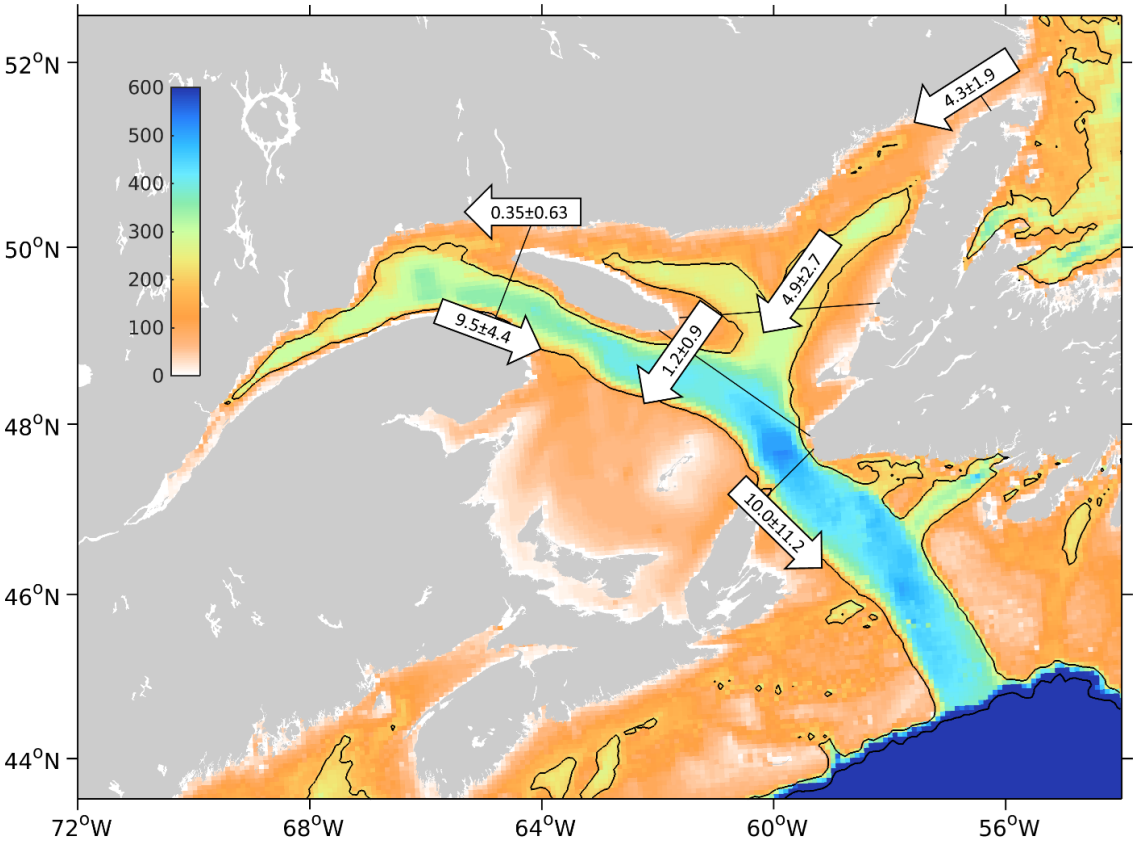

Figure 5.6. Simulated seasonal section-integrated sea-ice transport (km^3) during 1998-2010. Numbers in the arrow are mean ± one standard deviation. Color shading shows the bathymetry, and the contours are isobaths of 200 and 1000 m depth, respectively.

The sea-ice advection has different characteristics among the four subregions of the GSL. In the NW subregion, sea-ice is generally exported from this subregion throughout the ice season (Figure 5.5a), with the mean advection volume of ~9.5 km^3 and a standard deviation of ~4.4 km^3 (Figure 5.6). The seasonal-integrated net sea-ice advection volumes, with a maximum value of ~20 km^3 in winter 2003, can far exceed annual maximum ice volume inside the NW subregion, making the NW subregion the major sea-ice export subregion in the GSL. In the NE subregion, sea-ice advection can shift between net import and export frequently (Figure 5.5b), because the ice import through the SBI and export to southwestward have similar magnitude but slightly different timing (Figure 5.6). The ice

export from the NE to the SE subregions, southwest of Newfoundland Island, is primarily along the southeastern coast of the Anticosti Island (Urrego-Blanco and Sheng 2014b). A significant part of transported ice is melted in the SE subregion (Figure 5.5d), and a mean of 1.2 km^3 of ice is exported from the SE to the Laurentian Channel with a standard deviation of 0.9 km^3 (Figure 5.6). In the SW subregion, between the Gaspe Peninsula and Cape Breton, as early formed ice in the NW subregion is exported by the Gaspe Current and accumulated in the SW subregion (Figure 5.6), sea-ice advection is often a net import in the early season and turns to the net export in the late season (Figure 5.5c). The ice volume exported to the eastern Scotian Shelf through Cabot Strait reaches about 10.0±11.2 km^3, which is comparable to the estimation by Galbraith et al. (2011) at about 9.7±8.8 km^3. For the whole GSL, the volume of imported ice from the SBI is much smaller than the ice accumulated in the GSL, while a significant volume of ice can be exported through Cabot Strait with a maximum value of ~38 km^3 in 2003.

The annual sea-ice volume transport through the SBI is estimated as 4.3±1.9 km^3, which is in line with ~5 km^3 estimation based on 49-year climatology of the CIS charts (Brickman and Drozdowski 2012). However, the model simulated sea-ice transport does not include sea-ice generated north of the model open boundary (~54.5°N), as the northern boundary is closed for sea-ice in this model. Based on the model experiments shown in Appendix D, the sea-ice open boundary forcing is the major source for the simulated sea-ice on the Labrador and Newfoundland Shelf after February, but minimal for the simulated sea-ice in the GSL over the winter, except for occasionally intrusion into the northeastern GSL after February.

5.3.3 Sea-Ice Volume Budget and the Upper Ocean Processes

The ice volume budget for the GSL is examined in this section based on the primary thermodynamic processes and hydrodynamics in the upper ocean. The thermodynamic contribution of sea-ice includes open water ice formation (frazil ice formation), ice growth at ice-ocean interface (congelation ice growth), snow ice formation due to the flooding of snow, basal melt at ice-ocean interface, and surface melt at ice-air interface. Analysis of model results indicates that the ice formation in the GSL is dominated by the frazil ice formation, which is more than an order of magnitude larger than the snow ice formation.

At the ice bottom, where growth (melt) is determined by the heat divergence (convergence) at the ice-ocean interface, the basal melt overwhelms the congelation ice growth. The congelation ice growth only occurs occasionally near the Labrador coasts and southwestern coast of the GSL with magnitudes of an order less than the typical values of the basal melt. It should be noted that the convergence of the ice due to advection is the primary driver for the ice thickening in the GSL, based on model results. Thus, in the following discussion, the frazil ice formation (basal melt) is used to represent the ice formation (melt) in the study region.

From the daily mean model outputs, we calculate the regional-integrated ice volume, daily volume change (ΔV), and seasonal-accumulated frazil ice formation (Formation) and basal melt (Melt), for the years 2007-2010. In Figure 5.7b, the daily ΔV, Formation, and Melt are adjusted with a factor of 10, 0.1, and 0.1, respectively. Except for the accumulated Formation and Melt, all the other variables in Figure 5.7 are smoothed with a 3-week running average filter. The blue (red) colour shading indicates ice growth (melt) phases, which are determined by positive (negative) values of the smoothed daily ΔV (red lines in Figure 5.7b).

The seasonal variability of the SST produced by the model is very large in the GSL, due mainly to strong air-sea interactions (Figure 5.7). In summer, the regional mean SSTs are very similar to that of the air temperatures in the GSL (Figure 5.7a), with the maxima up to ~ 18 °C due to the summer heating of over 100 W m^{-2} (Figure 5.7c). As the air temperature drops quickly in fall with the increasing ocean heat loss at the air-sea interface, the heat content at the upper mixed layer is depleted by roughly late November when the sea-ice starts to form. The SST reaches its minimum in winter and is very close to the freezing temperature of the sea water in the GSL (~-1.8 °C), corresponding to the favourable condition for the ice formation in the GSL.

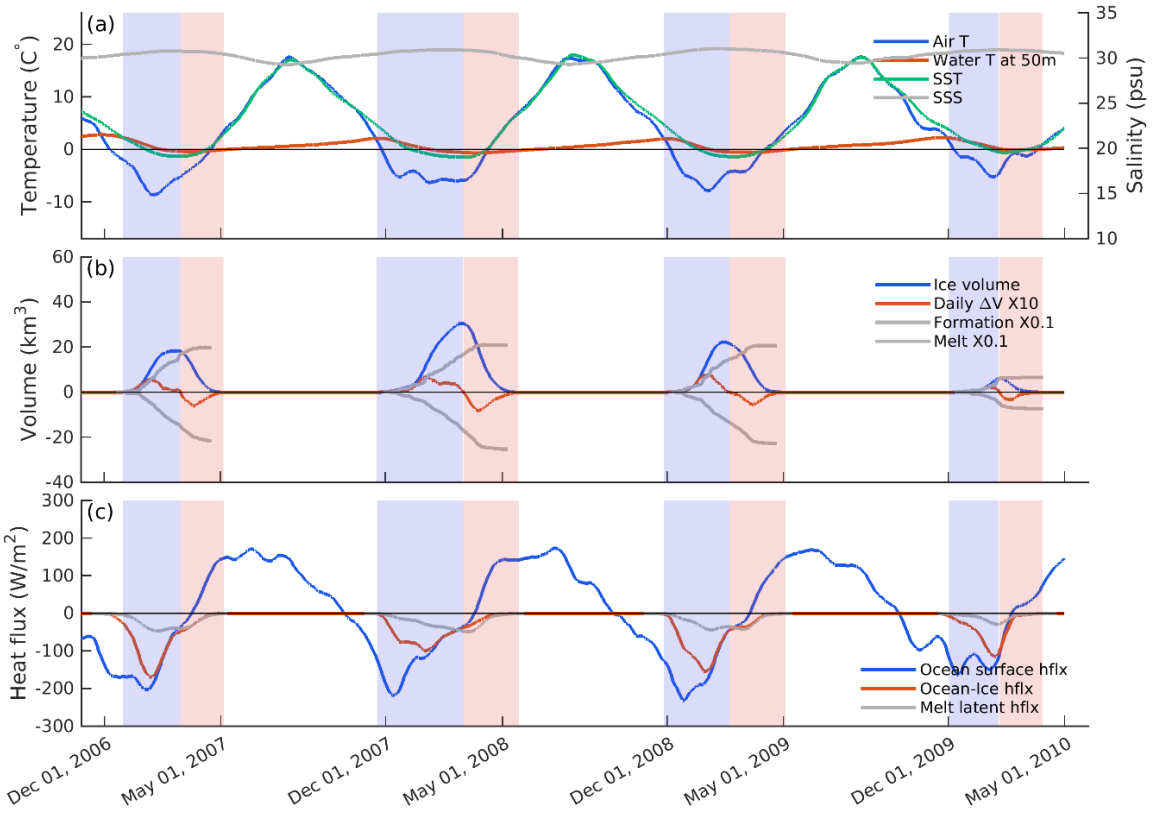

Figure 5.7. Daily mean time series during 2007-2010 of regional-integrated (over the whole GSL) for (a) air temperature (Air T), water temperature at 50 m depth (Water T at 50 m), SST, and SSS, (b) ice volume, daily ΔV × 10, Formation × 0.1, and Melt × 0.1, (c) ocean surface heat flux, ocean-ice heat flux, and Melt latent heat flux. These heat fluxes have positive values when the net heat flux is downward into the ocean. The blue (red) colour shading indicates ice growth (melt) phases.

As the sea ice is accumulated extensively in the GSL from December to February, the growing ice cover tends to reduce the ocean surface heat loss (Figure 5.7c), which in turn reduces the sea-ice formation rate. The ice continues to accumulate in March, although ocean heat loss decreases along with the rising air temperature. The ocean surface heat flux (blue) is a sum of ocean-ice heat flux (red) and ocean-air heat flux in open waters and leads. Once the total ocean surface heat flux (blue) becomes larger than the ocean-ice interface heat flux (red), the ice melt phase starts, as open waters start to receive net downward heat flux. Timings of the growth and melt phase largely depend on the winter atmospheric forcing, i.e., the air temperature cycle (Figure 5.7a).

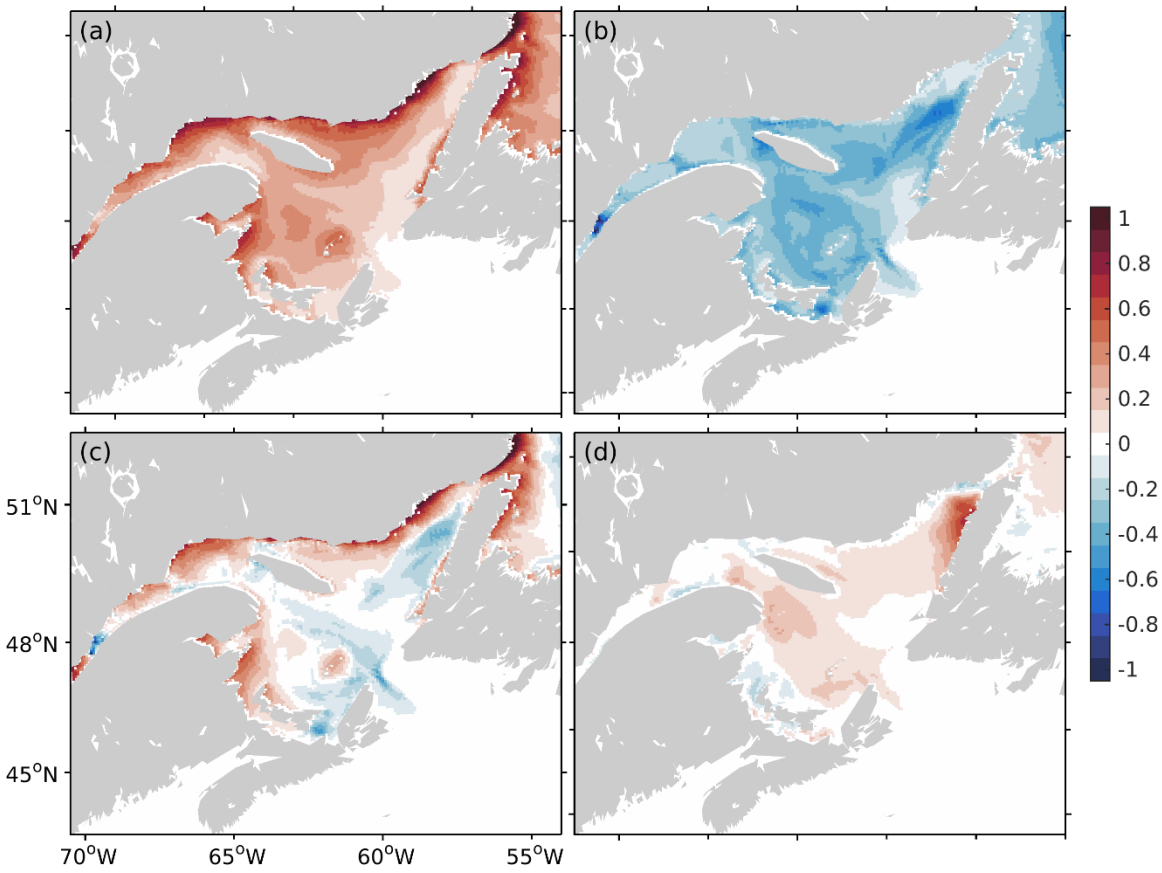

Figure 5.8. Distributions of the temporal accumulated, over February 2008, (a) frazil ice formation, (b) sea-ice basal melt, (c) net sea-ice thermodynamic contribution, and (d) sea-ice volume change, in unit of m.

In the GSL, model results show that the newly formed ice is primarily compensated by the basal melt due to oceanic heat convergence at the ice-ocean interface (Figure 5.7b). Both the Formation and Melt are more than 5 times larger than the sea-ice volume (blue), and the differences between those two thermodynamic processes significantly affect the variability of the sea-ice volume (Figure 5.7b). Sea-ice melts during the ice melt phase due to the elevated solar heating and air temperature, e.g. in the Arctic Ocean (Perovich et al. 2008). However, during the ice growth phase (Figure 5.7), the upper layer of the water column is at the freezing temperature beneath the sea-ice and the ocean surface is losing heat. The natural question is what happens to that substantial ice melt?

Over a typical winter month in the ice growth phase (February 2008), both the frazil ice formation and basal melt occur over the whole GSL. The ice is mainly formed near the

coast with the maximum values over 0.8 m along the northern and southwestern coasts of the GSL (Figure 5.8a). Basal melt exhibits a different spatial distribution in comparison with the ice formation due to the ice advection and localized heat source, e.g., the polynya at the Laurentian Channel head (Figure 5.8b). The net thermodynamic contribution, including effects of all thermodynamic processes of sea-ice, is dominated by the two major components, the frazil ice formation and basal melt (Figure 5.8c). Considering all processes including ice advection, modelled ice grows by about 0.2 m over the northeastern and southwestern GSL, with a maximum value of ~0.7 m along the northwestern coast of the Newfoundland (Figure 5.8d).

The latent heat fluxes required for ice melt are calculated by the mass of ice melt and the latent heat for ice fusion (3.35×10^5 J kg^{-1}), and is shown as Melt latent heat flux (grey line) in Figure 5.7c. The heat flux required for the simulated ice melt ranges from 0 to ~60 W m^{-2}. Those values are larger than the estimated values of 0.2-2 W m^{-2} in the Arctic (Maykut and Untersteiner 1971; Shaw et al. 2009), but is in a similar range as the estimated values of 5-50 W m^{-2} in the Antarctic from (Weller 1968; Allison 1981). To compensate an excessive ice formation in the GSL, oceanic heat fluxes of 10 to 40 W m^{-2} were applied in a standalone sea-ice model (DeTracey 1995), which fall in similar range to our calculation. Apparently, in the GSL, the sea-ice melt over the whole ice season has a primary role in determining the ice volume, and is associated with the heat flux from subsurface warm waters primarily, particularly during the ice growth phase. The heat fluxes to the upper layer of the ocean waters, associated with the entrainment and mixing with deep waters, are constrained by the stratification in the GSL (Smith et al. 2006b). The winter stratification in the GSL is largely affected by salinity (Koutitonsky and Bugden 1991), of which up to 20 psu anomaly near the sea surface can be attributed to the tidal dynamics (Wang et al. 2020b). As an example of the stratification impact on the sea-ice budget, results from the experiment without tidal dynamics (see NoTide in Table 4.1) is shown in Figure 5.9.

In NoTide, the modelled sea-ice growth (Figure 5.9) is more intense than that in WithTide (Figure 5.5) over the northern GSL (see also Figure 4.15). In particular, the ice volume and export in the NW subregion are more than doubled in NoTide than in WithTide

due to the super fresh surface layer that restricts the exchange with warm deep waters (Figure 4.12). As a result, a total ice volume of up to 50 km^3 (winter 2003) is exported annually to the SW subregion in NoTide. Although the seasonally maximum ice volumes of the whole GSL nearly match the observations, the upper layer temperature and salinity differ significantly from observations in NoTide (Chapter 4).

Furthermore, the discharge of the St. Lawrence River (SLR), which is the major freshwater source in the GSL, can also affect the upper layer salinity in the GSL, particularly over the northwestern and western regions of the GSL. One of important questions to be addressed is what is the role of the interannual variability of the freshwater discharge from the SLR on the sea-ice growth? In a numerical experiment for the years 2006-2010 using monthly SLR discharge instead of the climatology used in Chapter 4, the monthly discharge can be up to 50% larger than the corresponding climatology (See Appendix E). Although the near surface salinity is freshened by over 1 psu in the NW subregion in winter, the overall contribution in the ice volume is only a few percentages in the GSL.

In summary, analyses of our model results demonstrated that the regional-integrated sea-ice volume in the GSL is controlled mainly by the leading balance between two processes: the frazil ice formation and the basal melt at the ice-ocean interface. The former was suggested to be affected by air temperature (Martin 1981), while the latter can be significantly altered by the stratification.

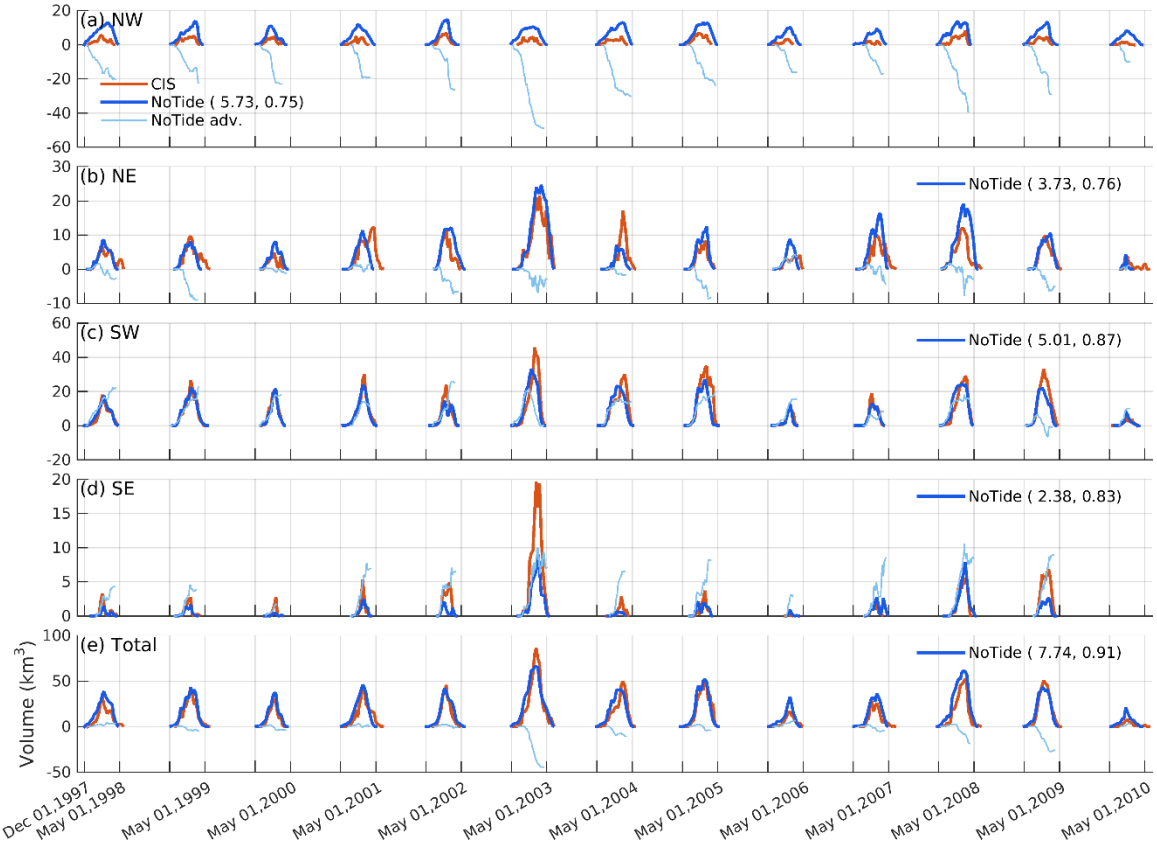

Figure 5.9. Same as Figure 5.5 but for the results from NoTide (Table 4.1) in contrast to WithTide shown in Figure 5.5.

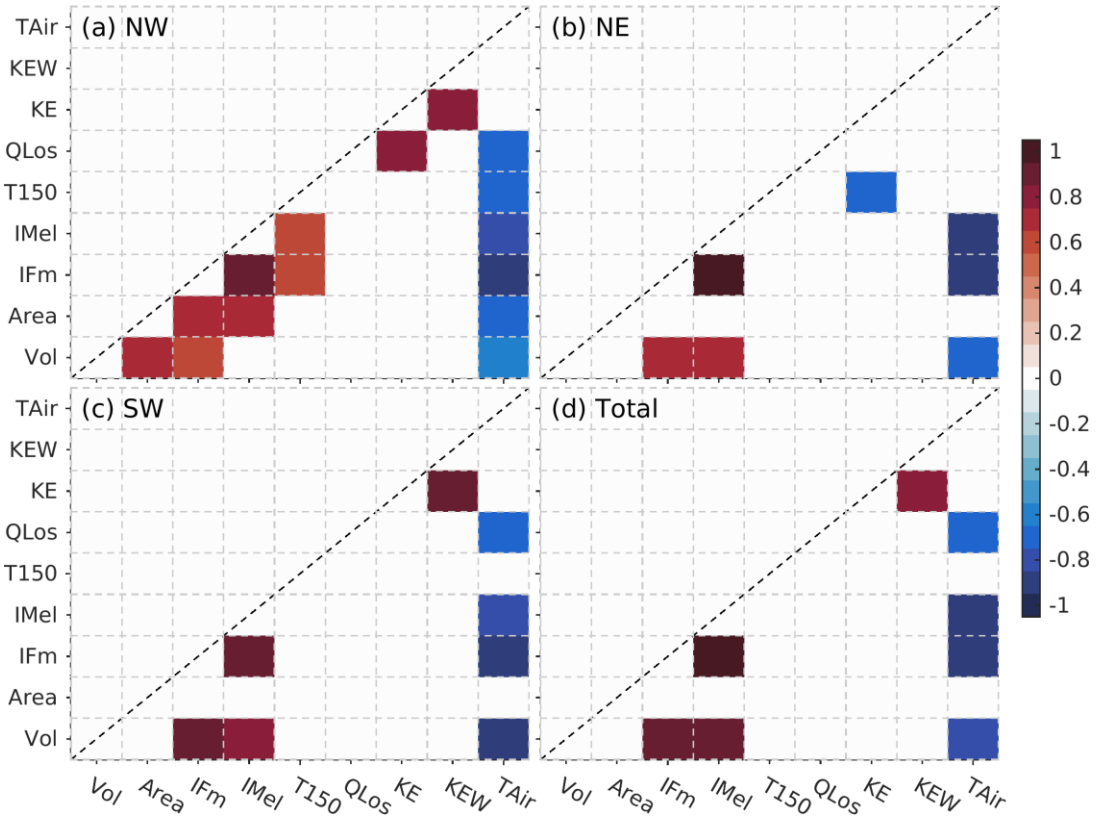

Figure 5.10. Color-coded correlation coefficients of the time series at the 95% significance level for the (a) NW, (b) NE, (c) SW subregions, and (d) the whole GSL. The nine indicators are: 1) the mean over January, February, and March (JFM) of each ice season for the air temperature (TAir), kinetic energy of near surface wind (KEW), kinetic energy of surface ocean currents (KE), net upward heat flux at ocean surface (QLos), and water temperature at 150 m depth, 2) the seasonal-accumulated basal melt (IMel, being positive when ice melt), and frazil ice formation (IFm), and 3) seasonal maximum of the sea-ice area (Area) and Volume (Vol).

To quantify the relationship between the two primary processes in the sea-ice volume budget and environmental factors, a regional and seasonal-averaged analysis is used to minimize the impact of advection and timing variation of the ice season. Based on daily mean model results for the period 1998-2010, nine indicators are calculated in three groups. The first group is the seasonal-mean over January, February, and March (JFM) of each ice season for the air temperature (TAir), kinetic energy of near surface wind (KEW), kinetic energy of surface ocean currents (KE), net upward heat flux at the ocean surface (QLos), and water temperature at 150 m depth, respectively. The second group is the seasonal-accumulated basal melt (IMel, being positive when ice melts), and frazil ice formation

(IFm), respectively. The third group is the seasonal maximum of the sea-ice area (Area) and Volume (Vol), respectively. Color-coded correlation coefficients of the interannual variability are presented in Figure 5.10 (only correlations with the significance value $p<0.05$ are shown). The SE subregion has relative minor contribution in the sea-ice budget in the GSL, which is not shown. Although the sample size is relatively small (13 years in total), significant correlation coefficients are still meaningful.

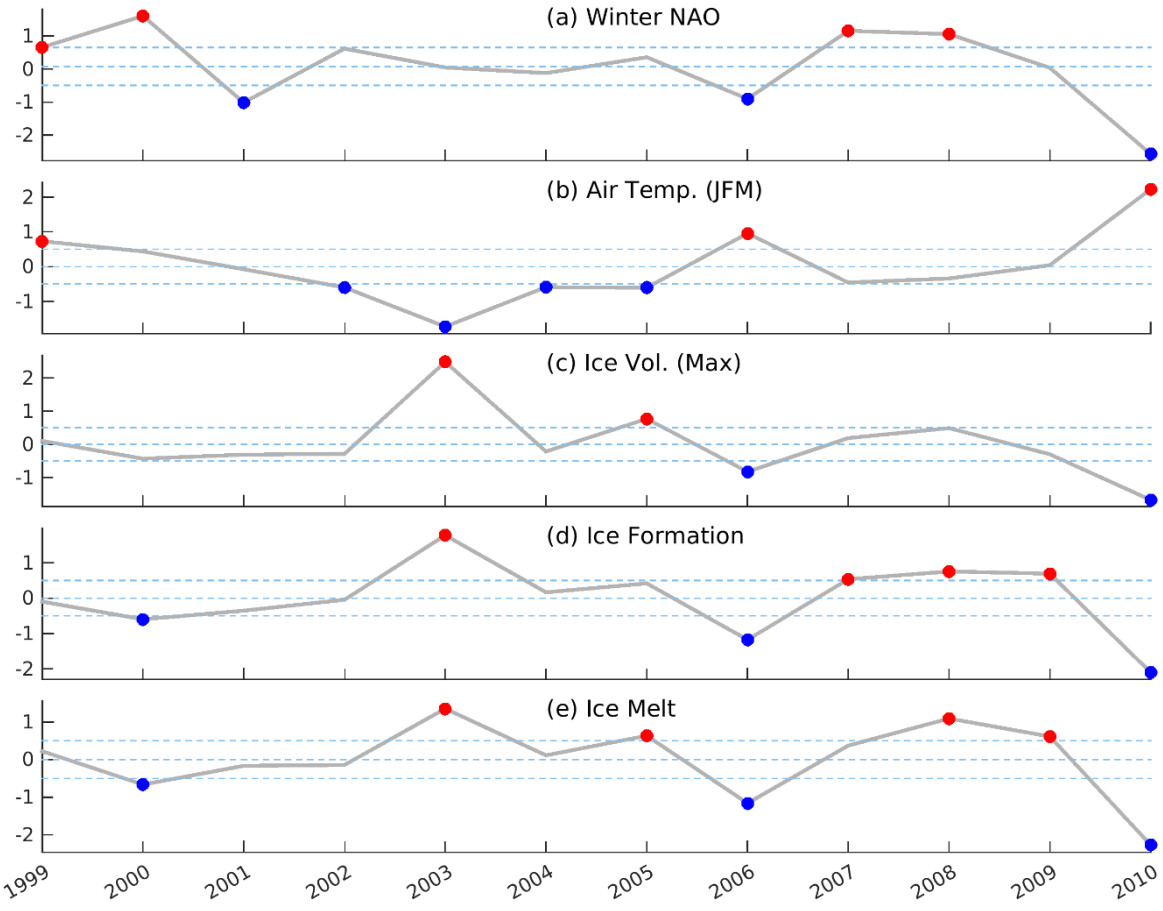

Figure 5.11. Normalized indices (solid grey line) with mean and ±0.5 standard deviation (cyan dashed line) for (a) Winter NAO, (b) air temperature (JFM mean over the GSL), (c) annual ice volume maximum, (d) accumulated ice formation, (e) accumulated ice melt. Extreme positive (negative) years are mark in red (blue).

The winter air temperature (TAir) is an effective indicator in the magnitude of the seasonal ice formation (IFm) with very high correlation coefficients (~0.9) over the GSL. In comparison, the sea-ice area (Area) and volume (Vol) have relatively lower correlation coefficients (0.5-0.8), or even insignificant, to the winter air temperature. The significant correlation coefficient between the ice formation (IFm) and ice melt (IMel) is expected, since they nearly balance each other.

The momentum transfer from the wind forcing to ocean currents is effective during the winter in the GSL, with a positive correlation coefficient (0.8-0.9) between the kinetic energy of wind (KEW) and current (KE), except for the NE subregion. It implies the momentum transfer between the wind and current is still viable in presence of ice cover in winter over the most GSL. This correlation may be disturbed in the NE subregion due to other processes. It should be noted that the water temperature at 150 m (T150) and the kinetic energy of currents (KE) in the NE subregion have a negative correlation coefficient (-0.7), indicating more energetic circulation is correlated with the cooler winter water mass (and greater volumes). In fact, the winter water mass of the NE subregion has the deepest winter convection (>200 m) in the GSL, with also significant contributions of the Arctic origin water mass from the SBI (Galbraith 2006; Smith et al. 2006b).

The statistically significant negative correlation coefficient (-0.66) for T150 and IMel/IFm occurs in the NW subregion, indicating that the colder winter results in the higher the water temperature at 150 m. The depth of 150 m is the depth for a typical lower boundary of the Cold-Intermediate Layer in the GSL (Galbraith 2006), with underlying warm slope waters (>3 °C) centred at ~270 m depth (Figure C.2j). The significant correlation between the ice melt/formation magnitude and the water temperature at 150 m indicates a negative response, in contrast to a simply intensified convection scenario (e.g. Allison 1981; Weller 1968). This implies an enhanced estuarine circulation in severe winters in comparison with the mild winters.

5.4 Discussion

Two important questions are raised when examining the temporal and spatial variability of sea-ice in the GSL. What is the source of the heat flux leading to substantial basal melt of ice when the surface layer heat content is depleted? What is the interaction between sea-ice and circulation in the NW subregion? To address these questions, a composite analysis is used here. Composite groups are determined by a normalized ice formation index (Figure 5.11d), where the positive group for harsh winters (CPos) includes year 2003, 2007-2009 and the negative group for mild winters (CNeg) includes year 2000, 2006, and 2010. Although the small sample size is a main limitation for the significance of the results, it is still worthwhile to present here as an example for the analysis of model results.

Composite temperatures in February, during the ice growth phase, in the GSL are shown in Figure 5.12. The sea surface temperatures (SSTs) are near the freezing point (~-1.8 °C) almost all over the GSL in CPos due to cold air and extensive ice cover (Figure 5.2). The southeastern GSL and adjacent areas are ice free because of the relatively warm (0-1 °C) inflow through the eastern Cabot Strait. The SST in CNeg is generally warmer than that in CPos by up to 1.2 °C over the eastern GSL. The surface circulation is characterized by the well-known cyclonic Gulf-wide circulation, which is consistent with earlier studies (e.g. Urrego-Blanco & Sheng, 2014). The surface currents are intensified in CPos during harsh winters, leading to stronger westward inflow through the SBI and equatorward outflow at the western Cabot Strait. Another significant difference in the circulation between CPos and CNeg is that the location of the cyclonic Anticosti Gyre shifts northwestward due to the detached Gaspe Current in CPos, which is associated with the instability of the Gaspe Current (Sheng 2001).

At 50 m, the water temperature in CPos is cooler than that in CNeg, due to enhanced cold water mass formation in harsh winters than in mild winters (Galbraith 2006). However, the water mass is warmer in CPos than in CNeg along the coast over the northwestern GSL (Figure 5.12f), which results from the uplift of the thermocline and is distinct from the other areas in the GSL. Such features in the Lower St. Lawrence River estuary and the Anticosti Gyre were also observed by moorings in winter 2003 (Smith et al., 2006). The

warm water (0-1 °C) entering the GSL over eastern Cabot Strait also erodes the near freezing water mass in the northeastern and southwestern GSL.

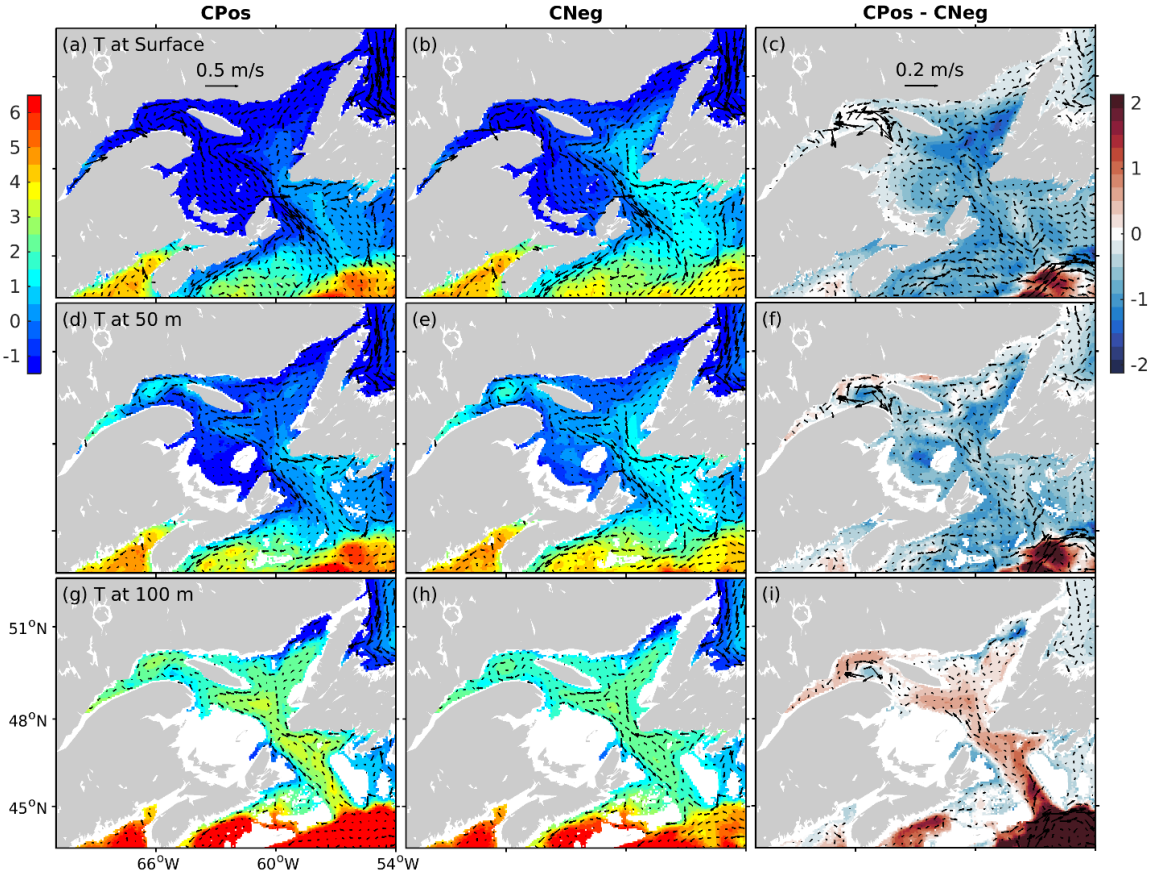

Figure 5.12. Composite temperature in February at (from top to bottom) surface, 50 m, 100 m depth for (from left to right) CPos (positive group), CNeg (negative group), and CPos minus CNeg.

At 100 m, the water mass is in a transition to relatively warm subsurface waters over the Laurentian Channel and the northeastern GSL, except for the Mecatina Trough in the northeastern GSL (Figure 5.12g). It should be noted that the deepest (over 200 m) cold water mass reservoir in the GSL occurs in the Mecatina Trough, and such cold water mass has larger volumes in harsh winters than mild ones (Galbraith, 2006). In comparison with CNeg, the two sources of warm waters in CPos are indicated (Figure 5.12i): (1) the enhanced shoaling of warm waters in the northwestern GSL, which has significant positive

correlation to the ice melt volume (Figure 5.10a); and (2) the warm slope waters entering the Laurentian Channel. The latter is suggested to result from the weakening of the Labrador Current on shelf break, in response to the positive winter NAO index with a 1-2 years lag (Greene and Pershing 2003). The winter NAO index (Hurrell, 1995, PC-based December to March North Atlantic Oscillation Index, climatedataguide.ucar.edu) shown in Figure 5.11a indicates that the years 2003, 2008 and 2009 in the CPos composite follow a positive winter NAO one-year prior. This is consistent with that the water temperatures in the Laurentian Channel at (and below) 100 m depth are warmer in the CPos than the CNeg.

Indeed, the two warm water sources are suggested to provide heat fluxes to the upper layer in the GSL. One warm water source is uplifted from deeper depth in the northwestern GSL and the other propagates along the Channel from the shelf-break of Newfoundland. The circulation differences also exhibit an organized northward flow through Cabot Strait, a sign of the compensation flow in an estuarine circulation (Figure 5.12i). Note that, the small sample size (4 years in the CPos composite, and 3 years in the CNeg) is one of limitations in this analysis. The t-test for the composite differences, shown in Figure 5.12, gives p-values up to 0.15 at 100 m depth and even larger at 50 m and the surface. It should be noted that, the composite differences are significant with p-value<0.05 at 150 depth in the St. Lawrence Estuary. The oceanic heat fluxes, important for the sea-ice dynamics, still need future investigations using observations and a longer model run.

It should be noted that the NAO is not the dominant factor for influencing the winter air temperature over the GSL (Greatbatch 2000). The air temperature variability (JFM mean over the GSL) derived from the CFSR forcing (Figure 5.11b) shows a weak correlation to the winter NAO, implying the importance of processes other than the NAO affecting the sea ice variability in the GSL. Thus, the winter NAO is not an optimal predictor for the sea-ice variation in the GSL.

5.5 Summary

A coupled ocean circulation-ice model based on NEMO was used to simulate the sea-ice conditions over the Gulf of St. Lawrence (GSL) for the period 1998-2010. The model was driven by a suite of external forcings including the atmospheric forcing at the surface, river runoff, tides and large-scale ocean influences introduced at the lateral open boundaries. The model performance for simulating circulation over the eastern Canadian Shelf was assessed previously in Chapter 4. The model performance is further assessed in Appendix C using observations from meteorological stations, CTD, and remote sensing in the GSL. The coupled ice-ocean circulation model was found to have good skill in simulating the time-varying and 3D circulation and hydrographic distributions in the GSL. The coupled model also reproduces basic features in the observed variability of the sea-ice area and volume, although it underestimates the sea-ice volume over the southwestern GSL.

The GSL was divided into four subregions for analyzing the simulated sea-ice conditions for the 13-year period. The NW subregion is characterized by the strongest stratification and freshest surface layer in the GSL due to the St. Lawrence River discharge, producing a large volume of sea-ice. The NE subregion features significant ice import from the Labrador Shelf and intense local ice formation. The SW subregion has broad shallow areas (<60 m), receiving a great amount of ice from the NW subregion and exporting ice to the Scotian Shelf. The SE subregion receives relatively warm inflow from Cabot Strait and is often ice free. The sea-ice export from the NW subregion accounts for a great portion of the ice volume variability in the GSL and over the eastern Scotian Shelf. The SW subregion is the primary reservoir of sea-ice in the GSL, affecting the ice export through Cabot Strait to the northeastern Scotian Shelf. The ice import into the GSL through the SBI is important for the eastern GSL but has only a minor impact on the western GSL (Figure 5.6). For the simplicity of the model setup, the northern open boundary of the coupled model is closed for the ice transport. A comparison of model results with observations implied that the ice transport from the northern Labrador Shelf north of 54°N, which was not considered in this study, may play an important role in the ice volume over the NE subregion of the GSL during late ice-season (April-May) (Figure 5.5b).

The sea-ice volume budget in the GSL was examined from model results to identify the primary processes affecting the sea-ice conditions in the GSL. The frazil ice formation and the basal melt at the ice-ocean interface were found to be the two primary processes (one order larger than the others in magnitude) in the sea-ice volume budget for the GSL. The sea-ice conditions in the GSL are sensitive to the balance between the two primary processes which nearly compensate each other. Thus, the model performance in simulating sea-ice conditions requires accurate simulations of these two primary processes in the GSL. The frazil ice formation, dominant sea-ice formation process in the GSL, was found to have a strong correlation to the winter air temperature in the GSL. The basal melt is significantly affected by the stratification and circulation. Tides were also found to have a substantial impact on the stratification and the sea-ice budget in the whole GSL, especially in the northwestern and southwestern GSL.

For understanding the oceanic heat flux supply to the surface during the ice growth phase, the circulation and temperature of the upper layer in the GSL were analyzed to investigate the oceanic response to the winter forcing. By contrasting the simulated sea-ice conditions during the harsh and mild winters, the composite analysis suggested that the warm slope water provides an anomalous water mass into the Laurentian Channel that shoals in the St. Laurence Estuary in response to the winter forcings. This indicates that, in a severe winter, an intensified estuarine circulation leads to enhanced thermocline uplift in the northwestern GSL along with anomalous slope water entering the GSL (Sections in 5.4). Consequently, there are positive anomalous heat fluxes entering the upper layer in the GSL, leading to more ice melting due to the heat convergence at the ice-ocean interface. Such an oceanic response acts as a negative feedback to the enhanced ice formation in the harsh (cold) winter, but the statistical significance of the composite analysis is tempered due to relatively short model run (15-year). Further study is required to confirm this response with observations and an extended model run.

The sea-ice open boundary forcing at the northern boundary of the model (~54.5°N) is found to be the major source of the sea-ice simulated on the Labrador and Newfoundland Shelf in late winter (after February). Those north origin sea-ice can occasionally make their way to the GSL through the SBI, but only becomes noticeable in the simulated sea-ice in

the northeastern GSL in late winter. Observations indicate a significant volume of sea-ice (~10 km^3) can pour into the northeastern GSL through the SBI in a few weeks, e.g., in March 2004 (Figure D.2m). Nevertheless, the source and dynamics of those anomalous sea-ice transport is not well simulated in the model, which may associate with the missing dynamics of the iceberg in the model. Known as "Iceberg Alley", the Labrador Shelf has a annual flux of 500 to 2500 icebergs transported equatorward (Murray 1969). Surface plumes fueled by melt waters from icebergs can affect the local stratification and dynamics (Yankovsky and Yashayaev 2014). Icebergs are also suggested to have "dynamical forcing effects" on sea-ice, inducing sea-ice ridging and frazil ice formation (Hunke and Comeau 2011). The iceberg is not simulated in the model used in this study, although observed high iceberg activities in the vicinity of the SBI in late winter often occurs with model deficit, comparing to observations, in simulated sea-ice volume in the northeastern GSL. Further studies are required to understand the impact of icebergs in the sea-ice thermodynamics, rheology, and transport in the Labrador and Newfoundland Shelf.

CHAPTER 6

CONCLUSIONS

Motivated by the need to accurately simulate the three-dimensional (3D) circulation and its temporal and spatial variability over the eastern Canadian shelf (ECS) and in the adjacent northern North Atlantic (nNA), this thesis research is a combination of studies on the dynamics of the large-scale depth-mean circulation in the nNA and the main physical processes affecting the 3D circulation and sea-ice over the ECS. Numerical ocean circulation models with different levels of complexity and several useful methodologies for analyzing the model results were used.

A barotropic streamfunction decomposition method (Greatbatch et al. 1991; 2010) was extended and developed to examine the influence of the four main dynamic terms in the vertically-averaged momentum equations on the barotropic transport in the nNA. The method was applied to the results of the high-resolution ocean model configuration, VIKING20. The knowledge obtained from this diagnostic method not only improved our understanding of the circulation dynamics, but also can be used in identifying model deficiency in simulating circulation features such as, for example, in the Northwest Corner region (Lazier, 1994; Drews et al., 2015).

Since tides were not included in VIKING20, a coupled ice-ocean circulation model based on NEMO v3.6 was developed for the ECS and adjacent deep waters of the nNA. The coupled model was integrated for the years 1996-2010, and forced by a suite of external forcings including the tides, freshwater runoffs, atmospheric forcings at the sea surface, and large-scale currents at the model open boundaries. The model results for the years 1998-2010 were used to examine the role of tides in the dynamics of the seasonal

circulation, hydrographic variability, and sea-ice over the ECS, with a particular focus on the Gulf of St. Lawrence in the case of sea-ice.

A summary of major scientific findings is given below, followed by discussion on the significant contributions of this thesis and possible future work.

6.1 Main Research Results

6.1.1 Dynamics of Barotropic Transport in the Northern North Atlantic Ocean

The barotropic (i.e., depth-integrated) transport produced by VIKING20 for the years 1960-2009 was decomposed using a linear shallow water model (SWM) to quantify the main dynamic processes affecting the transport in the model. VIKING20 is a high-resolution (1/20°) ocean model configuration and has good skill at simulating the 3D circulation in the northern North Atlantic Ocean (Behrens 2013; Böning et al. 2016; Breckenfelder et al., 2017). The SWM was driven by forcings, derived from the VIKING20 output, for each of the four dynamic terms in the vertically-averaged momentum equations (see details in Appendix A). As a result, the SWM can be used to quantify the contributions to the barotropic transport by the corresponding dynamic terms, namely mean flow advection (MFA), eddy momentum flux (EMF), potential energy (PE), and wind stress (for a uniform density ocean) (WS), respectively.

For the time-mean barotropic transport in the nNA during the period 1960–2009, as simulated by VIKING20, the PE term was found to be the dominant forcing except over the western boundary current regions. Both the PE and MFA terms were found to play an important role in driving the transport around the rim of the Labrador Sea. The three terms of MFA, EMF, and PE were found to drive the Gulf Stream and its extension, the North Atlantic Current. By comparison, the wind stress contribution (direct wind forcing for a uniform density ocean) plays a secondary role except over the Mid-Atlantic-Ridge. It should be noted that the spatial distribution of the EMF contribution to the barotropic transport determined by the SWM is very similar, but of smaller magnitude, to that found by Greatbatch et al. (2010) who used satellite-derived forcings. The magnitude of the EMF contributions determined in this study was justified by the surface intensified vertical

profile of the EMF term from VIKING20, which differs from the linear vertical profile assumed by Greatbatch et al. (2010).

In contrast to the classical diagnosing methods, the SWM results do not need spatial smoothing, and retain the information of several quasi-steady meso-scale recirculation features which are challenging to be reproduced in circulation models. For instance, the circulation in the Northwest Corner centered at 50°N and 45°W was found to be driven by the PE and MFA terms, with modest contributions from the EMF term (Figure 2.2). The Mann Eddy, to the east of the Grand Banks, was found to be primarily driven by the MFA and EMF term over its eastern half, and by the PE term over its western half. By comparison, the local vorticity budget based on the vertically-averaged momentum equations is too noisy to infer the relative importance of the forcing terms in driving these meso-scale circulation features (Figure A.1).

The time-mean barotropic streamfunctions decomposed from the vertically-integrated momentum equations are characterized by the classical wind-driven gyre circulation of the flat-bottom Sverdrup-transport and the significant contribution of the Bottom Pressure Torque (BPT). The inferred contribution of the BPT terms is primarily compensated by that of the MFA term, in the interior of the Labrador Sea and, in particular, along the shelf-edge of Greenland, Labrador Shelf, Newfoundland Shelf, and the separation point of the Gulf Stream near Cape Hatteras. It indicates that the mean flow has significant impact on the interaction between the circulation and the sloping bottom topography.

50-year time series of the contributions by the four forcing terms were also obtained by using the SWM for each year during the period 1960-2009. The combined contributions of the four forcings explain over 85% of the total variance in the barotropic streamfunction in VIKING20 over most of the nNA. Large differences between the combined contributions of the four forcings and the VIKING20 streamfunctions occur in: (1) the continental shelves, where the bathymetry within the domain of the SWM was deliberately smoothed for numerical stability; and (2) the areas near the southern boundary where the closed southern boundary of the SWM blocks the f/H contours. Among these four forcings, the PE term is the dominant forcing that accounts for the most variance over the nNA. The PE

and MFA terms, along with a moderate contribution from the EMF term, are responsible for the variance along the pathways of the Gulf Stream and the North Atlantic Current where large interannual variability (standard deviation>20 Sv) occurs. The MFA and EMF terms also explain a significant portion of the variance along the rim of the Labrador Sea. For the Gulf Stream transport, no significant response to the winter North Atlantic Oscillation (NAO) is found at lead year 0. However, at lead year 1 both the MFA and EMF contributions show a significant positive role (more positive winter NAO greater transport). At lead year 2, the role of the MFA weakens, while the PE contribution starts to play a significant role, indicating the emergence of the baroclinic response to the winter NAO (see Eden and Willibrand (2001)).

It should be noted that the transport variability associated with a particular term diagnosed by the SWM can be masked by that of the other terms. This can be seen in the barotropic transport response to the winter NAO. Over the Labrador Sea and Irminger Sea, a significant correlation to the winter NAO is shown in the streamfunction associated with the PE term, indicating that the more positive the winter NAO is, the higher transport associated with the PE term is in the subpolar gyre. However, such correlation is diminished for the total streamfunction due to the different responses to the winter NAO associated with the MFA and EMF terms. Meanwhile, a significant autocorrelation occurs in the streamfunction variability associated with the PE term in the Labrador Sea and Irminger Sea, implying a multi-decadal oscillatory behaviour intrinsic to the density field (see Eden and Greatbatch (2003)). Nevertheless, such autocorrelation is much less evident from the total streamfunction variability due to masking by the contributions from the other terms.

The decomposition method based on the SWM presented in this thesis exhibits three major advantages: (1) extracting the contribution of each term independently for the quantitative comparison of their relative importance; (2) retaining meso-scale patterns; (3) efficient in applying to existing model results and diagnosing with a linear SWM.

6.1.2 Processes Affecting Circulation and Sea-Ice over the Eastern Canadian Shelf

A coupled ocean circulation-ice model based on NEMO v3.6 was developed for the eastern Canadian shelf (ECS) and the adjacent northwest Atlantic Ocean with a suite of external forcings, including tidal forcing that was not included in VIKING20. The coupled ocean circulation-ice model was integrated for the 15-year period 1996-2010. The performance of the coupled model was assessed using observations from tide gauges, CTDs, and satellite remote sensing.

Tidal elevations and currents are important over the ECS. The tidal-induced residual currents are an essential part of the total baroclinic circulation with significant spatial variability over the region. The control run with all the external forcings (WithTide) and the model run without tides (NoTide) were used to examine the tidal impacts on the circulation over the ECS. Both the model runs are purely prognostic without the use of correction techniques such as the semi-prognostic method (Sheng et al. 2001; Greatbatch et al. 2004) and spectral nudging (Thompson et al. 2006). The tidal impacts were found to play an important role in the general circulation in the Gulf of Maine (GoM), Bay of Fundy (BoF), western Scotian Shelf (ScS), Georges Bank (GeB), and adjacent continental slope, with greater impacts in summer than in winter. The tidal-driven currents enhance the shelf-ocean exchange through the Northeastern Channel of the GoM, which significantly affects the water mass in the GoM (Ramp et al. 1985). Such tidal impacts result in the significantly warmer (up to 4 °C) winter SST in WithTide than NoTide in the GoM (Figure 4.11), which agrees well with observations (Figure 4.2). In the Gulf of St. Lawrence (GSL) and eastern ScS, the tidal impacts are relatively large over shallow banks and inside the Laurentian Channel (LCh). The tidal impacts were also found to be particularly large in the St. Lawrence River Estuary (SLRE), with greater impacts in winter than in summer. Over the Labrador Shelf (LS) and Newfoundland Shelf (NfS), the tidal impacts are relatively small.

Analyses of model results demonstrated that tides generate significant hydrographic changes over the ECS, which are consistent with observations. The coupled ocean circulation-ice model was used to examine the generation and propagation of the tidal-induced hydrographic changes over the ECS (see Section 4.5.5 and 4.5.6). Such tidal impacts on temperature and salinity are the most significant near tidal fronts, where the

tidal mixing results in substantial vertical fluxes of salt and heat between the upper and lower layers. Frontal circulation usually compensates the impacts of tidal mixing, while the horizontal residual circulation can spread the tidal impacts generated in frontal areas into broader areas. At the sea surface, the tidal-induced anomalies in SST (up to 10 °C) and SSS (up to 20 psu) are largely explained by the coupling between the tidal dynamics and seasonal stratification/circulation.

The tidal impacts on circulation and hydrography also result in significant changes in the sea-ice distributions in the GSL. In the study on the dynamics of the sea-ice in the GSL, the GSL was divided into four subregions for examining spatial variability in the dynamics and thermodynamics on the sea-ice conditions (Figure 5.1). The northwestern (NW) subregion is characterized by the freshest surface layer, with the strongest stratification, favouring ice formation, and is the major source of the ice in the GSL. With the strong Gaspe Current, the NW subregion exports a large amount of ice into the SW subregion with an annual mean of 9.5 km^3. The southwestern (SW) subregion is the major reservoir of the ice in the GSL and accounts for up to 60% of the ice in the GSL. A large portion of the ice in the SW subregion comes from the NW subregion. Significant ice formation also occurs near coasts of the southwestern GSL and over the Magdalen Shallows in the SW subregion. Sea-ice is exported from the SW subregion onto the eastern ScS in late winter, with significant interannual variability in magnitude. In the northeast (NE) subregion, the ice is locally formed or imported from the LS through the Strait of Belle Isle (SBI), and primarily exported to the southeast (SE). The SE subregion is a sink of ice in the GSL, which receives relative warm (>2 °C) inflow from Cabot Strait and is often ice free. The sea-ice transport from the northern open boundary plays significant role in the simulated sea-ice in the Labrador and Newfoundland Shelf after February but minor role in the northeastern GSL.

Despite the large seasonal and interannual variability in the modelled sea-ice volume in the GSL, the two primary thermodynamic processes affecting the sea-ice volume budget in the GSL are the frazil ice formation and the basal melt at the ice-ocean interface. The frazil ice formation and basal melt play the dominant roles in the ice formation and melt processes in the GSL, respectively. In fact, the modelled ice formation has a volume more

than five times of that of the ice accumulated in the GSL, with the modelled ice formation being primarily compensated by the basal melt due to the oceanic heat convergence at the ocean-ice interface. The differences between these two major processes significantly affect the variability of the sea-ice volume in the GSL. The magnitude of the ice formation is strongly related to the winter air temperature. On the other hand, the magnitude of ice melt is regulated by the oceanic heat flux, which corresponds to the ocean circulation and the upper layer stratification. The modelled oceanic response to the winter forcing suggests a negative feedback in which a severer winter leads to greater oceanic heat flux to the ice due to the circulation response. This negative feedback requires confirmation with longer model simulations and observations.

6.1.3 Summary of Most Important Findings

A brief summary on the most important scientific findings of this doctoral thesis research is given as follows:

- The improved method to decompose the barotropic streamfunction, by applying appropriate forcings to a linear SWM, has several advantages over the traditional diagnosis methods based on the local vorticity balance, especially for identifying quasi-steady meso-scale features.
- The contribution from the non-linear advection terms in the momentum equation, i.e. the MFA and EMF terms, play significant roles in driving the barotropic transport along the pathways of the Gulf Stream, North Atlantic Current, and around the Labrador Sea. The importance of these terms was neither quantitatively estimated nor compared with the contributions of wind and baroclinic effects in earlier studies.
- The MFA term plays an important role in the interaction between the circulation and the continental slope, and has a strong influence on the bottom pressure torque.
- The PE contribution dominates the variability of the barotropic transport in most of the northern NA, while the MFA and EMF contributions are also important along the paths of the western boundary currents. The combined contributions of all forcing terms can mask the variability that is intrinsic to the density field.

- The residual circulation induced by tides plays a very important role in the circulation over the GoM-BoF, GeB, western ScS, and SLRE.
- The most significant tidal-induced hydrographic anomalies, generated by the tidal mixing and frontal circulation, were found to occur near tidal fronts and are spread with the horizontal residual circulation into broader areas.
- The two leading processes controlling the sea-ice volume in the GSL are: the ice formation in open water in response to the winter air temperature, and the basal melt in response to the oceanic heat flux associated with the ocean circulation and the upper layer mixing.

6.2 Future work

Although significant achievements were made in this thesis research in examining important processes affecting the temporal and spatial variability of hydrodynamics on the ECS and its adjacent nNA, there are more scientific questions remaining to be addressed.

A useful method was proposed in this thesis to decompose the barotropic transport streamfunction calculated from 3D model output produced by a high-resolution ocean model. This decomposition method, however, suffers from a few limitations regarding the input data and numerics of the SWM. Firstly, the f/H contours cutting off at the southern open boundary (~32° N) results in up to ~15 Sv transport in the subtropical gyre that is not captured by the SWM. If the southern open boundary of the source model, in this case VIKING20, were extended to cover the equator, the decomposition results would be considerably improved since then the f/H contours that access the northern hemisphere would not cross the southern boundary of the SWM. Secondly, the bathymetry used in the SWM required significant modifications on the continental shelf to suppress numerical instability associated with the steep topography. An improvement in the numerical schemes of the SWM could be made following Espelid et al. (2000), for example, who suggested a weighted 4-point-average for the Coriolis term based on the topography and the Coriolis parameter to conserve energy and maintain numerical stability in regions with varying depth. It would be interesting to modify the decomposition method presented here to include the shelf circulation using this technique.

Tides are not commonly included in current climate ocean models due to computational efficiency and stability concerns. The tidal impacts on the long-term variability of the circulation and hydrography were not addressed in the past. The tidal-induced root-mean-square differences (RMSDs) in the kinetic energy (KE), SST and SSS after the two months period (see Figure 4.16) implied considerable tidal impacts (in WithTide) on the circulation and hydrography in longer time scales (Chapter 4). Significant tidal impacts were also found, based on model results, to occur in the slope waters and waters in deep channels, including the Northeast Channel of the GoM and the Laurentian Channel of the GSL. Future research is needed to characterize the tidal-induced anomalies over these regions.

The results produced by the coupled ocean circulation-ice model demonstrated that strong internal tides are generated year-round on the shelf break to the southeast of GeB (Appendix B). The simulated low mode internal tide wave train radiates away from the shelf edge, with up to 80 m isopycnal displacement at 500 m depth. Although evidence of internal tides in this area has been found earlier (Katavouta et al. 2016; Kelly et al. 2016), many questions remain to be answered. Preliminary investigation indicates that the internal tides simulated by the coupled model are consistent with the satellite data (Jason-1 satellite, marine.copernicus.eu) in amplitude and phase, as well as showing the impact of the Gulf Stream. The simulated internal tides exhibit refraction/reflection on encountering the Gulf Stream. As a result, the internal tide activity is ubiquitous in the slope water region between the Gulf Stream and the ECS. However, little is known on how internal tides of such magnitude can affect the Gulf Stream and its associated eddies. On the other hand, previous studies suggested significant shelf edge mixing induced by internal tides (Petrie 1975; Sandstrom and Elliott 1984), but the source of the internal tides has not been identified. Kelly et al. (2016) suggested a scenario in which the internal tides are reflected back to the shelf by the Gulf Stream. Further studies are required to characterise this internal tide and understand its potential impact on the Gulf Stream and coastal waters.

The 15-year model run used in Chapter 5 should be extended in order to have more robust analysis of the interannual sea-ice variability in the GSL. A diagnosis of the advective/diffusive oceanic heat flux should also improve the understanding of the budget for the oceanic heat content in the GSL. Future research is needed to examine the role of

non-local forcing on the magnitude and lag of the sea-ice variability in response to large-scale climate signals, e.g., the NAO. In turn, how does sea-ice, a moderator of the air-sea interaction, affect the regional circulation and shelf-ocean exchange?

The Labrador Shelf, known as "Iceberg Alley", has a annual flux of 500 to 2500 icebergs transported equatorward (Murray 1969). Melt waters from icebergs affect local stratification and dynamics (Yankovsky and Yashayaev 2014). The motion of icebergs is suggested to apply "dynamical forcing effects" on sea-ice, inducing sea-ice ridging and frazil ice formation (Hunke and Comeau 2011). However, the impacts of icebergs on the variability of sea-ice and hydrodynamics on the Labrador Shelf and adjacent waters are not understood. The observed high iceberg activity in the vicinity of the Strait of Belle Isle in late winter often occurs when the model underestimates sea-ice concentration and thickness compared to observations in the northeastern GSL (Appendix D). Further studies are encouraged to examine the impact of icebergs in the sea-ice thermodynamics, rheology, and transport on the Labrador Shelf and adjacent waters.

The ScS is frequently influenced by cyclones and winter storms. Storms can lead to intense currents of O(1 m s^{-1}) and vertical mixing (Greatbatch 1983, 1984; Sanford et al. 1987; Sheng et al. 2006). During Hurricane Ivan in 2004, which passed the outer shelf and slope in the northeastern Gulf of Mexico, for an example, ADCP arrays on the shelf-edge recorded intense near-inertial flows O(1 m s^{-1}) extending down to 500 m (Teague et al. 2007), implying considerable shelf-ocean exchange. However, the shelf-ocean exchanges induced by extreme weather events are poorly understood over the ECS. A process study, based on the coupled model presented in Chapter 4 and a storm vortex insertion method following Sheng et al. (2006), evaluated the shelf-ocean exchange induced by three extreme storms that approached the ScS. The model results demonstrated significant storm-induced circulation variability depending on the path and intensity of the storm. Accumulated week-long warm slope water intrusion on the ScS induced by Hurricane Juan in 2003 was found to make a significant contribution to that of the whole year 2003 simulated by the model. In-situ observations during extreme events are very limited. Numerical studies validated by observations will be very useful to evaluate the impact of extreme events on circulation and biogeochemistry in coastal waters.

APPENDIX A

GOVERNING EQUATIONS FOR THE STREAMFUNCTION DECOMPOSITION

This Appendix presents the governing equations for the Shallow Water Model (SWM) used in Chapter 2 and 3, and the calculation of the forcing terms from the output of the VIKING20 nest component. The appendix also shows the equations for the local vorticity balance, a diagnosis of the vorticity balance for the vertically-averaged momentum equations from VIKING20 (Figure A.1) and a vertical profile of the eddy momentum flux terms from VIKING20 (Figure A.2).

A.1 The Derivation of Governing Equations

The momentum and continuity equations for a continuously stratified Boussinesq ocean in steady state can be written as

$$\boldsymbol{u} \cdot \nabla \boldsymbol{u} + \boldsymbol{f} \times \boldsymbol{u} = -\frac{\nabla p}{\rho_0} - g\boldsymbol{k} \tag{A.1a}$$

$$\nabla \cdot \boldsymbol{u} = 0 \tag{A.1b}$$

where $\boldsymbol{u} = (u, v, w)$ is the velocity and u, v, w are the velocity components respectively in the eastward, northward and vertically upwards directions, $\boldsymbol{f} = f\boldsymbol{k}$ is the Coriolis parameter in the vector form, where **k** is a unit vector in the upward vertical direction, p

the pressure, ρ_0 the reference density for sea water, and g is the acceleration due to gravity. The viscous terms are left out for simplicity. The kinematic boundary conditions for the vertical velocity component are given as

$$w = \begin{cases} 0 & \text{at } z = 0 \\ -\left[u\dfrac{\partial H}{\partial x} + v\dfrac{\partial H}{\partial y}\right] & \text{at } z = -H \end{cases} \tag{A.2}$$

where the Cartesian coordinates (x, y, z), in the eastward, northward and vertical direction, respectively, are used for convenience. A linearized kinematic condition is assumed at the free surface, z = 0, and the ocean bottom is at z = -H. In a Boussinesq ocean, the advection term can be rewritten in flux form as,

$$(\boldsymbol{u} \cdot \nabla \boldsymbol{u})_{\boldsymbol{i}} = \frac{\partial}{\partial x_j}(u_i u_j) \tag{A.3}$$

where $(x_1, x_2, x_3) = (x, y, z)$, $(u_1, u_2, u_3) = (u, v, w)$, and $\frac{\partial}{\partial x_j}(u_i u_j) = \sum_{j=1}^{3} \frac{\partial}{\partial x_j} u_i u_j$. We then replace dynamical variables by a long-time average (denoted by an overbar) and its deviation (denoted by a prime). Time-averaging the momentum equation then gives

$$\frac{\partial \bar{u}_i \bar{u}_j}{\partial x_j} + \frac{\partial \overline{u_i' u_j'}}{\partial x_j} + (\boldsymbol{f} \times \bar{\boldsymbol{u}})_{\boldsymbol{i}} = -\frac{(\nabla \bar{p})_i}{\rho_0} - \delta_{i3} g \tag{A.4}$$

where the overbar refers to an annual mean following Rieck et al. (2015) and δ is the Kronecker delta. In this study, the vertical momentum equation is approximated by the hydrostatic equation so that

$$\bar{p} = g\int_z^0 \bar{\rho} dz + p_a \tag{A.5}$$

with $\bar{\rho}$ denoting a mean profile of in situ density, and p_a is the atmospheric pressure here taken to be a uniform constant.

The momentum equation is then integrated in the vertical direction (denoted by <·>). Using the Leibniz Integral Rule and the boundary conditions, it follows that for the mean flow advection term

$$\begin{aligned}\langle\frac{\partial \bar{u}_i\bar{u}_j}{\partial x_j}\rangle &= \int_{-H}^{0}\frac{\partial \bar{u}_i\bar{u}_j}{\partial x_j}dz \\ &= \left[\frac{\partial}{\partial x}\int_{-H}^{0}\bar{u}\bar{u}_i dz + \frac{\partial}{\partial y}\int_{-H}^{0}\bar{v}\bar{u}_i dz + [\bar{w}\bar{u}_i]_{-H}^{0}\right. \\ &\qquad \left. - \frac{\partial H}{\partial x}\bar{u}\bar{u}_i|_{z=-H} - \frac{\partial H}{\partial y}\bar{v}\bar{u}_i|_{z=-H}\right] \\ &= \frac{\partial}{\partial x}\int_{-H}^{0}\bar{u}\bar{u}_i dz + \frac{\partial}{\partial y}\int_{-H}^{0}\bar{v}\bar{u}_i dz\end{aligned} \tag{A.6}$$

Likewise, for the eddy momentum flux term,

$$\langle\frac{\partial \overline{u_i'u_j'}}{\partial x_j}\rangle = \frac{\partial}{\partial x}\int_{-H}^{0}\overline{u'u_j'}dz + \frac{\partial}{\partial y}\int_{-H}^{0}\overline{v'u_j'}dz \tag{A.7}$$

Vertically integrating the horizontal pressure gradient term gives

$$
\begin{aligned}
\langle \nabla \bar{p} \rangle &= \int_{-H}^{0} \nabla \bar{p} dz \\
&= \nabla \int_{-H}^{0} \bar{p} dz - \bar{p}_b \nabla H \\
&= \nabla \left([z\bar{p}]_{-H}^{0} - \int_{-H}^{0} z \frac{\partial \bar{p}}{\partial z} dz \right) - \bar{p}_b \nabla H \\
&= \nabla (H\bar{p}_b + \rho_0 \bar{\Phi}) - \bar{p}_b \nabla H \\
&= H \nabla \bar{p}_b + \rho_0 \nabla \bar{\Phi}
\end{aligned} \tag{A.8}
$$

where p_b is the bottom pressure and $\Phi = \frac{g}{\rho_0} \int_{-H}^{0} z\rho dz$ is the potential energy per unit area referenced to the surface $z = 0$.

Similarly, the Reynolds-averaged continuity equation is given as $\nabla \cdot \overline{\boldsymbol{u}} = 0$ by assuming the incompressibility of the ocean water. The vertically integrated form is,

$$
\begin{aligned}
0 &= \int_{-H}^{0} \nabla \cdot \overline{\boldsymbol{u}} dz \\
&= \frac{\partial}{\partial x} \int_{-H}^{0} \bar{u} dz + \frac{\partial}{\partial y} \int_{-H}^{0} \bar{v} dz + [w]_{-H}^{0} - \frac{\partial H}{\partial x} \bar{u}|_{z=-H} - \frac{\partial H}{\partial y} \bar{v}|_{z=-H} \\
&= \frac{\partial}{\partial x} \int_{-H}^{0} \bar{u} dz + \frac{\partial}{\partial y} \int_{-H}^{0} \bar{v} dz
\end{aligned} \tag{A.9}
$$

Including the surface wind stress (τ_s^x, τ_s^y), the vertically- and Reynolds-averaged form of the horizontal momentum equations and the continuity equation can now be written as,

$$-\frac{f}{H}\langle\bar{v}\rangle = -\frac{1}{\rho_0}\frac{\partial\bar{p}_b}{\partial x} - \frac{1}{H}\frac{\partial\bar{\Phi}}{\partial x} - \frac{1}{H}\left(\frac{\partial}{\partial x}\int_{-H}^{0}\bar{u}\bar{u}dz + \frac{\partial}{\partial y}\int_{-H}^{0}\bar{u}\bar{v}dz\right)$$

$$-\frac{1}{H}\left(\frac{\partial}{\partial x}\int_{-H}^{0}\overline{u'u'}dz + \frac{\partial}{\partial y}\int_{-H}^{0}\overline{u'v'}dz\right) + \frac{\overline{\tau_s^x}}{\rho_0 H} \tag{A.11a}$$

$$\frac{f}{H}\langle\bar{u}\rangle = -\frac{1}{\rho_0}\frac{\partial\bar{p}_b}{\partial y} - \frac{1}{H}\frac{\partial\bar{\Phi}}{\partial y} - \frac{1}{H}\left(\frac{\partial}{\partial x}\int_{-H}^{0}\bar{v}\bar{u}dz + \frac{\partial}{\partial y}\int_{-H}^{0}\bar{v}\bar{v}dz\right)$$

$$-\frac{1}{H}\left(\frac{\partial}{\partial x}\int_{-H}^{0}\overline{v'u'}dz + \frac{\partial}{\partial y}\int_{-H}^{0}\overline{v'v'}dz\right) + \frac{\overline{\tau_s^y}}{\rho_0 H} \tag{A.11b}$$

$$0 = \frac{\partial\langle\bar{u}\rangle}{\partial x} + \frac{\partial\langle\bar{v}\rangle}{\partial y} \tag{A.11c}$$

The Shallow Water Model (SWM) used in this study is driven by each of the potential energy, eddy momentum flux, mean flow advection, and wind stress terms (denoted by (Z, M) in the following equations, where Z is the zonal component and M the meridional component) separately, and includes linear bottom friction $(\frac{ru}{H}, \frac{rv}{H})$ and Laplacian lateral viscosity $(A_h\frac{\partial^2 u}{\partial x^2}, A_h\frac{\partial^2 v}{\partial y^2})$, where A_h is the uniform horizontal viscosity coefficient. For simplicity, the < > and overbars are now dropped and u, v are the vertically-averaged velocities. The SWM is then formulated as,

$$-fv = Z - \frac{1}{\rho_0}\frac{\partial p_b}{\partial x} - \frac{ru}{H} - A_h\frac{\partial^2 u}{\partial x^2} \tag{A.12a}$$

$$fu = M - \frac{1}{\rho_0}\frac{\partial p_b}{\partial y} - \frac{rv}{H} - A_h\frac{\partial^2 v}{\partial y^2} \tag{A.12b}$$

$$0 = \frac{\partial(Hu)}{\partial x} + \frac{\partial(Hv)}{\partial y} \tag{A.12c}$$

Using the spherical coordinate, the above SWM can be written as,

$$-fv = Z - \frac{1}{\rho_0 a cos\theta}\frac{\partial p_b}{\partial \lambda} - \frac{ru}{H} - F_x \tag{A.13a}$$

$$fu = M - \frac{1}{\rho_0 a}\frac{\partial p_b}{\partial \theta} - \frac{rv}{H} - F_y \tag{A.13b}$$

$$0 = \frac{1}{acos\theta}\left[\frac{\partial Hu}{\partial \lambda} + \frac{\partial cos\theta Hv}{\partial \theta}\right] \tag{A.13c}$$

where a is the radius of the Earth, (λ, θ) are longitude and latitude, (F_x, F_y) represents the Laplacian lateral mixing term given by

$$F_x = A_h\left[\frac{1}{Ha^2cos^2\theta}\frac{\partial^2 Hu}{\partial \lambda^2} + \frac{1}{Ha^2cos^2\theta}\frac{\partial}{\partial \theta}\left(cos\theta\frac{\partial Hu}{\partial \theta}\right) + \frac{1}{Ha^2}\left((1 - tan^2\theta)Hu - \frac{2tan\theta}{cos\theta}\frac{\partial Hv}{\partial \lambda}\right)\right] \tag{A.14a}$$

$$F_y = A_h\left[\frac{1}{Ha^2cos^2\theta}\frac{\partial^2 Hv}{\partial \lambda^2} + \frac{1}{Ha^2cos^2\theta}\frac{\partial}{\partial \theta}\left(cos\theta\frac{\partial Hv}{\partial \theta}\right) + \frac{1}{Ha^2}\left((1 - tan^2\theta)Hv - \frac{2tan\theta}{cos\theta}\frac{\partial Hu}{\partial \lambda}\right)\right] \tag{A.14b}$$

For each of the four terms, the (Z, M) have the form

A. The potential energy term:

$$Z = -\frac{1}{Hacos\theta}\left[\frac{\partial}{\partial \lambda}\left\langle g\frac{\overline{(\rho - \rho_m)}}{\rho_0}z\right\rangle\right] \tag{A.15a}$$

$$M = -\frac{1}{Ha}\left[\frac{\partial}{\partial \theta}\left\langle g\frac{\overline{(\rho - \rho_m)}}{\rho_0}z\right\rangle\right] \tag{A.15b}$$

B. Mean-flow advection:

$$Z = -\frac{1}{Hacos\theta}\left[\frac{\partial\langle\overline{u}\,\overline{u}\rangle}{\partial\lambda} + \frac{\partial cos\theta\langle\overline{u}\,\overline{v}\rangle}{\partial\theta}\right] \tag{A.16a}$$

$$M = -\frac{1}{Hacos\theta}\left[\frac{\partial\langle\overline{v}\,\overline{u}\rangle}{\partial\lambda} + \frac{\partial cos\theta\langle\overline{v}\,\overline{v}\rangle}{\partial\theta}\right] \tag{A.16b}$$

C. Eddy momentum flux:

$$Z = -\frac{1}{Hacos\theta}\left[\frac{\partial\langle\overline{u'u'}\rangle}{\partial\lambda} + \frac{\partial cos\theta\langle\overline{u'v'}\rangle}{\partial\theta}\right] \tag{A.17a}$$

$$M = -\frac{1}{Hacos\theta}\left[\frac{\partial\langle\overline{u'v'}\rangle}{\partial\lambda} + \frac{\partial cos\theta\langle\overline{v'v'}\rangle}{\partial\theta}\right] \tag{A.17b}$$

D. The wind stress term:

$$Z = \frac{\overline{\tau_s^x}}{\rho_0 H} \tag{A.18a}$$

$$M = \frac{\overline{\tau_s^y}}{\rho_0 H} \tag{A.18b}$$

Note that ρ_m is the horizontally-averaged density at each z and is removed to reduce noise (note that ρ_m makes no contribution when taking the curl of the momentum equations).

A.2 Calculation of the Forcing Terms

As a first step, based on the derived forms presented above, the 5-day-mean output extracted from the nest component of VIKING20 over the northern North Atlantic (nNA)

is used to calculate the annual means and anomalies (following Rieck et al. (2015)) of the horizontal velocity components along the orthogonal curvilinear model grid. Subsequently, the mean and anomalous horizontal velocity components are collocated, rotated from curvilinear axes to geospatial axes and the required products are computed. Then, time averaging over the full 50 years of model integration is performed and a vertical integral on the native VIKING20 grid is applied, denoted by the < >, recognizing partial steps of the vertical axis. Thereby, the $\langle \overline{u}\,\overline{u} \rangle$, $\langle \overline{v}\,\overline{v} \rangle$, $\langle \overline{u}\,\overline{v} \rangle$, $\langle \overline{u'u'} \rangle$, $\langle \overline{v'v'} \rangle$, and $\langle \overline{u'v'} \rangle$ are calculated on the native VIKING20 grids. Similarly, the in-situ density is derived from potential temperature and salinity, and $\left\langle g \frac{\overline{(\rho - \rho_m)}}{\rho_0} z \right\rangle$ is then calculated on the VIKING20 grid, where $\rho_0 = 1024\ \mathrm{kg \cdot m^{-3}}$, ρ is the in-situ density, and ρ_m is the horizontally domain-average vertical profile of the in-situ density. The wind stress components $\overline{\tau_s^x}$ and $\overline{\tau_s^y}$ are averaged directly from the VIKING20 output respectively, then collocated and rotated from curvilinear axes to geospatial axes. At the end, all terms are linearly interpolated from the native VIKING20 grid to the SWM grid, which is an Arakawa C-grid, such that the horizontal derivatives in (A.15-A.17) are computed on the SWM grid by centered differences.

A.3 Vorticity Balance

We start with the vertically- and Reynolds-averaged form of the momentum and continuity equation (A.11). $\frac{\partial}{\partial x}$ of (A.11b) minus $\frac{\partial}{\partial y}$ of (A.11a) gives the vorticity balance for the vertically-averaged momentum equations:

$$\langle\overline{v}\rangle\frac{\partial}{\partial y}\frac{f}{H}+\langle\overline{u}\rangle\frac{\partial}{\partial x}\frac{f}{H}=\left[\frac{\partial}{\partial y}\left(\frac{1}{H}\right)\frac{\partial\overline{\Phi}}{\partial x}-\frac{\partial}{\partial x}\left(\frac{1}{H}\right)\frac{\partial\overline{\Phi}}{\partial y}\right]$$

$$-\left[\frac{\partial}{\partial x}\left(\frac{1}{H}\frac{\partial\langle\overline{u}\,\overline{v}\rangle}{\partial x}+\frac{1}{H}\frac{\partial\langle\overline{v}\,\overline{v}\rangle}{\partial y}\right)-\frac{\partial}{\partial y}\left(\frac{1}{H}\frac{\partial\langle\overline{u}\,\overline{u}\rangle}{\partial x}+\frac{1}{H}\frac{\partial\langle\overline{u}\,\overline{v}\rangle}{\partial y}\right)\right]$$

$$-\left[\frac{\partial}{\partial x}\left(\frac{1}{H}\frac{\partial\langle\overline{u'v'}\rangle}{\partial x}+\frac{1}{H}\frac{\partial\langle\overline{v'v'}\rangle}{\partial y}\right)-\frac{\partial}{\partial y}\left(\frac{1}{H}\frac{\partial\langle\overline{u'u'}\rangle}{\partial x}+\frac{1}{H}\frac{\partial\langle\overline{u'v'}\rangle}{\partial y}\right)\right] \tag{A.19}$$

$$+\left[\frac{1}{\rho_0}\left(\frac{\partial}{\partial x}\left(\frac{\overline{\tau_s^y}}{H}\right)-\frac{\partial}{\partial y}\left(\frac{\overline{\tau_s^x}}{H}\right)\right)\right]$$

Defining the streamfunction Ψ by

$$\frac{\partial\Psi}{\partial x}=\langle\overline{v}\rangle$$

$$\frac{\partial\Psi}{\partial y}=-\langle\overline{u}\rangle \tag{A.20}$$

(A.19) can be rewritten as

$$J\left(\Psi,\frac{f}{H}\right)=J\left(\overline{\Phi},\frac{1}{H}\right)+\boldsymbol{k}\cdot\nabla\times\frac{MFA}{H}+\boldsymbol{k}\cdot\nabla\times\frac{EMF}{H}+\frac{1}{\rho_0}\boldsymbol{k}\cdot\nabla\times\left(\frac{\overline{\boldsymbol{\tau}_s}}{H}\right) \tag{A.21}$$

where J is the Jacobian, and $J(\mathrm{A},B)=\frac{\partial A}{\partial x}\frac{\partial B}{\partial y}-\frac{\partial B}{\partial x}\frac{\partial A}{\partial y}$, $\boldsymbol{\tau}_s=(\tau_s^x,\tau_s^y)$ and

$$\mathrm{MFA}=-\left(\frac{\partial\langle\overline{u}\,\overline{u}\rangle}{\partial x}+\frac{\partial\langle\overline{u}\,\overline{v}\rangle}{\partial y},\frac{\partial\langle\overline{u}\,\overline{v}\rangle}{\partial x}+\frac{\partial\langle\overline{v}\,\overline{v}\rangle}{\partial y},0\right)$$

$$EMF=-\left(\frac{\partial\langle\overline{u'u'}\rangle}{\partial x}+\frac{\partial\langle\overline{u'v'}\rangle}{\partial y},\frac{\partial\langle\overline{u'v'}\rangle}{\partial x}+\frac{\partial\langle\overline{v'v'}\rangle}{\partial y},0\right)$$

$J\left(\overline{\Phi},\frac{1}{H}\right)$ is the JEBAR term which represents the contribution from the potential energy terms, while $\boldsymbol{k}\cdot\nabla\times\frac{MFA}{H}$ and $\boldsymbol{k}\cdot\nabla\times\frac{EMF}{H}$, represent the contribution from the mean flow advection and eddy momentum fluxes, respectively, and $\frac{1}{\rho_0}\boldsymbol{k}\cdot\nabla\times\frac{\overline{\boldsymbol{\tau_s}}}{H}$ is the contribution from the surface wind stress. Meanwhile, the topographic Sverdrup transport is computed using

$$J\left(\Psi,\frac{f}{H}\right)=\frac{1}{\rho_0}\boldsymbol{k}\cdot\nabla\times\left(\frac{\overline{\boldsymbol{\tau_s}}}{H}\right) \tag{A.22}$$

On the other hand, multiplying (A.11a) and (A.11b) by H and then following the same procedure leads to vorticity balance for the vertically-integrated momentum equations:

$$\begin{aligned}\langle\overline{v}\rangle\frac{\partial f}{\partial y}=&\frac{1}{\rho_0}\left[\frac{\partial H}{\partial y}\frac{\partial\bar{p}_b}{\partial x}-\frac{\partial H}{\partial x}\frac{\partial\bar{p}_b}{\partial y}\right]\\&-\left[\frac{\partial}{\partial x}\left(\frac{\partial\langle\overline{u}\,\overline{v}\rangle}{\partial x}+\frac{\partial\langle\overline{v}\,\overline{v}\rangle}{\partial y}\right)-\frac{\partial}{\partial y}\left(\frac{\partial\langle\overline{u}\,\overline{u}\rangle}{\partial x}+\frac{\partial\langle\overline{u}\,\overline{v}\rangle}{\partial y}\right)\right]\\&-\left[\frac{\partial}{\partial x}\left(\frac{\partial\langle\overline{u'v'}\rangle}{\partial x}+\frac{\partial\langle\overline{v'v'}\rangle}{\partial y}\right)-\frac{\partial}{\partial y}\left(\frac{\partial\langle\overline{u'u'}\rangle}{\partial x}+\frac{\partial\langle\overline{u'v'}\rangle}{\partial y}\right)\right]\\&+\left[\frac{1}{\rho_0}\left(\frac{\partial\overline{\tau_s^y}}{\partial x}-\frac{\partial\overline{\tau_s^x}}{\partial y}\right)\right]\end{aligned} \tag{A.23}$$

which can be rewritten as

$$\beta\langle\overline{v}\rangle=\frac{1}{\rho_0}J(\bar{p}_b,H)+\boldsymbol{k}\cdot\nabla\times MFA+\boldsymbol{k}\cdot\nabla\times EMF+\frac{1}{\rho_0}\boldsymbol{k}\cdot\nabla\times\overline{\boldsymbol{\tau_s}} \tag{A.24}$$

where $\beta = \frac{\partial f}{\partial y}$, $\frac{1}{\rho_0} J(\bar{p}_b, H)$ is the Bottom Pressure Torque (BPT) term, while $\boldsymbol{k} \cdot \nabla \times MFA$, $\boldsymbol{k} \cdot \nabla \times EMF$, and $\frac{1}{\rho_0} \boldsymbol{k} \cdot \nabla \times \overline{\boldsymbol{\tau}_s}$ represent the contribution from the mean flow advection, eddy momentum fluxes and wind stress terms respectively. Similarly, the flat-bottom Sverdrup transport is computed using

$$\beta \langle \overline{v} \rangle = \frac{1}{\rho_0} \boldsymbol{k} \cdot \nabla \times \overline{\boldsymbol{\tau}_s} \tag{A.25}$$

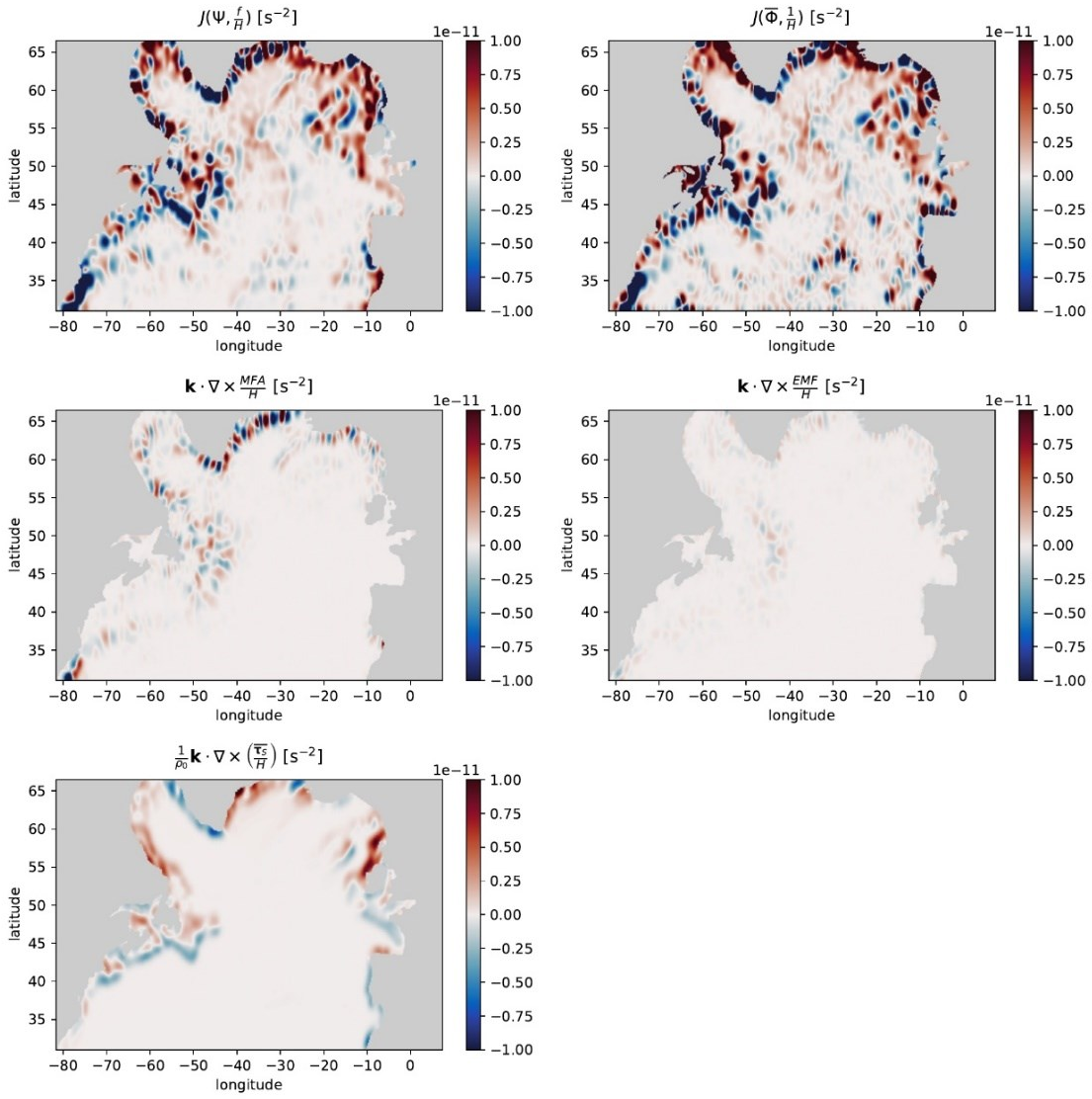

Figure A.1. The local vorticity budget based on the vertically-averaged momentum equations (see Eq. (A.21)), where Ψ is the mean barotropic streamfunction diagnosed from the VIKING20 nest component. All fields have been smoothed using a Gaussian filter with a standard deviation of 0.5 degrees both in longitude and latitude.

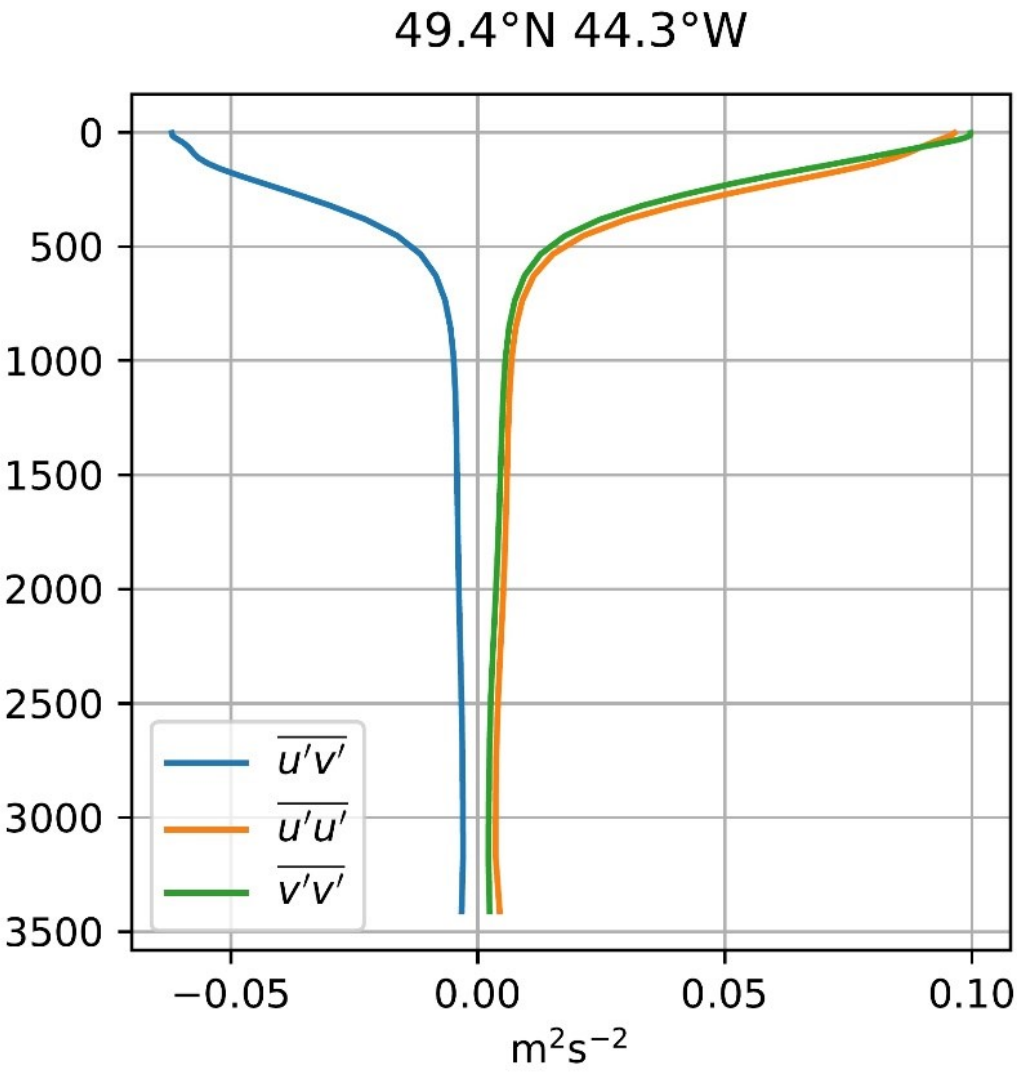

Figure A.2. The vertical profile of the horizontal eddy momentum flux terms at a location near the northwest corner where they play a role on the local vorticity budget (see Figure A.1). Shown are 50-year averages covering the analysis period 1960-2009.

APPENDIX B

MODEL SIMULATED TIDAL SURFACE ELEVATIONS, CURRENTS AND INTERNAL TIDES

The coupled circulation-ice model for the eastern Canadian shelf was presented in Chapter 4. Figure B.1 shows amplitudes and phases of the M_2 and K_1 surface elevations in the GSL, GoM-BoF, and ScS from model results in WithTide. The M_2 surface elevations in the GSL feature a cyclonic rotation of tidal waves with two amphidromic points, the major one located near the MI and a secondary one to the west of the Prince Edward Island. The amplitudes of M_2 reach more than 1.0 m in the SLRE. The K_1 tide rotates cyclonically around an amphidromic point to the southeast of the GSL. The K_1 amplitudes reach over 0.26 m over the Northumberland Strait and SLRE. The model simulated K_1 amplitudes are larger than observations at tidal gauges by up to 4 cm (Table 4.2), and this overestimation in the GSL is likely due to the cut off the St. Lawrence River channel near Saint Joachim in the model. The simulated M_2 elevations in the ScS and GoM-BoF demonstrate a cyclonic rotation around an amphidromic point over the Nantucket Shoals to the southwest of the GoM. The M_2 amplitudes monotonically increase from the outer GoM to the head of the BoF, reaching more than 6.0 m in the Minas Basin, about 2.0 m at the mouth of the BoF, and less than 0.5 m over the GeB, ScS and adjacent deep waters. The simulated K_1 amplitudes increase from the ScS to the upper BoF, reaching a maximum value of about 0.19 m. Overall, the M_2 and K_1 amplitudes and phases from WithTide in the GSL, GoM-BoF, and ScS agree well with the solutions of OTIS and previous studies (Xue et al. 2000; Lu et al. 2001; Dupont et al. 2002; Saucier et al. 2003).

Internal tides and internal gravity waves are generated in stratified waters by interactions between barotropic tidal currents and variable bottom topography (Garett et al. 2007), and play an important role in coastal ocean mixing (Sandstrom and Oakey 1995). Earlier studies revealed the internal tide generation over the northern flank of GeB where strong tidal currents, density fronts, and steep topography present (Marsden 1986; Loder et al. 1992; Brickman and Loder 1993; Lamb 1994; Dale 2003). Previous modelling studies demonstrated the existence of the internal tides southeastward of GeB with internal tide energy radiating offshore from the shelf break southeast of GeB (Chen et al. 2011). Kelly et al. (2016) also simulated internal tides radiating offshore southeast of GeB with a coupled-mode shallow-water model.

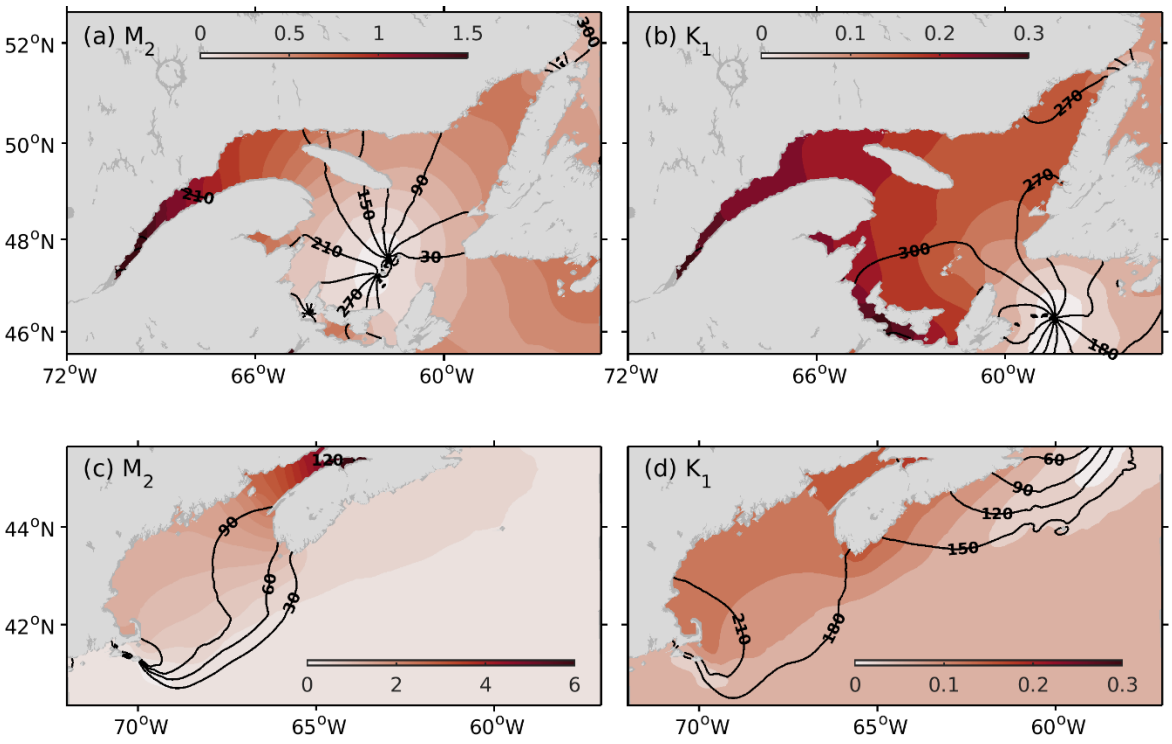

Figure B.1. Co-amplitudes (color image, in m) and co-phases (contours, in degree relative to the midnight GMT) of the two major tidal constituents M_2 (left) and K_1 (righ) obtained from model results in WithTide over the GSL and adjacent waters (upper row) and GoM-BoF and ScS (lower row). The contour intervals are 30° for phase and 0.10 m (0.03 m) for M_2 (K_1) amplitude in the GSL, and 0.25 m (0.03 m) for M_2 (K_1) amplitude in the GoM-BoF, respectively.

Figure B.2 presents distributions of the surface M_2 tidal current ellipses from BaroTide (blue) and WithTide (red). The results of the two simulations are similar over most of the model domain. Noticeable differences occur over shallow banks in the eastern ScS and the eastern GoM, and the largest differences appear in the deep waters to the southeast of GeB. These differences represent the importance of internal tides. Over the shelf edges of southern GeB and southwestern ScS, the M_2 surface currents have large amplitudes, and the major axes of the ellipses direct normal to the local isobaths. These are the conditions favoring the generation of internal tides (Baines 1973). The surface M_2 tidal currents from BaroTide are very weak in the deep waters beyond the 1000 m isobath, but decrease gradually from the shelf edge off the southeastern GeB to the deep water (the area in the black box in Figure B.2) in WithTide. This is consistent with the results of Katavouta et al. (2016).

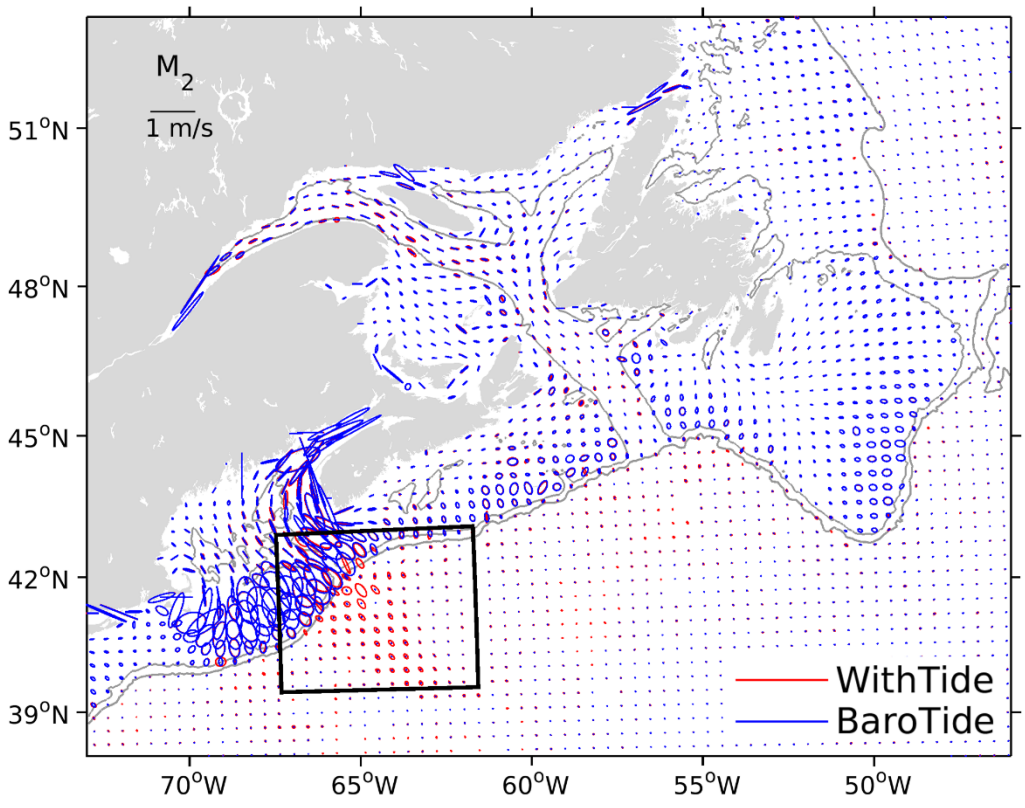

Figure B.2. Distributions of M_2 surface tidal current ellipses obtained by BaroTide (blue) and WithTide (red) simulations. Tidal current ellipses are shown at every 4^{th} (8^{th}) grid points along the latitudinal (longitudinal) direction. The contours are isobaths of 200 m and 1000 m, respectively.

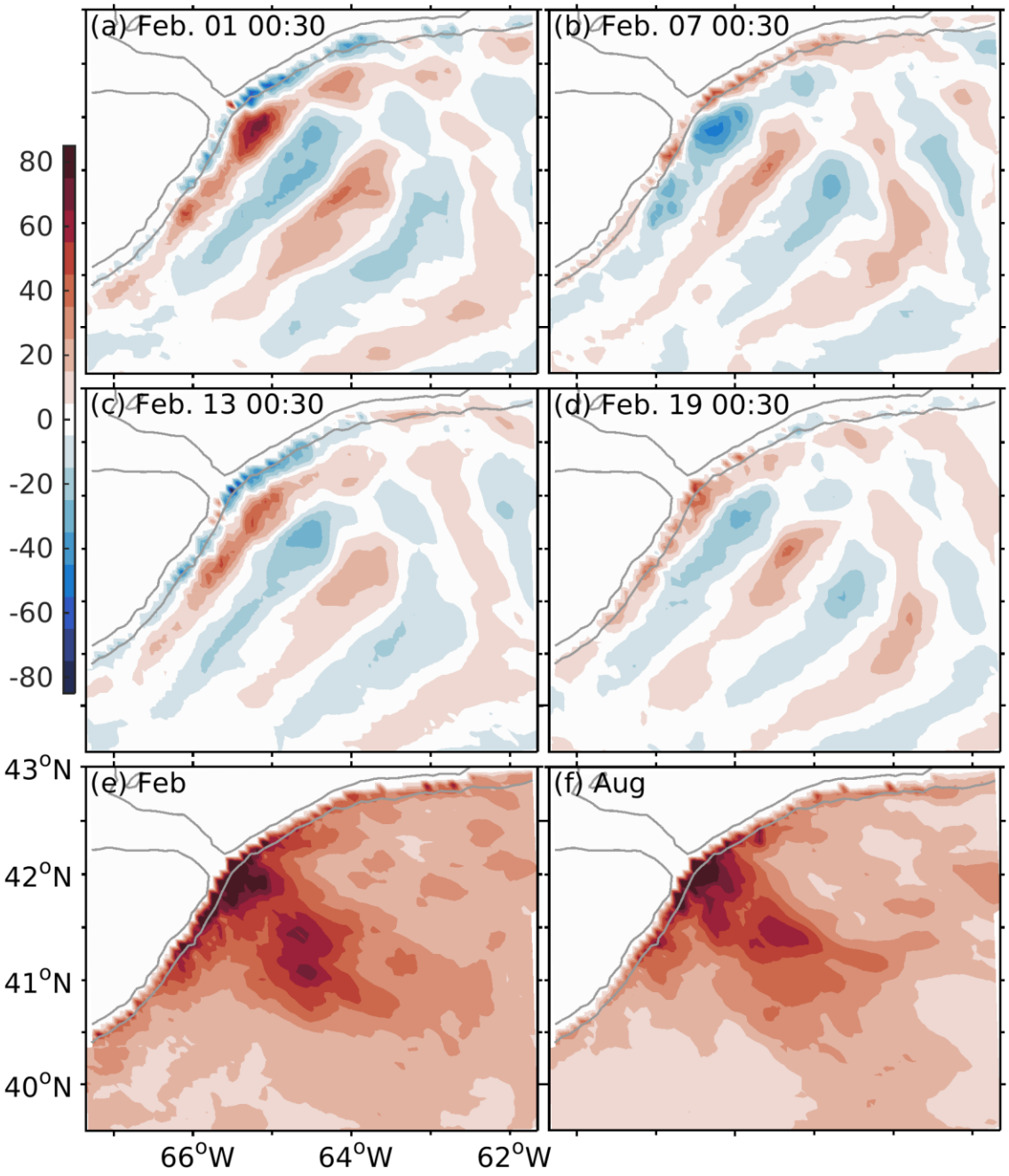

Figure B.3. Distributions of simulated isopycnal displacements (color shading, in m) in the black box (Figure A2) based on the simulation of WithTide at 500 m at the first hour of (a) February 1, (b) February 7, (c) February 13, and (d) February 19 in 2006, and the maximum amplitudes of isopycnal displacements during (e) February and (f) August 2006. Contours are isobaths of 200 m and 1000 m, respectively.

The internal tides in the boxed region in Figure B.2 are primarily generated on the shelf edge and propagate offshore. Figure B.3 presents distributions of internal tides over this region in terms of the isopycnal displacement at the mean depth of 500 m, calculated from deviations of hourly density profiles from the mean states (time-mean over the period) based on the results of WithTide in 2006. A 26-hour high-pass filter is applied to the density time series to remove the slowly changing signals, such as eddies and fronts. The spatial distribution in Figure B.3a shows a series of streaks, with amplitudes up to 80 m near the 1000 m isobath and averaged distance of about 65 km between adjacent troughs and peaks. The opposite patterns of peaks and troughs occur after 6 days (~11.5 M_2 cycle) at the first hour of February 7 (Figure B.3b), as well for distributions at February 4.13 and 4.19 (Figures B.3c and B.3d). In addition to the series of streaks parallel to the isobaths, there are streaks almost normal to the local isobaths over the northeastern part of this area, with relatively smaller magnitudes (up to 30 m) than those parallel to isobaths. The maximum isopycnal displacements in February 2006 (Figure B.3e) reach about 100 m over the shelf-edge adjacent to the mouth of the Northeast Channel of the GoM and large values of more than 60 m extend about 100 km southeastward into the deep water. This area with large isopycnal displacements corresponds well with the area with large amplitudes of surface currents of internal tides (Figure B.2). Large isopycnal displacements are also shown in August 2006 (Figure B.3f), indicating that internal tides in this area are generated year-round. Further studies are required to investigate the variability of the internal tides in this area due to the impact of the Gulf Stream as suggested by Kelly et al. (2016).

APPENDIX C

MODEL VALIDATION FOR THE GULF OF ST. LAWRENCE

C.1 Observational Data

Two hydrographic observation datasets are used in this model validation, and the two datasets are both interpolated onto model grids for the further analysis. The first type is a very high resolution (~1km) remote sensing dataset (https://podaac.jpl.nasa.gov/dataset/MUR-JPL-L4-GLOB-v4.1). Such dataset is produced by combining multiple available satellite and sub-skin SST observations with a wavelet based optimal interpolation approach at the Jet Propulsion Lab Physical Oceanography Distributed Active Archive Center. The second type is hydrographic profiles at four observational transects in the Gulf of St. Lawrence (GSL) (see Figure 5.1): BBA (in the northeastern GSL), MLO (in the northwestern GSL), IMA (in the southeastern GSL), and CAB (over Cabot Strait). Those observations (during 1999-2010) are retrieved from the Atlantic Zone Monitoring Program (AZMP) (meds-sdmm.dfo-mpo.gc.ca/isdm-gdsi/azmp-pmza/hydro/index-eng.html).

Observed daily mean air temperature from three meteorological stations were taken from the Environment Canada website (climate.weather.gc.ca/historical_data/search_historic_data_e.html). The three stations are station 7053KGR in the central GSL, 7051163 in the northern Gaspe Peninsula, and 8401335 in northwestern Newfoundland (see Figure 5.1). To examine the air temperature at various frequencies, the time series are decomposed by running averaging into three bands, the mean annual cycles, low frequency anomaly (with period longer than 30 days), and high frequency anomaly (with period shorter than 30 days). For an unfiltered time series Ψ_o, high frequency anomaly is obtained as the residual of running averaged Ψ_o with a window of 30 days. Ψ_o' (the low pass filtered Ψ_o)

is then averaged over years to have a mean annual cycle. The low frequency anomaly is obtained by subtracting the mean annual cycles from the Ψ_o'.

C.2 Model Validation

C.2.1 Ocean Temperature and Salinity

The performance of the modelled sea surface temperature (SST) in the GSL is validated against the high resolution (~1km) remote sensing dataset. Since the reliable SST is not available when the ocean is covered by sea-ice, the SSTs measured in December (beginning of the ice season) and April (end of the ice season) are used to validate the model performance in simulating the SSTs in winter (Figure C.1). In December, cold Arctic origin water (~0 °C) enters the Strait of Belle Isle (SBI) and flows along the northern coast, and the surface water in the northwestern GSL cools down faster than the other areas in the GSL due to shallower surface layer. The observed SSTs gradually increase equatorward to about 7 °C at the shelf break of the eastern Scotian Shelf. The simulated SSTs show a similar pattern but are relative warmer than observed values in the GSL and the Bay of Fundy. The largest differences (~2 °C) occur along the western coast of Newfoundland and northeastern coast of Nova Scotia. At the end of the ice season in April, near freezing (<0 °C) cold water continues entering the SBI and extends over the northeastern GSL. SSTs are still cold (~0 °C) in the GSL except for the northwestern GSL due to the polynya at the head of the Laurentian Channel and early opening of the ice cover (Wang et al., 2020b). The overestimated SST in the model could be partially attributed to the relatively warmer air temperature (~ 1.5 °C differences) in winter in the CFSR forcing than the observations (Figure C.4b).

To assess the model performance in simulating the 3D distributions of water temperature and salinity in the GSL, model results are compared with observed hydrographic profiles along the four transects during the period 1999-2010 (see Figure 5.1). The daily mean values from the model are selected when observations are available. For all the available data values, without applying averaging according to locations, the correlation coefficient and root mean square difference (RMSD) are calculated for observed and simulated hydrographic values along each transect, respectively.

The time-averaged hydrographic observations along the BBA transect over the northeastern GSL demonstrate a well-known three-layer structure (Banks 1966) in ice-free seasons (Figure C.2a and C.3a). The warm (>8 °C) and fresh (<32 psu) surface layer mainly represents the summer condition; the cold intermediate layer (CIL) with cold (<2 °C) and saltier (32 - 33 psu) waters below the surface layer and reaching 150 m depth; and a bottom layer with relative warm (~5 °C) and the saltiest (~34 psu) waters. The cold core of the CIL attaches to the northern coast of the GSL due to the strong winter convection along the northern coast and the Arctic origin cold inflow through the Strait of Belle Isle (Koutltonsky and Bugden 1991). The modelled hydrographic distributions (Figure C.2b and C.3b) have a very similar pattern as observations. Without time averaging, the observed and simulated hydrographic values have a correlation coefficient of 0.93 (0.86) and a RMSD of 1.41 (0.47) for temperatures (salinities) (Figure C.2c and C.3c). Nevertheless, the model obtains a warmer (up to 0.5 °C) and fresher (up to 0.3 psu) CIL, especially at the central part of the BBA. A low salinity anomaly at the surface near the northern shore, which is primarily attributed to freshening events in summer 2003 and 2005, is not simulated in the model.

Along the MLO transect, observations show a similar three-layer structure as along the BBA transect (Figure C.2d and C.3d). The distinct dome-shape thermocline is associated with the cyclonic Anticosti Gyre (Koutltonsky and Bugden 1991). The model well reproduces the basic patterns in observations. Overall, the observed and simulated hydrographic values have a correlation coefficient of about 0.92 for both temperatures and salinities. The RMSD is about 1.15 (0.65) for temperatures (salinities). The model discrepancies also exist. The model overestimates temperatures (~0.5 °C) in the CIL, and underestimates salinities for ~0.3 psu in the CIL and ~0.2 psu in the bottom layer. The model deficiencies in salinity are primarily associated with the variability in the near surface relatively fresh water masses (< 30 psu) (Figure C.3d and C.3f). The salinity variability is associated with the instability of the Gaspe Current which cannot be well resolved in this model with relative coarse horizontal resolution (~6 km in the GSL) (Sheng 2001).

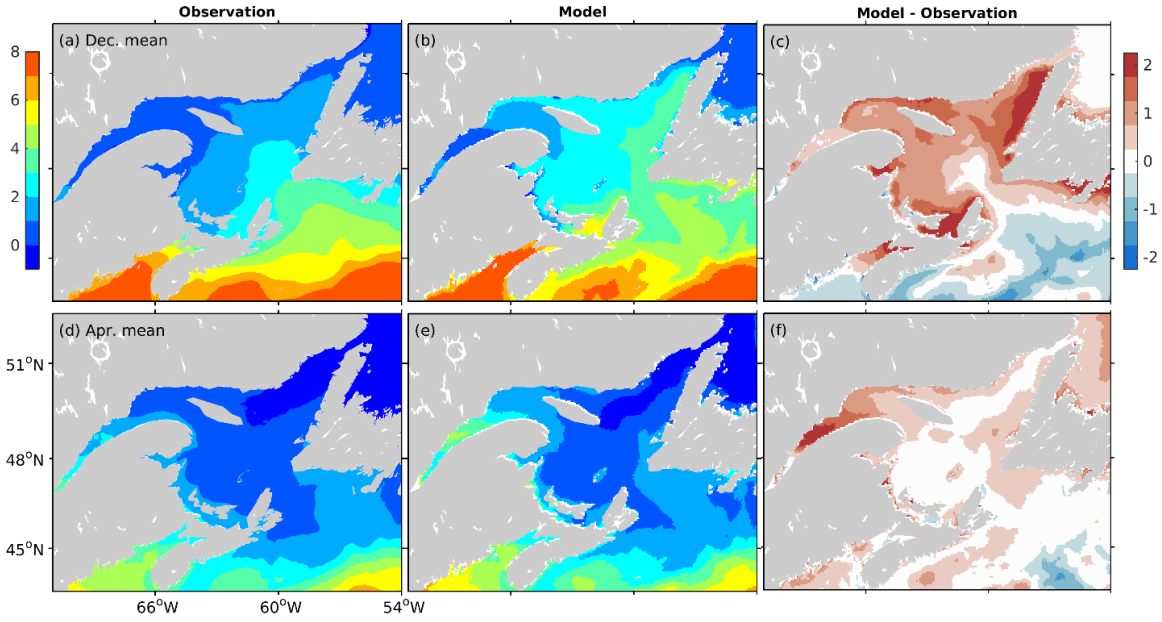

Figure C.1. Multi-year averaged (1998-2010) SST in the GSL in December (upper row) and April (lower row) from (from left to right) observations (based on GHRSST), the model, and the model minus observations.

Along the IMA transect, observations show a two-layer structure due to the relatively shallow (<100 m) bathymetry in this area (Figure C.2g and C.3g). The water column is strongly stratified by temperature due to summer heating, with surface temperatures over 15 °C and bottom temperatures below 0 °C. The low salinity water masses (<30 psu), due to strong freshwater runoffs in summer, is attached to the coast, and salty (>32 psu) water masses stay near the bottom. The model well simulates temperatures (Figure C.2g and C.2h) but overestimates the salinity of water masses near the coast by up to 2 psu (Figure C.3h and C.3i). The high salinity can be associated with the model underestimation of the coastal runoffs in this area. The observed and simulated hydrographic values have a correlation coefficient of 0.94 (0.75) and a RMSD of 1.24 (0.68) for temperatures (salinities) (Figure C.2i and C.3i).

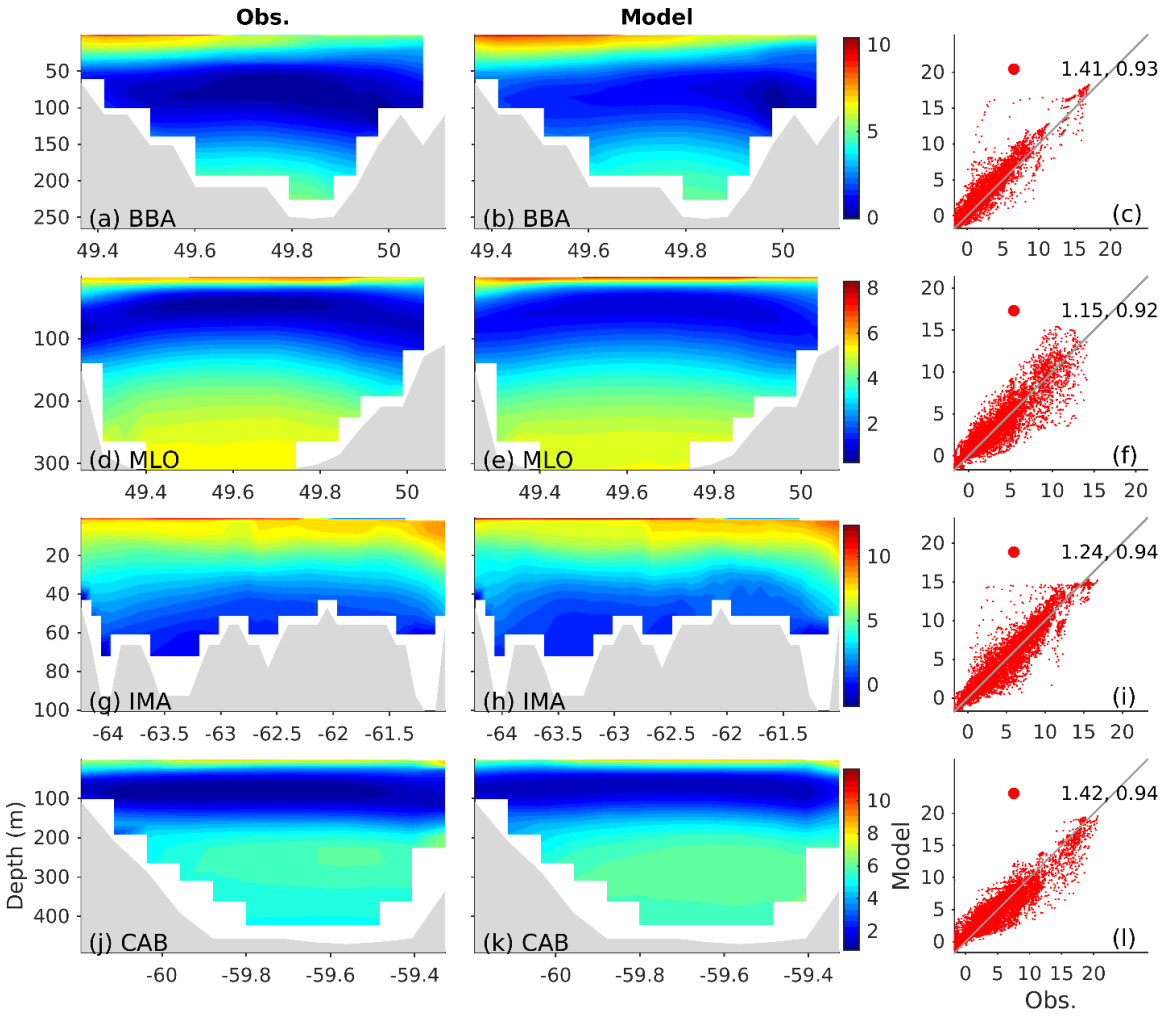

Figure C.2. Potential temperatures (in °C) from AZMP observations (left) and model results (center) at transects of, from top to bottom, BBA, MLO, IMA, and CAB. The x-axis is latitude for BBA and MLO, and longitude for IMA and CAB, respectively. The AZMP data collected during 1999-2010 are interpolated onto mode grids, and the daily mean model results are selected when observations are available. Averaging is applied to data values at the same location. Scatter diagrams (right) of observed vs. simulated temperature without averaging. Numbers in the legend are RMSD and correlation coefficient.

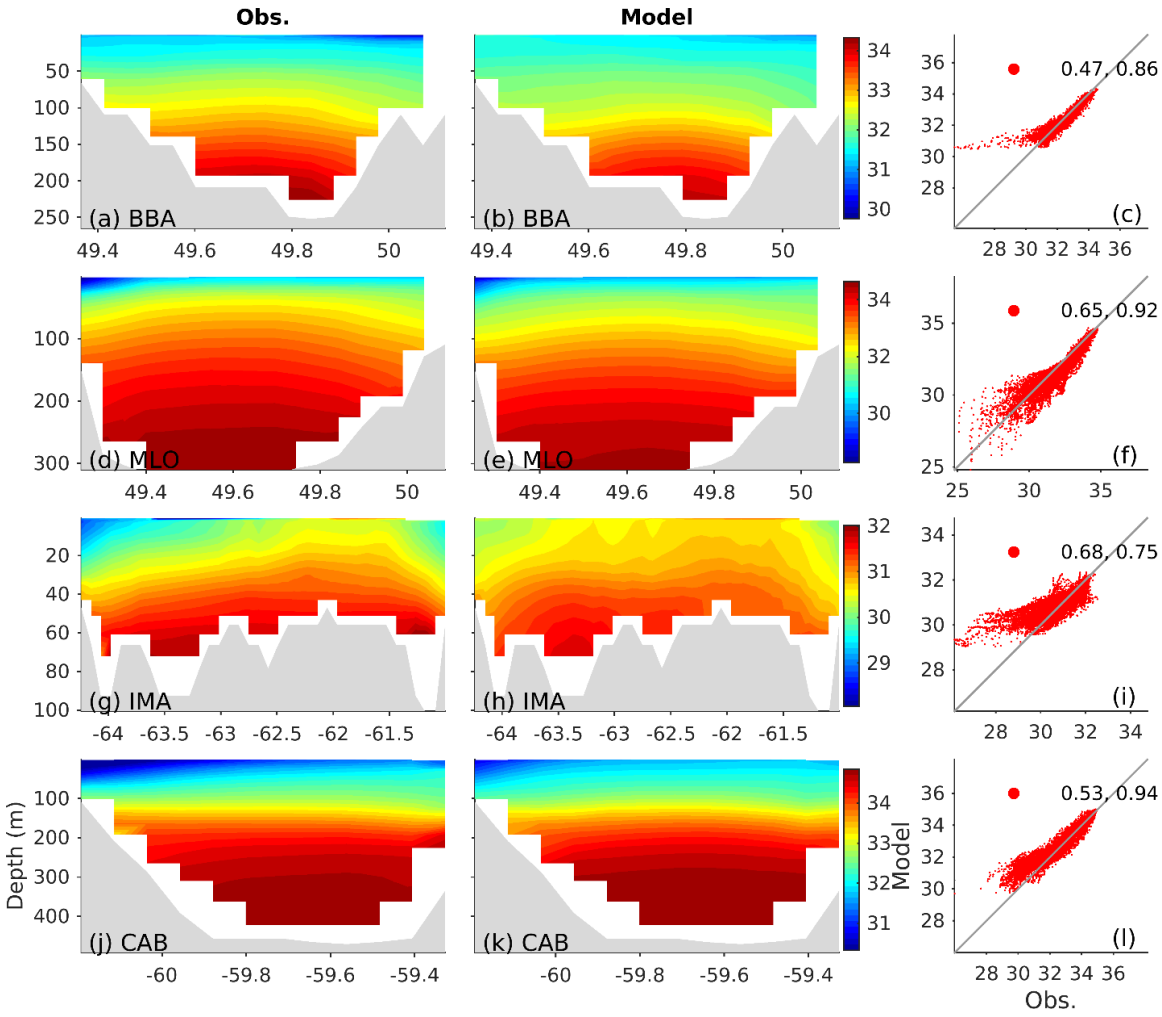

Figure C.3. Same as Figure C.2 but for salinity (psu).

Along the CAB transect, observations show a similar three-layer structure as along the BBA transect (Figure C.2j and C.3j). The bottom layer features a warm core at ~ 270 m depth, where the water mass is a mixture of the warm and salty North Atlantic Central Water and the cold and fresh Labrador Current Water (Gilbert et al. 2005). The observed and simulated hydrographic values have high correlation coefficients around 0.94 for both temperatures and salinities. The RMSD is about 1.42 (0.53) for temperatures (salinities) (Figure C.2l and C.3l). It should be noted that the coupled model overestimates the temperature by ~0.4 °C in the CIL and ~0.2 °C in the bottom layer. The salinity of the outflow, near surface on the western side of CAB, is underestimated in the model by up to 1 psu, which is similar in the IMA.

In general, the coupled ice-ocean circulation model reproduces reasonably well the basic patterns of the observed hydrography in the GSL, with relatively high correlation coefficients and low RMSDs using the in-situ hydrographic observations along the four transects in the GSL.

C.2.2 Air Temperature

Air temperature was found to play a very important role in determining the sea ice variability in the GSL (Drinkwater et al. 1999). To examine the accuracy of air temperature from the CFSR as external forcing, the air temperatures used to drive the model are compared to observations at the three representative stations in the GSL (Figure 1). The three stations are station 7053KGR in the central GSL, 7051163 on the northern Gaspe Peninsula, and 8401335 in northwestern Newfoundland.

Figure C4 presents time series of daily mean air temperatures from the observations (red line) and the CFSR fields (blue line) during 1996-2010. At station 7053KGR in the central GSL (Figure 5.1), the observed air temperatures show an annual cycle with large seasonal variability from ~18 °C in summer to ~-6 °C in winter. The annual cycle in CFSR has a high correlation coefficient (0.98) with observed, but is up to 1.5 °C warmer than observed values in winter with a RMSD of 1.02 °C. The observed low frequency anomaly has a range from -4 °C to 3 °C, and is closely followed by that in the CFSR with a RMSD of 0.40 °C and a correlation coefficient of 0.95. The observed high frequency anomaly, largely contributed by storms and other vigorous synoptic phenomena, has a substantial range from -12 °C to 10 °C. The performance of the CFSR at high frequency anomaly is poorer than that in the other bands, which may be limited by its relative coarse horizontal resolution (1/3°) to represent highly nonlinear synoptic phenomena. Overall, the air temperature in the CFSR has a good agreement to the in-situ observations at station 7053KGR with a RMSD of 1.86 °C and correlation coefficient of 0.98 (unfiltered time series). At the other two stations in the northern GSL, the CFSR also has a satisfactory performance in terms of RMSDs and correlation coefficients in all bands (Table C.1).

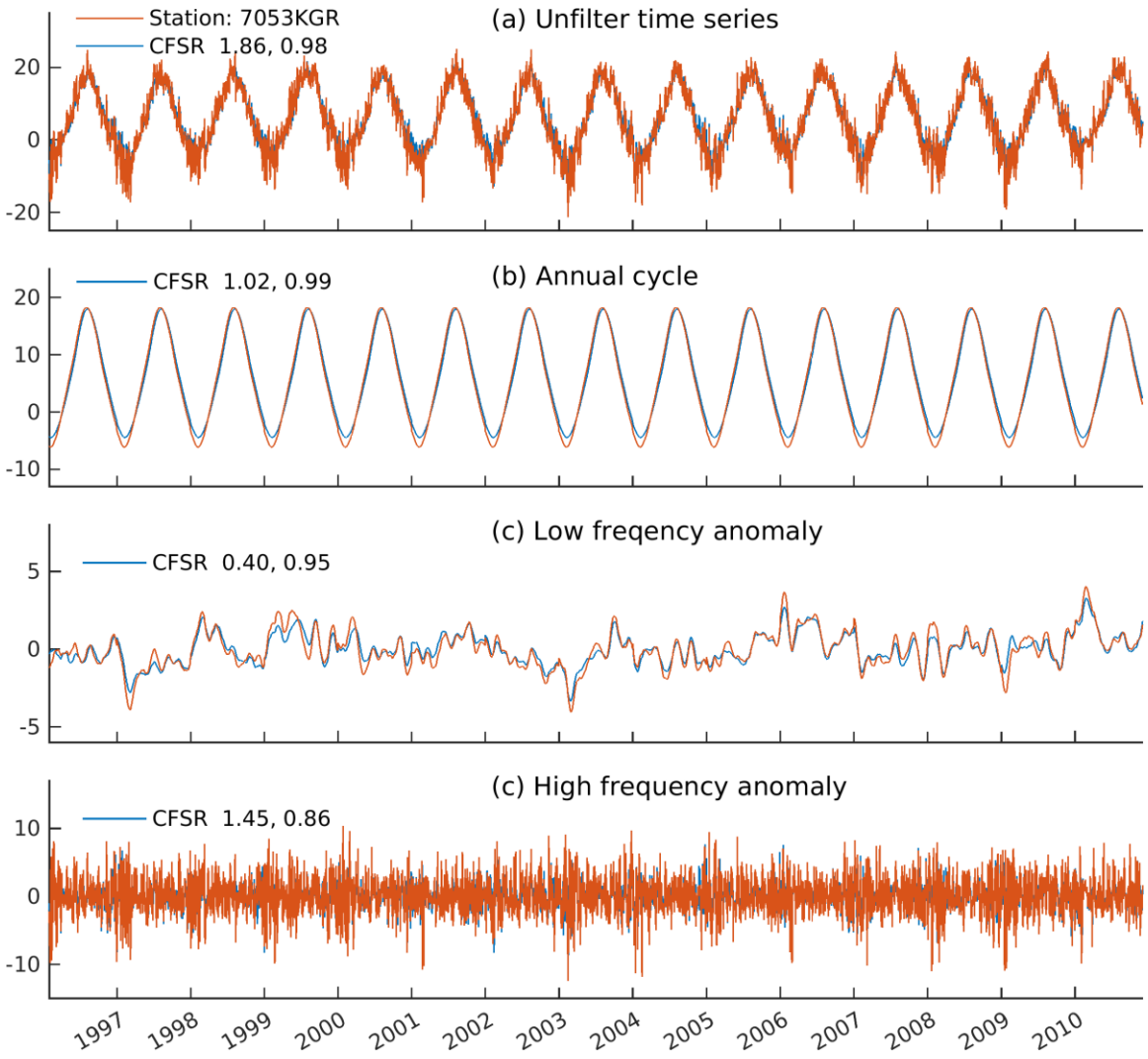

Figure C.4. Time series of daily mean air temperatures (a) from the CFSR (blue) used in the model and observed (red) at meteorological station 7053KGR. The numbers in legends are RMSDs and correlation coefficients for the CFSR air temperature in comparison with observed. Filtered time series consist of (b) annual cycles, (c) low frequency anomaly, and (d) high frequency anomaly.

Table C.1. RMSDs (°C) and correlation coefficients (in brackets) for the CFSR air temperature in comparison with observed.

	Stations		
	7053KGR	7051163	8401335
Unfiltered	1.86 (0.98)	2.54 (0.98)	2.56 (0.98)
Annual cycle	1.02 (0.99)	1.56 (1.00)	1.72 (1.00)
Low freq. anomaly	0.40 (0.95)	0.53 (0.92)	0.45 (0.95)
High freq. anomaly	1.45 (0.86)	1.86 (0.85)	1.80 (0.83)

C.2.3 Seasonal Cycle of Sea-ice in the Gulf of St. Lawrence

The mean seasonal cycle (over the years 1998–2010) of the observed and simulated sea-ice area and volume for the four subregions and the whole GSL are shown in Figures C.5. Those mean seasonal cycle and the associated standard deviation are computed from monthly mean of each year. In the GSL, the observed sea-ice area starts to build up in December in the northwestern (NW) subregion. The sea-ice area increases rapidly and reaches its maximum in March in every subregion. The sea-ice area retreats gradually, until completely gone in the NW subregion in April, in the southwestern (SW) and southeastern (SE) in May, and in the northeastern (NE) in June. In comparison, those seasonal cycles are well simulated in both mean and variance, especially in the SW and SE subregions, but slightly overestimated in mean values in the NW and NE subregions from January to March.

Similar patterns are shown in the observed sea-ice volume. However, the maximum sea-ice volume is reached in March in the NE, SW, and SE subregions and the whole GSL, respectively. As a result, the sea-ice volume draws down faster than its growth. In comparison, the simulated sea-ice volume well follows the observed seasonality but has considerable deficiencies in magnitudes. The sea-ice volume is well simulated in the NW and NE subregions, except for the overestimated February mean in the NW subregion and the underestimated means in the NE subregion since March. The sea-ice volume in the SW and SE subregions are generally underestimated in the means. As a result, the overall

simulated sea-ice volume is generally less than observed. Model deficiencies, and more details in the sea-ice spatial distribution and interannual variability are discussed in Section 5.3.

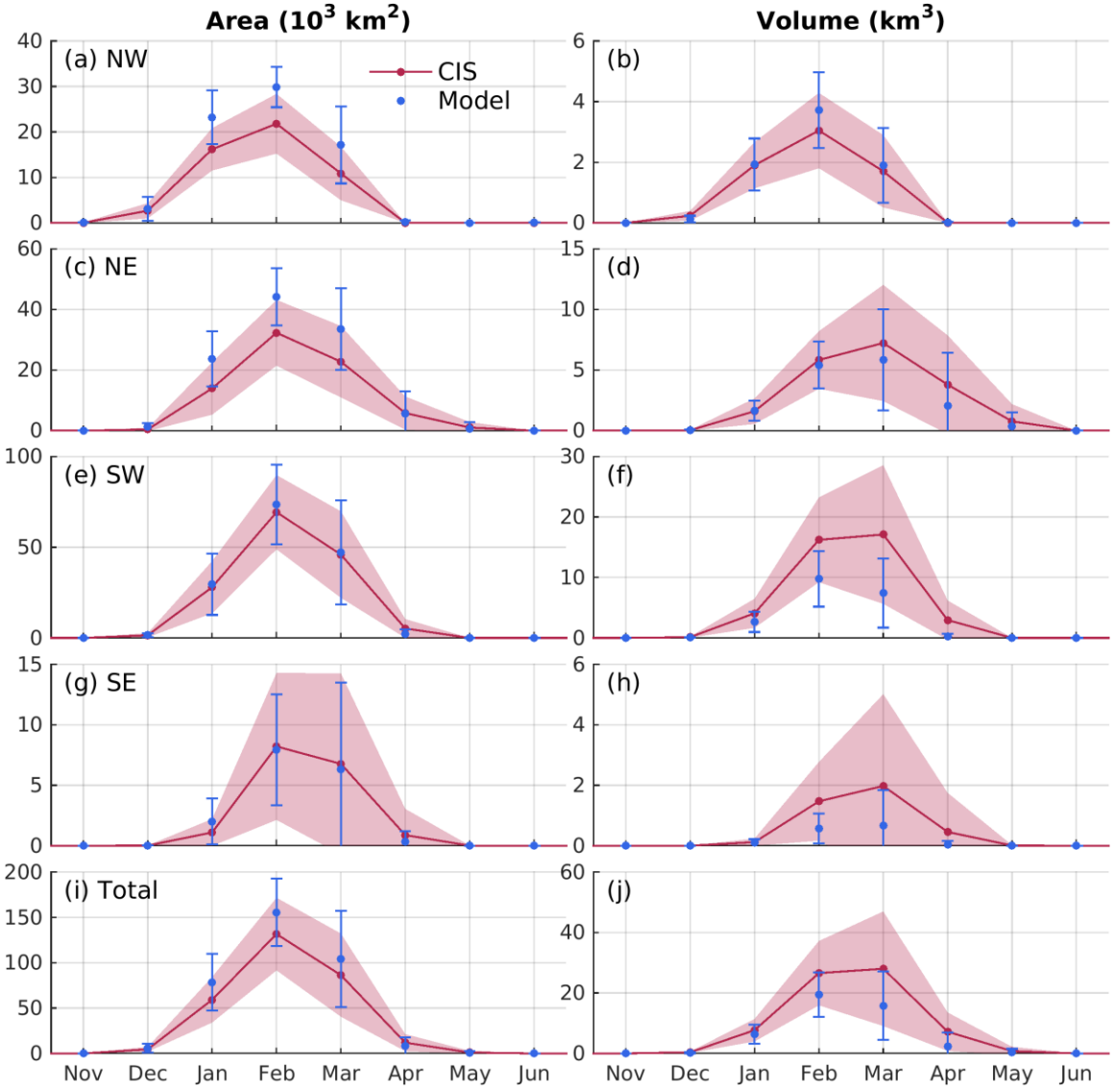

Figure C.5 Mean seasonal cycle (±1 standard deviation) of regional-integrated sea-ice area (left) and volume for the years 1998-2010 based on the CIS (red) and the model (blue) in the (from top to bottom) NW, NE, SW, SE subregions, and the whole GSL.

APPENDIX D

NUMERICAL EXPERIMENT WITH THE SEA-ICE OPEN BOUNDARY FORCING

D.1 Model Experiment

The Gulf of St. Lawrence (GSL) receives sea-ice import from the Labrador Shelf with a mean volume of 4.3 km^3 annually in the model (denoted as normal run (NR) in Appendix D) described in Section 5.2 (Figure 5.6). Such sea-ice transport is only contributed by the sea-ice generated on the Labrador Shelf south of the northern open boundary of the model (~54.5°N) (Figure 5.1), since the open boundaries are closed for the sea-ice in NR. The simulated sea-ice volume in the northeastern GSL in NR generally agrees with the Canada Ice Service (CIS) data, except for the underestimation in NR during late winter (after February) (Figure 5.5b). Particularly, in winter 2004, the simulated sea-ice volume in the northeastern GSL in NR is up to 12 km^3 less than that in the CIS in March and remains less than the CIS until May. However, the simulated sea-ice volume in the northeastern GSL in NR is very close to the CIS in winter 2005. One possibility is that this discrepancy can be explained by the flux of ice through the northern boundary that is missing in NR. As we show below, however, allowing for ice transport through the northern boundary does not improve the model performance in the northeastern GSL in 2004.

To examine the contribution of the sea-ice transport through the northern open boundary of the model domain, a numerical experiment with sea-ice open boundary forcing (denoted as WithIceOBC) is applied with the same model settings as NR, except for the sea-ice open boundary condition. Instead of closed sea-ice open boundary in NR, the sea-ice concentration and thickness are introduced at the northern open boundary in WithIceOBC,

using a flow relaxation scheme (Engedahl 1995) within a 10-grid wide relaxation zone. The sea-ice velocity normal to the northern open boundary is set equal to that at the adjacent grid point to its south if the latter is not ice free. Otherwise, the normal velocity of the sea-ice equals the ocean current velocity (Rousset et al. 2015).

The sea-ice concentration and thickness of the northern open boundary forcing are gridded from the CIS data with the same scheme described in Section 5.2.2. Note that, since the snow thickness is not available in the CIS data, the snow thickness is zero in the sea-ice open boundary forcing. WithIceOBC is integrated for eight months from November to June, initialized from the NR state at 00:00 UTC on November 1st of the year 2003 and 2004, respectively. Thus, the contributions of the sea-ice open boundary forcing are evaluated by the difference of the simulated sea-ice fields between WithIceOBC and NR.

D.2 Contributions of the Sea-ice Open Boundary Forcing

In 2004, the observed sea-ice thicknesses start to build up in February over the inner Labrador Shelf (see Figure D.2), with a significant volume of sea-ice clogging the SBI (Guard 2004). The sea-ice thickened significantly in March, with monthly mean thickness up to ~0.9 m over the inner Labrador Shelf and the SBI. Thick ice (>0.6 m) spreads over a large area of the northeastern GSL. In April, when the ice cover retreats in general, thick ice (>0.6 m) extending from the northern boundary remains over the inner Labrador Shelf. For the simulated sea-ice thickness, WithIceOBC well represents the ice thickness in January and February, and simulates the thickening of ice over the inner Labrador Shelf in March and April that is missing in NR. Clearly, the sea-ice open boundary forcing plays a very important role in the sea-ice volume in late winter (after February) in 2004 over the Labrador and Newfoundland Shelf. The sea-ice volume transport into the northeastern GSL through the SBI is also higher in WithIceOBC than NR in 2004 (Figure D.3a). However, in comparison with CIS, the simulated sea-ice thicknesses in WithIceOBC are underestimated in March and April away from the northern boundary over the southern Labrador Shelf and the northeastern GSL.

The model results for the year 2005 are shown in Figures D.4 and D.5. The observed sea-ice cover in January and February 2005 extends further to the outer shelf of the Labrador and Newfoundland Shelf with higher concentration and thickness than in 2004. In March, the observed ice thicknesses over the inner Labrador Shelf and the northeastern GSL are up to ~50 cm thinner than that in 2004. In May, the observed sea-ice cover over the Labrador and Newfoundland Shelf retreats further north in 2005 than in 2004. The simulated sea-ice concentration and thickness in WithIceOBC demonstrate the significant contribution of the sea-ice open boundary forcing over the Labrador and Newfoundland Shelf in March and April, which is consistent with that in 2004. The simulated ice volume transport through the SBI is increased by ~2.4 km^3 in March in WithIceOBC comparing to that in NR (Figure D.3b).

In general, the sea-ice open boundary forcing becomes the major source of the sea-ice over the Labrador and Newfoundland Shelf during late winter (after February), when the ocean surface often starts to receive net downward heat flux at similar latitudes in the GSL (Figure 5.7c). This sea-ice origin from north gradually melts along its southward voyage, especially in late winter, when the surface ocean is warming up. Only a small portion of this ice can go through the SBI and contribute to the sea-ice volume in the northeastern GSL. Comparing to simulated transport in NR, such north origin transport accounts for an additional 0.45 km^3 in 2004 and 2.40 km^3 in 2005, respectively (Figure D.3). As a result, the Root Mean Square Difference (RMSD) for the simulated ice volume in the northeastern GSL during the years 2004-2005 is slightly reduced in WithIceOBC than in NR (Figure D.6). On the other hand, the sea-ice open boundary forcing does not show noticeable impact on the simulated sea-ice in the other subregions of the GSL. The results suggest that the sea-ice open boundary only has negligible contribution to the sea-ice simulated in the GSL overall, except for the northeastern GSL in late winter. It is notable, however, that specifying sea-ice on the northern open boundary is not able to account for the discrepancy between the model and the CIS data in 2004 in the NE subregion of the Gulf (Figure D.4).

It should be noted that the net thermodynamic contribution of the sea-ice on the Labrador Shelf often turns negative from March due to increasing air temperature, which is clearly shown in NR (e.g., Figure D.2g, k, and p). The simulated sea-ice in WithIceOBC shows a

decreasing ice thickness from north to south on the Labrador Shelf in March and April, as those north origin sea-ice melts on the way. Such a pattern on the Labrador Shelf is consistent among simulated sea-ice in WithIceOBC in 2004 and 2005, and observed sea-ice in 2005 (Figure D.2 and D.5). By contrast, the observed sea-ice in 2004 well maintains its thickness on the inner shelf from the northern boundary to the Newfoundland coast in March and April (Figure D.2i and m). Since neither model run captures such a pattern, there must be some processes to compensate the ice melting that do not apply, even in WithIceOBC.

Indeed, the model has deficiency due to simplified sea-ice processes in this version of the LIM2 and imperfect forcings. Further studies are required to understand the sea-ice distribution on the Labrador and Newfoundland Shelf. For example, massive icebergs are widely spread over the Labrador and Newfoundland Shelf in winter, but the impact of icebergs on the sea-ice distribution in this area is unknown.

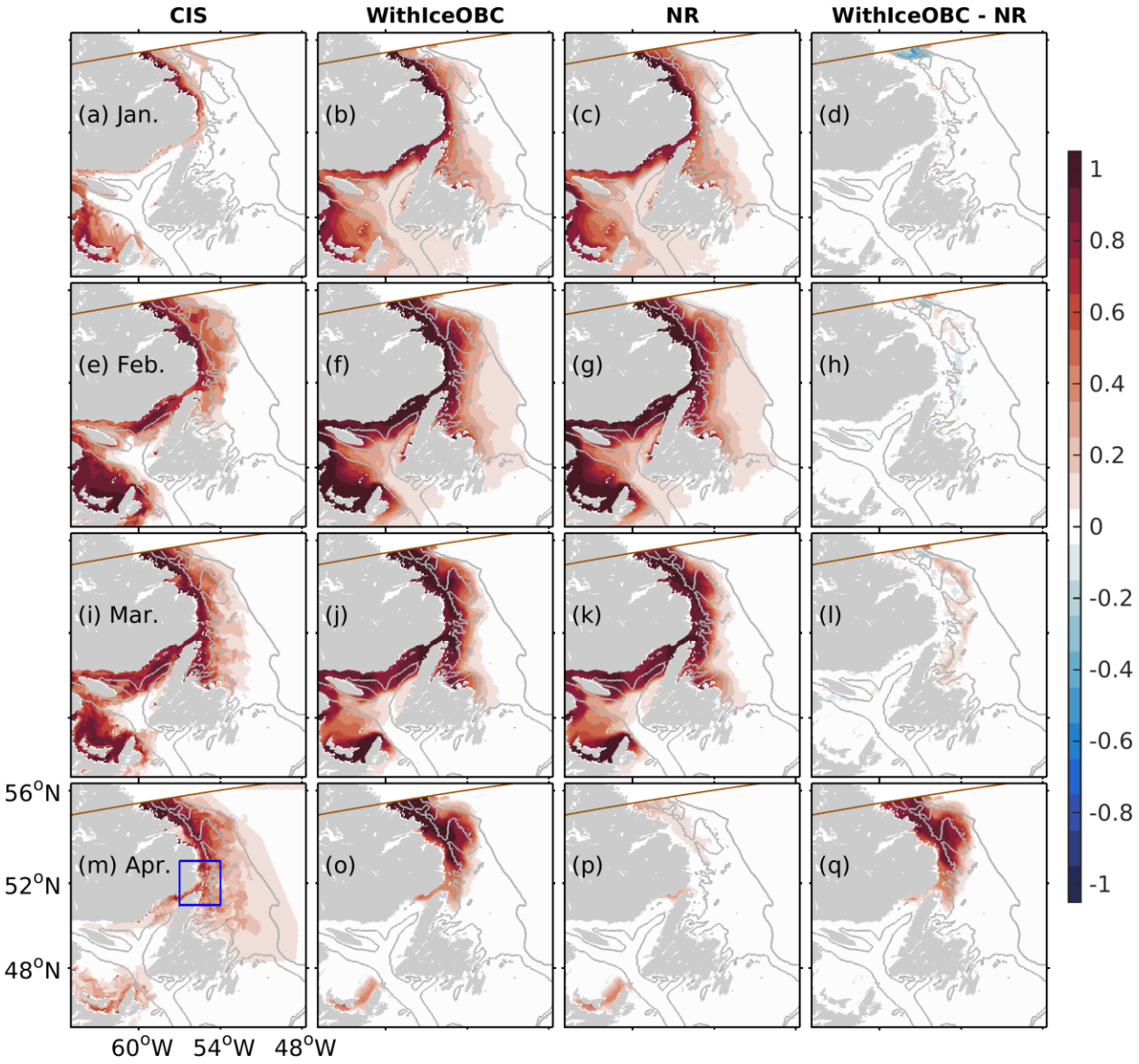

Figure D.1. Sea-ice concentrations in the GSL and Labrador and Newfoundland Shelf in (from top to bottom) January, February, and March in 2004 based on (from left to right) observations (based on the Canadian Ice Service charts), WithIceOBC, NR, and WithIceOBC minus NR. Black contours are isobaths of 200 m and 1000 m, respectively. The red line represents the north boundary of the model domain. The blue box is the vicinity of the SBI between 51°N-53°N and 53°W-56°W.

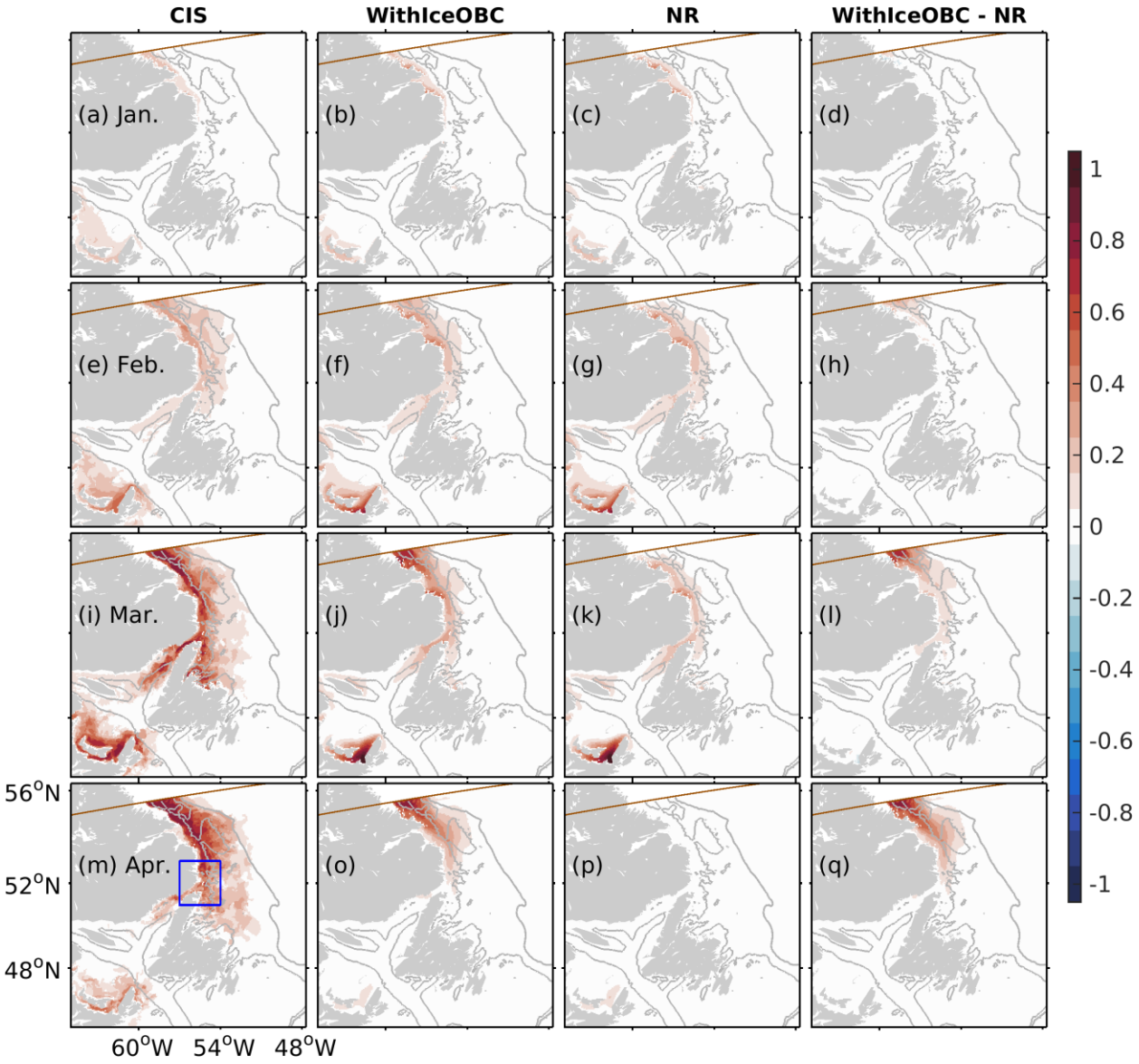

Figure D.2. Same as Figure D.1 except for sea-ice thicknesses (m).

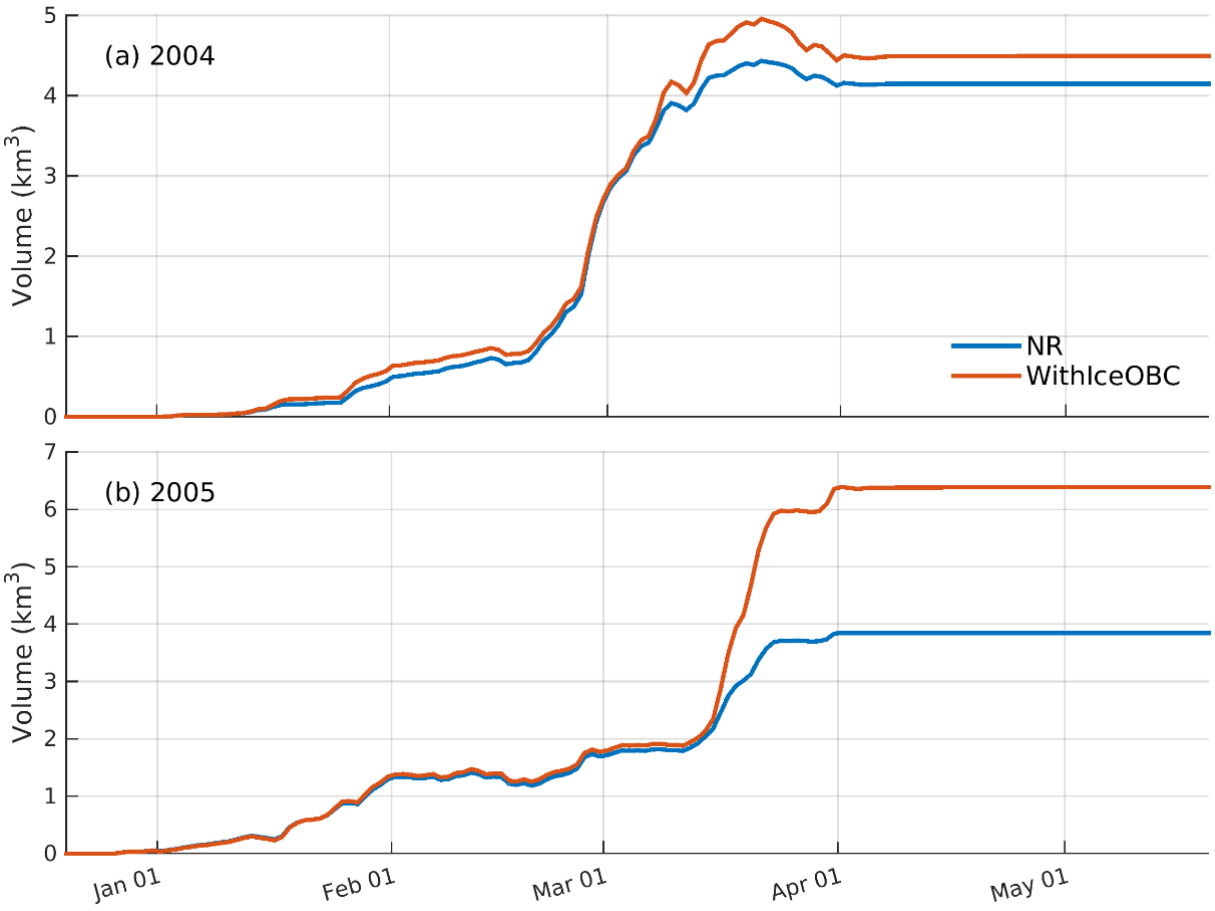

Figure D.3. Daily time series of accumulated sea-ice volume transport into the northeastern GSL through the SBI simulated in NR (blue) and WIthIceOBC (red) from January to May in (a) 2004 and (b) 2005.

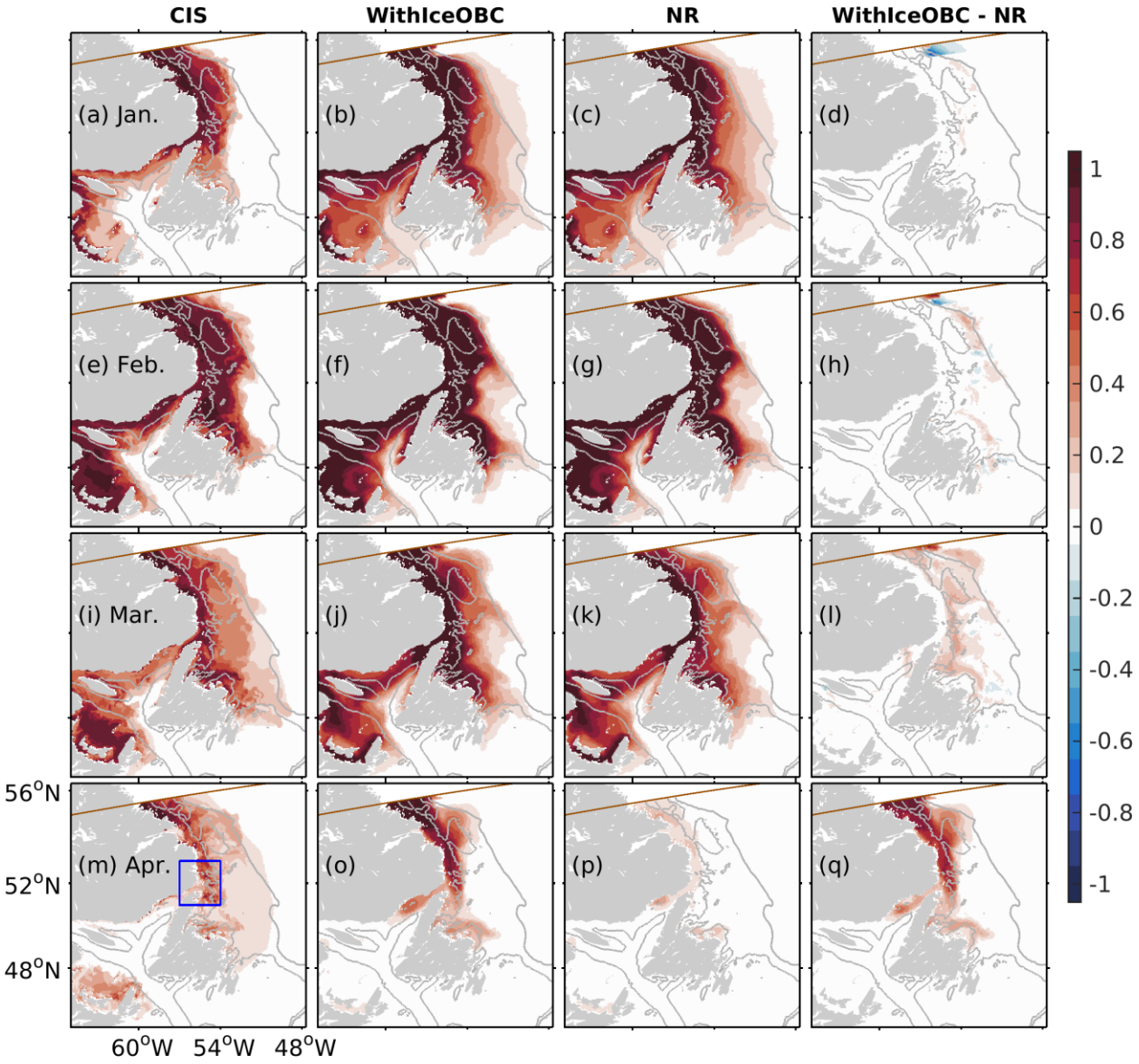

Figure D.4. Same as Figure D.1 except for the year 2005.

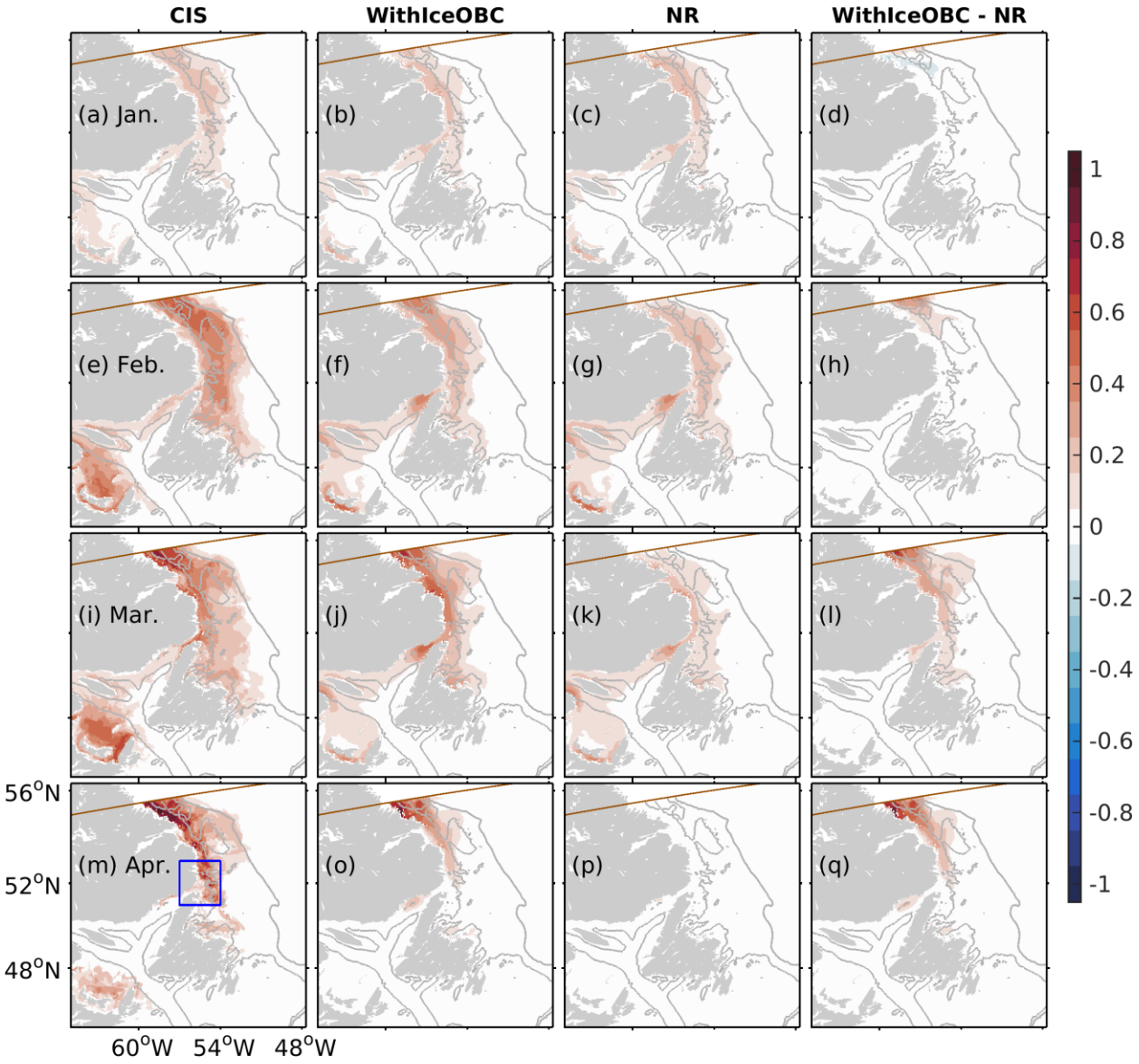

Figure D.5. Same as Figure D.4 except for sea-ice thicknesses (m).

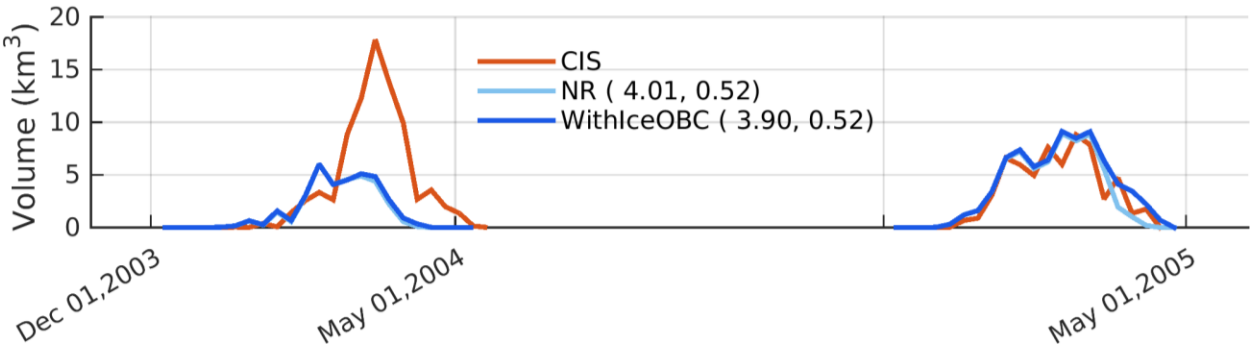

Figure D.6. Time series of weekly-mean regional-integrated sea-ice volume (km^3) in the northeastern GSL for the years 2004-2005 based on the CIS (red), NR (cyan), and WithIceOBC (blue). Numbers in the bracket are the RMSD and the correlation coefficient.

D.3 Icebergs in the Vicinity of the Strait of Belle Isle

The Labrador Shelf and upper continental slope are well known as 'Iceberg Alley', with 500 to 2500 icebergs transported southeastwards annually (Murray 1969). Those icebergs, calved off glaciers in Greenland and Baffin Island (Marsh et al. 2015; Marson et al. 2018), are driven by winds and currents over a long distance equatorward. Those icebergs can interact with seabeds, leaving scattered pits and ploughmarks on the Labrador Shelf. Eventually, icebergs break up and melt completely. The melt waters from the iceberg can result in surface buoyant plumes, affecting local stratification and dynamics (Yankovsky and Yashayaev 2014). Studies in Antarctica suggest iceberg dynamical forcing effects on sea-ice, as the iceberg movement induces sea-ice ridging in its direction of motion and creates open water on the other side favoring frazil ice formation (Hunke and Comeau 2011). However, little is known about the role of icebergs in local sea-ice thermodynamics production, sea-ice rheology, and sea-ice transport on the Labrador Shelf and the SBI, and icebergs are not simulated in the model used in this thesis study. Note that, the icebergs are not explicitly included in the CIS charts for sea-ice concentration and thickness, although their indirect effect is obviously present. Thus, the comparison in Section D.2 compares the simulated sea-ice without any account taken for icebergs to the observed sea-ice with iceberg impact.

The potential impact of icebergs is roughly estimated based on the iceberg counts inside the GSL and over the vicinity of the SBI, between 51°N-53°N and 53°W-56°W (the blue box in Figure D.1m). The iceberg counts are manually digitized from daily observation charts for iceberg counts at one degree resolution over the Labrador and Newfoundland Shelf (iceweb1.cis.ec.gc.ca/Archive). This dataset covers the years 2004-2020, thus the daily charts for January to May in 2004-2010 are analyzed. Note that, the volume of ice trapped in icebergs is not available, thus the estimation based on iceberg counts is still preliminary.

Most of the observed icebergs are found on the inner Labrador Shelf and near the eastern Newfoundland coast. Small number of icebergs occasionally are found inside the GSL, transported through the SBI, and always stay in the northeastern GSL until they eventually disappear. Monthly mean iceberg counts (±1 standard deviation) in the GSL and the vicinity of the SBI (orange dots) during January-May of 2004-2010 are shown in Figure D.7. The iceberg counts generally stay low in January and February; start to increase in March; and continue to rise in April and May with large variations. Large variations in iceberg counts may indicate active iceberg advection and/or break up. The largest daily iceberg counts reached 229 on May 1st, 2004. The monthly mean sea-ice volume in the northeastern GSL from the CIS and NR are shown in Figure D.7. The simulated sea-ice volume in NR often exhibits a deficit, to the CIS, in the late winter after February, which often occurs with large iceberg counts. Winter 2005 is a bit special, with least iceberg counts from March to May, when the simulated sea-ice volume agrees very well with observations.

Indeed, the relationship between the iceberg presence in the vicinity of the SBI and the sea-ice distribution in the northeastern GSL is still unclear. Further study is needed to examine the impact of the iceberg on the sea-ice thermodynamics production, rheology, and transport in the Labrador Shelf.

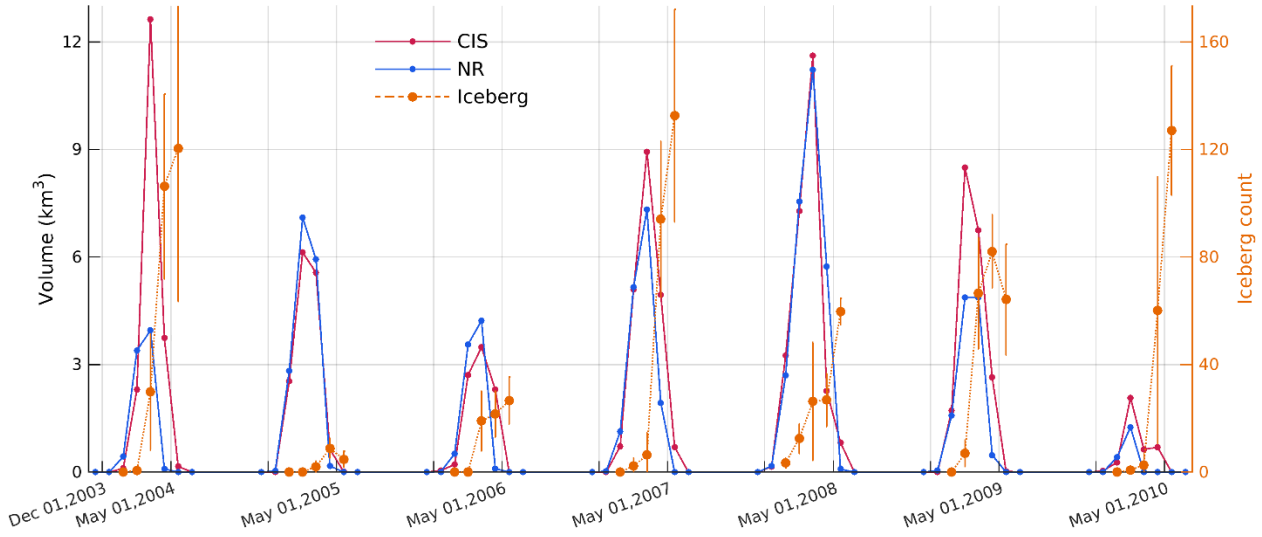

Figure D.7. Time series of monthly mean regional-integrated sea-ice volume (km^3) in the northeastern GSL for the years 2004-2010 based on the CIS (red) and NR (blue). Monthly mean iceberg counts ±1 standard deviation (orange) for icebergs in the GSL and vicinity of the SBI during January to May in the years 2004-2010.

APPENDIX E

NUMERICAL EXPERIMENT WITH DIFFERENT RUNOFF FROM ST. LAWRENCE RIVER

E.1 Monthly-Mean Runoff of the St. Lawrence River

To determine the impact of the interannual variability of runoff from the St. Lawrence River (SLR) in the sea-ice conditions in the GSL, a sensitivity experiment is conducted using a numerical experiment with monthly-mean SLR runoff rather than the climatology runoff. All the other model settings are the same as in Chapter 5. Time series of monthly-mean runoffs of the SLR during the period 2006-2010 is obtained from catalogue.ogsl.ca. This monthly-mean runoff is estimated using an empirical regression model based on the observed water-levels at Neuville near the mouth of the SLR (Bourgault and Koutitonsky 1999). Here, the sensitivity experiment is denoted as control run (CR), in contrast to the normal run (NR) described in Section 5.2. CR is initialized from the NR state at 00:00 UTC on January 1st, 2006 and integrated for the five years 2006-2010 when significant changes in the winter ice condition occurred (Figure 5.11). The last four-year results are used in the analysis. The monthly SLR runoffs during 2006-2010 are presented in Figure E.1 along with the climatology used in NR (Gauge Clim.). Significant interannual variability in the runoffs is demonstrated, with up to 40% differences in a specific month. It should be noted that the runoffs from the monthly data are generally larger than the Gauge Clim., with about 30% increase in magnitudes. It may result from the different origin of the data sources, where the Gauge Clim. is derived from gauges located 160-280 km upstream away from the SLR mouth. Thus, the results of CR not only represent the impact of interannual variability, but also the overall increase in the magnitude of the runoff.

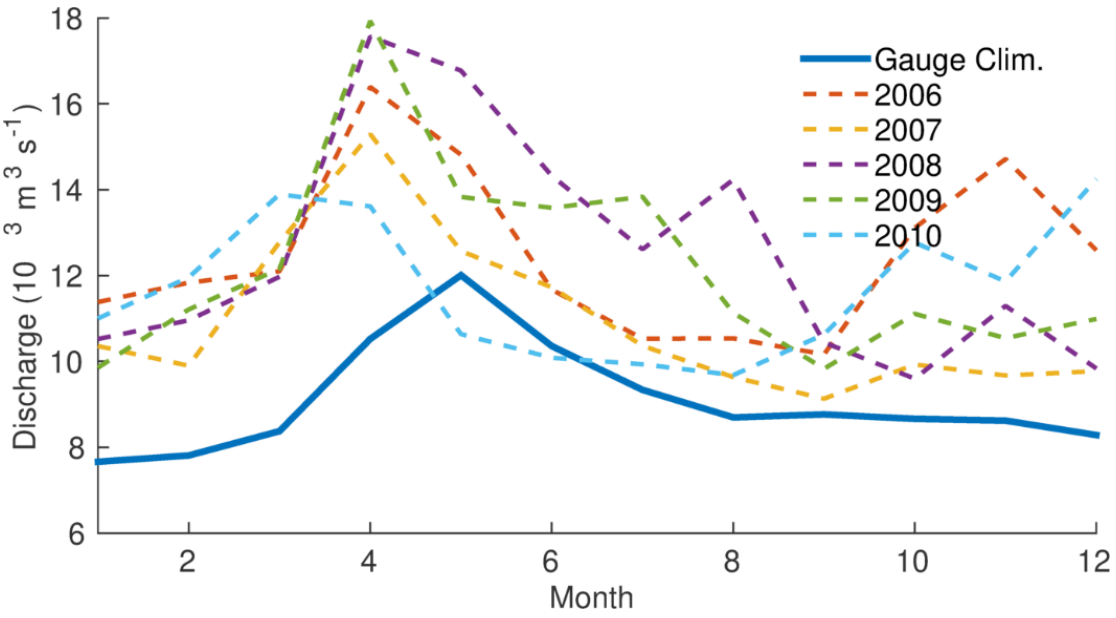

Figure E. 1. Annual cycle of the St. Lawrence River runoff (10^3 m^3 s^{-1}) of the Gauge Clim. (solid blue line) and new dataset (dashed lines).

E.2 Impact on the Hydrography

Figure E.2 presents the multi-year averaged (2007-2010) monthly-mean ΔSSS in the GSL as differences between CR and NR (CR - NR). The SLR runoffs in CR lead to negative ΔSSS over the western GSL and the Scotian Shelf, with minimum values <-2 psu occur in the northwestern GSL throughout the year. The magnitudes of the ΔSSS are reduced in the southwestern GSL (ΔSSS>-1 psu) and the Scotian Shelf (ΔSSS>-0.5 psu). In summer, the negative ΔSSSs spread over the southwestern GSL and the Scotian Shelf and are gradually diminished from August till December. In winter, the negative ΔSSSs are only retained over the northwestern GSL and along the southwestern coast of the GSL.

The simulated temperature and salinity are compared with in-situ hydrographic observations along the four AZMP transects in the GSL (locations shown in Figure 5.1). The observed data collected during 2007-2010 are interpolated onto model grids, while daily mean values from the simulation are selected when observations are available. Figure E.3 presents the scatter-diagram of observed versus NR (blue) and CR (red) values, respectively. The simulated temperature and salinity in both NR and CR are very close,

and considerable differences only appear in the simulated salinity along the MLO and IMA transects. In the MLO transect over the northwestern GSL, the increased SLR runoffs in CR leads to significant salinity drop comparing to NR (Figure E.2). These anomalies also occasionally result in water masses fresher than the observed with salinity <32 psu, associated with an increase in the root mean square difference (RMSD) of about 0.88 psu (Figure E.3d). Since only four years data are included in this analysis, the model underestimation in salinity can also be significantly contributed by the instability in the Gaspe Current, which is a challenge for this model (~6 km horizontal resolution in the GSL) to reproduce (Sheng 2001). In the IMA transect over the southwestern GSL, the SLR runoffs in CR significantly alleviates the overestimation of salinity near the coast in NR (Figure C.3h) by ~1 psu, and results in a smaller RMSD (0.61 psu) and a higher correlation coefficient (0.81) (Figure E.3f).

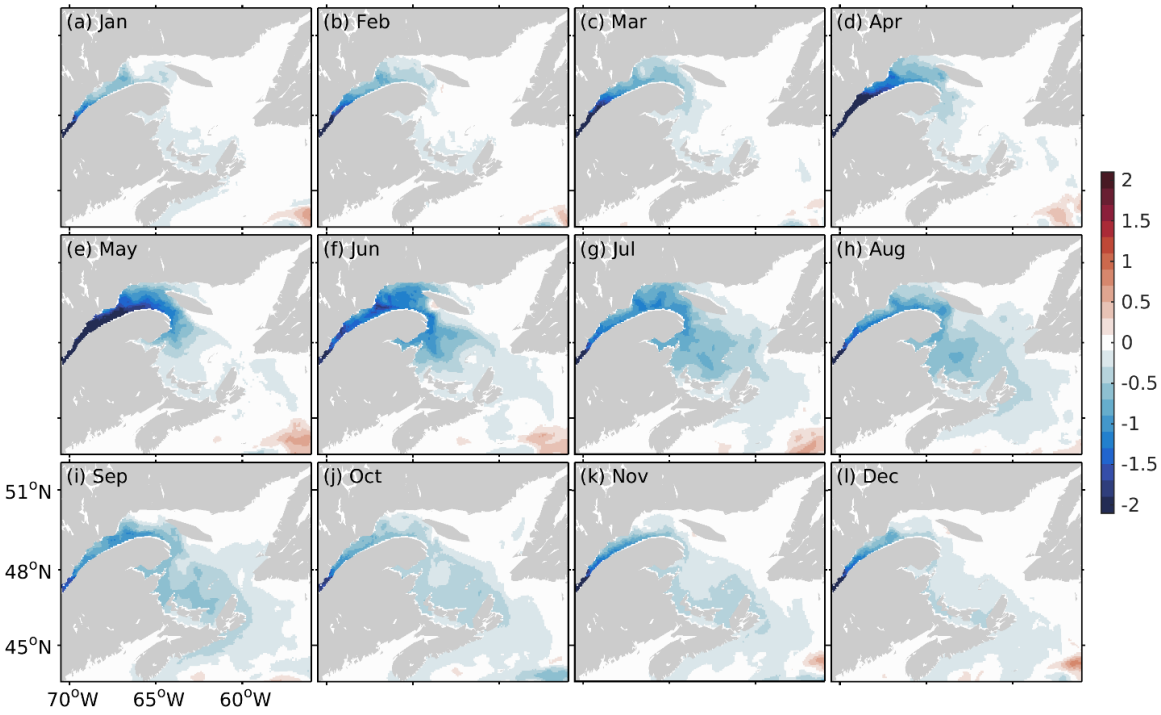

Figure E.2. Distributions of the multi-year averaged (2007-2010) monthly-mean ΔSSS (CR - NR).

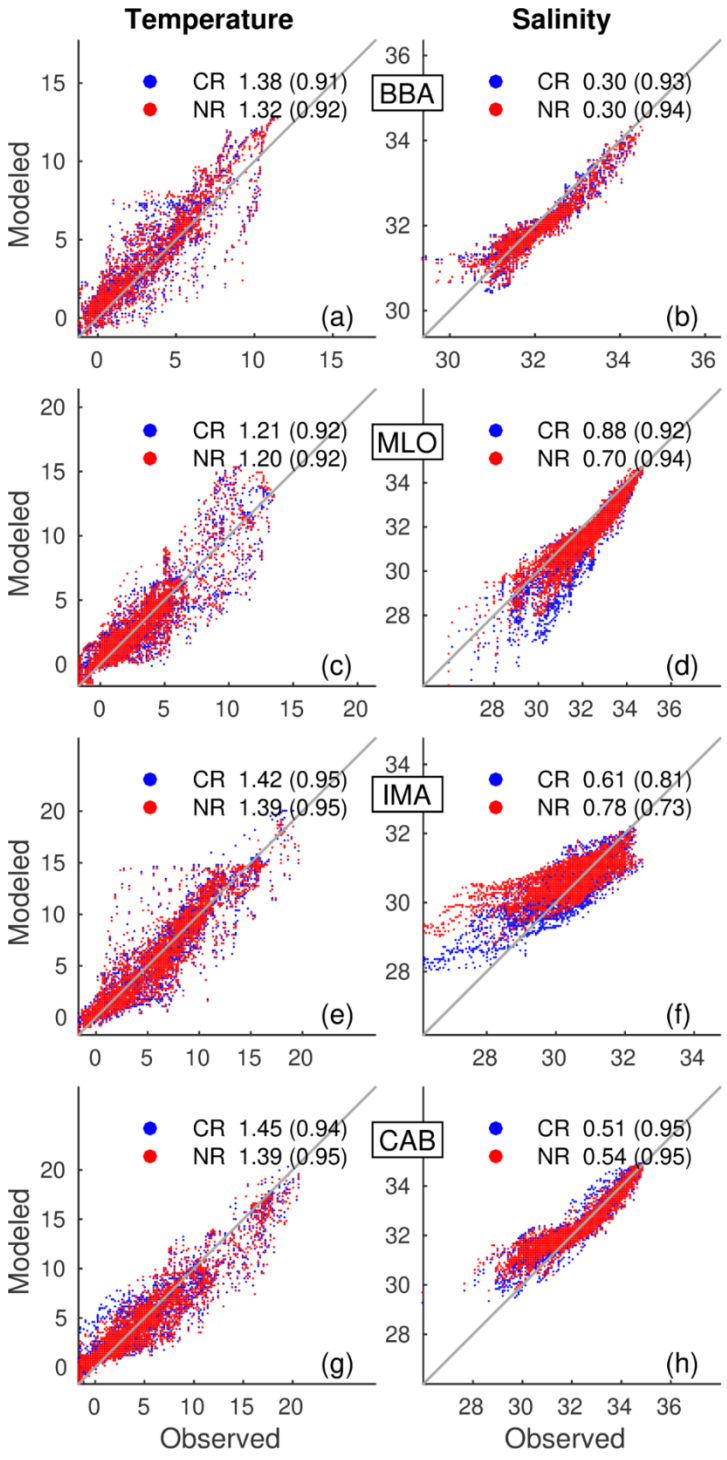

Figure E.3. Scatter diagrams of observed vs. simulated (left) temperature and (right) salinity, at the four AZMP transects with names in boxes. The AZMP data collected during 2007-2010 are interpolated onto mode grids, and the daily mean model results from NR and CR are selected when observations are available. The number outside (inside) brackets in the legend denotes RMSD (correlation coefficient).

E.3 Impact on the Sea Ice Distribution

Figure E.4 presents time series of regional-integrated sea-ice volume for the CIS, NR and CR in the four sub regions and the whole GSL, respectively. In general, the simulated ice volumes in CR are often larger in early winter than that in NR, but only account for <10% increase in total volumes. The ice growth rate in the GSL was suggested to be sensitive to the stratification before the winter. The stronger stratification results in significantly higher growth rates in January but smaller growth rates in the following months (Saucier 2003). In comparison with model results in NR, the modelled salinity in CR is generally lower than NR over the western GSL in fall. The greater ice volume in CR in early winter is noticeable in the southwestern and especially the northwestern GSL. The largest ice volume increase in early winter in CR than NR occurs in the NW subregion during 2007, associated with significantly increased freshwater runoff during fall 2006 (Figure E.1). The increased freshwater runoff does not always result in increases in the ice volume in the GSL. For instance, the simulated ice in the NW subregion in CR is less than NR by up to 8% in 2008, which is associated mainly with changes in ocean circulation and net heat flux at the sea surface, rather than the runoff from the SLR. In general, the ice volume changes due to the increased St. Lawrence River runoffs are relatively small (<10%) in the GSL.

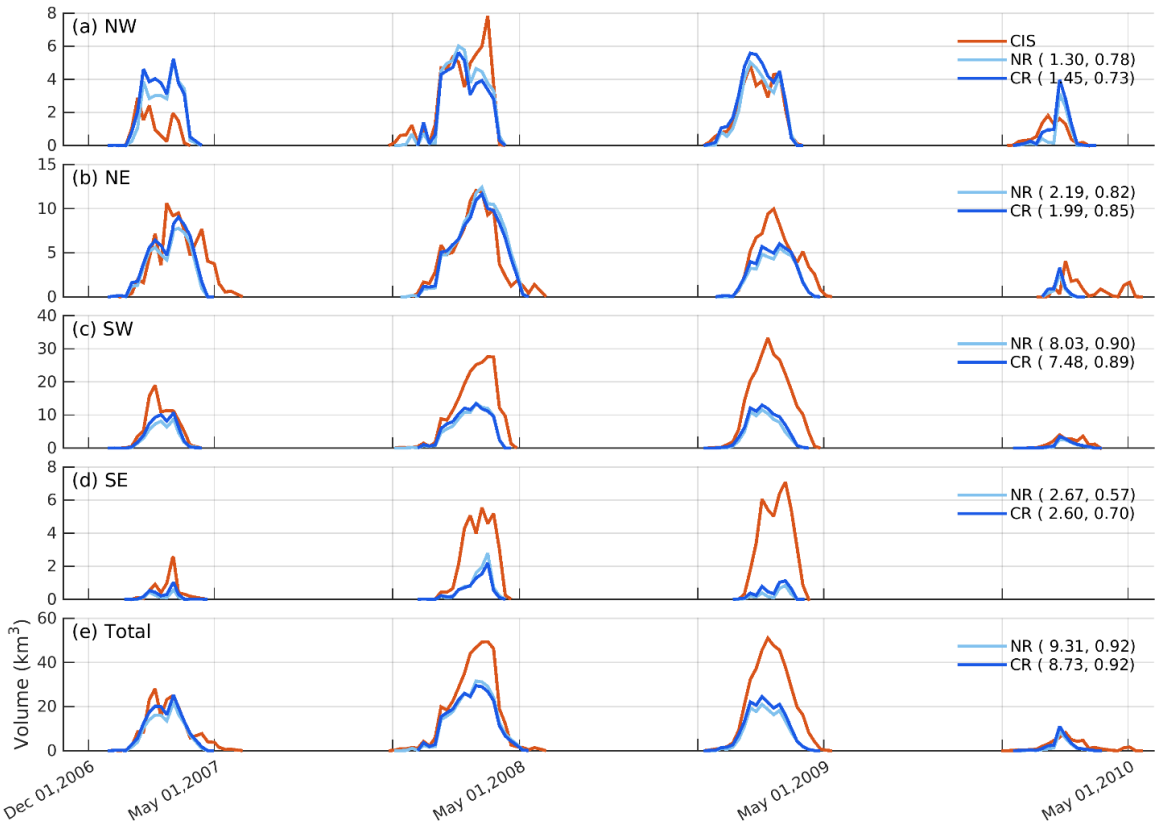

Figure E.4. Time series of regional-integrated sea ice volume (km^2) during the period 2007-2010 based on the CIS (red), NR (cyan), and CR(blue) in the (a) NW, (b) NE, (c) SW, (d) SE subregions, and (e) the whole GSL. Numbers in the bracket are the RMSD and correlation coefficient values.

APPENDIX F

COPYRIGHT PERMISSION

JOHN WILEY AND SONS LICENSE
TERMS AND CONDITIONS
Jul 08, 2021

This Agreement between Dr. Yuan Wang ("You") and John Wiley and Sons ("John Wiley and Sons") consists of your license details and the terms and conditions provided by John Wiley and Sons and Copyright Clearance Center.

License Number	5104531125506
License date	Jul 08, 2021
Licensed Content Publisher	John Wiley and Sons
Licensed Content Publication	Geophysical Research Letters
Licensed Content Title	Decomposition of the Mean Barotropic Transport in a High-Resolution Model of the North Atlantic Ocean
Licensed Content Author	Yuan Wang, Martin Claus, Richard J. Greatbatch, et al
Licensed Content Date	Nov 20, 2017
Licensed Content Pages	1
Type of use	Dissertation/Thesis
Requestor type	Author of this Wiley article

Format	Print and electronic
Portion	Full article
Will you be translating?	No
Title	Decomposition of the Mean Barotropic Transport in a High-Resolution Model of the North Atlantic Ocean
Institution name	Dalhousie University
Expected presentation date	Jul 2021
Requestor Location	Dr. Yuan Wang 1108-1094 Wellington St. Halifax, NS B3H 2Z9 Canada Attn: Yuan Wang
Publisher Tax ID	EU826007151
Total	0.00 CAD

Decomposing Barotropic Transport Variability in a High-Resolution Model of the North Atlantic Ocean

Author: Yuan Wang, Richard J. Greatbatch, Martin Claus, et al

Publication: Journal of Geophysical Research: Oceans

Publisher: John Wiley and Sons

Date: Apr 27, 2020

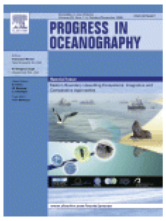

Examining tidal impacts on seasonal circulation and hydrography variability over the eastern Canadian shelf using a coupled circulation-ice regional model

Author: Yuan Wang,Jinyu Sheng,Youyu Lu

Publication: Progress in Oceanography

Publisher: Elsevier

Date: November–December 2020

Journal Author Rights

Bibliography

Allen, S. E. S., X. Durrieu de Madron, and X. D. De Madron, 2009: A review of the role of submarine canyons in deep-ocean exchange with the shelf. *Ocean Sci. Discuss.*, **6**, 1369–1406.

Allison, I., 1981: Antarctic sea ice growth and oceanic heat flux. *Sea level, ice Clim. Chang.*, **131**, 161–170.

Aretxabaleta, A. L., D. J. McGillicuddy, K. W. Smith, and D. R. Lynch, 2008: Model simulations of the Bay of Fundy Gyre: 1. Climatological results. *J. Geophys. Res. Ocean.*, **113**, 1–16.

Baines, P. G., 1973: The generation of internal tides by flat-bump topography. *Deep Sea Research and Oceanographic Abstracts*, Vol. 20, 179–205.

Banks, R. E., 1966: The cold layer in the Gulf of St. Lawrence. *J. Geophys. Res.*, **71**, 1603–1610.

Behrens, E., 2013: The oceanic response to Greenland melting: the effect of increasing model resolution. Christian-Albrechts-Universität, Kiel, 8-diss-136843 pp.

Bell, M. J., 1999: Vortex stretching and bottom torques in the Bryan-Cox ocean circulation model. *J. Geophys. Res. Ocean.*, **104**, 23545–23563.

Black, W. A., 1961: Geographical Branch program of ice surveys of the Gulf of St. Lawrence, 1956 to 1962. *Cah. Geogr. Que.*, **6**, 65–74.

Bleck, R., 2002: An oceanic general circulation model framed in hybrid isopycnic-Cartesian coordinates. *Ocean Model.*, **4**, 55–88.

Böning, C. W., E. Behrens, A. Biastoch, K. Getzlaff, and J. L. Bamber, 2016: Emerging impact of Greenland meltwater on deepwater formation in the North Atlantic Ocean. *Nat. Geosci.*, **9**, 523–527.

Bouillon, S., M. A. Morales Maqueda, V. Legat, and T. Fichefet, 2009: An elastic-viscous-plastic sea ice model formulated on Arakawa B and C grids. *Ocean Model.*, **27**, 174–184.

Bourgault, D., and V. G. Koutitonsky, 1999: Real-time monitoring of the freshwater discharge at the head of the St. Lawrence Estuary. *Atmosphere-Ocean*, **37**, 203–220.

Bower, A. S., and W.-J. J. von Appen, 2008: Interannual variability in the pathways of the North Atlantic Current over the mid-atlantic ridge and the impact of topography. *J. Phys. Oceanogr.*, **38**, 104–120.

Breckenfelder, T., M. Rhein, A. Roessler, C. W. Böning, A. Biastoch, E. Behrens, and C.

Mertens, 2017: Flow paths and variability of the North Atlantic Current: A comparison of observations and a high-resolution model. *J. Geophys. Res. Ocean.*.

Brennan, C. E., L. Bianucci, and K. Fennel, 2016: Sensitivity of Northwest North Atlantic Shelf Circulation to Surface and Boundary Forcing: A Regional Model Assessment. *Atmosphere-Ocean*, **54**, 230–247.

Brickman, D., and J. W. Loder, 1993: Energetics of the Internal Tide on Northern Georges Bank. *J. Phys. Oceanogr.*, **23**, 409–424.

——, and A. Drozdowski, 2012: *Development and validation of a regional shelf model for Maritime Canada based on the NEMO-OPA circulation model*. Canadian Technical Report of Hydrography and Ocean Sciences.

Brickman, D., D. Hebert, and Z. Wang, 2018: Mechanism for the recent ocean warming events on the Scotian Shelf of eastern Canada. *Cont. Shelf Res.*, **156**, 11–22.

Brink, K. H., 2016: Cross-Shelf Exchange. *Ann. Rev. Mar. Sci.*, **8**, 59–78.

Bugden, G. L., 1988: Oceanographic conditions in the deeper waters of the Gulf of St. *Lawrence Relat. to local Ocean. forcing. NAFO SCR Doc.*, **88**, 87.

Bugden, G. L., 1991: Changes in the temperature-salinity characteristics of the deeper waters of the Gulf of St. Lawrence over the past several decades. *Gulf St. Lawrence small Ocean or big estuary*, 139–147.

Caldwell, P. C., M. M. A., and T. P. R., 2015: *Sea level measured by tide gauges from global oceans — the Joint Archive for Sea Level holdings (NCEI Accession 0019568), Version 5.5*.

Canadian Ice Service, 2006: Canadian Ice Service Digital Archive–Regional Charts: History, Accuracy, and Caveats.

——, 2009: *Canadian Ice Service Arctic Regional Sea Ice Charts in SIGRID-3 Format, Version 1*.

Canadian Ice Service Archive Documentation, 2007: Regional charts: Canadian Ice Service Ice Regime Regions (CISIRR) and sub-regions with associated data quality indices.

Cavalieri, D. J., and C. L. Parkinson, 2012: Arctic sea ice variability and trends, 1979-2010. *Cryosphere*, **6**, 881–889.

Chapman, D. C., and R. C. Beardsley, 1989: On the origin of shelf water in the Middle Atlantic Bight. *J. Phys. Oceanogr.*, **19**, 384–391.

Chassignet, E. P., and D. P. Marshall, 2008: Gulf stream separation in numerical ocean models. *Geophys. Monogr. Ser.*, **177**, 39–61.

Chegini, F., Y. Lu, A. Katavouta, and H. Ritchie, 2018: Coastal Upwelling Off Southwest Nova Scotia Simulated With a High-Resolution Baroclinic Ocean Model. *J. Geophys. Res. Ocean.*, 1–14.

Chen, C., and Coauthors, 2011: Tidal dynamics in the Gulf of Maine and New England Shelf: An application of FVCOM. *J. Geophys. Res.*, **116**, C12010.

De Coëtlogon, G., C. Frankignoul, M. Bentsen, C. Delon, H. Haak, S. Masina, and A. Pardaens, 2006: Gulf Stream variability in five oceanic general circulation models. *J. Phys. Oceanogr.*, **36**, 2119–2135.

Condron, A., and P. Winsor, 2011: A subtropical fate awaited freshwater discharged from glacial Lake Agassiz. *Geophys. Res. Lett.*, **38**, 1–5.

Cuny, J., P. B. Rhines, P. P. Niiler, and S. Bacon, 2002: Labrador Sea boundary currents and the fate of the Irminger Sea Water. *J. Phys. Oceanogr.*, **32**, 627–647.

Curry, R. G., and M. S. McCartney, 2001: Ocean Gyre Circulation Changes Associated with the North Atlantic Oscillation. *J. Phys. Oceanogr.*, **31**, 3374–3400.

Cyr, F., D. Bourgault, P. S. Galbraith, and M. Gosselin, 2015: Turbulent nitrate fluxes in the Lower St. Lawrence Estuary, Canada. *J. Geophys. Res. Ocean.*, **120**, 2308–2330.

Czaja, A., and C. Frankignoul, 2002: Observed impact of Atlantic SST anomalies on the North Atlantic oscillation. *J. Clim.*, **15**, 606–623.

Dale, A. C., 2003: The front on the Northern Flank of Georges Bank in spring: 1. Tidal and subtidal variability. *J. Geophys. Res.*, **108**, 8009.

Delworth, T., S. Manabe, and R. J. Stouffer, 1993: Interdecadal Variations of the Thermohaline Circulation in a Coupled Ocean-Atmosphere Model. *J. Clim.*, **6**, 1993–2011.

Delworth, T. L., and Coauthors, 2012: Simulated climate and climate change in the GFDL CM2. 5 high-resolution coupled climate model. *J. Clim.*, **25**, 2755–2781.

DeTracey, B., 1995: Modelling interannual sea ice variability in the Gulf of St. Lawrence.

Dever, M., D. Hebert, B. J. W. Greenan, J. Sheng, and P. C. Smith, 2016: Hydrography and Coastal Circulation along the Halifax Line and the Connections with the Gulf of St. Lawrence. *Atmos. - Ocean*, **54**, 199–217.

Dickson, R., J. Lazier, J. Meincke, P. Rhines, and J. Swift, 1996: Long-term coordinated changes in the convective activity of the North Atlantic. *Prog. Oceanogr.*, **38**, 241–295.

DiNezio, P. N., L. J. Gramer, W. E. Johns, C. S. Meinen, and M. O. Baringer, 2009: Observed interannual variability of the Florida Current: Wind forcing and the North

Atlantic Oscillation. *J. Phys. Oceanogr.*, **39**, 721–736.

Drews, A., and R. J. Greatbatch, 2016: Atlantic Multidecadal Variability in a model with an improved North Atlantic Current. *Geophys. Res. Lett.*, **43**, 8199–8206.

——, and ——, 2017: Evolution of the Atlantic Multidecadal Variability in a Model with an Improved North Atlantic Current. *J. Clim.*, **30**, 5491–5512.

——, R. J. Greatbatch, H. Ding, M. Latif, and W. Park, 2015: The use of a flow field correction technique for alleviating the North Atlantic cold bias with application to the Kiel Climate Model. *Ocean Dyn.*, **65**, 1079–1093.

Drinkwater, K. F., and G. L. Bugden, 1994: *Variability in the Position of the Shelf/Slope Front Near the Mouth of the Laurentian Channel*.

——, R. G. Pettipas, G. Bugden, and P. Langille, 1999: Climatic data for the Northwest Atlantic: A sea ice database for the Gulf of St. Lawrence and the Scotian Shelf. *Can. Tech. Rept. Hydrogr. Ocean Sci.*, **199**.

Dupont, F., C. Hannah, and D. Greenberg, 2002: *Modelling system for tides for the Northwest Atlantic coastal ocean*. http://www.iob.gc.ca/science/research-recherche/ocean/webtide/documents/WebTide_report4.pdf.

Eden, C., and T. Jung, 2001: North Atlantic interdecadal variability: oceanic response to the North Atlantic Oscillation (1865–1997). *J. Clim.*, **14**, 676–691.

——, and J. Willebrand, 2001: Mechanism of interannual to decadal variability of the North Atlantic circulation. *J. Clim.*, 2266–2280.

——, and R. J. Greatbatch, 2003: A damped decadal oscillation in the North Atlantic Climate System. *J. Clim.*, **16**, 4043–4060.

Egbert, G. D., and R. D. Ray, 2000: Significant dissipation of tidal energy in the deep ocean inferred from satellite altimeter data. *Nature*, **405**, 775.

——, and S. Y. Erofeeva, 2002: Efficient inverse modeling of barotropic ocean tides. *J. Atmos. Ocean. Technol.*, **19**, 183–204.

——, and R. D. Ray, 2003: Semi-diurnal and diurnal tidal dissipation from TOPEX/Poseidon altimetry. *Geophys. Res. Lett.*, **30**.

Engedahl, H., 1995: Use of the flow relaxation scheme in a three-dimensional baroclinic ocean model with realistic topography. *Tellus A*, **47**, 365–382.

Espelid, T. O., J. Berntsen, and K. Barthel, 2000: Conservation of energy for schemes applied to the propagation of shallow-water inertia-gravity waves in regions with varying depth. *Int. J. Numer. Methods Eng.*, **49**, 1521–1545.

Fichefet, T., and M. A. M. M. Maqueda, 1997: Sensitivity of a global sea ice model to the treatment of ice thermodynamics and dynamics. *J. Geophys. Res. Ocean.*, **102**, 12609–12646.

Fischer, J., and Coauthors, 2015: Intra-seasonal variability of the DWBC in the western subpolar North Atlantic. *Prog. Oceanogr.*, **132**, 233–249.

Flather, R. A., 1994: A storm surge prediction model for the northern Bay of Bengal with application to the cyclone disaster in April 1991. *J. Phys. Oceanogr.*, **24**, 172–190.

Flato, G., and Coauthors, 2013: Evaluation of Climate Models. In: Climate Change 2013: The Physical Science Basis. Contribution of Working Group I to the Fifth Assessment Report of the Intergovernmental Panel on Climate Change. *Clim. Chang. 2013*, **5**, 741–866.

Fofonoff, N. P., 1954: Steady flow in a frictionless homogeneous ocean. *J. Mar. Res*, **13**, 254–262.

Forrester, W. D., 1974: INTERNAL TIDES IN ST-LAWRENCE ESTUARY. *J. Mar. Res.*, **32**, 55–66.

Forward, C. N., 1952: Ice distribution in the Gulf of St. Lawrence during the breakup season.

Fox-Kemper, B., and Coauthors, 2019: Challenges and prospects in ocean circulation models. *Front. Mar. Sci.*, **6**, 1–29.

Fratantoni, P. S., and R. S. Pickart, 2007: The Western North Atlantic Shelfbreak Current System in Summer. *J. Phys. Oceanogr.*, **37**, 2509–2533.

——, and M. S. McCartney, 2010: Freshwater export from the Labrador Current to the North Atlantic Current at the Tail of the Grand Banks of Newfoundland. *Deep. Res. Part I Oceanogr. Res. Pap.*, **57**, 258–283.

Fuglister, F. C., 1963: Gulf stream'60. *Prog. Oceanogr.*, **1**, 265-373.

Galbraith, P. S., 2006: Winter water masses in the Gulf of St. Lawrence. *J. Geophys. Res. Ocean.*, **111**, C06022.

Galley, R. J., D. Babb, M. Ogi, B. G. T. Else, N. -X. Geilfus, O. Crabeck, D. G. Barber, and S. Rysgaard, 2016: Replacement of multiyear sea ice and changes in the open water season duration in the Beaufort Sea since 2004. *J. Geophys. Res. Ocean.*, **121**, 1806–1823.

Garett, C., E. Kunze, C. Garrett, and E. Kunze, 2007: Internal tide generation in the deep ocean. *Annu. Rev. Fluid Mech.*, **39**, 57–87.

Garrett, C., 1972: Tidal Resonance in the Bay of Fundy and Gulf of Maine. *Nature*, **238**,

441–443.

——, J. R. Keeley, and D. A. Greenberg, 1978: Tidal mixing versus thermal stratification in the Bay of Fundy and Gulf of Maine. *Atmosphere-Ocean*, **16**, 403–423.

Gilbert, D., B. Sundby, C. Gobeil, A. Mucci, and G.-H. Tremblay, 2005: A seventy-two-year record of diminishing deep-water oxygen in the St. Lawrence estuary: The northwest Atlantic connection. *Limnol. Oceanogr.*, **50**, 1654–1666.

Global Runoff Data Center Germany, F. I. of H., and U. N. E. International Hydrological Programme Scientific and Cultural Organization, 2001: Monthly Discharge Data for World Rivers (except former Soviet Union).

Goosse, H., and T. Fichefet, 1999: Importance of ice-ocean interactions for the global ocean circulation: A model study. *J. Geophys. Res. Ocean.*, **104**, 23337–23355.

Gordon, A. L., and B. A. Huber, 1990: Southern Ocean winter mixed layer. *J. Geophys. Res. Ocean.*, **95**, 11655–11672.

Greatbatch, R. J., 1983: On the Response of the Ocean to a Moving Storm: The Nonlinear Dynamics. *J. Phys. Oceanogr.*, **13**, 357–367.

——, 1984: On the response of the ocean to a moving storm: Parameters and scales. *J. Phys. Oceanogr.*, **14**, 59–78.

——, 1987: A model for the inertial recirculation of a gyre. *J. Mar. Res.*, **45**, 601–634.

——, 2000: The north Atlantic oscillation. *Stoch. Environ. Res. Risk Assess.*, **14**, 213–242.

——, and X. Zhai, 2006: Influence of assimilated eddies on the large-scale circulation in a model of the northwest Atlantic Ocean. *Geophys. Res. Lett.*, **33**.

——, A. F. Fanning, A. D. Goulding, and S. Levitus, 1991: A diagnosis of interpentadal circulation changes in the North Atlantic. *J. Geophys. Res. Ocean.*, **96**, 22009–22023.

——, J. Sheng, C. Eden, L. Tang, X. Zhai, and J. Zhao, 2004: The semi-prognostic method. *Cont. Shelf Res.*, **24**, 2149–2165.

——, X. Zhai, M. Claus, L. Czeschel, and W. Rath, 2010: Transport driven by eddy momentum fluxes in the Gulf Stream Extension region. *Geophys. Res. Lett.*, **37**.

Greenberg, D. A., 1979: A numerical model investigation of tidal phenomena in the Bay of Fundy and Gulf of Maine. *Mar. Geod.*, **2**, 161–187.

——, 1983: Modelling the mean barotropic circulation in the Bay of Fundy and Gulf of Maine. *J. Phys. Oceanogr.*, **13**, 886–904.

Greene, C. H., and A. J. Pershing, 2003: The flip-side of the North Atlantic Oscillation and modal shifts in slope-water circulation patterns. *Limnol. Oceanogr.*, **48**, 319–322.

Griffies, S. M., and Coauthors, 2015: Impacts on ocean heat from transient mesoscale eddies in a hierarchy of climate models. *J. Clim.*, **28**, 952–977.

Guard, U. S. C., 2004: *Report of the International Ice Patrol in the North Atlantic, 2004 Season*.

Hallberg, R., and P. Rhines, 1996: Buoyancy-driven circulation in an ocean basin with isopycnals intersecting the sloping boundary. *J. Phys. Oceanogr.*, **26**, 913–940.

Han, G., C. G. Hannah, J. W. Loder, and P. C. Smith, 1997: Seasonal variation of the three-dimensional mean circulation over the Scotian Shelf. *J. Geophys. Res. Ocean.*, **102**, 1011–1025.

——, J. W. Loder, and P. C. Smith, 1999: Seasonal-Mean Hydrography and Circulation in the Gulf of St. Lawrence and on the Eastern Scotian and Southern Newfoundland Shelves. *J. Phys. Oceanogr.*, **29**, 1279–1301.

——, Z. Lu, Z. Wang, J. Helbig, N. Chen, and B. de Young, 2008: Seasonal variability of the Labrador Current and shelf circulation off Newfoundland. *J. Geophys. Res. Ocean.*, **113**, 1–23.

Hannah, C. G., J. A. Shore, J. W. Loder, and C. E. Naimie, 2001: Seasonal circulation on the western and central Scotian Shelf. *J. Phys. Oceanogr.*, **31**, 591–615.

——, F. Dupont, and M. Dunphy, 2009: Polynyas and Tidal Currents in the Canadian Arctic Archipelago. *ARCTIC*, **62**, 83–95.

Hasegawa, D., J. Sheng, D. A. Greenberg, and K. R. Thompson, 2011: Far-field effects of tidal energy extraction in the Minas Passage on tidal circulation in the Bay of Fundy and Gulf of Maine using a nested-grid coastal circulation model. *Ocean Dyn.*, **61**, 1845–1868.

Hogg, N. G., 1992: On the transport of the Gulf Stream between Cape Hatteras and the Grand Banks. *Deep Sea Res. Part A, Oceanogr. Res. Pap.*, **39**, 1231–1246.

——, and H. Stommel, 1985: On the relation between the deep circulation and the Gulf Stream. *Deep Sea Res. Part A. Oceanogr. Res. Pap.*, **32**, 1181–1193.

——, R. S. Pickart, R. M. Hendry, and W. J. Smethie, 1986: The northern recirculation gyre of the Gulf Stream. *Deep Sea Res. Part A. Oceanogr. Res. Pap.*, **33**, 1139–1165.

Holland, W. R., 1973: Baroclinic and topographic influences on the transport in western boundary currents. *Geophys. Astrophys. Fluid Dyn.*, **4**, 187–210.

——, and A. D. Hirschman, 1972: A Numerical Calculation of the Circulation in the North Atlantic Ocean. *J. Phys. Oceanogr.*, **2**, 336–354.

Holliday, N. P., A. Meyer, S. Bacon, S. G. Alderson, and B. de Cuevas, 2007: Retroflection

of part of the east Greenland current at Cape Farewell. *Geophys. Res. Lett.*, **34**, 1–5.

Hunke, E. C., and D. Comeau, 2011: Sea ice and iceberg dynamic interaction. *J. Geophys. Res. Ocean.*, **116**, 1–9.

Hurrell, J. W., 1995: Decadal trends in the North Atlantic Oscillation: regional temperatures and precipitation. *Sci. Pap. Ed.*, **269**, 676–678.

——, Y. Kushnir, G. Ottersen, and M. Visbeck, 2003: An overview of the north atlantic oscillation. *Geophys. Monogr. Ser.*, **134**, 1–35.

Ingram, R. G., 1983: Vertical mixing at the head of the Laurentian Channel. *Estuar. Coast. Shelf Sci.*, **16**, 333–338.

Joyce, T. M., and R. Zhang, 2010: On the Path of the Gulf Stream and the Atlantic Meridional Overturning Circulation. *J. Clim.*, **23**, 3146–3154.

——, J. K. B. Bishop, and O. B. Brown, 1992: Observations of offshore shelf-water transport induced by a warm-core ring. *Deep Sea Res. Part A. Oceanogr. Res. Pap.*, **39**, S97–S113.

——, C. Deser, and M. A. Spall, 2000: The relation between decadal variability of subtropical mode water and the North Atlantic Oscillation. *J. Clim.*, **13**, 2550–2569.

Käse, R. H., and G. Siedler, 1982: Meandering of the subtropical front south-east of the Azores. *Nature*, **300**, 245–246.

Katavouta, A., K. R. Thompson, Y. Lu, and J. W. Loder, 2016: Interaction between the Tidal and Seasonal Variability of the Gulf of Maine and Scotian Shelf Region. *J. Phys. Oceanogr.*, **46**, 3279–3298.

Keeley, S. P. E., R. T. Sutton, and L. C. Shaffrey, 2012: The impact of North Atlantic sea surface temperature errors on the simulation of North Atlantic European region climate. *Q. J. R. Meteorol. Soc.*, **138**, 1774–1783.

Kelly, S. M., P. F. J. Lermusiaux, T. F. Duda, and P. J. Haley, 2016: A Coupled-Mode Shallow-Water Model for Tidal Analysis: Internal Tide Reflection and Refraction by the Gulf Stream. *J. Phys. Oceanogr.*, **46**, 3661–3679.

Killworth, P. D., 1987: Topographic instabilities in level model OGCMs. *Ocean Model.*, **75**, 9–12.

Koutitonsky, V. G., and G. L. Bugden, 1991: The Physical Oceanography of the Gulf of St. Lawrence: A Review with Emphasis on the Synoptic Variability of the Motion. *Gulf St. Lawrence small Ocean or big estuary?*, 57–90.

Kowalik, Z., and A. Y. Proshutinsky, 2013: The Arctic Ocean Tides. *The Polar Oceans and their role in shaping the global environment*, Vol. 85 of, Wiley Online Library,

137–158.

Krauss, W., 1986: The North Atlantic Current. *J. Geophys. Res.*, **91**, 5061–5074.

Lamb, K. G., 1994: Numerical experiments of internal wave generation by strong tidal flow across a finite amplitude bank edge. *J. Geophys. Res.*, **99**, 843.

Large, W. G., and S. G. Yeager, 2004: Diurnal to decadal global forcing for ocean and sea--ice models: {The} data sets and flux climatologies. *NCAR Tech. Note*, **TN--460+ST**, 105pp.

——, and ——, 2009: The global climatology of an interannually varying air–sea flux data set. *Clim. Dyn.*, **33**, 341–364.

Lavender, K. L., R. E. Davis, and W. B. Owens, 2000: Mid-depth recirculation observed in the interior Labrador and Irminger seas by direct velocity measurements. *Nature*, **407**, 66–69.

Lazier, J. R. N., 1994: Observations in the northwest corner of the North Atlantic Current. *J. Phys. Oceanogr.*, **24**, 1449–1463.

——, and D. G. Wright, 1993: Annual velocity variations in the Labrador Current. *J. Phys. Oceanogr.*, **23**, 659–678.

Li, Y., 2000: Intraseasonal and Interannual Variability of Sea Ice in the Gulf of St. Lawrence.

Loder, J. W., 1980: Topographic rectification of tidal currents on the sides of Georges Bank. *J. Phys. Oceanogr.*, **10**, 1399–1416.

——, and D. G. Wright, 1985: Tidal rectification and frontal circulation on the sides of Georges Bank. *J. Mar. Res.*, **43**, 581–604.

——, and D. A. Greenberg, 1986: Predicted positions of tidal fronts in the Gulf of Maine region. *Cont. Shelf Res.*, **6**, 397–414.

——, D. Brickman, and E. P. W. Horne, 1992: Detailed structure of currents and hydrography on the northern side of Georges Bank. *J. Geophys. Res.*, **97**, 14331.

——, G. Han, C. G. Hannah, D. A. Greenberg, and P. C. Smith, 1997: Hydrography and baroclinic circulation in the Scotian Shelf region: winter versus summer. *Can. J. Fish. Aquat. Sci.*, **54**, 40–56.

——, B. Petrie, and G. Gawarkiewicz, 1998: The coastal ocean off northeastern North America: a large-scale view. *Sea*, **11**, 105–133.

——, C. G. Hannah, B. D. Petrie, and E. A. Gonzalez, 2003: Hydrographic and transport variability on the Halifax section. *J. Geophys. Res. Ocean.*, **108**, 8003.

Lu, Y., K. R. Thompson, and D. G. Wright, 2001a: Tidal currents and mi×ing in the Gulf of St. Lawrence: an application of the incremental approach to data assimilation. *Can. J. Fish. Aquat. Sci.*, **58**, 723–735.

——, D. G. Wright, and D. Brickman, 2001b: Internal tide generation over topography: Experiments with a free-surface z-level ocean model. *J. Atmos. Ocean. Technol.*, **18**, 1076–1091.

Lynch, D. R., J. T. C. Ip, C. E. Naimie, and F. E. Werner, 1996: Comprehensive coastal circulation model with application to the Gulf of Maine. *Cont. Shelf Res.*, **16**, 875–906.

Madec, G., 2008: NEMO reference manual, ocean dynamic component: NEMO-OPA. *Note du Pôle modélisation, Inst. Pierre Simon Laplace, Fr. Tech. Rep.*, **27**.

Maqueda, M. A. M., A. J. Willmott, and N. R. T. Biggs, 2004: Polynya dynamics: A review of observations and modeling. *Rev. Geophys.*, **42**.

Marsden, R. F., 1986: The internal tide on Georges Bank. *J. Mar. Res.*, **44**, 35–50.

Marsh, R., and Coauthors, 2015: NEMO-ICB (v1.0): Interactive icebergs in the NEMO ocean model globally configured at eddy-permitting resolution. *Geosci. Model Dev.*, **8**, 1547–1562.

Marshall, J., and G. Nurser, 1986: Steady, free circulation in a stratified quasi-geostrophic ocean. *J. Phys. Oceanogr.*, **16**, 1799–1813.

——, H. Johnson, J. Goodmann, and J. Goodman, 2001: A study of the interaction of the North Atlantic oscillation with ocean circulation. *J. Clim.*, **14**, 1399–1421.

Marson, J. M., P. G. Myers, X. Hu, and J. Le Sommer, 2018: Using Vertically Integrated Ocean Fields to Characterize Greenland Icebergs' Distribution and Lifetime. *Geophys. Res. Lett.*, **45**, 4208–4217.

Martin, S., 1981: Frazil ice in rivers and oceans. *Annu. Rev. Fluid Mech.*, **13**, 379–397.

Maykut, G. A., and N. Untersteiner, 1971: Some results from a time-dependent thermodynamic model of sea ice. *J. Geophys. Res.*, **76**, 1550–1575.

McCarthy, G. D., T. M. Joyce, and S. A. Josey, 2018: Gulf Stream Variability in the Context of Quasi-Decadal and Multidecadal Atlantic Climate Variability. *Geophys. Res. Lett.*, **45**, 11,257-11,264.

McCartney, M. S., 1992: Recirculating components to the deep boundary current of the northern North Atlantic. *Prog. Oceanogr.*, **29**, 283–383.

Mecking, J. V, N. S. Keenlyside, and R. J. Greatbatch, 2015: Multiple timescales of stochastically forced North Atlantic Ocean variability: A model study. *Ocean Dyn.*,

65, 1367–1381.

Meinen, C. S. S., 2001: Structure of the North Atlantic Current in stream-coordinates and the circulation in the Newfoundland basin. *Deep. Res. Part I Oceanogr. Res. Pap.*, **48**, 1553–1580.

Mellor, G. L., C. R. Mechoso, and E. Keto, 1982: A diagnostic calculation of the general circulation of the atlantic ocean. *Deep Sea Res. Part A. Oceanogr. Res. Pap.*, **29**, 1171–1192.

Mertens, C., M. Rhein, M. Walter, C. W. Böning, E. Behrens, D. Kieke, R. Steinfeldt, and U. Stöber, 2014: Circulation and transports in the Newfoundland Basin, western subpolar North Atlantic. *J. Geophys. Res. Ocean.*, **119**, 7772–7793.

Mertz, G., and D. G. Wright, 1992: Interpretations of the JEBAR term. *J. Phys. Oceanogr.*, **22**, 301–305.

Minobe, S., A. Kuwano-Yoshida, N. Komori, S.-P. Xie, and R. J. Small, 2008: Influence of the Gulf Stream on the troposphere. *Nature*, **452**, 206–209.

Müller, M., H. Haak, J. H. Jungclaus, J. Sündermann, and M. Thomas, 2010: The effect of ocean tides on a climate model simulation. *Ocean Model.*, **35**, 304–313.

Munk, W., and C. Wunsch, 1998: Abyssal recipes II: Energetics of tidal and wind mixing. *Deep. Res. Part I Oceanogr. Res. Pap.*, **45**, 1977–2010.

Munk, W. H., 1950: On the wind-driven ocean circulation. *J. Atmos. Sci.*, **7**, 80–93.

Murray, J. E., 1969: The drift, deterioration and distribution of icebergs in the North Atlantic Ocean.

Murty, T. S., and J. D. Taylor, 1970: A numerical calculation of the wind-driven circulation in the Gulf of St. Lawrence. *J. Oceanogr.*, **26**, 203–214.

Myers, P. G., 2005: Impact of freshwater from the Canadian Arctic Archipelago on Labrador Sea Water formation. *Geophys. Res. Lett.*, **32**, 1–4.

——, A. F. Fanning, and A. J. Weaver, 1996: JEBAR, bottom pressure torque, and Gulf Stream separation. *J. Phys. Oceanogr.*, **26**, 671–683.

——, C. Donnelly, and M. H. Ribergaard, 2009: Structure and variability of the West Greenland Current in Summer derived from 6 repeat standard sections. *Prog. Oceanogr.*, **80**, 93–112.

O'Reilly, C. H., S. Minobe, and A. Kuwano-Yoshida, 2016: The influence of the Gulf Stream on wintertime European blocking. *Clim. Dyn.*, **47**, 1545–1567.

Ohashi, K., and J. Sheng, 2013: Influence of St. Lawrence River discharge on the

circulation and hydrography in Canadian Atlantic waters. *Cont. Shelf Res.*, **58**, 32–49.

——, ——, K. R. Thompson, C. G. Hannah, and H. Ritchie, 2009: Effect of stratification on tidal circulation over the Scotian Shelf and Gulf of St. Lawrence: A numerical study using a three-dimensional shelf circulation model. *Ocean Dyn.*, **59**, 809–825.

Ouellet, P., A. Olga, V. Bui, D. Lavoie, J. Chassé, N. Lambert, N. Ménard, and P. Sirois, 2013: Seasonal distribution, abundance, and growth of larval capelin (Mallotus villosus) and the role of the Lower St. Lawrence Estuary (Gulf of St. Lawrence, Canada) as a nursery area. *Can. J. Fish. Aquat. Sci*, **70**, 1–23.

Parkinson, C. L., and D. J. Cavalieri, 2008: Arctic sea ice variability and trends, 1979-2006. *J. Geophys. Res. Ocean.*, **113**, 1979–2006.

Pellerin, P., H. Ritchie, F. J. Saucier, F. Roy, S. Desjardins, M. Valin, and V. Lee, 2004: Impact of a Two-Way Coupling between an Atmospheric and an Ocean-Ice Model over the Gulf of St. Lawrence. *Mon. Weather Rev.*, **132**, 1379–1398.

Penduff, T., B. Barnier, W. K. Dewar, and J. J. O'Brien, 2004: Dynamical response of the oceanic eddy field to the North Atlantic Oscillation: A model–data comparison. *J. Phys. Oceanogr.*, **34**, 2615–2629.

Perovich, D. K., J. A. Richeter-Menge, K. F. Jones, and B. Light, 2008: Sunlight, water, and ice: Extreme Arctic sea ice melt during the summer of 2007. *Geophys. Res. Lett.*, **35**, 2–5.

Pershing, A. J., and Coauthors, 2002: Oceanographic responses to climate in the Northwest Atlantic. *Oceanogr. DC-OCEANOGRAPHY Soc.*, **14**, 76–82.

Petrie, B., 1975: M_2 surface and internal tides on the scotian shelf and slope.

——, and C. Anderson, 1983: Circulation on the newfoundland continental shelf. *Atmosphere-Ocean*, **21**, 207–226.

——, and K. Drinkwater, 1993: Temperature and salinity variability on the Scotian Shelf and in the Gulf of Maine 1945–1990. *J. Geophys. Res.*, **98**, 20079.

——, K. Lank, and S. de Margerie, 1987: Tides on the Newfoundland Grand Banks. *Atmosphere-Ocean*, **25**, 10–21.

——, B. Toulany, and C. Garrett, 1988: The transport of water, heat and salt through the Strait of Belle Isle. *Atmosphere-Ocean*, **26**, 234–251.

Pickart, R. S., W. M. Smethie, and W. M. Smethie Jr, 1993: How does the deep western boundary current cross the Gulf Stream? *J. Phys. Oceanogr.*, **23**, 2602–2616.

——, F. Straneo, and G. W. K. Moore, 2003: Is Labrador Sea water formed in the Irminger basin? *Deep Sea Res. Part I Oceanogr. Res. Pap.*, **50**, 23–52.

Pingree, R. D., and D. K. Griffiths, 1980: A numerical-model of the m2-tide in the gulf of st-lawrence. *Oceanol. Acta*, **3**, 221–225.

Postlethwaite, C. F., and Coauthors, 2011: The effect of tides on dense water formation in Arctic shelf seas. *Ocean Sci.*, **7**, 203–217, https://doi.org/10.5194/os-7-203-2011.

Prather, M. J., 1986: Numerical advection by conservation of second-order moments. *J. Geophys. Res. Atmos.*, **91**, 6671–6681.

Ramp, S. R., R. J. Schlitz, and W. R. Wright, 1985: The Deep Flow through the Northeast Channel, Gulf of Maine. *J. Phys. Oceanogr.*, **15**, 1790–1808.

Read, J. F., 2000: CONVEX-91: water masses and circulation of the Northeast Atlantic subpolar gyre. *Prog. Oceanogr.*, **48**, 461–510.

Reid, J. L., 1994: On the total geostrophic circulation of the North Atlantic Ocean: Flow patterns, tracers, and transports. *Prog. Oceanogr.*, **33**, 1–92.

Renssen, H., H. Goosse, and T. Fichefet, 2002: Modeling the effect of freshwater pulses on the early Holocene climate: The influence of high-frequency climate variability. *Paleoceanography*, **17**.

Reynolds, R. W., T. M. Smith, C. Liu, D. B. Chelton, K. S. Casey, and M. G. Schlax, 2007: Daily high-resolution-blended analyses for sea surface temperature. *J. Clim.*, **20**, 5473–5496.

Rhein, M., and Coauthors, 2013: Observations: ocean. In 'Climate Change 2013: the Physical Science Basis. Contribution of Working Group I to the Fifth Assessment Report of the Intergovernmental Panel on Climate Change.' *Cambridge Univ. Press. Cambridge, United Kingdom New York, NY, USA*.

Rieck, J. K., C. W. Böning, R. J. Greatbatch, and M. Scheinert, 2015: Seasonal variability of eddy kinetic energy in a global high-resolution ocean model. *Geophys. Res. Lett.*, **42**, 9379–9386.

Robinson, I. S., 2004: *Measuring the oceans from space: the principles and methods of satellite oceanography*. Springer Science & Business Media.

Roemmich, D., and Coauthors, 2019: On the future of Argo: A global, full-depth, multi-disciplinary array. *Front. Mar. Sci.*, **6**, 439.

Roessler, A., M. Rhein, D. Kieke, and C. Mertens, 2015: Long-term observations of North Atlantic Current transport at the gateway between western and eastern Atlantic. *J. Geophys. Res. Ocean.*, **120**, 4003–4027.

Rossby, T., 1996: The North Atlantic Current and surrounding waters: At the crossroads. *Rev. Geophys.*, **34**, 463.

——, C. Flagg, and K. Donohue, 2010: On the variability of Gulf Stream transport from seasonal to decadal timescales. *J. Mar. Res.*, **68**, 503–522.

Rousset, C., and Coauthors, 2015: The Louvain-La-Neuve sea ice model LIM3.6: Global and regional capabilities. *Geosci. Model Dev.*, **8**, 2991–3005.

Saba, V. S., and Coauthors, 2015: Enhanced warming of the Northwest Atlantic Ocean under climate change. *J. Geophys. Res. Ocean.*, **120**, 1–15.

——, and Coauthors, 2010: NCEP Climate Forecast System Reanalysis (CFSR) 6-hourly Products, January 1979 to December 2010.

Sandstrom, H., and J. a. Elliott, 1984: Internal tide and solitons on the Scotian Shelf: A nutrient pump at work. *J. Geophys. Res.*, **89**, 6415.

——, and N. S. Oakey, 1995: Dissipation in Internal Tides and Solitary Waves. *J. Phys. Oceanogr.*, **25**, 604–614.

Sanford, T. B., P. G. Black, J. R. Haustein, J. W. Feeney, G. Z. Forristall, and J. F. Price, 1987: Ocean response to a hurricane. Part I: Observations. *J. Phys. Oceanogr.*, **17**, 2065–2083.

Sarkisyan, A., and V. F. Ivanov, 1971: Joint effect of baroclinicity and bottom relief as an important factor in the dynamics of sea currents, Izv. Acad. Sci. USSR. *Atmos. Ocean. Phys*, **7**, 116–124.

Saucier, F. J., 2003: Modeling the formation and circulation processes of water masses and sea ice in the Gulf of St. Lawrence, Canada. *J. Geophys. Res.*, **108**, 3269.

——, and J. Chassé, 2000: Tidal circulation and buoyancy effects in the St. Lawrence Estuary. *Atmosphere-Ocean*, **38**, 505–556.

Scaife, A. A., and Coauthors, 2011: Improved Atlantic winter blocking in a climate model. *Geophys. Res. Lett.*, **38**.

——, and Coauthors, 2014: Skillful long-range prediction of European and North American winters. *Geophys. Res. Lett.*, **41**, 2514–2519.

Schmitz, W. J., and M. S. McCartney, 1993: On the North Atlantic Circulation. *Rev. Geophys.*, **31**, 29–49.

Semtner Jr, A. J., 1976: A model for the thermodynamic growth of sea ice in numerical investigations of climate. *J. Phys. Oceanogr.*, **6**, 379–389.

Shaw, W. J., T. P. Stanton, M. G. McPhee, J. H. Morison, and D. G. Martinson, 2009: Role of the upper ocean in the energy budget of Arctic sea ice during SHEBA. *J. Geophys. Res. Ocean.*, **114**.

Sheng, J., 2001: Dynamics of a Buoyancy-Driven Coastal Jet: The Gaspé Current. *J. Phys. Oceanogr.*, **31**, 3146–3162.

——, and K. R. Thompson, 1996: A robust method for diagnosing regional shelf circulation from scattered density profiles. *J. Geophys. Res. Ocean.*, **101**, 25647–25659.

——, R. J. Greatbatch, and D. G. Wright, 2001: Improving the utility of ocean circulation models through adjustment of the momentum balance. *J. Geophys. Res.*, **106**, 16711.

——, X. Zhai, and R. J. Greatbatch, 2006: Numerical study of the storm-induced circulation on the Scotian Shelf during Hurricane Juan using a nested-grid ocean model. *Prog. Oceanogr.*, **70**, 233–254.

Smeed, D. A., and Coauthors, 2018: The North Atlantic Ocean Is in a State of Reduced Overturning. *Geophys. Res. Lett.*, **45**, 1527–1533.

Smith, G. C., F. J. Saucier, and D. Straub, 2006a: Response of the lower St. Lawrence Estuary to external forcing in winter. *J. Phys. Oceanogr.*, **36**, 1485–1501.

——, ——, and ——, 2006b: Formation and circulation of the cold intermediate layer in the Gulf of Saint Lawrence. *J. Geophys. Res.*, **111**, C06011.

Smith, P. C., and H. Sandstrom, 1988: Physical Processes at the Shelf Edge in the Northwest Atlantic. *J. Northwest Atl. Fish. Sci.*, **8**, 5–13.

——, and F. B. Schwing, 1991: Mean circulation and variability on the eastern Canadian continental shelf. *Cont. Shelf Res.*, **11**, 977–1012.

Spall, M. a., and R. S. Pickart, 2001: Where Does Dense Water Sink? A Subpolar Gyre Example*. *J. Phys. Oceanogr.*, **31**, 810–826.

Stammer, D., and C. Wunsch, 1999: Temporal changes in eddy energy of the oceans. *Deep Sea Res. Part II Top. Stud. Oceanogr.*, **46**, 77–108.

Stefan, J., 1891: Über die Theorie der Eisbildung, insbesondere über die Eisbildung im Polarmeere. *Ann. der Phys. und Chemie*, **42**, 269–286.

Stommel, H., 1948: The westward intensification of wind-driven ocean currents. *Eos, Trans. Am. Geophys. Union*, **29**, 202–206.

Straneo, F., R. S. Pickart, and K. Lavender, 2003: Spreading of Labrador sea water: An advective-diffusive study based on Lagrangian data. *Deep. Res. Part I Oceanogr. Res. Pap.*, **50**, 701–719.

Sverdrup, H. U., 1947: Wind-Driven Currents in a Baroclinic Ocean; with Application to the Equatorial Currents of the Eastern Pacific. *Proc. Natl. Acad. Sci.*, **33**, 318–326.

Taylor, A. H., and J. a. Stephens, 1998: The North Atlantic Oscillation and the latitude of the Gulf Stream. *Tellus A*, 134–142.

Teague, W. J., E. Jarosz, D. W. Wang, and D. A. Mitchell, 2007: Observed Oceanic Response over the Upper Continental Slope and Outer Shelf during Hurricane Ivan*. *J. Phys. Oceanogr.*, **37**, 2181–2206.

Tee, K. T., P. C. Smith, and D. Lefaivre, 1993: Topographic upwelling off southwest Nova Scotia. *J. Phys. Oceanogr.*, **23**, 1703–1726.

Thompson, K. R., and E. Demirov, 2006: Skewness of sea level variability of the world's oceans. *J. Geophys. Res. Ocean.*, **111**, 1–11.

——, D. G. Wright, Y. Lu, and E. Demirov, 2006: A simple method for reducing seasonal bias and drift in eddy resolving ocean models. *Ocean Model.*, **13**, 109–125.

——, R. H. Loucks, and R. W. Trites, 1988: Sea surface temperature variability in the shelf-slope region of the Northwest Atlantic. *Atmosphere-Ocean*, **26**, 282–299.

Tivy, A., S. E. L. Howell, B. Alt, S. McCourt, R. Chagnon, G. Crocker, T. Carrieres, and J. J. Yackel, 2011: Trends and variability in summer sea ice cover in the Canadian Arctic based on the Canadian Ice Service Digital Archive, 1960-2008 and 1968-2008. *J. Geophys. Res. Ocean.*, **116**.

Trenberth, K. E., and J. M. Caron, 2001: Estimates of meridional atmosphere and ocean heat transports. *J. Clim.*, **14**, 3433–3443.

Tulloch, R., and J. Marshall, 2012: Exploring Mechanisms of Variability and Predictability of Atlantic Meridional Overturning Circulation in Two Coupled Climate Models. *J. Clim.*, **25**, 4067–4080.

Urrego-Blanco, J., and J. Sheng, 2012: Interannual Variability of the Circulation over the Eastern Canadian Shelf. *Atmosphere-Ocean*, **50**, 277–300.

——, and ——, 2014a: Study on subtidal circulation and variability in the Gulf of St. Lawrence, Scotian Shelf, and Gulf of Maine using a nested-grid shelf circulation model. *Ocean Dyn.*, **64**, 385–412.

——, and ——, 2014b: Formation and distribution of sea ice in the Gulf of St. Lawrence: A process-oriented study using a coupled ocean-ice model. *J. Geophys. Res. Ocean.*, **119**, 7099–7122.

Våge, K., and Coauthors, 2011: The Irminger Gyre: Circulation, convection, and interannual variability. *Deep. Res. Part I Oceanogr. Res. Pap.*, **58**, 590–614.

Wang, Y., M. Claus, R. J. Greatbatch, and J. Sheng, 2017: Decomposition of the Mean Barotropic Transport in a High-Resolution Model of the North Atlantic Ocean. *Geophys. Res. Lett.*, **44**, 11,537-11,546.

——, R. J. Greatbatch, M. Claus, and J. Sheng, 2020a: Decomposing barotropic transport variability in a high-resolution model of the North Atlantic Ocean. *J. Geophys. Res. Ocean.*, 1–13.

——, J. Sheng, and Y. Lu, 2020b: Examining tidal impacts on seasonal circulation and hydrography variability over the eastern Canadian shelf using a coupled circulation-ice regional model. *Prog. Oceanogr.*, **189**, 102448.

Wang, Z., Y. Lu, D. G. Wright, and F. Dupont, 2010: Sea ice sensitivity to the parameterisation of open water area. *J. Oper. Oceanogr.*, **3**, 3–9.

Watelet, S., J.-M. Beckers, and A. Barth, 2017: Reconstruction of the Gulf Stream from 1940 to the Present and Correlation with the North Atlantic Oscillation. *J. Phys. Oceanogr.*, **47**, 2741–2754.

Weatherall, P., and Coauthors, 2015: A new digital bathymetric model of the world's oceans. *Earth Sp. Sci.*, **2**, 331–345.

Weller, G., 1968: Heat-energy transfer through a four-layer system: Air, snow, sea ice, sea water. *J. Geophys. Res.*, **73**, 1209–1220.

Worthington, L. V., 1976: *On the north Atlantic circulation*. Johns Hopkins University Press.

Wu, Y., C. Tang, and C. Hannah, 2012: The circulation of eastern Canadian seas. *Prog. Oceanogr.*, **106**, 28–48.

Xue, H., F. Chai, and N. R. Pettigrew, 2000: A Model Study of the Seasonal Circulation in the Gulf of Maine. *J. Phys. Oceanogr.*, **30**, 1111–1135.

Yankovsky, A. E., and I. Yashayaev, 2014: Surface buoyant plumes from melting icebergs in the Labrador Sea. *Deep. Res. Part I Oceanogr. Res. Pap.*, **91**, 1–9.

Yashayaev, I., 2007: Hydrographic changes in the Labrador Sea, 1960–2005. *Prog. Oceanogr.*, **73**, 242–276, https://doi.org/10.1016/j.pocean.2007.04.015.

Yeager, S., 2015: Topographic coupling of the Atlantic overturning and gyre circulations. *J. Phys. Oceanogr.*, **45**, 1258–1284.

Zhai, X., R. J. Greatbatch, and J. Sheng, 2004: Advective spreading of storm-induced inertial oscillations in a model of the northwest Atlantic Ocean. *Geophys. Res. Lett.*, **31**, 4–7.

Zhang, R., and G. K. Vallis, 2007: The role of bottom vortex stretching on the path of the North Atlantic western boundary current and on the northern recirculation gyre. *J. Phys. Oceanogr.*, **37**, 2053–2080.

——, T. L. Delworth, A. Rosati, W. G. Anderson, K. W. Dixon, H. Lee, and F. Zeng, 2011:

Sensitivity of the North Atlantic Ocean circulation to an abrupt change in the Nordic Sea overflow in a high resolution global coupled climate model. *J. Geophys. Res. Ocean.*, **116**.